UNIVERSIDADE DE SANTIAGO DE COMPOSTELA
Departamento de Física de Partículas
Instituto Galego de Física de Altas Enerxías

TESE DE DOUTORAMENTO

Measurement of the inelastic *pp* cross-sections using the LHCb experiment and development of a new vertex detector

Presentada por Álvaro Dosil Suárez

Dirixida por Prof. Abraham Antonio Gallas Torreira

Santiago de Compostela, Febreiro de 2017

USC
UNIVERSIDADE
DE SANTIAGO
DE COMPOSTELA

Measurement of the inelastic pp cross-sections using the LHCb experiment and development of a new vertex detector

Author: Álvaro Dosil Suárez
Advisor: Abraham Antonio Gallas Torreira

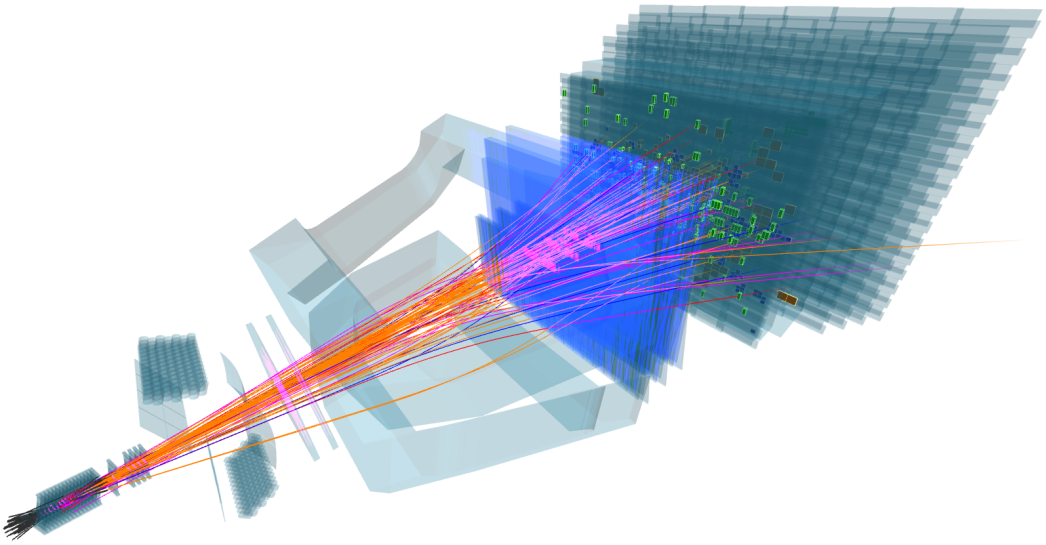

Figure 1: *Typical LHCb pp event collected in July 2015.* From the LHCb event display.

Text printed in Santiago de Compostela
First edition, February 2017

USC
UNIVERSIDADE
DE SANTIAGO
DE COMPOSTELA

D. ABRAHAM ANTONIO GALLAS TORREIRA, Profesor Contratado Doutor de Física Atómica, Molecular e Nuclear da Universidade de Santiago de Compostela, informa:

Que a memoria titulada "*Measurement of the inelastic pp cross-sections using the LHCb experiment and development of a new vertex detector*" foi realizada por Álvaro Dosil Suárez baixo a súa dirección e que constitúe a Tese que presenta para optar ao Grado de Doutor en Física.

Santiago de Compostela, a 17 de Febreiro de 2017.

Asdo. Abraham Antonio Gallas Torreira

Asdo. Álvaro Dosil Suárez

USC
UNIVERSIDADE
DE SANTIAGO
DE COMPOSTELA

Acknowledgements

There are plenty of people who helped me in many different ways along these years. It is not possible to explicitly mention all of them, I apologise for that and I hope that they feel my gratitude anyway.

Fist of all, I would like to express my gratitude to my supervisor Abraham Gallas for his support, advise and instruction. He is the first responsible of me finally completing my Ph.D. I thank also Bernardo Adeba for giving me the opportunity of joining the experimental high energy physics group of Santiago.

I also would like to thank all the members of the VELO upgrade group, specially Martin van Beuzekom, who creates around him a very comfortable environment to learn, even in the more stressful moments. To Heinrich Schindler, Paula Collins, Lars Eklund and Kazu Akiba that always had a prompt and very precise answer for any rising question.

My gratitude also to my co-workers in all tasks that I performed these years. To the members of the AIDA TLU group, David Cussans, Francesco Crescioli and Igor Rubinsky, the Heavy Ions and Fixed Target LHCb working group members and the QEE LHCb working group conveners and subconveners, specially to Alex Grecu. Thanks also to my co-analysts in the *pp* cross sections Xabier Cid, María Vieites, Cibrán Santamarina, Antonio Romero, Michael Schmelling and Abraham Gallas. A very special thanks to Eliseo Pérez and Antonio Pazos from whom I learned a lot about instrumentation and electronics, to Xabier who always kindly helped me to fix many issues, and to Marcos for keeping alive the CPD and also all our PCs. Thanks also to Nestor Armesto for helping me with the Monte Carlo generators tuning and for advising me about nice conferences where to present my work.

I thank the Fundación Barrié for the financial support that allowed me a closer participation in all my research activities.

Tamén teño que agradecerlles a todos os membros do Grupo de Altas Enerxías da Universidade de Santiago o gran entorno de traballo creado, en especial aos os meus compañeiros de despacho nas distintas épocas: Xabier, Paula, Víctor, Marcos, Brais, María, Julián, Carlos e Toño. Non poden faltar nestas liñas os compañeiros de mesa diarios: María, Julián, Toño, Pablo, Edgar, Juan, Martino, Eliseo e Abraham. Despois de tanto tempo con tan profundas conversas debemos estar moi cerca de atopar o sentido da vida, do universo e todo o demais. Tamén ao resto do grupo co cal, dunha forma ou outra, tiven o pracer de traballar: Cibrán, Diego, Antonio Fernandez, Antonio Pazos, Miriam, Miguel, Veronika, Jessica, José Angel e Máximo.

Por suposto, non pode faltar o meu amigo Pablo Rodríguez. Durante moito tempo compartimos inquedanzas, longas noites de toma de datos e kebab, e outros moitos momentos. Nada disto se poderá repetir, pero de ningunha forma se vai olvidar.

No eido mais persoal en primeiro lugar teño que agradecerlles a meus pais, Manolo e María Carmen, absolutamente todo. Sen o voso apoio e axuda non tería feito unha tese nin outras moitas cousas que me levaron a ser a persoa que son hoxe. Moitas grazas tamén ao meu irmán Alex que sempre está aí para o que precise. Grazas tamén a miña tía Tera que sempre me apoia en todo e aos meus avós, tanto os que están coma os que xa nos deixaron.

Un agradecemento moi especial tamén para Toño, Almu, Danieliña e ao novo pequecho; todas esas inquedanzas e problemas de doutorandos que compartimos axudan a ver mellor o camiño a seguir. Moitas grazas a todos os meus amigos de Cuns: Daniel, Manuel, Martín, Jos, Alberto, Pablo, Fran, Ramón, Pablo (Teso), Jorge e todos os demais; convosco cerca sempre me sentín capaz de todo. Aos meus compañeiros de SOMOSCuns non podo agradecerlles nada que me levara a acabar antes esta tese. Se non batéramos probablemente tería rematado a tese moito antes; pero seguramente o mundo sería un pouco peor e eu sentiríame menos realizado. Moitas grazas tamén aos meus compañeiros de fatigas do CC Revotas por axudarme a desconectar.

Finalmente quero darlle as grazas Sandra. San, fuches a persoa que mais sufríu esta tese, seguramente incluso mais ca min. Moitas gracias pola túa paciencia, os teus ánimos, o teu consello e por ese sorriso que ilumina todo ao teu redor e que me alegra todos os días.

Álvaro

"Non lle poñades chatas â obra namentras no se remata. O que pense que vai mal que traballe n´ela; hay sitio para todos."

Álbum Nós (1931),
Alfonso Daniel Rodríguez Castelao

USC
UNIVERSIDADE
DE SANTIAGO
DE COMPOSTELA

Abstract

In this thesis, measurements of the inelastic cross-sections of proton-proton collisions at centre-of-mass energies of $\sqrt{s} = 5\,\text{TeV}$ and $\sqrt{s} = 13\,\text{TeV}$ with the LHCb detector are presented. The cross-section measurements are performed using pp collisions with at least one prompt long-lived charged particle in the pseudorapidity range $2 < \eta < 5$ and momentum $p > 2\,\text{GeV}/c$. The extrapolation to the full phase-space is also performed using the official LHCb simulation generated using the Pythia 8 event generator.

During the second long shut down of the LHC (2018-2019), the LHCb experiment will be upgraded, and all its subdetectors will be modified. Specifically, the Vertex Detector (VELO) will move from silicon strips to silicon pixels. The new readout ASIC will be the VeloPix, a successor of the Medipix family of ASICs. The Single Event Upset robustness of the Medipix3 chip, an ancestor of the VeloPix, is studied in order to evaluated the radiation hardness of the VeloPix. the Medipix3 chip, was addressed. Different beam tests at a cyclotron facility were designed and performed with the subsequent data analysis.

Using the Timepix3, a successor of the Medipix3, a telescope was developed. This telescope was designed to test the sensors and readout electronics prototypes for the VELO upgrade. The design and the performance of this telescope under very high particle incident rates are also presented.

USC
UNIVERSIDADE
DE SANTIAGO
DE COMPOSTELA

Limiar

Nesta tese, preséntanse as medidas da sección eficaz de colisións potón-protón a enerxías no centro de masas $\sqrt{s} = 5\,\text{TeV}$ e $\sqrt{s} = 13\,\text{TeV}$ usando o experimento LHCb. Para estas medidas da sección eficaz de colisións pp usáronse trazas cargadas, xeradas directamente na colisión dos protóns, que viviron o suficiente como para atravesar os subdetectores de trazado e no rango de pseudorapidez $2 < \eta < 5$ e $p > 2\,\text{GeV}/c$. Ademais, a extrapolación a todo o espazo de fase foi calculado usando a simulación oficial de LHCb, xerada usando o xerador de eventos Pythia 8.

Durante a segunda parada técnica larga do LHC, o experimento LHCb será mellorado e modificaranse todos os seus subdetectores. En concreto, o VELO pasará de ser un detector de micro-pistas de silicio a un detector de píxeles de silicio. O novo ASIC de lectura será o VeloPix, que é un sucesor da familia de ASICs Medipix. Para avaliar a resistencia á radiación dos compoñentes do VeloPix estudouse a resistencia aos *Single Event Upsets* de un dos seus antepasados, o Medipix3. Deseñáronse e leváronse a cabo varios tests con feixes de partículas nun ciclotrón e posteriormente analizáronse os datos obtidos.

Usando o sucesor do Medipix3, chamado Timepix3, o grupo de mellora do VELO desenvolveu o telescopio Timepix3. Este telescopio foi deseñado para probar os sensores e os prototipos de electrónica de lectura para a mellora do VELO. O deseño e a resposta deste telescopio baixo unha moi alta intensidade de partículas incidentes tamén se presenta.

USC
UNIVERSIDADE
DE SANTIAGO
DE COMPOSTELA

Contents

USC
UNIVERSIDADE
DE SANTIAGO
DE COMPOSTELA

1 Introduction

The Standard Model (SM) of Particles Physics is the theory that describes the fundamental particles and their interactions in nature. It incorporates three fundamental forces, strong, electromagnetic and weak, with which it explains most of the phenomena observed in Nature. The SM unifies electromagnetism and weak interactions as the electroweak (EW) force, and also includes the strong force. Despite of huge efforts from the theoretical community, gravity could not be included in the SM yet.

The SM is a very successful theory. It explains the behaviour of particles with very high accuracy and all predictions are self-consistent. Nevertheless, it cannot explain the existence of dark energy and dark matter, the non-zero mass of the neutrinos or the ratio between matter and antimatter. The SM is able to explain the matter/antimatter asymmetries found by the experiments so far, but it cannot explain the matter/antimatter asymmetry observed in the visible universe. Because of this, many New Physics models have been developed in the last years to cope with these problems. These models can be tested in High Energy Physics (HEP) experiments.

Calculating the SM predictions for some processes is reasonably easy, but for other cases it is really complicated and theorist have to rely on phenomenological models to make predictions. This is the case of strong interactions with low momentum transfer between particles. These phenomenological models use the available data and extrapolate the results to unexplored regions. They provide a very accurate description of the known region, but predictions suffer from large uncertainties when moving away from there. Thus, more data is required to improve the precision of the predictions. These models are included in particle physics simulation frameworks to recreate as realistic as possible particle interactions.

The Large Hadron Collider (LHC) is a circular particle accelerator located at CERN, near Geneva (Switzerland). Currently, it is the largest and most powerful particle accelerator in the world. The LHC was designed to collide protons at a nominal centre-of-mass energy of $\sqrt{s} = 14\,\text{TeV}$, nevertheless very stable beam conditions are attainable at $\sqrt{s} = 13\,\text{TeV}$ so this was the maximum energy achieved so far is $\sqrt{s} = 13\,\text{TeV}$. Collisions take place in four different points of the LHC ring, where the four experiments ATLAS, CMS, LHCb and ALICE are located. The LHC can also accelerate heavy ions, and provide p-Pb, Pb-p or Pb-Pb collisions. The four LHC experiments have different designs in order to study specific physics processes. ATLAS and CMS are general purpose detectors, LHCb is a flavour physics dedicated experiment and ALICE is designed to study heavy ion collisions.

The research in this thesis has been done within the LHCb collaboration. As afore-

mentioned, LHCb was designed to study *CP*-violating processes and search for rare *B* and *D* decays. Nevertheless, in the last years LHCb has proven its feasibility as a general purpose experiment, performing analyses with neutrinos and joining the LHC heavy ions runs. The physics goals of the experiment led to a forward spectrometer design allowing to record low angle products of the *pp* interaction. Furthermore, it has an excellent vertex, momentum, and a very discriminating particle identification.

The first part of this thesis aims to understand one of the most abundant and inclusive of LHC processes, proton-proton inelastic collisions. Since the earlies days of hadron collider physics, total *pp* cross-sections have been measured and puzzled over. The inelastic cross-section is a fundamental observable in high-energy hadronic interactions, and currently it is not possible to calculate its value from first principles. It is also important in astroparticle physics where one of the shower maximum, that is one of the most important observables, strongly depends on the inelastic proton-air cross-section. The calculation of the hadron-nucleus cross-sections require the knowledge of the inelastic *pp* cross-section. Currently, it is not possible to calculate its value from first principles

In this thesis results of the inelastic *pp* cross-section measurements at the centre-of-mass energies of $\sqrt{s} = 5\,\text{TeV}$ and $\sqrt{s} = 13\,\text{TeV}$ using the LHCb detector are presented. Due to the special LHCb design, measurements are obtained in a unique kinematic region, complementary to ATLAS, CMS and ALICE measurements.

LHCb is performing much better than expected since it started in 2010, and nowadays most of physics analyses are dominated by statistical uncertainties. The current data acquisition system permits to collect up to $\sim 1.5\,\text{fb}^{-1}$. Keeping this data collection rate, duplicate the current statistics would take four years more, what is not very rewarding. To increase the acquisition rate the detector must be modified. The core of the upgrade will be focused on the modification of the trigger system, but all subdetectors will be upgraded as well.

The VErtex LOcator (VELO) is the detector surrounding the *pp* interaction point. It is the first measurement point of the emerging particles and it must be able to separate the primary interaction vertex from the decay vertices of *B* and *D* hadrons. The upgraded VELO will be based in planar silicon pixel technology sensors, which will be read out by a dedicated Application Specific Integrated Circuit (ASIC) called VeloPix. The VeloPix is the last successor of the Medipix family of chips. Two years ago, before the arrival of the Timepix3, the Medipix3 was the most advanced chip from the Medipix family. Hence, it was studied to optimize the VeloPix design. The new VELO will have to work under heavy radiation conditions. In this thesis, the beam test and subsequent data analysis of the Medipix3 chip under heavy ions irradiation is presented. This beam test provided valuable information about the behaviour of the basic technology cells that would be used in the VeloPix.

In order to evaluate the electronics and sensor prototypes behaviour under particle radiation, we need to reconstruct these particle trajectories. In the beam tests, the particle tracks that go through the device under test are reconstructed using a telescope. The VELO upgrade group decided to change. The Timepix chip based telescope for a new one based on Timepix3 chips. The performance of the new telescope under high particle incident rate is also described.

This thesis is divided as follows. Chapter 2 overviews the most important aspects of the Standard Model and Quantum Chromodinamics. It also motivates the measurement

of the pp cross-section and describes how the soft QCD processes are generated in simulations. The LHCb experiment is presented in chapter 3, describing the detector and its performance. Chapter 4 presents the measurement of the pp inelastic cross-sections at centre-of-mass energies of $\sqrt{s} = 5\,\text{TeV}$ and $\sqrt{s} = 13\,\text{TeV}$. Chapter 5 details the plans to upgrade the detector, with an emphasis on the upgrade of the VELO. Chapter 6 presents the evaluation of the Single Event Upsets (SEU) tolerance of the Medipix3. In Chapter 7, the performance of the Timepix3 telescope under high intensity particle rate is studied. Finally, the conclusions are shown in Chapter 8.

USC
UNIVERSIDADE
DE SANTIAGO
DE COMPOSTELA

2 Theory

2.1 The Standard Model of particle physics

The Standard Model (SM) [1] is a Quantum Field Theory (QFT) that provides a description of three of the four known forces of nature and all particles that have been identified so far [2–5]. Figure 2.1 shows the particle content of the SM. It contains two types of particles: fermions and gauge bosons (or "force-carriers"). Each fermion f has an anti-particle $\bar{f}$, which carries the opposite quantum numbers, but the same mass. The charged particles (quarks, electrons, muons, taus and W-bosons) can interact by exchanging photons, and in general all fermions can interact through the the weak force by exchanging W or Z bosons. This interactions are described by Quantum Electrodinamics (QED). On the other hand, quarks can interact by exchanging gluons, and these interactions are described by Quantum Chromodinamics (QCD). Quantum Chromodinamics corresponds to the symmetry group $SU(3)_C$ of color (C), while the EW interaction is described by the group $SU(2)_T \otimes U(1)_Y$ of weak-isospin (T) and hypercharge (Y). Then, the full gauge symmetry group of interactions in the SM is given as the direct product

$$G_{SM} = SU(3)_C \otimes SU(2)_T \otimes U(1)_Y. \tag{2.1}$$

Quantum Chromodynamics is the gauge theory for strong interactions that bind quarks together. QCD also mediates the interaction forces of hadrons and thus controls de formation of nuclei. The QCD Lagrangian defines the quark and gluon interactions and their propagators. It is given by

$$\mathcal{L} = \sum_f \bar{\psi}_{f,a}(i\gamma^\mu \partial_\mu \delta_{ab} - g_s \gamma^\mu t^C_{ab} \mathcal{A}^C_\mu - m_f \delta_{ab})\psi_{fb} - \frac{1}{4} F^A_{\mu\nu} F^{\mu\nu}_A, \tag{2.2}$$

where γ^μ are the Dirac γ-matrices, f is the flavour index ($f = u, d, c, s, t, b$) and m_f the mass of the quarks, with a colour index a that runs from a $= 1$ to $N_c = 3$. This means that the quarks come in three *colours* (red, green and blue), and the corresponding anti-colours. Of course, the colour charge does not have any connection to visible light, it is just a label. The notion of colour charge was introduced to explain how quarks could coexist inside hadrons, in otherwise identical quantum states without violating the Pauli exclusion principle.

The $\mathcal{A}^C_\mu$ correspond to the gluon fields, with C running from 1 to $N_c^2 - 1 = 8$, *i.e.* there are 8 kinds of gluon. g_s is the gauge coupling parameter which is related to the strong coupling constant by $\alpha_s = \frac{g_s^2}{4\pi}$. Finally, $F^A_{\mu\nu}$ is the gauge invariant gluon field strength

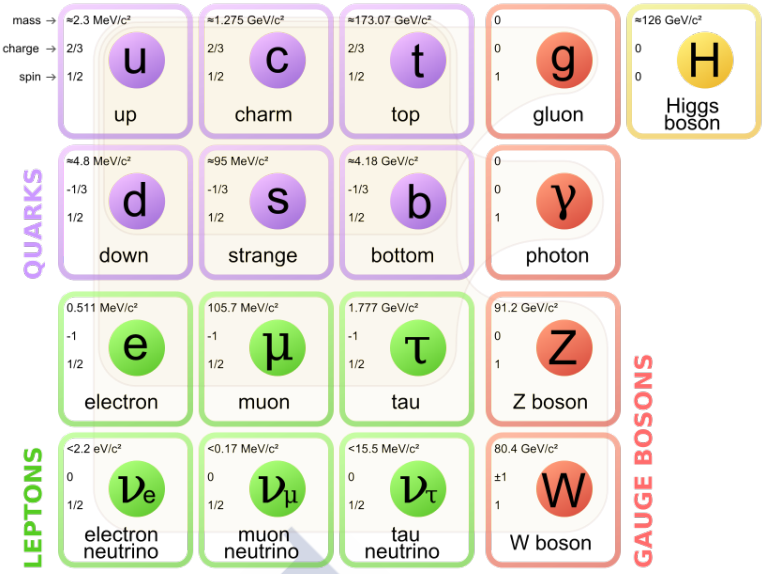

Figure 2.1: The particle content of the Standard Model [6], showing fermions in blue (quarks) and green (leptons) and the gauge bosons in red (g, γ, Z and W) and yellow (Higgs).

tensor

$$F^A_{\mu\nu} = \partial_\mu \mathcal{A}^A \nu - \partial_\nu \mathcal{A}^A_\mu - g_s f^{ABC} \mathcal{A}^B_\mu \mathcal{A}^C_\nu, \tag{2.3}$$

where f_{ABC} are the structure constants of the SU(3) group.

Each gluon carry some combination of colour charges and anti-charge. Consequently, they can interact with quarks as well as with other gluons. Gluons and quarks are the only particles carrying a colour charge, so these are the only particles of the Standard Model that interact through QCD.

Even though α_s is called a constant, it is not constant at all. As it can be seen in Figure 2.2, it has a strong dependence on the momentum transfer within an interaction. This has two important effects. At low energies α_s increases dramatically and leads to an effect called *confinement*. This phenomenon describes the fact that colour charges cannot be isolated. Towards large energies, α_s is very small and leads to an *asymptotic freedom* of the coloured particles. This means that quarks behave as (quasi-)free particles while they keep at small distances. Furthermore, the asymptotic freedom also leads to the fact that only colour-neutral objects can exist, so quarks cannot be found as free particles. The particles composed by particles interacting strongly (hadrons), are either made of three quarks (baryons) or quark-antiquark pairs (mesons). Recently a four-quark state was discovered [7]. It is called tetra-quark, but it is not clear if it is an actual four-quark particle or a molecule-like two-meson system.

As it was already mentioned, the $SU(2)_T \otimes U(1)_Y$ symmetry group represent the unified electroweak sector of the SM. Gauge theory predicts that a triplet of massless bosons, W_μ, is associated to the $SU(2)_T$ group of the weak interaction. The conserved quantum number is the weak isospin T. Another massless boson, B_μ, appears associated to the $U(1)_Y$ group of the electromagnetic interaction. The conserved quantum number in this case is the hypercharge Y. It is constructed by $Y = Q + T_3$, where Q is the electric charge and T_3 is the third component of the weak isospin. The W_μ bosons can only

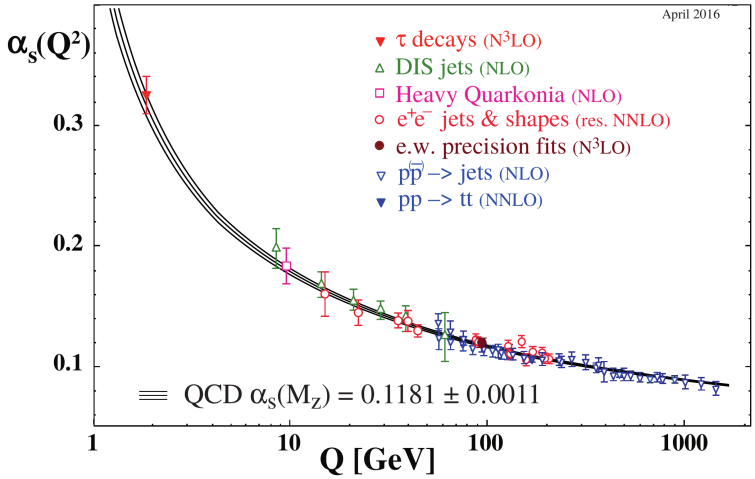

Figure 2.2: Summary of measurements of α_s as a function of the energy scale Q. The degree of QCD perturbation theory used in the extraction of α_s is indicated in brackets (NLO: next-to-leading order; NNLO: next-to-next-to-leading order; res. NNLO: NNLO matched with resumed next-to-leading logs; N^{3}LO: next-to-NNLO) [8].

interact with left-handed particles or right-handed anti-particles with weak isospin. As all particles carry hypercharge, the B_μ boson can couple to all particles.

The symmetry of the electroweak interaction is spontaneously broken by the Higgs mechanism. As a result of the interaction with the Higgs field, EW bosons combine into the massive particles $W^\pm$ ($\approx 80\,\text{GeV}$) and Z ($\approx 91\,\text{GeV}$) and the massless photon. $W^\pm$ bosons are the mediators of the charged currents and couple only to left-handed particles. Z is the mediator of the neutral current and couples with different strength to left- and right-handed particles. Due to the high mass of $W^\pm$ and Z bosons, the weak interaction is only short-ranged. The interaction with the Higgs field gives also masses to the elementary fermions.

The electromagnetic mediator is the photon, γ. It is a massless and chargeless particle. It couples to the electric charge of particles but does not self-interact, since it does not carry charge itself. As it is a massless particle, the range of the electromagnetic interaction is infinite.

According to gauge symmetry, the fundamental particles described by the SM have to be massless. Mass terms, such as for massive W and Z bosons, would violated the local gauge invariance of the theory. The Higgs mechanism [9, 10] solves this issue by introducing an additional doublet of complex scalar (spin 0) fields. A combination of these fields creates the Higgs potential which has a non-zero ground state and spontaneously breaks the electroweak symmetry. This leads to the massive bosons of the weak interaction but also predicts another massive spin 0 particle that was called the Higgs boson. This particle was discovered at the LHC in 2012 [11,12]. Furthermore, also the fermion masses are generated by Yukawa interactions which describe the coupling between fermion fields and the Higgs potential.

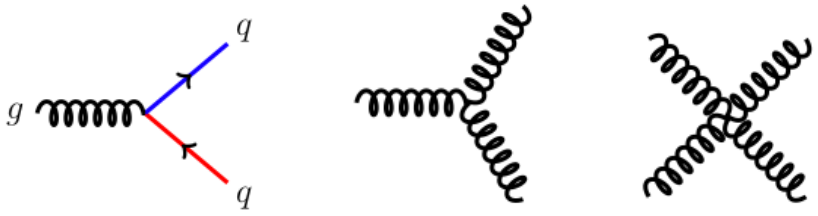

(a) (b)

Figure 2.3: Basic building blocks of the QCD Feynman diagrams. (a) Two quarks interacting with one gluon. (b) Interaction of three (left) and four (right) gluons.

2.1.1 QCD predictions

Searches of new physics can be made through direct or indirect searches. In direct searches the idea is to look for kinematic observables or mass of new particles. This method is likely to be used in processes not described by the standard model, but the problem is that it is only sensitive to particles in the mass range of the system energy. Indirect searches look for new physics by observing deviations from predictions. They can access higher energy scales and observe new physics before direct searches. Typical indirect searches make use of processes which occur to first order through loop transitions. The observables associated to such processes, such as the branching ratio, are typically low and can be altered by the incorporation of any undiscovered particle in the loop process. The problem is that indirect searches need precise predictions.

New particles will most likely appear as either missing energy signatures or through their decays to known particles. In the former case, it is necessary to have a detailed understanding of the particle background at the LHC, produced by pile-up or by multiple quark-quark interactions within a hadron collision. In the later case a very precise measurement of the known particles decays is needed, so that unusual decays can be identified. In both cases, these searches rely upon SM results and in particular the theory of QCD.

QCD is a non-linear theory so it cannot be analytically solved and directly tested. Nevertheless, there are plenty of indirect evidences that supports this theory. QCD interaction is so strong that perturbative approximations often fail. So, few precise predictions can be made from the theory. The Feynman rules of QCD involve a quark-antiquark-gluon ($q\bar{q}g$) vertex, a 3-gluon vertex (both proportional to g_s), and a 4-gluon vertex (proportional to g_s^2). Figure 2.3 shows these types of vertices in a schematic representation known as Feynman diagrams [13].

As shown in Figure 2.2, α_s increases very quickly at low Q^2. This makes very difficult to calculate the cross-section for QCD interactions. The cross-section for a particular process is proportional to the square of the matrix element for that process. The matrix element is calculated by adding all the contributions from all the Feynman diagrams that could be responsible for that process. Each diagram gives a contribution proportional to ${\alpha_s}^{n/2}$, where n is the number of vertices. When $\alpha_s \ll 1$ the matrix element can be evaluated using a perturbative approximation.

Perturbation theory (pQCD) models the QCD interactions assuming no interactions and applying small corrections over them. The simplest diagrams for an interaction (Lead-

ing Order, LO) must have at least two vertices, and so give contributions proportional to α_s. More complex diagrams (Next-to-Leading Order, NLO, Next-to-Next-to-Leading Order, NNLO, and so on), give contributions with larger powers of α_s. Thus, when $\alpha_s \ll 1$, the LO diagrams are a small correction to the ground state, and NLO diagrams even a smaller correction. Therefore, in order to calculate a matrix element with reasonable precision only requires to calculate the lowest level diagrams, although greater accuracy is achieved by adding higher order contributions.

At Q^2 values with $\alpha_s \simeq 1$, the perturbative approximation becomes invalid, since the contribution from higher order diagrams cannot be considered small. There are therefore two regimes of QCD: perturbative and non-perturbative, called also hard and soft QCD respectively in reference to the size of the momentum transfer. In a complete high-energy collision, many different physics (sub-)processes contribute to the total observed activity. The factorisation theorem [14] permits to treat separately these two regimes, using perturbative methods to calculate the matrix elements for hard processes and different models to calculate soft QCD processes. In the following a brief review of the soft QCD main aspects that are relevant for hadron-hadron collisions is shown.

2.1.1.1 Parton distribution functions

Protons and neutrons are made up of 3 valence quarks, but assuming that they consist just of these three quarks in a bag is too simple. Actually, those valence quarks are embedded in a sea of gluons and virtual quark-antiquark pairs. This is easily illustrated by comparing the $\sim$2 MeV mass of the up quark and the $\sim$5 MeV mass of the down quark with the total mass of the proton 938 MeV. All of these particles composing the hadrons are called partons.

Parton distribution functions (PDFs) represent the probability of finding a parton with a certain momentum fraction x inside the proton at a squared energy scale, Q^2. The probability of a certain interaction is governed by these PDFs. Even though computational methods such lattice QCD calculations are making progresses in calculating PDFs, it is not possible to calculate them from first principles. The known parton distribution functions are instead obtained by fitting observables to experimental data.

Different methods of fitting to experimental results produce PDF sets with different behaviour when they are extrapolated beyond the energy range of those results. The CT14 PDFs [15] provided by the CTEQ collaboration are shown in Figure 2.4.

2.1.1.2 Proton-proton interaction types

Nowadays, the proton-proton interactions are understood to consist of two interaction types: *elastic* and *inelastic*.

Elastic scattering consists of all reactions of the type

$$A(p_A)B(p_B) \longrightarrow A(p'_A)B(p'_B), \tag{2.4}$$

where A and B are particles with four momenta p_A and p_B. The only exchanged quantity is momentum, remaining all quantum numbers and masses unaltered. Inelastic scattering covers every other interaction type

$$AB \longrightarrow X \neq AB. \tag{2.5}$$

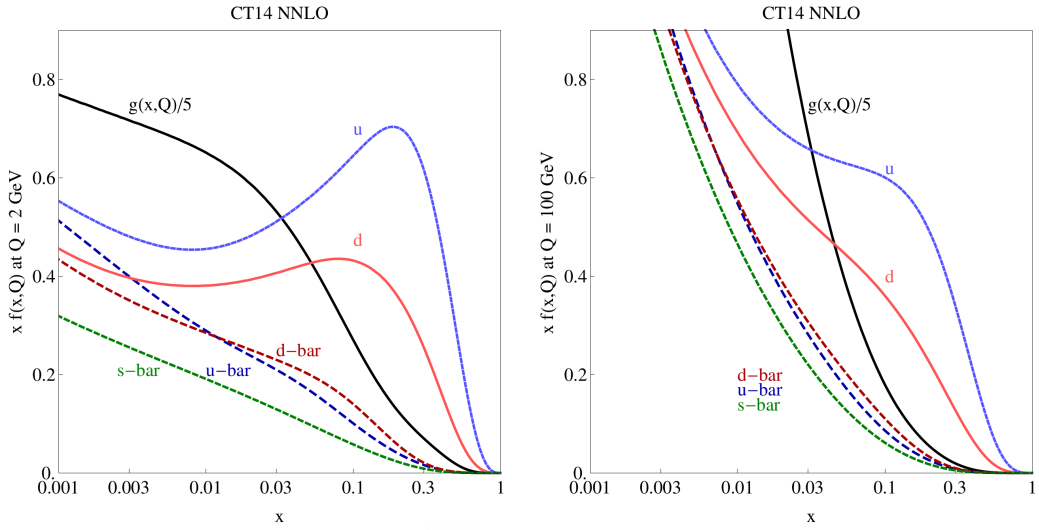

Figure 2.4: PDFs of quarks and gluons (scaled by 5) as a function of the Bjorken x scaling variable provided by the CTEQ collaboration, at $Q^2 = 2\,\text{GeV}$ (left) and $Q^2 = 100\,\text{GeV}$ (right).

In this case one or more quantum numbers are changed and one or more particles are produced. Thus, the total hadron-hadron cross section can be divided in two components,

$$\sigma_{tot}(s) = \sigma_{el}(s) + \sigma_{inel}(s), \tag{2.6}$$

where s is the Mandelstam variable $s = (p_A + p_B)^2$, the squared collision energy in the centre-of-mass frame.

A qualitative classification of the inelastic interactions can be made, based on whether the final states looks like the decay of an excitation of the beam particles (*diffractive*) or not (*non-diffractive*). This two topologies can be distinguished by finding large rapidity gaps somewhere in the final state that would separate such excitations. The rapidity of a particle is defined as

$$y = \frac{1}{2} \ln \frac{E + |\mathbf{p}|c}{E - |\mathbf{p}|c}, \tag{2.7}$$

where E is the particle total energy and $|p|$ is the magnitude of the four-momentum. The "large" rapidity gap is of arbitrary definition, being usually between 3 and 5 rapidity units, so there is not an observable giving a correct classification.

The diffractive events at the same time can be classified in three classes depending on their topology:

Double-diffractive events (DD): Both beam particles are diffractively excited and hence neither of them survive the collision intact ($p + p \to X + X$).

Single-diffractive events (SD): Only one of the beam particles gets excited and the other survives intact ($p + p \to p + X$).

Central diffractive events (CD): Both of the beam particles survive intact, leaving an excited system in the central region between them ($p + p \to p + X + p$). See for example Ref. [16]. Since the protons can in turn dissociate or not, one has to distinguish between elastic and inelastic central exclusive processes.

From the experimental point of view, the identification of diffractive processes is very difficult. LHCb cannot measure elastic interactions, so they are not going to be considered in this thesis.

The inelastic cross-section can be written as

$$\sigma_{inel}(s) = \sigma_{DD}(s) + \sigma_{SD}(s) + \sigma_{CD}(s) + \sigma_{ND}(s). \tag{2.8}$$

Here the non-diffractive (ND) cross-section corresponds to events which do not contain rapidity gaps.

Non-diffractive events make up the bulk of the inelastic cross-section and are modelled reasonably well by tuned Monte Carlo generators. Diffractive events are poorly understood, and their comprehension is critical to an understanding of the inelastic cross-section.

2.1.1.3 Underlying event

In events containing a hadron-hadron interaction, the underlying event (UE) represents the activity which is not directly associated with the interaction. This is primarily multi parton interactions (MPI) activity but measurements may unavoidably include contributions from other effects, as beam remnant or pile-up of different beam-beam interactions. Particles in the underlying event come in general from soft QCD processes and the energy scales involved are too low for perturbative methods to be used. Instead, these processes are described by approximate models, with free parameters adjusted to match experimental results. As well as potentially improving understanding of soft QCD, if the underlying event can be accurately modelled then it can be removed from the analyses of hard scattering processes where it is an inconvenient background. Nevertheless, the three main components of the underlying event do not vary in the same way with the centre-of-mass energy of the collision, so a good understanding of the UE at 5 TeV do not guarantee a match at 13 TeV.

2.1.1.4 Multiple parton interactions

As it was already pointed out, the proton is a very complicated structure. If in the study of a hadronic collision only isolated parton collisions are considered the result obtained is not physical. For example, the calculation of the two partons cross-section at $\sqrt{s} = 1\,\text{GeV}$ producing two jets with $p_\text{T} > 2\,\text{GeV}/c$ becomes much larger than the observed cross-section for proton-proton collisions, as can be seen in Figure 2.5.

The approach to fix this issue is to include the possibility of having multiple partonic interactions within a single hadron-hadron collision, considering the protons as a bunch of partons. Hence, if a single hadron collision contains two partonic interactions, it will count twice towards σ_{parton} but only once towards σ_{hadron}. Therefore, each hadron collision will contain a mean number of parton interactions $\bar{n} = \sigma_{parton}/\sigma_{hadron}$. Each interaction is assumed to happen independently, and so the number of interactions in a particular hadron collision is Poisson-distributed.

The MPI approach is supported experimentally by the pairs of jets with balanced p_T within multi-jet events. If all jets would be generated in the same parton-parton interaction they would all conserve p_T as an ensemble.

MPIs cannot be completely described by perturbative QCD, and this requires a phenomenological description involving parameters that must be tuned with the help of data.

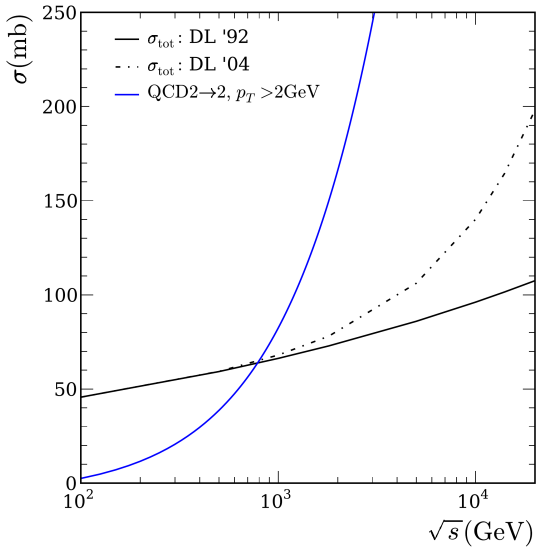

Figure 2.5: Total cross-section (black) modelled using two different parametrizations [17,18] and QCD jet production cross section above 2 GeV (blue) [19].

MPI models give good performance simulating hadron collisions, and are commonly used in general purpose Monte Carlo generators.

2.1.2 *pp* collisions at the LHC

The LHC collides protons at a centre-of-mass energy of up to $\sqrt{s} = 13\,\text{TeV}$. At these energies, the interaction between the protons becomes very complex. If the momentum transfer of the interaction is small, the collision can be described by scattering of two compound objects. When the momentum transfer is large, the proton breaks up and the quarks and gluons join the collision. In a proton-proton collision quark-quark, gluon-gluon or quark-gluon interactions can happen, and depending on the momentum transfer the interactions can be classified in hard or soft processes.

A hard scattering process involves necessarily one or two partons which carry a large momentum fraction. The resulting large momentum transfer in the interaction is of the order of the "hard" energy scale, which is typically $\leq 1\,\text{GeV}/c^2$. In this processes, the production rates and event properties can be calculated using perturbation theory. The large amount of energy involved in a hard process allows the creation of heavy particles. The emerging kind of particles depend on the mass of the produced particles, the available energy in the process and the colliding particle species. The production cross section for specific particles in proton-(anti)proton collisions is shown in Figure 2.6.

In real life, processes with a very low cross-section are contaminated by soft interactions. The typical momentum transfer in soft processes is of the order of a few hundred MeV^2. They cannot be calculated using perturbative methods and their description is made using a phenomenological approach. Predictions are less precise, mainly when working at unexplored high energies.

Figure 2.7 shows a typical proton-proton interaction at the LHC. In the picture, time evolves from left to right. Thus, in the left part of the image the two incident protons can

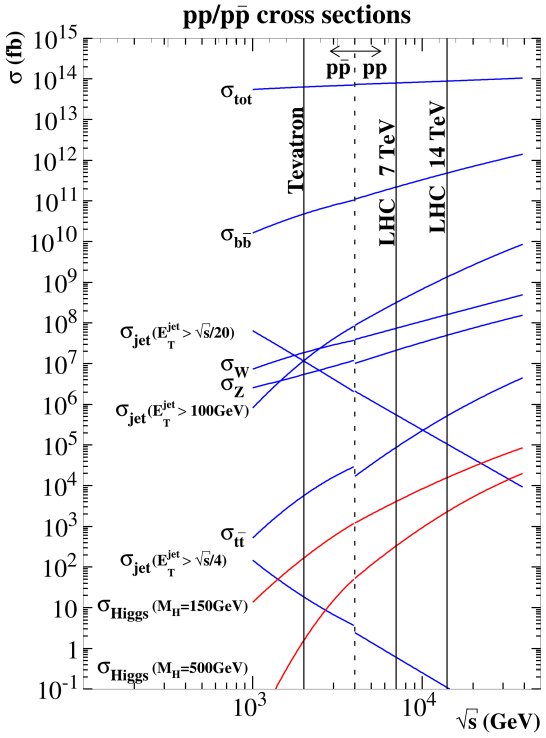

Figure 2.6: Proton-(anti)proton cross-sections as function of $\sqrt{s}$. The kink represents the transition from $p\bar{p}$ to pp [20].

be seen. The interaction takes place between their partons by strong interaction. Part of the original proton usually survives the collision and it is only slightly deflected from its original flight direction. This part is the so-called *beam remnant*. In a hard parton interaction a heavy resonance can be produced, such as the Z boson in this process. Hard processes are accompanied by initial-state radiation (ISR) of photons or soft gluons. In analogy, the generated partons radiate bremsstrahlung or gluon-strahlung, producing the final-state radiation (FSR). Furthermore, the soft interactions between partons also produce quarks or gluons that finally result in multiple particle production of light hadrons.

As quarks and gluons cannot be found isolated in nature, the partons produced by the mentioned processes must all form colour-neutral hadrons. This procedure is called hadronisation. Due to the low momentum transfer between partons it cannot be calculated using perturbative methods and thus it is studied using phenomenological models. This soft component of a collision is the underlying event, and is crucial for most of the data analyses.

2.2 Monte Carlo event generators

Monte Carlo generators (MC) are programs that simulate particle physics events with the same probability as they occur in nature. They are widely used for signal and background estimates. The simulation of a pp collision is a very complex procedure, and the different generators have different approaches to the problem.

Where possible, the probability distributions are calculated from first principles. In MC

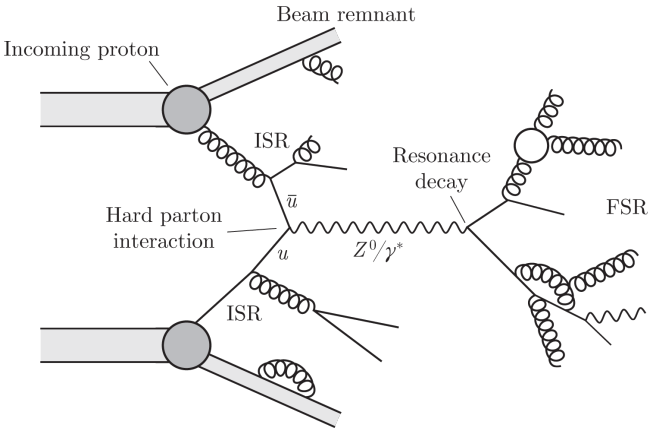

Figure 2.7: Illustration of an inelastic pp collision at the LHC. Figure taken from [21].

event generators a typical event is factorized into steps: the hard process calculation, initial state radiation (ISR), final state radiation (FSR), underlying event, and hadronization. In this way the hard QCD regime of the first three steps can be separated from the soft QCD regime of the final two steps to provide a complete event description. However, the underlying event and hadronization are not predicted via perturbative QCD. The models also include free parameters, which are adjusted to best reproduce experimental measurements. This process is called *tuning*. Technically, the tuning parameters can be modified independently, but this can lead to non physical results. Thus, the parameters need to be modified in groups. Each of these group of parameters, optimized by comparing generator predictions to real data distributions, is called a "tune". Each MC generator can have many tunes.

2.2.1 The Pythia generator

Pythia is a general purpose event generator to simulate collisions between e^-, e^+, p and $\overline{p}$ in various combinations. It is used widely used by the high-energy physics community. It splits between an older (Pythia 6 [22]) and a newer (Pythia 8 [23]) version of the generator. The newer is a complete re-write of the older Fortran code in C++, with some new features introduced as well. Furthermore is the only maintained version. However, the basic physics content is the same. Pythia treats each hadron as a set of partons characterized by parton distributions. Initial parton shower is started by a parton from each set. One parton from each of the initial showers participates in a hard collision, where a number of outgoing partons is produced. Other partons from the showers may experience semihard interactions. The fragmentation process into the colourless hadrons takes place via the string fragmentation (so-called Lund model is used), cluster decays and decays of unstable particles and resonance.

2.2.1.1 Pythia tunes

The Pythia generator includes many steering parameters which define physics processes and control phenomenological models. These parameters are typically tested and optim-

ised using data. A fundamental input to these parameters are various soft QCD measurements, such as charged particle multiplicities, cross-section measurements, energy flow or production ratios of different particle species.

One of these tunes is the LHCb tune [24]. It contains the default parameters to simulate pp collisions in LHCb. It can be implemented in Pythia 6 as well as Pythia 8, providing almost identical results.

More examples of Pythia tunes are "Tune 4Cx", "ATLAS MB Tune A2-CTEQ6L1", "Monash 2013" and many others.

2.2.2 The EPOS generator

EPOS provides within a unique theoretical scheme the initial conditions for a hydrodynamical evolution in proton-proton, proton-ion, and Heavy Ion collisions. EPOS stands for **E**nergy conserving quantum mechanical multiple scattering approach, based on **P**artons (parton ladders) **O**ff-shell remnants **S**plitting of parton ladders. The initial conditions are generated in the Gribov-Regge [25] multiple scattering framework. Gribov-Regge theory starts from the hypothesis that the T-matrix of the scattering process can be written as a product of elementary objects called Pomerons. Each Pomeron is identified with a parton ladder, that is composed of a pQCD hard process plus initial and final state linear parton emission. Several parameters that tune the soft elementary interaction are essentially are essentially optimized to reproduce measured pp cross-section distributions from different experiments and various centre-of-mass interaction energies. The produced partons are generally off-shell, giving rise again to parton emissions.

A dedicated version of EPOS was released for LHC. EPOS LHC is tuned with a single parameter set to reproduce any kind of hadronic interactions from h-A to A-B, where h can be π, K or p and A or B range from 1 to 210 nucleons. The energy range is from 40 GeV in the laboratory frame to more than 1000 TeV centre-of-mass energy (about 10^{21} eV in the lab frame).

USC
UNIVERSIDADE
DE SANTIAGO
DE COMPOSTELA

3
Experimental setup

3.1 CERN accelerator complex

The European Organisation for Nuclear Research (CERN) [26] was founded in 1954 and since then it was one of the most prestigious research centres in the world. Many important discoveries as the discovery of the W and Z bosons [27] and more recently the Higgs Boson [28] have been made at CERN. These discoveries lead to Carlo Rubbia and Simon van der Meer in the first case and Peter W. Higgs and François Englert for the second to be awarded with the Nobel Prize [29, 30]. These big goals could be achieved through the accelerator infrastructure provided.

What were high energy colliders in their own are now parts of the injection chain to the current world largest and most powerful particle accelerator, the Large Hadron Collider (LHC) [31], as it can be seen in Figure 3.1. The LHC is a 27 km long circular accelerator, with power provided to the beam by bunched Radio-Frequency cavities and bending power via more than 1200 superconducting dipole magnets. It is mainly a proton-proton collider, but it can also accelerate and collide ions like Pb. The nominal collision energy at the centre-of-mass in a *pp* collision is 14 TeV. The protons inside the LHC are not spread uniformly around its circumference, instead the particles are arranged in bunches. Each proton beam at full intensity will consist of 2808 bunches per beam. Each bunch contains 1.15×10^{11} protons per bunch at the start of nominal fill. Furthermore, these bunches are contained in RF buckets. The accelerator crosses the bunches trajectories at four different points creating the collisions. Depending of the fill configuration, the bunches can be separated 25 ns or 50 ns. It was designed to work with an instantaneous luminosity of $10^{34}\,\mathrm{cm}^{-2}\mathrm{s}^{-1}$. To achieve such energies, the LHC superconducting magnets must be cooled below -271.3°C, that is lower than the outer space. It is located between 45 m and 170 m underneath the surface in the French and Swiss countryside near Geneva.

At the beginning of the accelerator chain, the protons are produced by stripping the electrons from hydrogen atoms supplied by a bottle. The protons are then accelerated to 50 MeV through the LINAC 2, that is a linear accelerator. Protons are then injected into a booster ring and accelerated to 1.4 GeV and afterwards injected to the Proton Synchroton (PS). The PS boost the proton bunches to 25 GeV and sends them to the SPS, that increases its energy to 450 GeV and finally injects them in the LHC for the final boost to collision energies. LHC can collide protons in four different crossing points. These points are indicated in Figure 3.1 and there are located the four largest LHC experiments: ATLAS [32], CMS [33], LHCb [34, 35] and ALICE [36].

ATLAS (*A Toroidal LHC AparatuS*) and CMS (*Compact Muon Solenoid*) are general

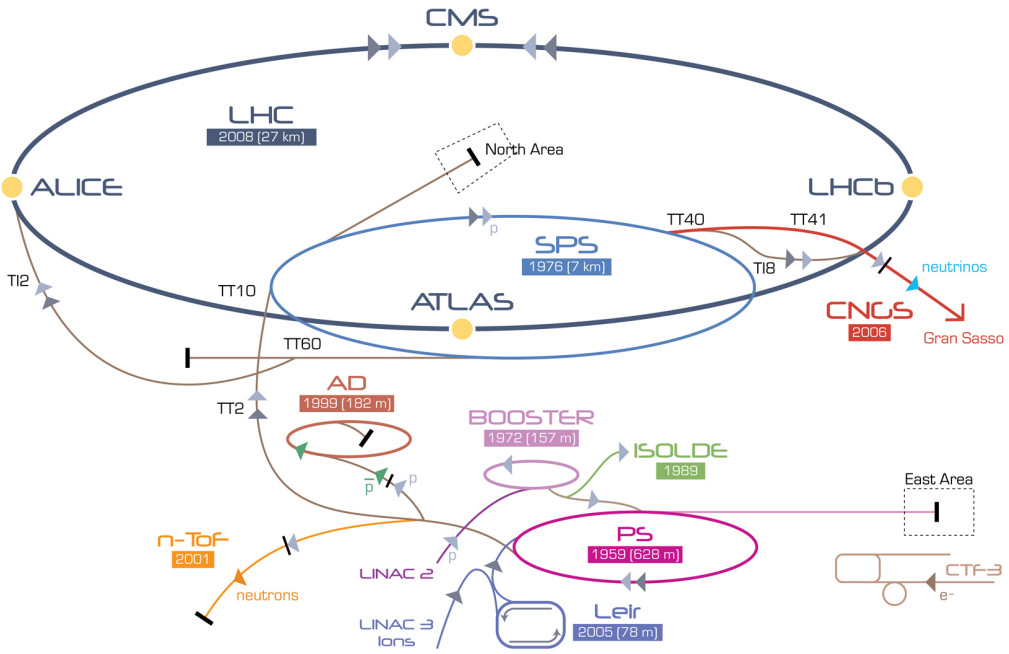

Figure 3.1: CERN accelerator complex.

purpose experiments, *i.e.* their configuration is not thought to perform any specific study but allow them to reach the largest physics analysis as possible. ALICE (*A Large Ion Collider Experiment*) is designed to study the quark and gluon plasma that was formed at the very early moments of the universe. Finally LHCb (*LHC beauty experiment*) is an experiment dedicated to flavour physics. ATLAS, CMS and ALICE present a barrel configuration. As the name says, the three detectors have a barrel shape and the interaction point is located in their geometrical centre. This configuration allows these spectrometers to detect particles emitted from the interaction point in all the directions (full solid angle coverage). On the other hand, LHCb detects particles in a narrow solid angle with full instrumentation in the forward direction and limited detection in the backward region. A schematic view of these four experiments is shown in Figure 3.2.

In the LHC ring other 3 smaller experiments can be found. TOTEM [37] and LHCf [38] study the protons and ions emitted in the very forward directions, and MoEDAL [39] is focused in the existence of the magnetic monopole.

In addition to injecting to the LHC the intermediate accelerators can also send the beam to different places where other experiments are located. One of these installations is the CERN North Area [40], which is fed by the SPS. At the entrance of the area are located two target areas: T2 and T4. These targets consist of beryllium sheets and they can be used to convert the proton beam into a range of secondary beam types or just to attenuate the SPS beam intensity. When the SPS proton beam hits the targets produce pions and electrons. The momentum of these emerging particles is selected in a spectrometer located just after the targets. By increasing the amount of material in the target, or by including an optional filter after the start of the spectrometer, the electron contribution to the beam composition can be significantly decreased.

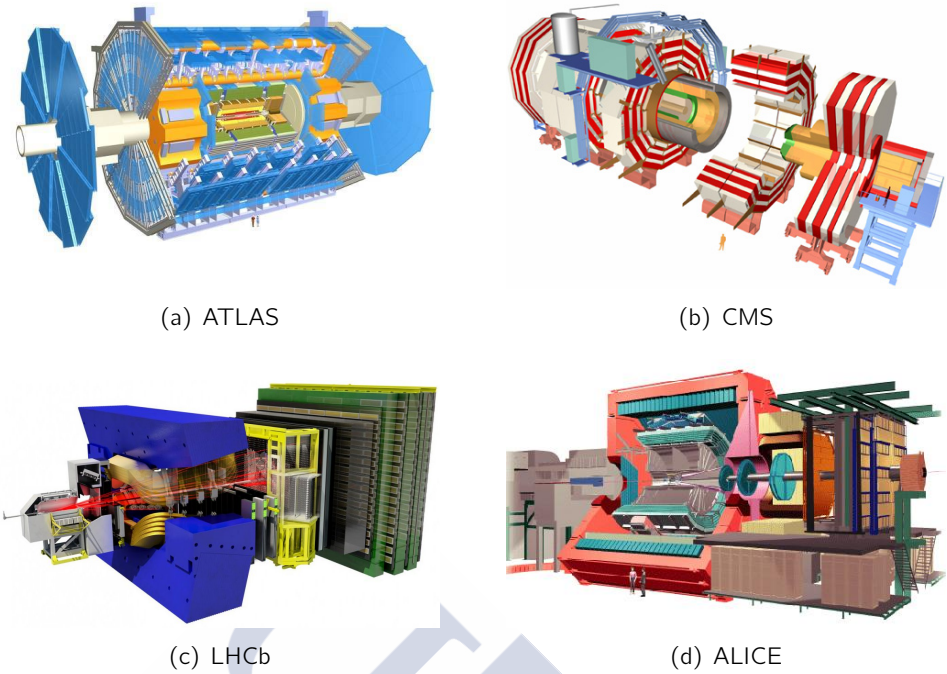

(a) ATLAS (b) CMS

(c) LHCb (d) ALICE

Figure 3.2: Main LHC experiments

3.2 The LHCb experiment

LHCb is a forward spectrometer designed to study flavour physics exploiting the enormous production cross sections of heavy hadrons at the LHC. LHCb design luminosity is $2 \times 10^{32}\,\mathrm{cm}^{-2}\mathrm{s}^{-1}$, that is smaller than the LHC nominal $10^{34}\,\mathrm{cm}^{-2}\mathrm{s}^{-1}$. This instant luminosity reduction is achieved by changing the crossing angle of the beams in the LHCb interaction point and by defocusing them. The reason to do so is easing the correct identification of the point where the proton-proton collision took place (primary vertex) and the point where other short-lived particles decay in flight (secondary vertex), as this is essential for the physics measurements performed by the collaboration. Its angular coverage is from 10 to 300 (250) mrad in the horizontal (vertical) plane with respect to the incoming proton beams. The choice of the detector geometry is justified by the fact that at high energies both the b and $\overline{b}$ hadrons are predominantly produced in the same forward or backward cone, as it can be seen in Figure 3.3. The detector covers about 2% of the solid angle and around 27% of the b quarks produced [41]. Figure 3.4 shows the LHCb layout and its subdetectors. The right-handed coordinate system adopted has the z axis along the beam, and the y axis almost along the vertical (since there exists a $\sim$3.7 mrad tilt compared to the actual geometrical vertical). LHCb is located at the intersection Point 8 of the LHC. This point was used by the DELPHI experiment during the LEP time. A modification to the LHC optics, displacing the interaction point by 11.25 m from the centre, has permitted maximum use to be made of the existing cavern for the LHCb detector components. The subdetectors can be classified in two groups depending on their function: the tracking detectors and the particle identification detectors.

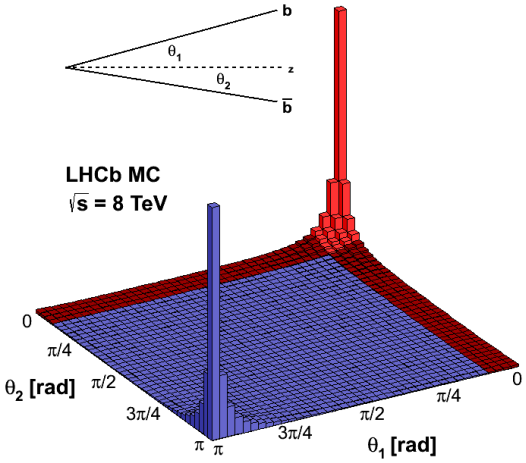

Figure 3.3: Angular distribution of b and $\overline{b}$ quarks in collisions at $\sqrt{s} = 8\,\text{TeV}$.

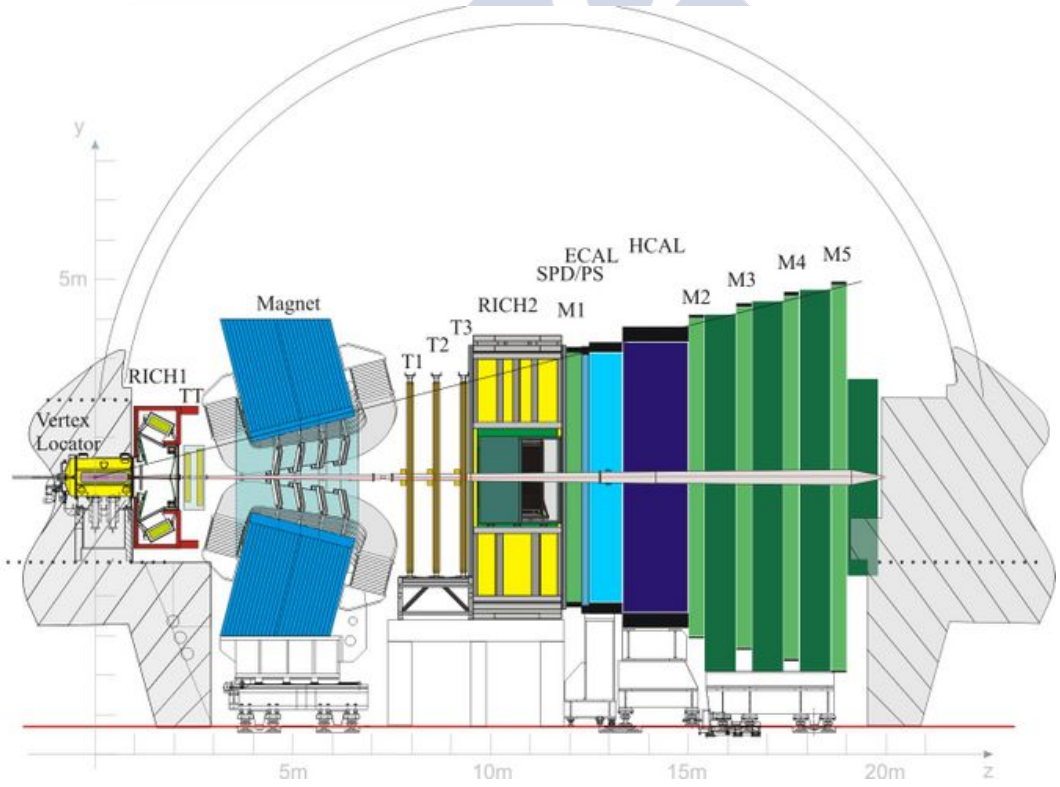

Figure 3.4: Schematic cross section of the LHCb detector showing its subdetectors.

3.2.1 Tracking detectors

An efficient and precise reconstruction of the trajectories of charged particles is of paramount importance for LHCb. The goal of the tracking system is to measure the decay lengths of long lived particles, momentum of charged final states and reconstruct the full decay by matching the information from all subdetectors. The LHCb tracking system is composed of the following parts: The VErtex LOcator (VELO) [42], the Silicon Tracker (ST) comprising the Tracker Turicensis (TT) [43] and the Inner Tracker (IT) [44], the Outer Tracker (OT) [45].

3.2.1.1 The VELO

The VELO is designed to measure the coordinates of tracks close to the interaction point, allowing the decay of the b and c hadrons to be separated from the primary pp interaction. Furthermore, it provides information to measure their decay times, impact parameters and tracking information upstream the dipole magnet. The VELO is a key detector in LHCb since it provides information that cannot be collected by any other subdetector and is basic for many physics analyses. As any other tracking station it is required to have high spatial resolution and minimal material. Moreover, since it measures the first interaction point of the particles, it is required to sit as close as possible to the interaction point.

To achieve such requirements VELO was designed as a silicon strip detector. Each internal module consists of two n^+-on-n, 300 μm thick sensors with R and ϕ geometries glued back to back and arranged perpendicular to the beam axis. R and ϕ design means that the sensors are produced with strip implants in either a radial or a circular pattern, permitting to determine one R-ϕ point by each module. Figure 3.5(a) shows a schematic of the R and ϕ sensors. In Figure 3.5(b) a photo of the real modules can be seen, where the readout chips can be appreciated around the sensor edge, mounted on the PCB and attached via a pitch adaptor to the metal readout lines patterned on the sensor. The acceptance of VELO covers the pseudorapidity range $1.6 < \eta < 4.9$ for particles coming from primary vertices in the range $|z| < 10.6\,\text{cm}$. In order to fulfil the design requirements for angular coverage and the minimum number of hits per track (4) it was constructed using 42 modules arranged as shown in Figure 3.5(c). In addition to these 42 modules, VELO has 4 more modules containing only R-type sensors and located upstream the VELO. This part is called the *pile-up veto system* and it was initially conceived for pile-up veto in the trigger, although it never was implemented. The vertex determination accuracy is inverse proportional to the distance between the primary vertex and the first interaction point. Furthermore, it strongly depends on the amount of material found in between these two points. To obtain the better precision, the VELO was designed without a beam pipe to contain the LHC beam and, instead, it is separated from the LHC vacuum by an aluminium corrugated 300 μm Radio Frequency (RF) foil, which additionally shields the modules from beam-induced RF noise. This allows the innermost sensitive region to sit at 8.1 mm from the beam axis. During the LHC injection, the beam spread is wider than this 8.1 mm so, in order to avoid severe radiation damage a minimal distance of 3 cm is required when LHC is being filled. Thus, the detector was designed as two retractable halves, mounted on opposing sides of the beam. The two VELO halves can be retracted by around 30 mm from their working position, permitting the VELO to remain safe while the beam is injected. Once the beam is stable and ready to start the collisions the two

parts close symmetrically up to their working position. VELO is cooled by a bi-phase CO_2 system, where the heat transfer proceeds by evaporative cooling. Figure 3.5(c) shows an artistic view of the VELO, where each of its parts can be identified.

3.2.1.2 The Silicon Tracker

The ST is composed of the TT and IT that are located upstream and downstream the spectrometer magnet respectively. These two subdetectors are grouped together since their are both based on silicon microstrips.

TT: The TT main function is to link VELO tracks with those produced in the tracking stations downstream the magnet. It is located just before the dipole magnet and it is $\sim$150 cm wide and $\sim$130 cm high, covering the full detector acceptance. It consist on 4 planes of silicon p^+-on-n, 500 μm thick strip sensors and a strip pitch of 183 μm. The second and third layers are rotated -5° and +5° with respect to the vertical axis respectively. Figure 3.6 shows a picture of the TT.

IT: The IT is located just downstream the magnet. It covers a 120 cm wide and 40 cm high cross shaped region close to the beam pipe and surrounded by the OT. It consists in three subdetectors T1, T2 and T3, each of them composed by 4 silicon strip sensor layers oriented at angles 0°, -5°, +5° and 0° with respect to the vertical axis, as the TT. The sensors are p^+-on-n type with two different thicknesses: 320 μm for the sensors above and below the beam, and 410 μm for those to the left and right. The pitch is 198 μm and it is common for all sensors. IT and OT cover different regions of the same planes. Figure 3.7 shows one plane of the IT.

3.2.1.3 The Outer Tracker

The particle flux falls off considerably with increasing distance from the beam so silicon was chosen for the inner region to provide greater granularity and improved hit resolution. The total area of the downstream tracker (IT + OT) is around 30 m^2 so, since applying this solution to the whole surface was prohibitively expensive, it was decided to base the OT in straw tubes technology. The total active area of a station is 6×5 m The OT sensors layout is similar to the IT. The straw tubes planes are arranged in sets of 4 per station, with the second and third planes rotated -5° and +5° respectively. These sensors are made up of 4.9 mm diameter cylindrical gas tubes, with a 25.4 μm thick gold-plated tungsten wire running through the centre. The gas used is a mixture of 70% Ar and 30% CO_2. It provides a drift time below 50 ns and a drift-coordinate resolution of 200 μm is achieved. Figure 3.8 shows a cross section of the OT.

3.2.1.4 Magnet

The aim of the LHCb dipole magnet [46] is to bend the charged particles in the horizontal plane of the detector to permit the measurement of their momenta. The dipole is a room temperature magnet that covers the forward acceptance of ±250 mrad vertically and ±300 mrad horizontally (bending plane). The magnet provides an integrated magnetic field of 4 Tm. Its direction can be switched up and down to reduce systematic uncertainties

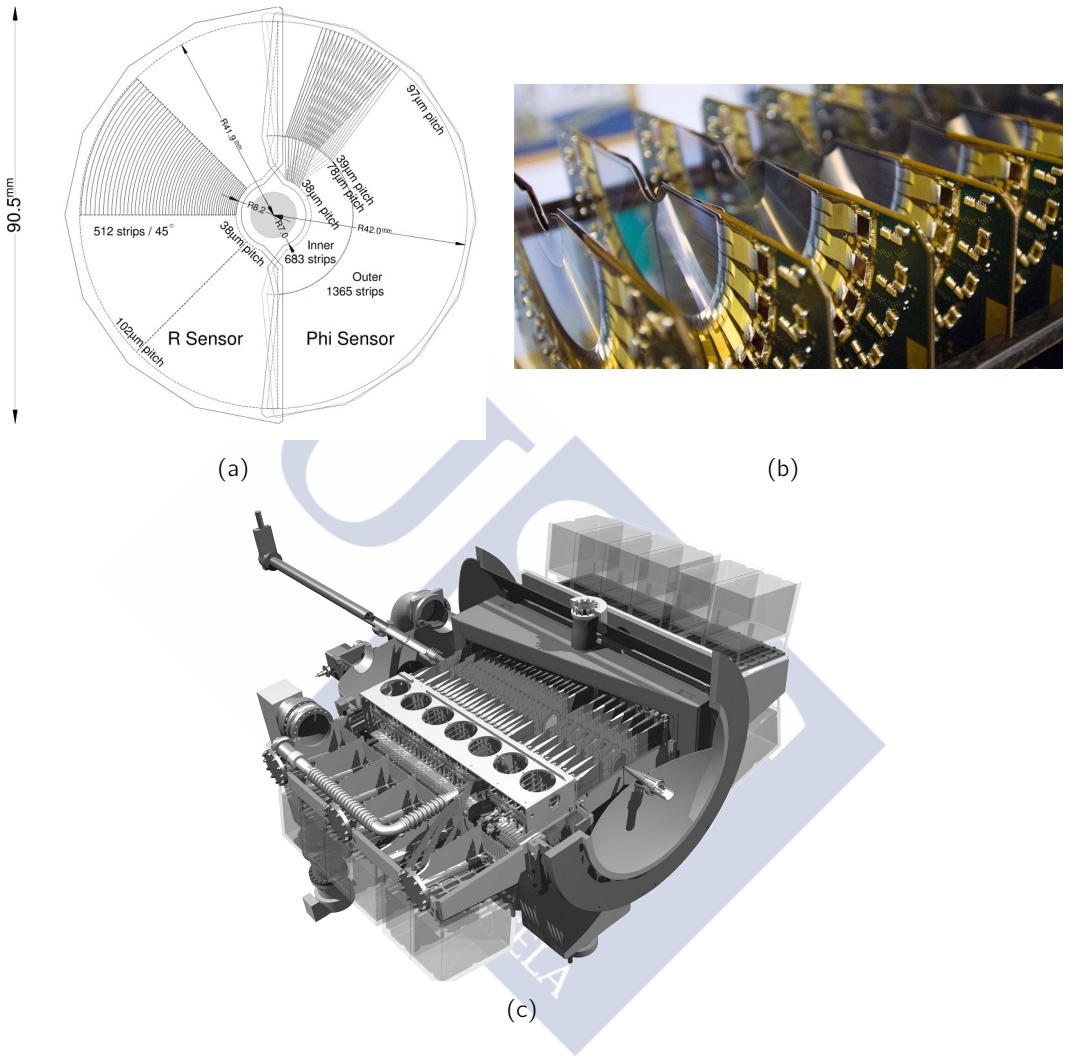

Figure 3.5: Figure (a) shows an schematic of the two VELO type sensors, R and ϕ. In (b) a real photo of the VELO sensors can be seen. In the picture the front-end read out chips (Beetle) can be seen surrounding the sensors and attached to them via the pith adapters. Figure (c) shows an artistic view of the VELO, where its internal distribution can be appreciated.

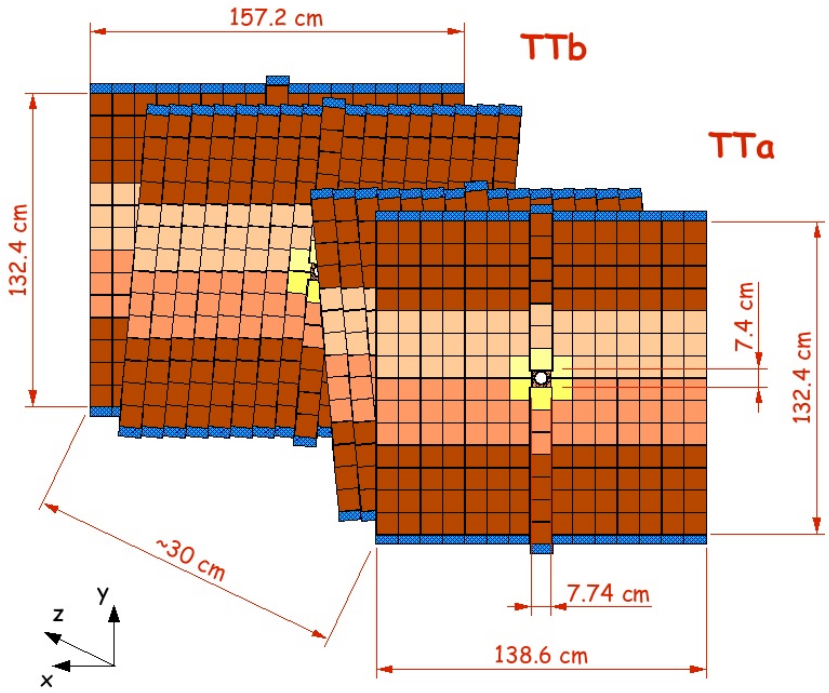

Figure 3.6: Schematic view of the TT.

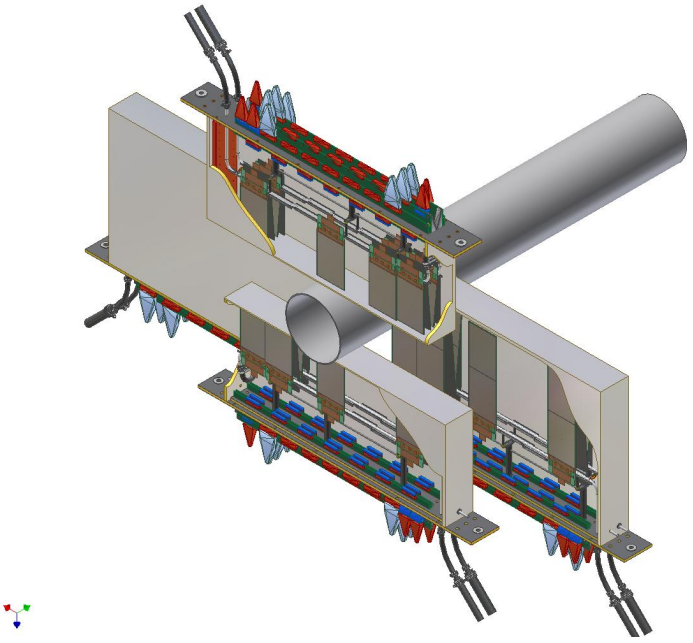

Figure 3.7: Schematic view of one plane of the IT.

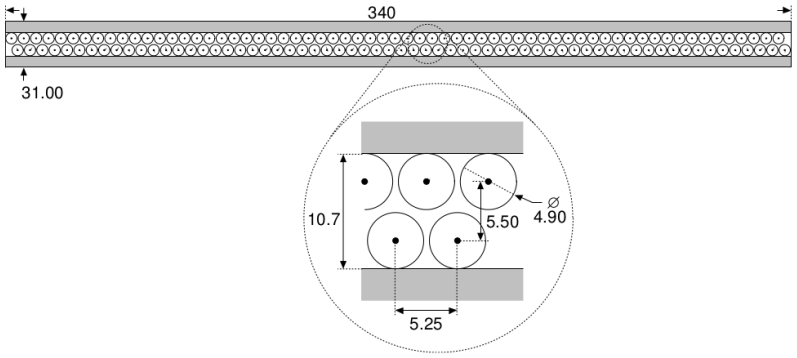

Figure 3.8: Cross section of one module of the OT.

that might affect *CP* violation studies. In the following these two configurations of the magnet will be called magnet up (MU) and magnet down (MD). The field is mapped inside the tracking volume with an accuracy of 4×10^{-4}. Figure 3.9 shows the measured magnetic field (B_y component) along the z axis. In Figure 3.10 it can be seen a picture of the magnet during the LHCb installation.

3.2.1.5 Tracking and vertexing

As explained, one of the key points for the event reconstruction at LHCb is the determination of the trajectories of all charged particles (tracks) and the position where they were generated (vertices) both whether this was a proton-proton collision (PVs) or the decay point of some other particle (SVs). The LHCb tracking algorithms [47] combine hits in the tracking detectors and look for the best possible precision in determining the slopes and momentum of the tracks. In the case of vertices, the best resolution is searched for in the 3D position. Finally, the tracking and vertexing algorithms are different online and offline. As already said, the online reconstruction has to be quicker, and this is achieved by reducing the precision with respect to offline.

As it is shown in Figure 3.11, depending on the origin of the hits used to define the track, they can be classified as:

- Long tracks: They present hits in every tracking stations. They provide the most precise momentum measurement, and therefore are the most used in the physics analyses.

- Upstream tracks: They have hits in VELO and TT. These are mainly low momentum particles that were deflected out the detector by the magnet.

- Downstream tracks: These traverse only the TT and IT or OT. They are usually produced by long-living particles decaying outside the VELO, such as K_s^0 or Λ.

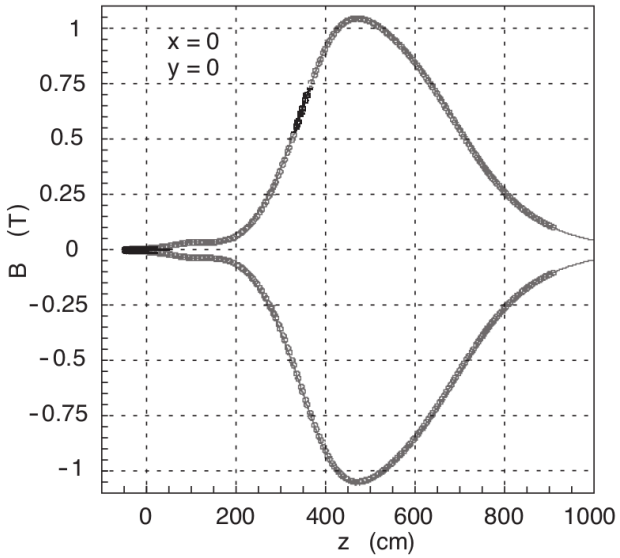

Figure 3.9: Magnetic field created by the LHCb magnet along the z axis.

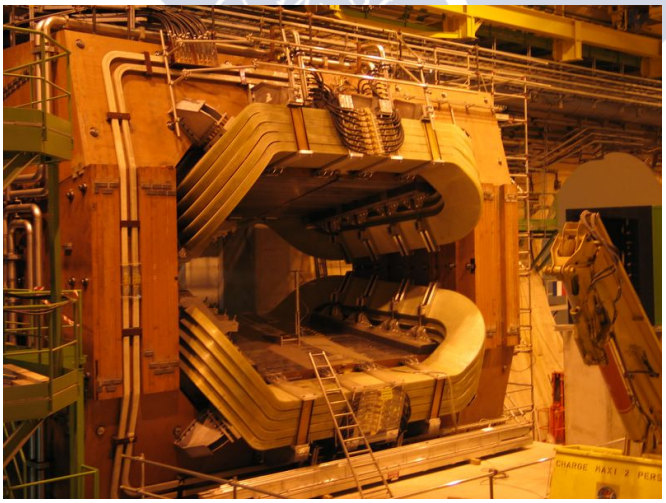

Figure 3.10: Photo of the LHCb magnet being installed.

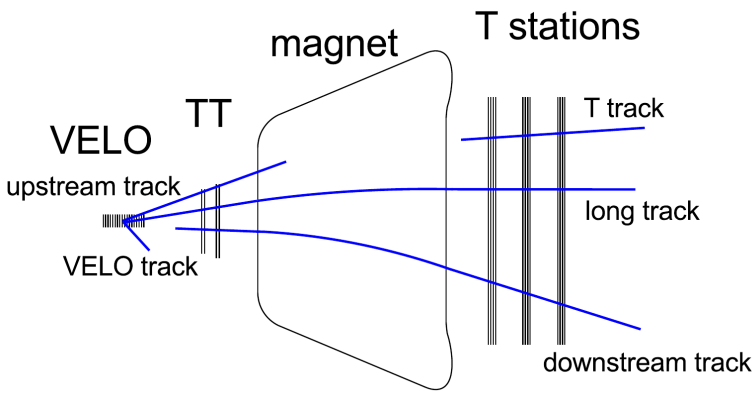

Figure 3.11: Different track types in LHCb.

- VELO tracks: They are only detected in the VELO. They are typically large angle or backward tracks, useful to reconstruct the primary vertex.
- T-tracks: They have only hits in the T-stations (IT and OT). They are typically produced by particles generated in secondary interactions.

This is more than just a useful nomenclature, as the resolution of the detector is different for each type of track.

Different algorithms are used to reconstruct each type of track. In order to reconstruct long tracks, the algorithms look first for track seeds in the VELO and then match them with hits from the other tracking subdetectors to form the final tracks. Once the long track is found, it is refitted using Kalman fitter algorithm [48], that accounts for multiple scattering and energy loss caused by traversed materials. The χ^2 of the fit indicates whether the track is a real track or just a combination of random hits (ghost tracks). There is also the possibility of reconstructing the same track through different algorithms. In this case, the tracks are called clones, and only the one with the lower χ^2/nDoF is kept.

The main performance criteria for the tracking systems are the track reconstruction efficiency, the momentum resolution and the track resolution parameters (consisting of the related single hit, vertex, and impact parameter (IP) resolutions).

The efficiency to reconstruct long tracks in LHCb has been evaluated using muons from J/ψ decays [49]. The performance plots as function of momentum and pseudorapidity on data and MC simulation can be seen in Figure 3.12. Hadronic interactions not taken into account in this calculation are reflected in a 1.4% additional systematic uncertainty. The track reconstruction efficiency for long tracks is around 95%.

The momentum resolution is also very important for the physics results, since it is one of the most important input parameters to calculate the mass of the mother particles. Figure 3.13 shows the momentum resolution measured using muons from J/ψ decays as a function of the momentum itself. The momentum resolution comes defined as $\delta p/p$ and it is better than 1% across the full momentum range (up to 200 GeV/c).

The accurate measurement of production and decay vertices is another important issue for most of LHCb physics analyses. The primary and secondary vertices are reconstructed using VELO tracks [50]. At least 5 VELO tracks and up to 150 are required to reconstruct

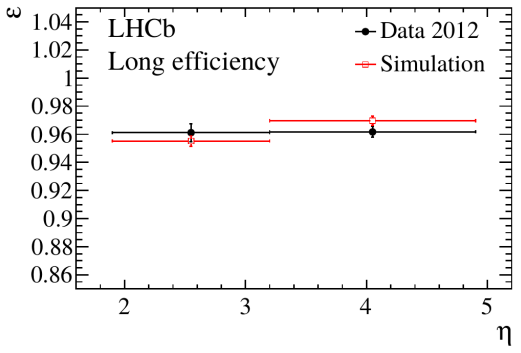

(a)

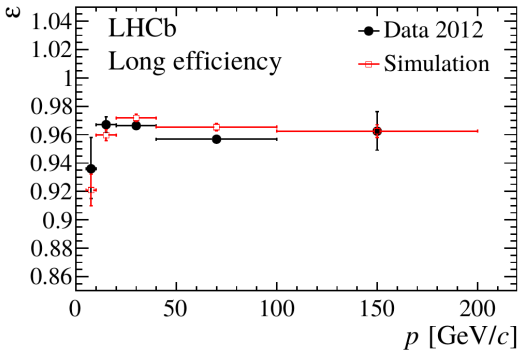

(b)

Figure 3.12: (a) Tracking efficiency *vs.* pseudorapidity and (b) Tracking efficiency *vs.* p. In both cases black dots represent the results using real data from 2012 and red dots represent the results from weighted MC simulation.

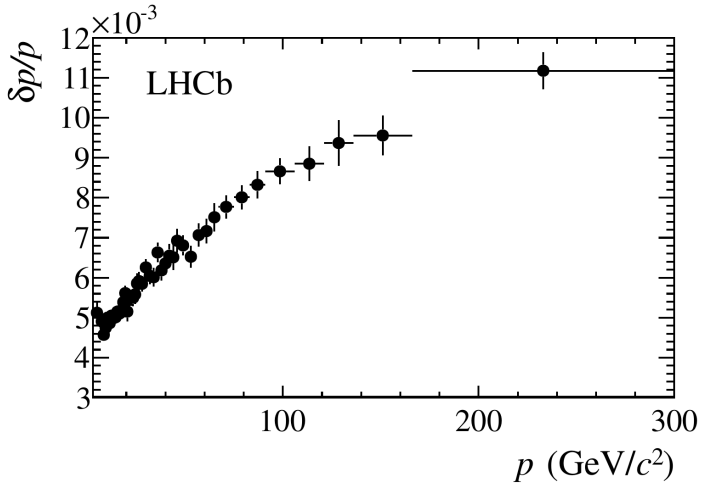

Figure 3.13: Relative momentum resolution defined as $\delta p/p$ versus p for long tracks in 2011 data obtained using J/ψ decays.

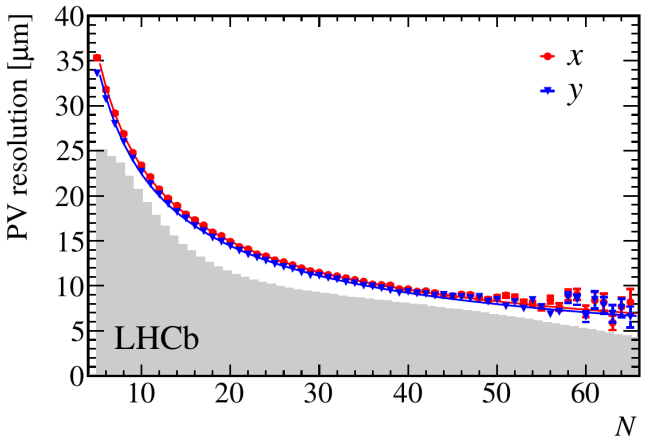

Figure 3.14: Primary vertex resolution in x (read) and y (blue) coordinates as function of the PV multiplicity. The shadowed area represents the histogram of the number of tracks per reconstructed primary vertex for all events that pass the HLT and using data registered in 2012 at $\sqrt{s} = 7$ and 8 TeV.

a vertex and the resolution improves significantly with the number of tracks used, as it can be seen in Figure 3.14.

The IP of the tracks is one of the most important parameters. The IP is defined as the geometrical distance between a reconstructed track and a certain vertex. Tracks originating from the primary proton-proton interaction should have an IP compatible with zero, while large impact parameters are expected for tracks originated from decays of long lived particles. The IP resolution depends on the p_T of the tracks. Figure 3.15 shows the IP_x (IP projection on the x axis) resolution as function of $1/p_T$ using data registered in 2012 at $\sqrt{s} = 7$ and 8 TeV and compared with the one in MC simulation. As it can be seen, both results are quite similar. The difference between data and MC comes from the description of the detector material and the interaction of the particles with it in the simulation.

The LHCb proper-time resolution is at the level of ∼50 fs. This excellent precision allows to resolve the fast B_s^0-$\bar{B}_s^0$ oscillation. The B_s^0 oscillation frequency measured by LHCb is $\Delta m_s = 17.768 \pm 0.023(stat) \pm 0.006(syst)\,\text{ps}^{-1}$ [51].

3.2.2 Particle Identification

The second group of subdetectors mentioned at the beginning of the section are those which identify the particle type. These subdetectors are also very important at LHCb, since the ability to tag the flavour of B mesons or to reject backgrounds that are kinetically and topologically similar rely in the particle identification system. These subdetectors are: RICH1 and RICH2, that are Ring-Imaging Cherenkov detectors placed in front of the magnet and downstream behind the tracking stations respectively [52]; M1 to M5, that are five stations of muon detectors [53]; and the ECAL (Electromagnetic CALorimeter), HCAL (Hadronic CALorimeter), PS (Pre-Shower) and SPD (Scintillating Pad Detector) [54]. Once all tracks are reconstructed the information from the PID detectors is added in order to stablish hypotheses of the nature of the particles.

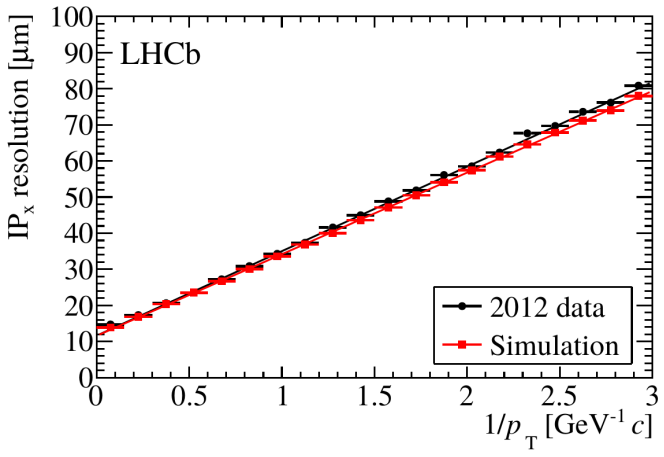

Figure 3.15: Impact parameter resolution in the x coordinate with respect to the inverse of the momentum for 2012 data (black dots) and MC (red squares).

3.2.2.1 RICH detectors

The separation of pions, kaons and protons in the final state over the full momentum range was a strong requirement in the design of the experiment. Since this separation power of one Cherenkov detector depends on the particle momentum, it was decided to mount two RICH detectors covering different momentum ranges. RICH1 covers the region from 1 to 60 GeV/c and RICH2 covers from 15 to over 100 GeV/c. Figure 3.16 shows the Cherenkov angle with respect to the particle momentum for muons, pions, kaons and protons. The configuration of the two RICH detectors is basically the same, but different optics due to the different radiators used. RICH1 contains aerogel and C_4F_{10} as radiators while RICH2 uses CF_{10}. RICH1 is located upstream the dipole magnet and covers the full LHCb acceptance from ±25 mrad to ±300 mrad in the horizontal plane and ±250 mrad in the vertical one. On the other hand, RICH2 has a limited angular acceptance from ∼ ±15 mrad to ±120 mrad in the horizontal plane and ±100 mrad in the vertical, where high momentum particles are abundant.

In both RICH detectors the Cherenkov light is focused using a combination of spherical and flat mirrors to reflect the image out of the spectrometer acceptance. Hybrid Photon Detectors (HPDs) are used to detect the Cherenkov photons in the wavelength range 200-600 nm. The HPDs are surrounded by external iron shields.

3.2.2.2 Calorimeter system

The aim of the calorimeter system is to select the transverse energy (E_T) hadron, electron and photon candidates for the first trigger level (L0) and to provide the identification of electrons, photons and hadrons as well as the measurement of their energies and positions.

The calorimeter system in LHCb consists of several independent subdetectors: the Electromagnetic CALorimeter (ECAL), the Hadronic CALorimeter (HCAL), the Scintillating Pad Detector (SPD) and the Pre-Shower (PS). All of these subdetectors are needed to properly discriminate between hadrons, electrons and photons, since the energy deposition in each of the calorimeter components will depend on the nature of the particles. The HCAL is located following the ECAL and they identify the hadronic and electro-

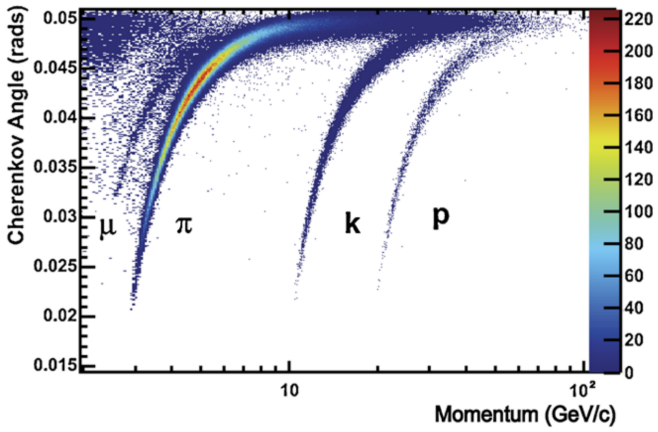

Figure 3.16: Cherenkov angle *vs.* particle momentum for muons, pions, kaons and protons using isolated tracks.

magnetic showers respectively. They are both sampling devices composed of alternating layers of scintillator and absorber. The only difference is that in the ECAL the absorber is lead and in the HCAL iron. In order to distinguish the $e^{\pm}$ among the huge amount of neutral and charged pions a longitudinal segmentation of the electromagnetic shower is needed. In LHCb this is achieved with the installation of a Scintillating Pad Detector and a Pre-Shower before the ECAL. A thin lead converter is installed between the PS and SPD.

The scintillation light from the whole calorimeter system is transmitted to Photo-Multipliers (PMTs), that turn this light into an electric signal. The sensitive area of the detector is 7.6 m wide and 6.2 m high. The ECAL employs alternating scintillating tiles and lead plates, with overall dimensions 7.8×6.3 m. The HCAL consists of thin iron plates interspaced with scintillating tiles arranged parallel to the beam pipe. Its dimensions are 8.4×6.8 m.

3.2.2.3 Muon system

The LHCb muon system consists of five tracking stations. The first station (M1) is located upstream the calorimeter preshower. The remaining four stations (M2, M3, M4 and M5) are located downstream the calorimeter, interleaved with three iron filters.

The inner and outer angular acceptances of the muon system are 20 (16) mrad and 306 (258) mrad in the bending (non-bending) plane. This acceptance is similar to that of the tracking system and provides a geometrical acceptance of about ∼20% of muons from b decays relative to the full solid angle. M1-M3 have good resolution in the bending plane in order to provide track direction and p_T measurement with ∼20% precision. On the other hand, M4 and M5 are mainly designed to identify the most penetrating particles.

The muon stations, except the innermost region of M1, are based in Multi Wire Proportional Chambers (MWPCs) operating with a gas mixture of Ar, CO_2 and CF_4 (40%, 55% and 5% in volume respectively). Because of the high particle rate in the M1 inner region, this muon chamber uses a triple-GEM detector. This detector consists of three gas electron multiplier (GEM). It uses the same gas mixture than the MWPCs (Ar,

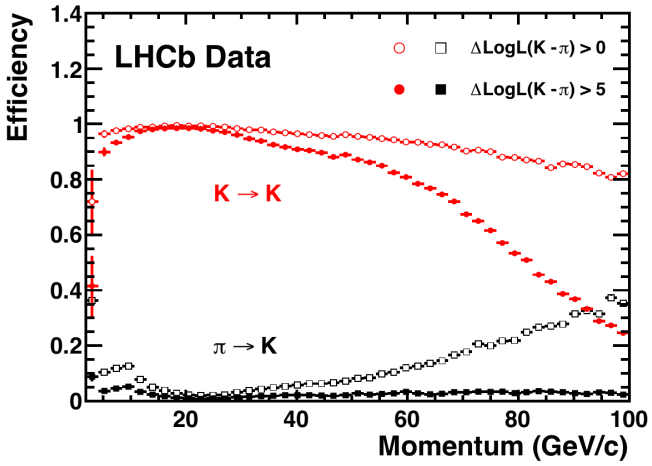

Figure 3.17: Kaon identification efficiency (red) and pion misidentification efficiency (black) using two different cuts in the DLL(K-π) and 2011 data.

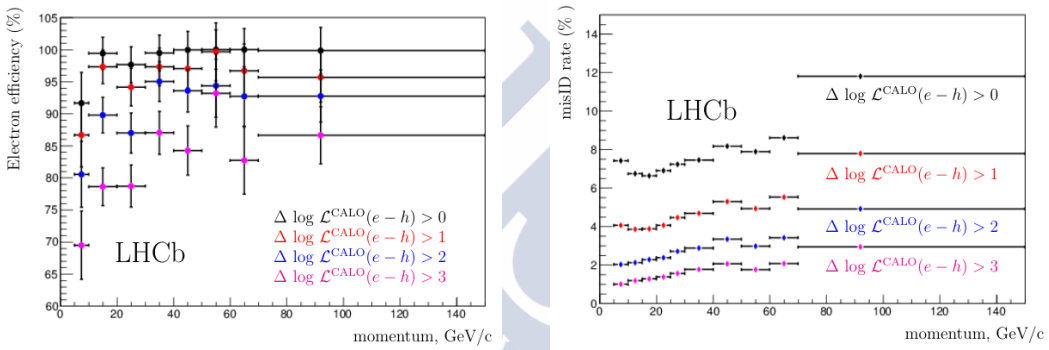

(a) (b)

Figure 3.18: (a) Electron identification efficiency *vs.* momentum for 4 different $\Delta\log\mathcal{L}_{e-h}$ cuts. (b) Electron misidentification *vs.* momentum using 4 different $\Delta\log\mathcal{L}_{e-h}$ cuts.

$C0_2$ and CF_4) but different concentrations (45%, 15% and 40% respectively).

3.2.2.4 PID performance

The PID efficiency varies between 90-100% for all particle types, varying with acceptable rate of misidentification. The LHCb PID from the different subdetectors are usually combined in a common likelihood, in order to maximise the efficiency and minimise the misidentification rate. Figures 3.17, 3.18 and 3.19 show the RICH PID, ECAL and muon system performances respectively.

3.2.3 Trigger system

The amount of data produced by the LHC collisions is too large to be directly stored. Thus, an online system selecting interesting events is needed. This system is the trigger system. At the LHC, proton bunches are synchronised to a 40 MHz clock. During operation not all

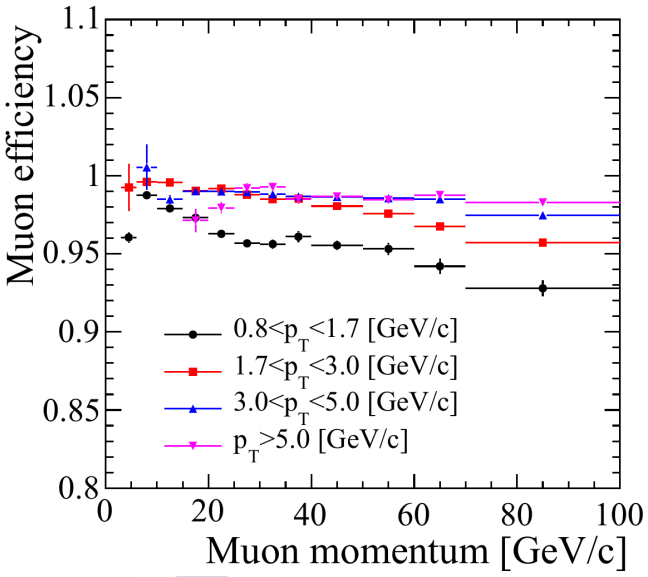

Figure 3.19: Muon identification efficiency calculated using the matching between the hits in the muon system to the track extrapolation as a function of the momentum and for different p_T ranges.

available bunch spacings are filled, and a total collision rate of up to 30 MHz is obtained in practice. The LHCb trigger system was designed to reduce the rate of visible interactions from the nominal ∼30 MHz to a maximum of ∼12.5 kHz, that is the maximum permitted by the long term data storage resources [55, 56]. This goal must be achieved with a minimum loss of interesting events for the physics analysis, that are mainly events with B and D mesons. These events present some typical signatures that the trigger system exploits: tracks with high p_T and with non-zero impact parameters. The IP is defined as the minimal geometrical distance between a track and the PV of the pp collisions.

The LHCb trigger strategy in 2015 can be seen in Figure 3.20. A hardware trigger (L0) takes information at 40 MHz from the calorimetry and muon systems and reduces the input rate to a maximum of 1 MHz. At this rate the whole detector can be read out. The calorimeters and muon chambers provide high p_T candidates (hadrons, leptons and photos), and the SPD provide a fast detection of high occupancy events. The L0 decision is distributed to the full range of subdetectors and the data for the selected bunch crossing are sent to the off-detector electronics. Once the subdetectors information is processed in these electronic equipments is combined with the information from the rest of the detectors and sent to the CPU farm. The CPU farm is composed by several thousands of CPU nodes and there the second trigger level (High Level Trigger, HLT) runs. The HLT is a C++ application and reduces the L0 output rate to the final maximum rate of about 12.5 kHz. The selected events are then saved on permanent storage. HLT is divided in two parts: HLT1 and HLT2. HLT1 performs a partial reconstruction and reduces the input rate to about 40 kHz. This is a selective reconstruction of particles taking into account that b-decays generally involve daughter particles originating from a displaced vertex and significant transverse momentum. Those events which contain well-fitted tracks which are displaced from all primary interactions and with high transverse momentum are saved to disk to be analysed later by the HLT2.

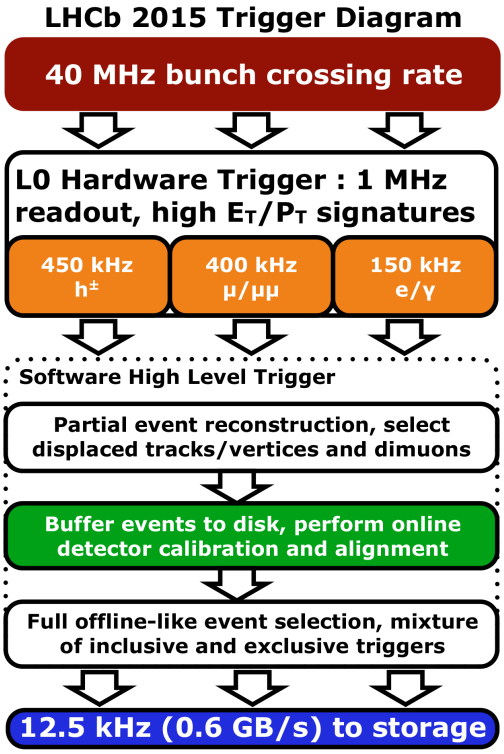

Figure 3.20: LHCb trigger strategy in 2015.

After an online calibration and alignment using the data on disk, a full reconstruction similar to the one done offline, is performed by HLT2. The HLT2 combines the different tracks to form composite particles ($J/\psi \to \mu^+\mu^-$, $K^{*0} \to K^+\pi^-$, ...) used as input to the different selections. Data passing the HLT2 are saved on disk.

3.2.4 The online system

The LHCb online system [57] is the responsible for transferring the data from the front-end electronics to the storage. It is composed of three subsystems: the Data Acquisition system (DAQ), which transfers the data selected by the trigger to storage; the Experiment Control System (ECS), which monitors and controls the detector; and the Timing and Fast Control system (TFC), which distributes the beam synchronous clock and fast control commands to drive all stages of data readout.

3.2.5 The LHCb software

The LHCb collaboration develops several software packages to generate simulated data and process the registered real data. These packages are based in the Gaudi [58] and Root [59] frameworks. In the following a brief overview of them is presented.

Gauss: The Gauss package [60] is used to generate particle or heavy ion collisions, the subsequent decays of particles produced and the interaction with the detector. It

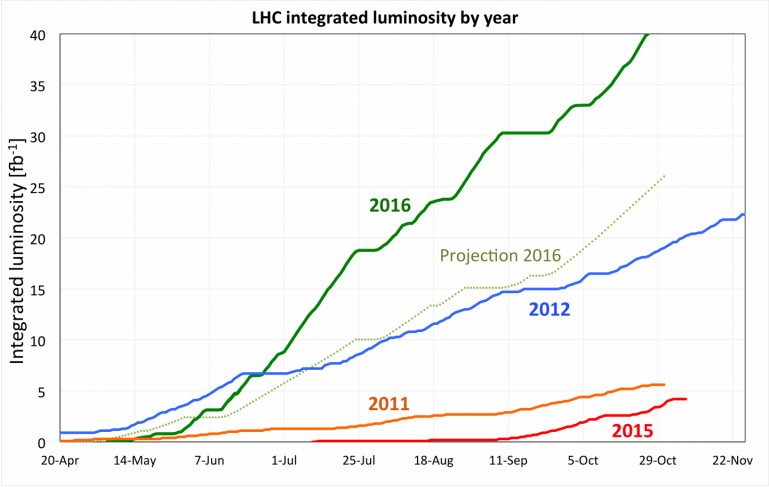

Figure 3.21: Integrated luminosity delivered by the LHC from 2010 to 2016.

uses other software packages to simulate the different phases. The simulation of the beam particle collisions is done by Pythia, EPOS [61], Herwig [19] or some other specific event-type generators depending on the collision type. The decays of hadronic particles are performed by EvtGen [62], the final state radiation is simulated by Photos [63] and, finally, the Geant4 [64] package simulate the interaction of the generated particles with the detector material.

Boole: The Boole package [65] digitises the output from Gauss. The output data mimics the real data coming from the actual detector.

Moore: The Moore package [66] provides information about trigger decisions for both simulated data from Gauss and Boole and data from the LHCb detector.

Brunel: The Brunel package [67] is the responsible for reconstructing the full event from raw data of the LHCb subdetectors. It is used for data and simulation.

DaVinci: DaVinci [68] is the LHCb analysis package. It allows particles to be combined into a decay chain and to select interesting events for the analysis. It uses data from Brunel and information from trigger. It can also be used for real data and simulation.

3.2.6 LHCb running conditions in 2015

The LHC experiments physics program started in 2010 with proton-proton collisions at 900 GeV and 7 TeV. Since then, the LHC provided to ATLAS, CMS, LHCb and ALICE proton-proton collisions at a centre-of-mass energy of $\sqrt{s} = 7\,\text{TeV}$ (2010 and 2011), $\sqrt{s} = 8\,\text{TeV}$ (2012), $\sqrt{s} = 5\,\text{TeV}$ (2015) and $\sqrt{s} = 13\,\text{TeV}$ (2015 and 2016). The integrated luminosity delivered by the LHC up to the end of 2016 is shown in Figure 3.21. In 2013 and 2014 took place the first long shut down. During this period the machine was adjusted to work at $\sqrt{s} = 13\,\text{TeV}$.

As it was explained in 3.2, LHCb design luminosity is $2 \times 10^{32}\,\text{cm}^{-2}\text{s}^{-1}$ but since 2012 it have being working at twice this value. As a consequence, the average number of visible

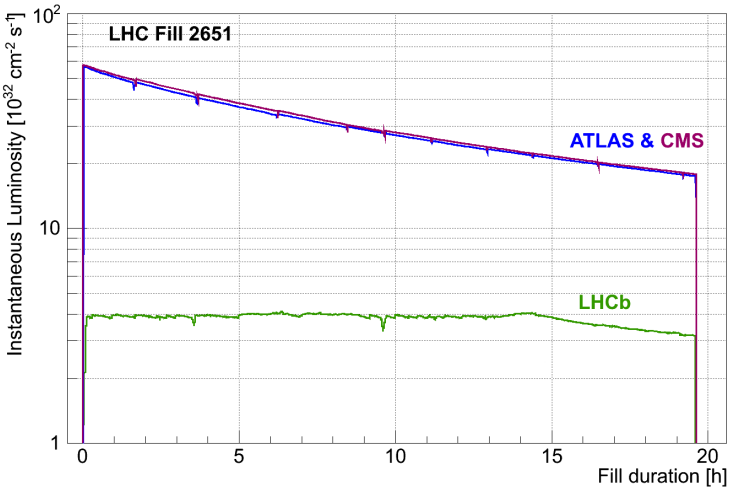

Figure 3.22: Instantaneous luminosity delivered to ATLAS, CMS and LHCb during LHC fill 2651. ATLAS and CMS accept the full instantaneous luminosity that LHC can deliver, and as time goes by the beam gets exhausted and the luminosity decreases continuously. LHCb changes the beams crossing angle and keeps the luminosity in a range of 5% for about 15 hours. At that moment, the beams are head on and the luminosity starts to decrease at the same pace than for the other two experiments. The final difference between the LHCb luminosity and the ATLAS and CMS is due to the beam focusing in the collision points.

interactions per bunch crossing increases to 1.6, that is four times the design value. To work at such luminosity LHCb needs to reduce the luminosity provided by LHC in almost two orders of magnitude. This is achieved by changing the beam focus and the crossing angle at the interaction point. Using these methods LHCb keeps the luminosity in a range of 5% for about 15 hours as it can be seen in Figure 3.22. The pp integrated luminosity collected by LHCb form 2010 to 2016 is showed in Figure 3.23.

LHCb was designed as a flavour physics experiment, but it proved the ability to access a general purpose physics program in the forward region. See for example Refs. [69, 70] In 2013 it joined the heavy ion physics program and collected data from p-Pb collisions at $\sqrt{s} = 5\,\text{TeV}$. Since then it took data of Pb-Pb collisions at $\sqrt{s} = 5\,\text{TeV}$ in 2015 and p-Pb data at $\sqrt{s} = 8\,\text{TeV}$ in 2016. Furthermore, injecting gas in the interaction region it can study p-gas collisions as a fixed target experiment. It already collected data from p-^{4}He, p-^{20}Ne and p-^{40}Ar. Thanks to its forward configuration it can provide complementary measurements to ATLAS, CMS, ALICE and also to the fixed target experiments.

The physics analyses performed in this thesis are based on the data taken by LHCb from the LHC proton-proton collisions at a centre-of-mass energy of $\sqrt{s} = 5\,\text{TeV}$ and $\sqrt{s} = 13\,\text{TeV}$ collected in 2015.

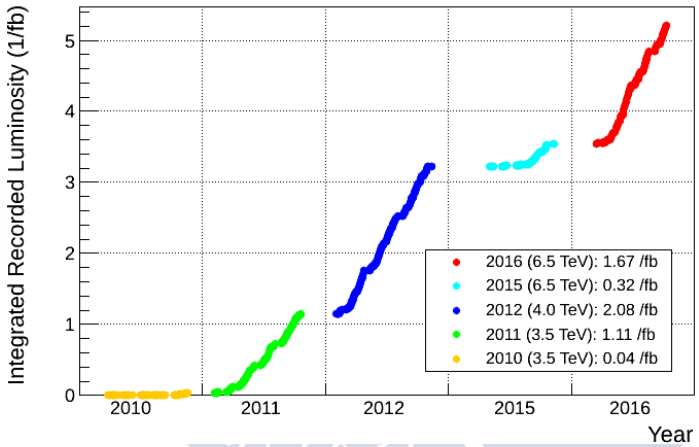

Figure 3.23: LHCb cumulative integrated recorded luminosity in *pp* by LHCb from 2011 to 2016.

USC
UNIVERSIDADE
DE SANTIAGO
DE COMPOSTELA

4

Measurement of the inelastic pp cross-section at $\sqrt{s} = 5$ and 13 TeV

In particle physics, the probability that two particles collide and react in a certain way is known as cross-section. This notion comes from the early experiments in particle physics when particles were thought to be hard spheres. These experiments aimed to measure the size of some particles by producing collisions between particles and observing their behaviour. In the case of hard spheres, the collision probability between particles is proportional to their size. Nowadays, we know that the idea of hard spheres is wrong, but the term cross-section persisted. The cross-section is noted as σ and it is measured in area units. In particle physics the conventional unit is the barn, b, being $1\,\mathrm{b} = 10^{-28}\,\mathrm{m}^2$.

Depending on whether the kinetic energy of the incident particles of a collision is conserved or not, collisions can be classified as elastic or inelastic, respectively. In inelastic collisions, part of the initial energy is used to excite the incident particles or to create new ones. The total cross-section is the sum of the elastic and inelastic cross-sections,

$$\sigma_{Tot} = \sigma_{El} + \sigma_{Inel}, \tag{4.1}$$

and it gives the upper bound in probability of any process in pp collisions.

The cross-section is a fundamental observable in high energy hadronic interactions. Currently it is not possible to calculate it using quantum chromodynamics (QCD) first principles. Many phenomenological approaches based on fundamental principles of quantum mechanics, such as unitarity and analycity can be used to accommodate the experimental results. These arguments imply a bound on the high energy behaviour of total hadronic cross-sections, the Froissart bound [71, 72]. This is independent of the details of the strong interaction dynamics and it states that the total cross-section cannot rise faster than $\ln^2(s)$, being s the squared collision energy in the centre-of-mass frame. The Froissart bound is also valid for the inelastic cross-section [73].

Measurements of the total cross-section at $\sqrt{s} = 7\,\mathrm{TeV}$ and $\sqrt{s} = 8\,\mathrm{TeV}$ were performed by ATLAS [74, 75] and TOTEM [76–79]. The inelastic cross-section was measured by the four LHC experiments at different energies and an increase with $\sqrt{s}$ [1] was found as expected. The ALICE collaboration measured the σ_{Inel} of pp collisions at $\sqrt{s} = 2.76\,\mathrm{TeV}$ [80]. The LHC experiments ATLAS, CMS, LHCb, ALICE and TOTEM measured the the pp inelastic cross-section at $\sqrt{s} = 7\,\mathrm{TeV}$ [79, 81–84], and ATLAS and CMS also at $\sqrt{s} = 13\,\mathrm{TeV}$ [85, 86]. Moreover, the Pierre Auger Collaboration measured the inelastic p-air cross-section at $\sqrt{s} = 57\,\mathrm{TeV}$ and extracted the σ_{Inel} using the Glauber

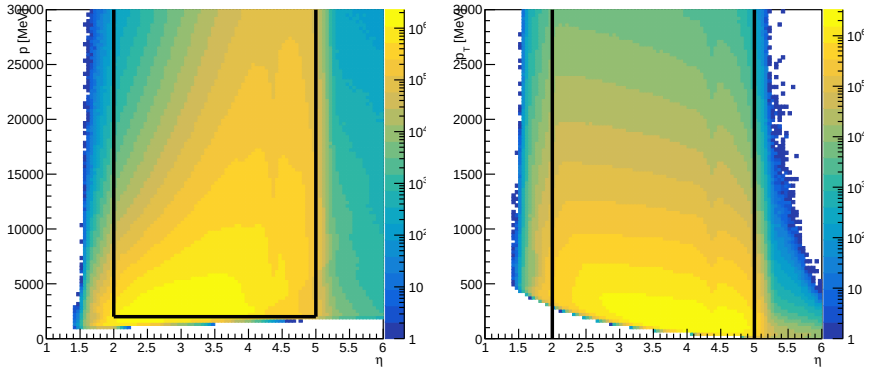

Figure 4.1: Kinematic region covered by the LHCb detector. Left plot shows p *vs.* η and the right plot p_T *vs.* η coordinates of reconstructed tracks from data collisions at 5 TeV. Black lines represent the limits of the kinematic acceptance defined in the analysis.

model [87]. However, this extrapolation have large uncertainty and provide relatively little information on the high-energy behaviour of the inelastic cross-section.

In this analysis, the measurement of the inelastic cross-section of pp collisions at two different centre-of-mass energies, 5 and 13 TeV, is presented using prompt long-lived charged particles in the pseudorapidity region $2 < \eta < 5$ and with a momentum $p > 2\,\text{GeV}/c$. Afterwards, the obtained result is extrapolated to the full phase space using Monte Carlo simulations.

4.1 Analysis strategy

The strategy followed in this thesis consists of measuring the inelastic cross-section in the fiducial area of the detector and then extrapolate it to the full phase-space using simulation. The fiducial cross-section is defined as the cross-section for inelastic pp collisions with at least one prompt long-lived charged particle in the LHCb acceptance with $p > 2\,\text{GeV}/c$ and $2 < \eta < 5$. In the following prompt long-live charged particles will be referred as signal particles. This area is delimited in Figure 4.1 using black lines. Long-lived particles are those quasi stable particles that live enough to traverse the tracking stations so they can be reconstructed as "long tracks". These particles are mainly e^-, μ^-, km, π^-, p and their respective antiparticles. Prompt particles are those that have originated directly from the pp interaction vertex or when the sum of the lifetime of their ancestors is less than 10 ps. As a consequence, decay products of beauty and charm hadrons are treated as prompt particles. Those particles that do not meet the prompt definition are called secondaries. These are for example pions decaying into muons.

In the following, the strategy for the two data samples at 5 and 13 TeV is described. Then, the details and results of each cross-section measurement are explained in Sections 4.2 and 4.3.

4.1.1 Cross-section measurements

The inelastic pp cross-section can be calculated as the number of interactions (N_{int}) divided by the integrated luminosity ($\mathcal{L}$) of the sample,

$$\sigma = \frac{N_{int}}{\mathcal{L}}. \tag{4.2}$$

Elastic interactions are not expected to be detected by LHCb, since the resulting particles will have a very low angle with respect to the beam pipe axis. Thus, an inelastic interaction can be identified by the detection of a long track in the detector originating from the luminous region. This is defined as the volume formed by the overlap of the two proton beams. As LHCb has a limited acceptance, only the cross-section in the detector acceptance can be measured. To extrapolate the result to the full phase-space volume, I need to lean on MC simulations. The extrapolation is done by calculating the fraction of events in the official LHCb MC composed by at least one signal particle with respect to all events composed by charged, prompt and long-lived particles produced in the full phase-space. The official LHCb MC [24] is generated using the LHCb tune of Pythia 8.

Inside the acceptance, N_{int} cannot be measured directly by the experiment due to the detector inefficiency. Nevertheless, it can be calculated easily as the total number of bunch crossings recorded (N_{Bx}) multiplied by the average number of visible interactions per bunch crossing (μ)

$$\sigma = \frac{N_{Bx}\mu}{\mathcal{L}}. \tag{4.3}$$

The number of interactions of a given type per bunch crossing is a random variable that follows a binomial distribution. Since the number of colliding particles is very large, the interaction count distribution is very close to the Poisson limit. The probability of finding a certain number of interactions in one bunch crossing can be calculated from

$$P_n = e^{-\mu}\frac{\mu^n}{n!}, \tag{4.4}$$

where μ is the Poisson average that coincides with the average number of interactions of a given type per bunch crossing. The easiest way to calculate μ is from the probability of finding a bunch crossing with no tracks as

$$\mu = -\ln P_0 = -\ln\left(1 - \frac{N_{vis}}{N_{Bx}}\right), \tag{4.5}$$

where N_{vis} is the number of visible events. A visible event is defined as one bunch crossing that produced at least one charged, prompt and long-lived particle inside the detector acceptance as a result of a pp collision. Since the detector is not perfect, equation 4.5 needs to be modified to take into account the efficiency of detecting an event, ε_{evt}, and the number of background events, N_{bkg}. Thus, the average number of interactions of a given type per bunch crossing can finally be calculated as

$$\mu = -\ln\left(1 - \frac{N_{vis} - N_{bkg}}{\varepsilon_{evt}\ N_{Bx}}\right). \tag{4.6}$$

As it will be seen later, the integrated luminosity is by far the dominant systematic contribution, so reducing its uncertainty will translate in a proportionally smaller cross-section uncertainty. The luminosity is calibrated using special runs assuming that all

bunches in the accelerator are similar. Then this calibration is applied to the full data sample and an integrated luminosity is obtained. Actually, the bunches in the fill are not identical since, for example, the leading bunches of a train have a higher intensity than average and thus higher luminosity. Hence, the integrated luminosity value measured by the luminosity group is only valid if no specific bunch of the fill is selected. A no bias data sample is composed by truly random triggers, so it contains events from any bunch crossing collision. The LHCb 5 TeV no bias data sample is fully composed by leading bunches collisions, so it is mandatory to perform an offline measurement of the integrated luminosity. In the 13 TeV data sample there is a no bias sample large enough to perform the cross-section analysis. Since the leading bunch collisions are expected to be cleaner due to the lack of *spillover* effects the no bias leading bunches sample is used for the two energies. Spillover measurements arise from the finite duration of the analogue signal produced by the front-end electronics if the amplitude of this signal is non-negligible when recording the new bunch crossing or event. Then this signal can be digitized and wrongly stored as a hit of the next event.

4.1.1.1 Event reconstruction efficiency

As detailed in Appendix 4.E, assuming that all final state particles in the acceptance are independently reconstructed with the same single track efficiency ε, the event efficiency is a function of ε and $\hat{q}_k$, $k = 1, .., \infty$,

$$\frac{1}{\varepsilon_{evt}} = 1 - \sum_{k=1}^{\infty} \hat{q}_k \left(\frac{\varepsilon - 1}{\varepsilon} \right)^k , \tag{4.7}$$

where $\hat{q}_k$ is the zero-suppressed measured multiplicity distribution, and k the number of tracks.

The single tracking efficiency can be calculated using MC. Furthermore, it can be factorised as the product of the acceptance efficiency (ε^{Acc}), the reconstruction efficiency (ε^{Reco}), the offline selection efficiency (ε^{Cuts}) and a data/MC correction factor $\rho^{Tracking}$,

$$\varepsilon = \varepsilon^{Acc} \times \varepsilon^{Reco} \times \rho^{Tracking} \times \varepsilon^{Cuts}. \tag{4.8}$$

The acceptance efficiency is calculated as the fraction signal particles that reach the end of the tracking stations.

The reconstruction efficiency is defined as the number of reconstructed particles with a ghost probability lower than 0.3 (GhostP < 0.3) divided by the number of particles going through all the tracking stations. The track ghost probability has been defined in order to better discriminate between real and ghost tracks, This is an estimate of the probability that a track is a ghost. The estimate is based on the output of a Neural Network (NN) which takes several tracking and kinematic quantities into account. The reconstruction efficiency of the detector is very dependent on the track multiplicity, decreasing towards higher values. As will be seen in the comparisons between data an MC, the multiplicity distributions are very different in data and MC, so the result obtained using MC is corrected by the actual data multiplicity. The final reconstruction efficiency is calculated as the integral of the normalised data multiplicity distribution weighted bin-by-bin by the MC

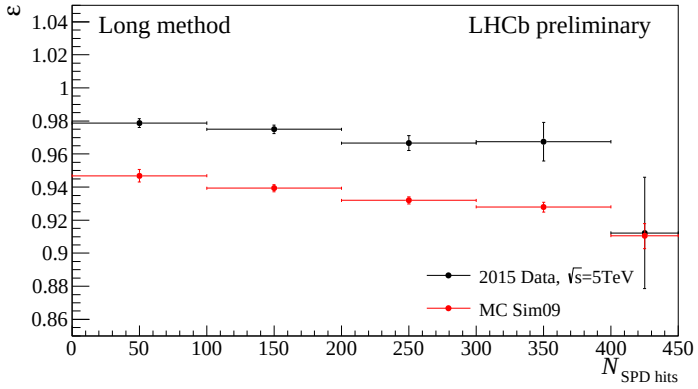

Figure 4.2: Data and MC tracking efficiencies *vs.* number of SPD hits calculated by the LHCb tracking group.

tracking efficiency of each multiplicity bin,

$$\varepsilon^{Reco} = \frac{\sum_i N_i}{\sum_i N_i/\varepsilon_i^{MC}}, \tag{4.9}$$

where N_i is the "i" bin in the data multiplicity distribution. Furthermore, it is known that the reconstruction efficiencies in simulation do not agree with data. Figure 4.2 shows the difference between the tracking efficiencies in 5 TeV data and MC samples with respect to the number of SPD hits (which is proportional to the multiplicity of charged particles in the event). The factor $\rho^{Tracking}$ is a value provided by the LHCb tracking group and it is the result of averaging the ratio of reconstruction efficiencies

$$\rho^{Tracking} = \frac{\varepsilon^{Real\,Data}_{LHCb}}{\varepsilon^{MC}_{LHCb}}.$$

ε^{Cuts} is the offline selection cuts efficiency. This efficiency is defined as the ratio of the reconstructed tracks that pass all the cuts in the analysis and the reconstructed tracks with a ghost probability lower than 0.3.

4.1.2 Event and track selection

In order to avoid any spillover, in this analysis I only use events from interactions of the leading bunches of a train. The leading bunches are selected using no bias trigger lines. Since these trigger lines select events randomly, the efficiency of the trigger is 100%. Furthermore, I require every collision to come from beam-beam interactions. A beam-beam (bb) interaction is produced when two bunches circulating in opposite directions in the LHC ring collide in one interaction point. If the LHC is not fully charged, it will contain bunches circulating in one direction with non corresponding bunches in the other. The events produced each time these bunches pass through the interaction point are called beam-empty (be or eb) events. Furthermore, the events produced synchronous with the LHC clock but without bunches passing through the interaction point are called empty-empty (ee) events.

The luminous regions in data and MC are studied for each energy.

Regarding track selection, the first cuts applied are those related to the detector acceptance $2 < \eta < 5$ and $p > 2$ GeV/c.

LHCb reconstruction software does not build the particle tracks by taking into account all the hits of the detector at the same time. Instead, it creates track segments in the subdetectors and then tries to combine them to form a larger track. In many occasions, the algorithm builds two or more long tracks sharing one VELO segment. In these cases, only one of these tracks is created by a real charged and long lived particle moving through the detector. The other tracks are called clone tracks, and they are created by segments of actual particles and hits from unstable particles or detector noise. Usually, these tracks do not fulfil the reconstruction quality requirements and the software can easily discard them, although sometimes they pass all filters and are reconstructed as good tracks. In this analysis I loop over all long reconstructed tracks in one event and search for shared VELO segments. From all long tracks sharing one VELO segment, only the track with the lowest fit χ^2 is kept.

The reconstruction of a PV requires at least three tracks pointing to the same point. Thus, the use of any primary vertex related variable biases the event sample used in the analysis to higher multiplicities. In absence of actual PV coordinates, the impact parameter of a track with respect to the PV cannot be rigorously calculated. In order to avoid this bias, I define a new variable called pseudo impact parameter (psIP).

The PV density can be parametrised using a three-dimensional Gaussian

$$\rho(r) = \frac{1}{(\sqrt{2\pi})^3 det(C)} exp\left[-\frac{1}{2}S^2\right] \quad \text{with} \quad S^2 = (r-v)^T C^{-1}(r-v), \tag{4.10}$$

where v is the column vector of the average PV positions: $v = (\overline{x}_{PV}, \overline{y}_{PV}, \overline{z}_{PV})^T$, r are the track positions $r = (x, y, z)$, C is the covariance matrix of the vertex coordinates: $C_{ii} = \sigma_i^2$, $C_{ij} = R_{ij}\sigma_i\sigma_j$, R_{ij} is the correlation coefficient between i and j and σ_i is the variance of the (vertex) coordinate i.

Since the transverse coordinates of the primary vertices are very well defined, while the longitudinal positions are smeared out, as it can be seen in Figure 4.3, the psIP is defined as the transverse distance of the estimated point of origin of a track to the average PV position

$$\text{psIP}^i = \sqrt{(x^i_{origin} - \overline{x}_{PV})^2 + (y^i_{origin} - \overline{y}_{PV})^2}. \tag{4.11}$$

Here $(x, y)^i_{origin}$ is the estimated point of origin of the track "i", defined as the point of a track that maximizes the vertex density $\rho(r)$. This is a kind of maximum likelihood estimate based on the known PV density.

Parametrising the trajectory by a straight line

$$r(\lambda) = g + \lambda p, \tag{4.12}$$

being g the column vector of the spatial coordinates of the first track state, p the column vector of the track 3-momentum components and λ a parameter enumerating the points on the trajectory. The point with the largest $\rho(r)$ is the one that minimizes the exponential in the 3D gaussian parametrization S^2, so

$$\frac{d}{d\lambda}\left(\left[(r-v)^T C^{-1}(r-v)\right]^2\right) = \frac{d}{d\lambda}\left(s^T C^{-1} s - 2\lambda p^T s + \lambda^2 p^T p\right) = 0 \tag{4.13}$$

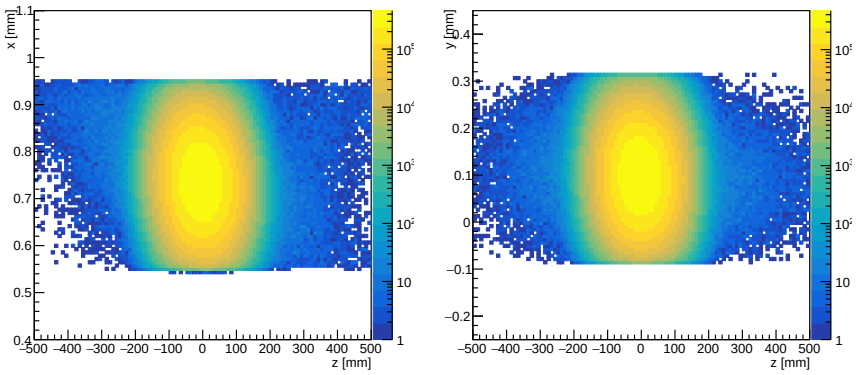

(a) 5 TeV data.

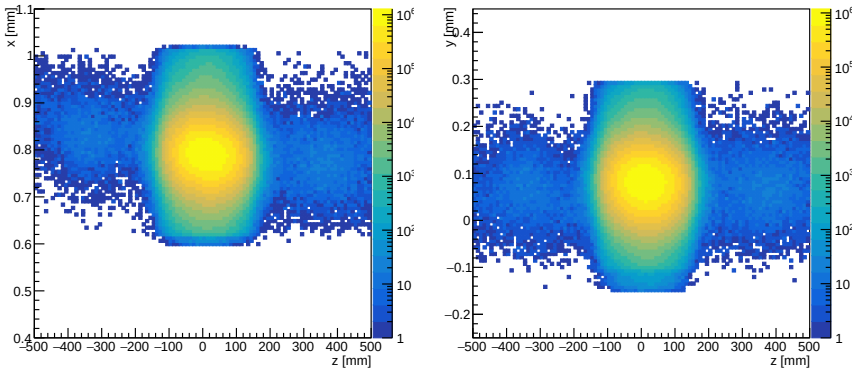

(b) 13 TeV MU data.

Figure 4.3: Reconstructed primary vertices positions of *pp* collisions at (a) 5 TeV and (b) 13 TeV. In both cases, *x vs. z* axis (left), *y vs. z* axis (right).

where $s = g - v$. Finally I obtain

$$\lambda = -\frac{p^T C^{-1} s}{p^T C^{-1} p} \quad \text{and} \quad S^2_{\text{min}} = s^T C^{-1} s - \frac{(p^T C^{-1} s)^2}{p^T C^{-1} p}. \tag{4.14}$$

More details are given in appendices 4.B and 4.C.

The selection of prompt and secondary tracks is based on MC simulation. It will be shown that the distributions of the charged, long-lived and prompt MC truth particles reconstructed (signal), the distributions of the reconstructed particles that cannot be matched to a MC truth particle (fake) and those matched to a secondary MC truth particle (secondary) follow approximately the same shapes in the MC samples at 5 and 13 TeV. Furthermore, the most signal/background discriminant variables are the ghost probability and the pseudo impact parameter. I define the background rejection as

$$\text{Bkg rejection} = \frac{\text{Signal}}{\sqrt{\text{Signal+Bkg}}}. \tag{4.15}$$

The values of ghost probability and pseudo impact parameter that maximise the background rejection will be applied as selection cuts.

4.1.2.1 The Background

Background events can be divided in two different classes, those not coming from a pp interaction and those with at least one reconstructed track in the detector acceptance but with none of its tracks produced by an actual signal particle.

In order to estimate the number of interactions not coming from a real pp interaction, I are going to study the fraction of visible events in beam-empty, empty-beam and empty-empty bunch crossings. Then, using the equation

$$f_{bkg} = q_0^{bb} \left(f_{bkg}^{be} + f_{bkg}^{eb} - f_{bkg}^{ee} \right), \tag{4.16}$$

it is straightforward estimate the number of background interactions in the data sample, being f_{bkg}^{ij} the fraction of visible events in the be, eb and ee samples, and f_{bkg} the fraction of background events in the data sample. The process to obtain the last equation is explained in detail in Appendix 4.A. Due to the lack of triggered be, eb and ee events in the 5 TeV sample this approach can only be used in the 13 TeV data sample.

To calculate the fraction of signal particles I can only use simulation. I am going to calculate the fraction of background events in MC and then extrapolate the result to real data, assuming that MC reproduces the real distributions correctly. The systematics associated to this assumption are discussed in Section 4.1.4.

4.1.3 Extrapolation to the full phase-space

The inelastic cross-section in the full-phase space is computed using the LHCb MC sample, multiplying the measured cross-section in the LHCb fiducial phase-space by a factor computed as the ratio of the number of events with one primary vertex and more than two protons in the final state and the number of events with one primary vertex and at least one prompt charged particle with $2 < \eta < 5$ and $p > 2\,\text{GeV}/c$.

4.1.4 Systematic uncertainties

The systematic uncertainties of the measurement are attributed to five different sources: integrated luminosity, beam energy, event reconstruction efficiency, differences between data and MC and background events. The integrated luminosity is by far the dominant systematic contribution, with the other systematics and the statistical uncertainties being negligible.

The beam energy uncertainty is 0.65% as indicated in [88]. This parameter is not taken into account in the analysis, so the systematic uncertainty will be calculated as the difference between the cross-sections predicted by the model proposed by Martin M. Block *et al.* in [89] for the extreme values of the one sigma interval around the nominal energy value.

The systematic uncertainties affecting the event efficiency come from the tracking efficiency correction and from the calculation method itself, that includes the biases of the long tracks multiplicity. The systematic due to the calculation method is determined from MC as the difference between the event efficiency obtained using our method and the result obtained from MC. Individual uncertainties coming from the two mentioned sources are assumed to be not correlated and added in quadrature.

I am going to assign a systematic to account for data/MC discrepancy. I calculate the cross-section moving the ghost probability cut to the position where the data proportions at both sides of the cut in real data are the same as in MC using the nominal cut. The difference between the cross-sections calculated with the two cuts is taken as a systematic uncertainty.

In order to compare the background in data and MC I created a Boosted Decision Tree (BDT) constructed using the TMVA package [90]. A Decision Tree is a succession of decision nodes used to categorize the events out of the sample as either signal or background. Each node uses only a single discriminating variable to decide if the event is signal-like ("goes right") or background-like ("goes left") The idea behind the boosting is, that signal events from the training sample, that end up in a background node (and vice versa) are given a larger weight than events that are in the correct leave node. This results in a re-weighed training event sample, with which then a new decision tree can be developed. The boosting can be applied several times (typically 100-500 times) and one ends up with a set of decision trees (a forest). Finally, a Boosted Decision Tree is an algorithm where the selection of an event is done by means of a majority vote on the result of several decision trees, which are all derived from the same training sample by supplying different event weights during the training.

The BDT created in this analysis uses the following variables: $\log(p_{\mathrm{T}})$, χ^2/nDoF, $\log(P(\texttt{GhostP}))$ and $\log(\texttt{psIP})$. This BDT is optimized using prompt tracks from simulation as signal, and non prompt and ghost tracks as background also from simulation. Afterwards, this BDT is applied to data and a Probability Density Function (PDF) with 3 components, prompt (signal), secondary and ghost tracks, is fitted to data. The comparison between the number of background tracks returned by the fit and the MC will give us an idea of how well the simulation reproduces the background events in real data. Even in the case of obtaining full similarity between data and MC, I could not assume that the number of background events are equal, since the method does not provide any information about the multiplicity distribution of the background tracks with respect to the multiplicity of the event. Because of this, I am going to assume a systematic uncertainty

of 100% for this background type.

In order to calculate the systematic uncertainties of the extrapolation to the full phase-space I generated some private MC samples using different Pythia 8 tunes and the default Pythia 6 tune. The Pythia 8 tunes used are: `4Cx` [91], a tune derived from the 2C-tune to CDF data and adapted to LHC; `A2-CTEQ6L1`, `A2-MSTW2008LO`, `AU2-CTEQ6L1` and `AU2-MSTW2008LO` minimum-bias and underlying event tunes by the ATLAS collaboration based on tune 4Cx, and using the CTEQ 6L1 and the MSTW2008 LO parton densities [92]; and `Monash 2013` [93], a tune based on both e^+e^- from LEP and SLD and pp ($\overline{p}$) from SPS, Tevatron and LHC data. In the extrapolation calculation all uncertainties are treated as systematics. Hence, the final systematic uncertainty is calculated as the square root of the quadratic sum of the statistical uncertainty of the extrapolation factor obtained from the official LHCb simulation and the standard deviation of the factors obtained from the different tunes of Pythia 8 and Pythia 6.

4.2 *pp* inelastic cross-section at 5 TeV

4.2.1 Data sets

In November 2015 LHCb collected *pp* collisions data at a centre-of-mass energy of $\sqrt{s} =$ 5 TeV and 25 ns of bunch spacing. To calculate the cross-section I am going to use the no bias data from the no bias stream. The no bias stream is fully composed by no bias events from leading bunches collisions. Table 4.1 shows the fill and run numbers of the sample. In the analysis only events registered in good working conditions of all detector sub-systems are used. Therefore, all runs from fills 4634 and 4647, as well as runs 168140, 168142, 168145, 168176 - 168181, 168233, 168260 are not used in this analysis. After removing these runs, the data sample used in this analysis corresponds to about 530 million events. The luminosity measurement provided by the LHCb luminosity group is not valid for this analysis since I am selecting only leading bunch crossings. Due operational problems the luminosity could not be calculated yet, and the result will be updated in the future. Meanwhile, I use the value provided by the LHCb luminosity group in order to fully develop the analysis. This integrated luminosity is $(3.37 \pm 0.12)\,\text{nb}^{-1}$. All the events were recorded in magnet down (MD) polarity and data was reconstructed under version Reco15a.

fill	runs
4634	167988, 167989
4638	168072
4639	168128, 168140 - 168146
4640	168171, 168176 - 168186, 168189 - 168196
4643	168233, 168234, 168237 - 168249, 168260, 168261
4647	168325, 168326, 168328, 168330, 168331, 168336, 168338 - 168350

Table 4.1: All *pp* collision runs collected by LHCb at 5 TeV in 2015.

Figure 4.4 shows the average number of primary vertices per run in the 5 TeV data sample. As it can be seen, the pile up variation from run to run is quite high.

A Monte Carlo sample of 1 million events, based on the LHCb tune of Pythia 8was generated with an average number of $\nu = 1.5$ *pp* interactions per bunch crossing and 25 ns of bunch space. The reconstruction version used was Reco15. The same trigger conditions were applied for data and MC.

Figure 4.5 shows the distributions for data and MC for some key variables after applying the LHCb acceptance cuts $p > 2\,\text{GeV}/c$ and $2 < \eta < 5$. In this figure it is shown how p and p_T distributions are quite well reproduced by the MC. Nevertheless, the multiplicity distributions are quite different.

4.2.2 Event and track selection

As it was mentioned in section 4.1.2 I requires no bias events from leading bunch interactions. In real data TCK, `0x0115014E`, the trigger line selecting this kind of events is

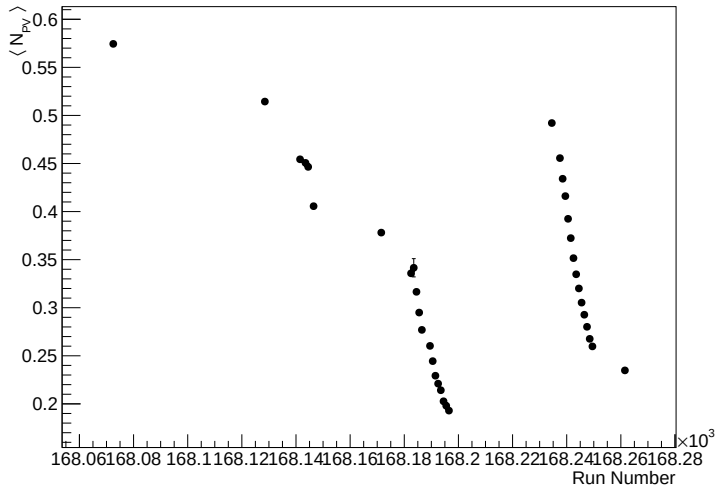

Figure 4.4: Average number of primary vertices per run for events with a random trigger.

`Hlt1NoBiasLeadingCrossing`. So I require all events to pass this trigger line and to come from a beam-beam interaction.

Figure 4.6 shows the one dimensional position distributions of the reconstructed primary vertices for MC and data. The luminous regions in data and MC are slightly displaced but, since the background of the two distributions is negligible, I am not going to apply any cut in the luminous area. The z-position distribution presents a right hand tail that is not observed in the left hand of the plot. These vertices are actual MC truth vertices generated as a consequence of the interaction of a particle with the detector material.

The 5 TeV and 13 TeV data were reconstructed using Reco15a and Reco15em versions respectively. These two releases present different cut values in χ^2/nDoF and ghost probability. These differences are shown in Table 4.2. In order to permit a better comparison between the two data samples and simplify the analysis I am going to apply a baseline cut of χ^2/nDoF < 3 and GhostP < 0.3 in both data samples. The GhostP cut is harder than the LHCb reconstruction cuts to permit the use of the tracking efficiency correction provided by the LHCb tracking group. As it was mentioned above, this correction was calculated using GhostP < 0.3.

	Reco15em	Reco15a
χ^2/nDoF	< 3	< 4
GhostP	-	< 0.4

Table 4.2: Cuts applied by LHCb reconstructions Reco15em and Reco15a.

Figure 4.7 shows the fraction of clone tracks found with respect to different variables. All tracks tagged as clones will be removed from the analysis.

Figure 4.8 shows the distributions of signal, fake and secondary tracks calculated using simulation. As mentioned above, it can seen that the most signal/background discriminant

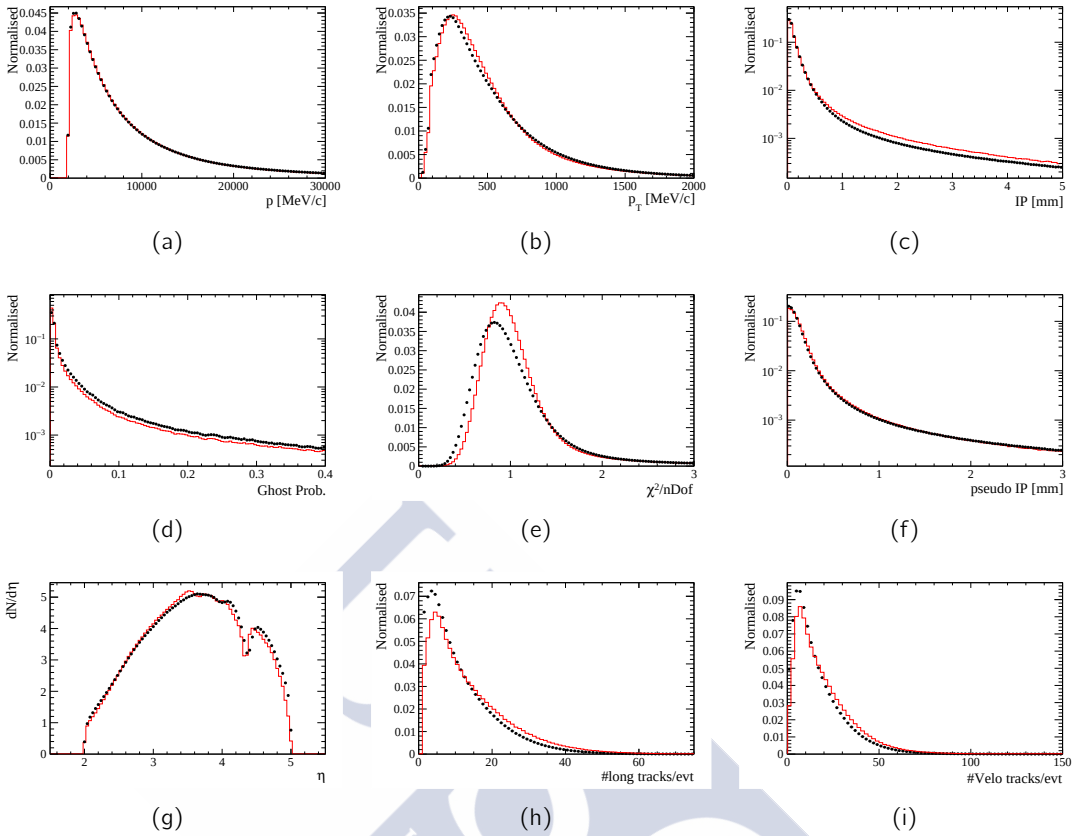

Figure 4.5: MC *vs.* data distributions of different variables after applying the acceptance cuts. (a) Momentum, (b) transverse momentum, (c) impact parameter with respect to the reconstructed primary vertex, (d) ghost probability, (e) χ^2 over the number of degrees of freedom, (f) pseudo impact parameter, (g) differential multiplicity over η with respect to η, (h) long tracks multiplicity, (i) VELO tracks multiplicity. In all cases MC distributions are represented with red lines and data using black dots.

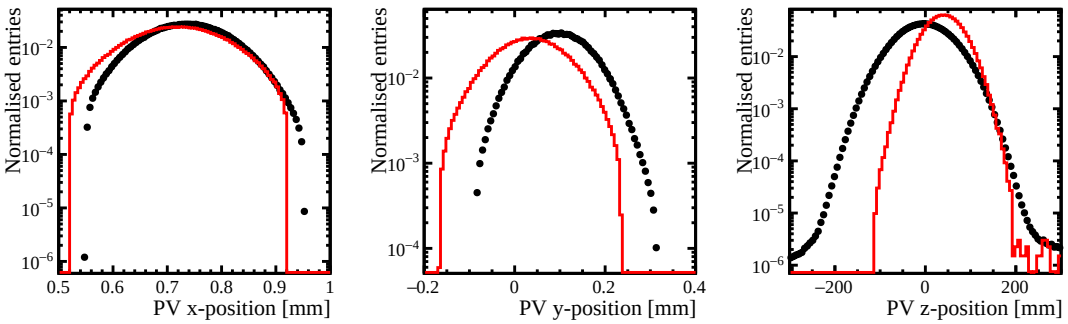

Figure 4.6: Projections of the luminous region in x, y and z axis for MC (red line) and data (black dots).

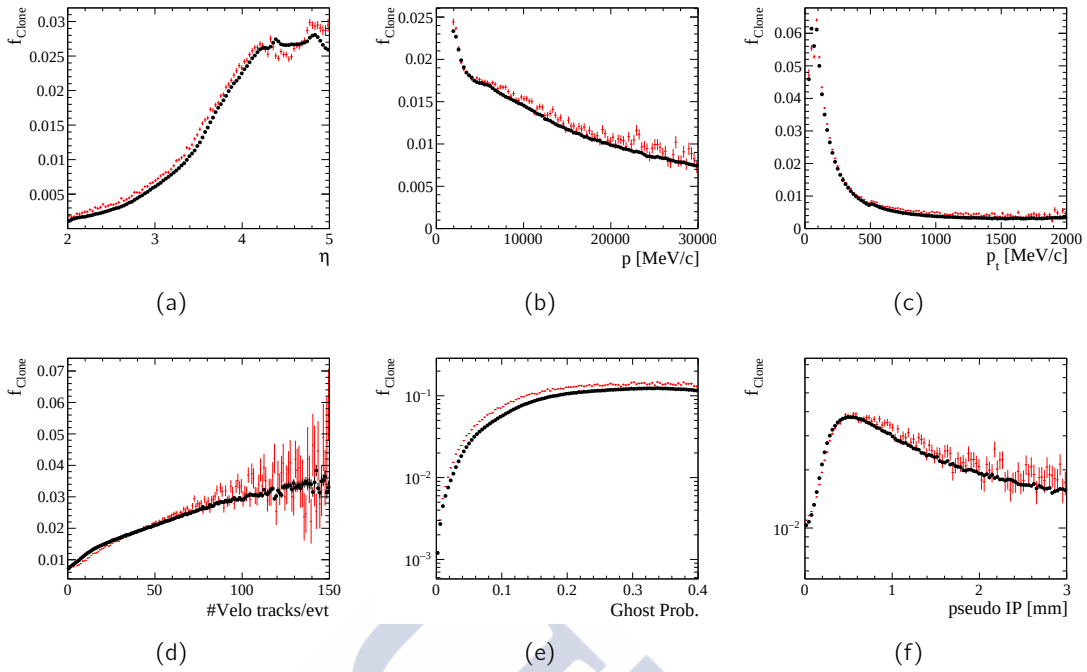

Figure 4.7: Fraction of clone tracks with respect to different variables. MC results are drawn using red lines and data using black dots. (a) Pseudorapidity, (b) momentum, (c) transverse momentum, (d) VELO tracks multiplicity, (e) ghost probability, (f) pseudo impact parameter.

variables are the ghost probability and pseudo impact parameter.

Figure 4.9 represents the background rejection as defined in Equation 4.15 with respect to the ghost probability and the pseudo impact parameter simultaneously. The maximum background rejection is obtained for GhostP < 0.13 and psIP < 0.93 mm.

A summary of the cuts applied to the 5 TeV data sample is shown in Table 4.3. These cuts remove 50.4% of background tracks with an efficiency in the signal of 97.1%. The resulting track sample has a purity of 91.6%.

Event cuts	`Hlt1NoBiasLeadingCrossingDecision == True` Bunch crossing type == beam-beam
Fiducial cuts	$2 < \eta < 5$ $p > 2$ GeV/c
Tracks selection	Clone == `False` χ^2/nDoF < 3 Pseudo IP < 0.93 mm Ghost Prob. < 0.13

Table 4.3: Summary of cuts applied to the 5 TeV sample.

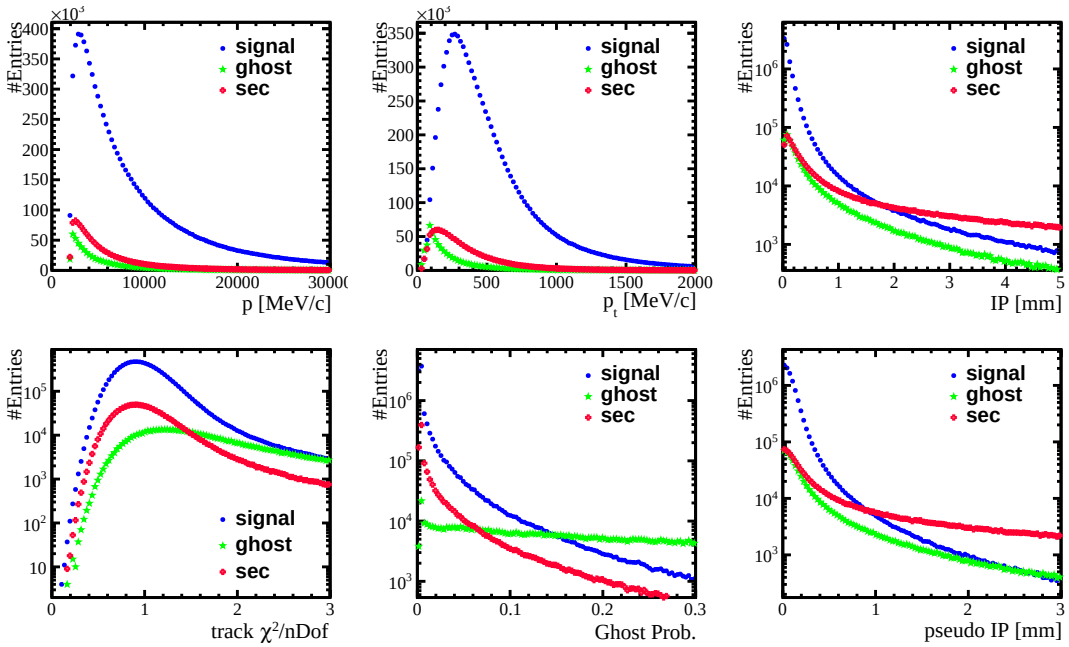

Figure 4.8: Distributions of signal, fake and secondary tracks obtained from the MC sample.

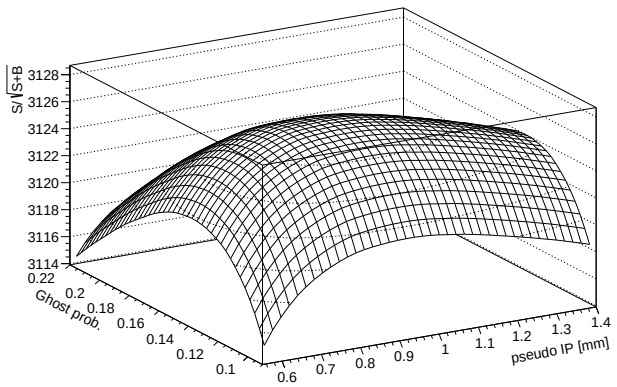

Figure 4.9: Background rejection defined as $S/\sqrt{S+Bkg}$ with respect to the ghost probability and the pseudo impact parameter.

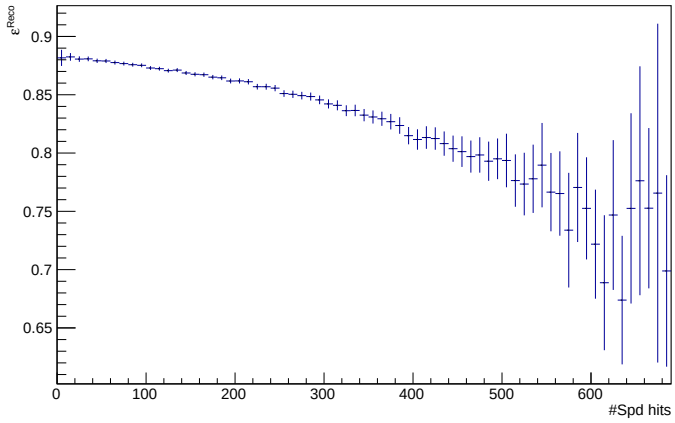

Figure 4.10: MC event efficiency with respect to the number of SPD hits.

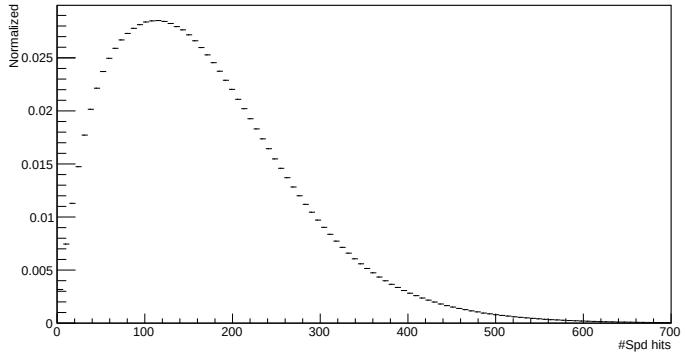

Figure 4.11: Data SPD hits distribution.

4.2.3 Measurement of the pp inelastic cross-section

4.2.3.1 Event efficiency

To calculate the event efficiency I need first to calculate the track efficiency. As indicated in section 4.1.1.1, track efficiency can be calculated using MC and then apply some corrections from data.

Using MC truth, I obtain an acceptance efficiency of

$$\varepsilon^{Acc} = 0.71481 \pm 0.00027(stat).$$

Figure 4.10 shows the reconstruction efficiency *vs.* number of SPD hits calculated using MC. As it can be seen in this figure, the reconstruction efficiency has a strong dependence on the multiplicity. Furthermore, since the MC multiplicities are higher than in data, as showed in Figure 4.5(i), the efficiency needs to be corrected to take into account this difference. The reconstruction efficiency obtained is

$$\varepsilon^{Reco} = 0.86257 \pm 0.00036(stat).$$

Taking the tracking efficiency corrections provided by the LHCb tracking group and averaging over the whole η and p range, I obtain the following tracking correction

$$\rho^{Tracking} = 1.0382 \pm 0.0023(stat) \pm 0.0083(syst).$$

The cut efficiency obtained is

$$\varepsilon^{Cuts} = 0.97600 \pm 0.00043(stat).$$

Finally, the tracking efficiency is

$$\varepsilon = 0.6248 \pm 0.0015(stat).$$

Using the equation 4.7 it is straightforward to calculate the event efficiency,

$$\varepsilon_{evt}^{Data} = 0.97558 \pm 0.00025(stat).$$

As a cross check I calculate the MC event efficiency using this method and compare the result to the MC true event efficiency. The MC true event efficiency is defined as the number of events with at least signal particle inside the fiducial area of the detector over the total number of generated events with at least one signal particle inside the fiducial region of the detector. The event efficiency calculated using MC true information is

$$\varepsilon_{evt}^{MC_{True}} = 0.9803 \pm 0.0014(stat),$$

and the result calculated from the reconstructed data

$$\varepsilon_{evt}^{MC} = 0.98554 \pm 0.00026(stat).$$

The later result is slightly higher than the true one. One of the reasons is that the ghost and secondary tracks bias the multiplicity distributions at low multiplicities and push the event efficiency to higher values. When removing the ghost and secondary tracks from the long tracks multiplicity distribution, I obtain

$$\varepsilon_{evt}^{MC} = 0.98348 \pm 0.00028(stat).$$

The difference between the two methods will be used as a systematic uncertainty.

4.2.3.2 Number of visible events

The total number of bunch crossings in the data sample is $N_{Bx} = 529837568$. From those, only $N_{vis} = 156531800 \pm 12511$ events pass the selection cuts and are tagged as visible events.

In the 5 TeV data sample all events come from bb interactions, thus I cannot estimate the fraction of background events due to be, eb and ee interactions. As shown in Section 4.3.3.2, in the 13 TeV sample there are be, eb and ee data available to perform this study. In the 13 TeV sample the conclusion is that this background contribution is negligible. So, I am going to assume the same behaviour in this sample and do not take it into account.

I define a background event from a pp interaction as those having only secondary or ghost tracks. The fraction of these events is calculated from MC. I find that from the total of 967414 MC events, 3693 pass the offline cuts only because of their secondary or ghost tracks. So the ratio of background events in MC is 0.38%. Extrapolating this result to data, and assuming that the ratio of background events is the same as in simulation, I obtain that 599019 data events are actually background. The systematic associated to the assumption of the two samples having the same fraction of secondary and ghost tracks is studied in Section 4.2.4.

4.2.3.3 Extrapolation to the full phase-space

The extrapolation factor obtained from the official LHCb simulation is

$$s_{ext} = 1.1555 \pm 0.0026,$$

where the uncertainty is statistical only.

4.2.4 Systematic uncertainties

The systematic uncertainty related to the integrated luminosity is the dominant. The integrated luminosity is measured by the LHCb luminosity group using different methods. At the moment of writing, the integrated luminosity at $\sqrt{s} = 5$ TeV had been measured only using the Beam-Gas Imaging method (BGI) [94, 95]. The uncertainty associated to this value is 3.63%, therefore the systematic uncertainty of the final cross-section due to the luminosity measurement is 2.06 mb.

Using the method explained above, and taking differences between the cross-sections predicted by the model proposed by Martin M. Block *et al.* in [89] for the extreme values of the one sigma interval around the nominal energy value I obtain a systematic uncertainty of 0.064 mb.

Calculating the event efficiency in the simulation using the method presented in this thesis and the MC truth information I obtain a systematic uncertainty of 0.0052. On the other hand, the tracking efficiency contributes with a systematic uncertainty of 0.00059 to the event efficiency. This contribution is one order of magnitude lower than the one from the method calculation, so it is neglected. The propagation of this uncertainty yields a systematic of 0.39 mb in the final cross-section.

As it can be seen in Figure 4.5(d) the MC and data ghost probability distributions do not agree very well. To account for this, I change the ghost probability upper bound in real data to a value (0.158) corresponding to equal proportions of events passing and being rejected by the cut as it is obtained in MC for the original cut value. The difference between the cross-sections calculated with these two cuts is taken as a systematic error. The value of the ghost probability cut obtained to calculate this systematic is 0.158, that propagated to the cross-section provides a systematic of 0.13 mb.

The number of background events is based in the assumption that the secondary and ghost tracks distributions are similar in data and MC. As shown in Figure 4.8, there are differences in some distributions between signal, ghost and secondary tracks. For instance, the ghost probability distribution for ghost tracks is very different from the distribution for signal and secondary tracks. The same happens with the psIP distribution, which is different for signal with respect to the other two. These differences are exploited combining them in a BDT. This BDT uses the following variables for each track: $\log(p_{\mathrm{T}})$, χ^2/nDoF, $\log(P(\texttt{GhostP}))$ and $\log(\texttt{psIP})$. The BDT is optimized using prompt tracks from the 5 TeV simulation as signal, and non prompt and ghost tracks as background. The comparison between variables for signal and background is shown in Figure 4.12. The BDT output for signal and background is shown in Figure 4.13.

Figure 4.14(a) shows the BDT data distributions before the fit. The fraction of the three components are fixed to what was obtained from MC. Figure 4.14(b) shows the distributions after fit. It can be seen that the final fit reproduces quite well the real data. The fraction of background events found is shown in Table 4.4. The fit gives higher

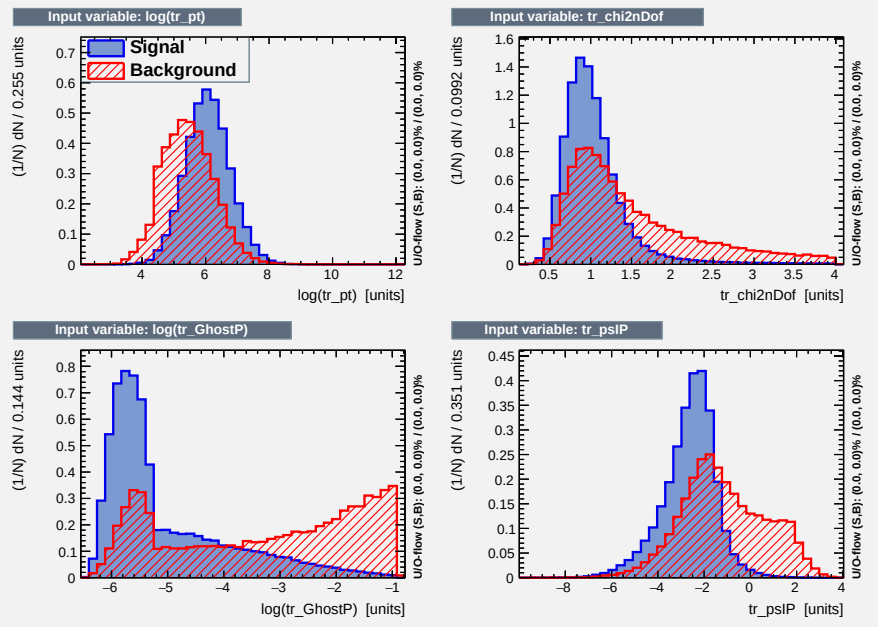

Figure 4.12: Variables used for the BDT optimization.

values than the Monte Carlo, but differences are covered applying a 100% systematic uncertainty. Finally, the propagation of the uncertainty from the number of background events yields a systematic of 0.26 mb in the final cross-section.

	5 TeV MC	5 TeV fit
f_{sec}	0.0924	0.1359 ± 0.0013
f_{ghost}	0.0880	0.0869 ± 0.0010

Table 4.4: Fraction of events in the Monte Carlo and obtained from a fit to the 5 TeV data sample.

Assuming that all the uncertainties are not correlated and adding them in quadrature, I obtain that the final value of the cross-section systematic is 2.12 mb.

The extrapolation systematic uncertainty is calculated using different Pythia 8 tunes and the default tune of Pythia 6. The extrapolation factors obtained are shown in Table 4.5. The final systematic uncertainty is calculated as the quadratic sum of the statistical uncertainty of the extrapolation factor obtained from the official LHCb MC and the standard deviation of the factors resulting from the private MC samples, that is 0.0078. The final systematic uncertainty associated to the extrapolation factor is 0.0082.

4.2.5 Results

The luminosity and its uncertainty calibrated by the LHCb luminosity group in this data sample correspond to

$$\mathcal{L} = 3.37 \pm 0.12\,\text{nb}^{-1}.$$

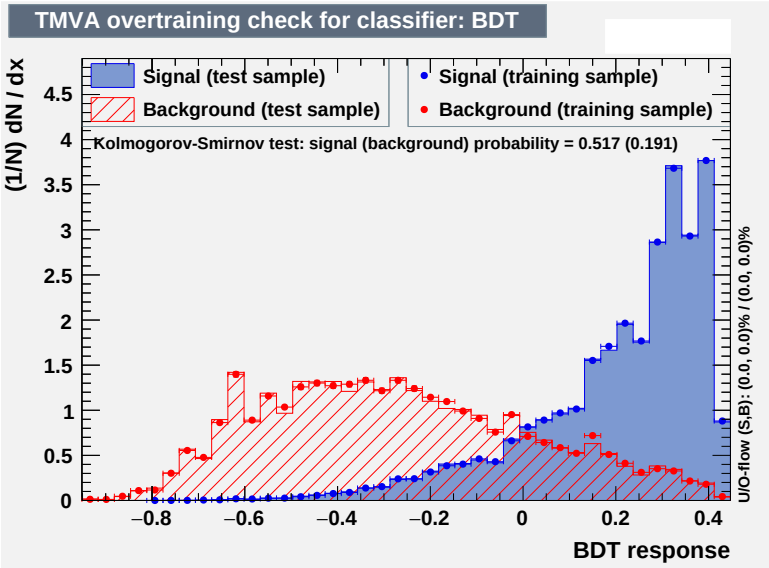

Figure 4.13: BDT output for signal (blue) and background (red).

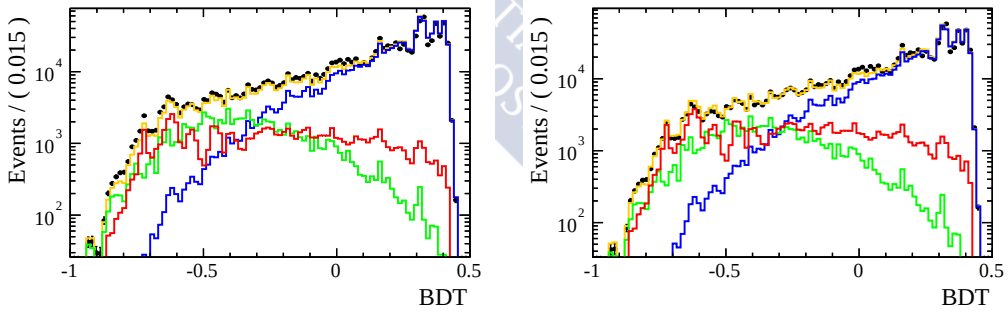

(a) (b)

Figure 4.14: BDT distributions (a) before and (b) after the fit to data in logarithmic scale. Black points represent real data and the lines represent results form MC. The blue line represents the signal distribution, the green line represent the ghost tracks and the red line the secondary tracks. The yellow line represent the sum of the three MC components.

Generator	Tune	s_{ext}
Pythia 8	LHCb	1.1555 ± 0.0026
Pythia 8	4Cx	1.1547 ± 0.0064
Pythia 8	A2-CTEQ6L1	1.1544 ± 0.0064
Pythia 8	A2-MSTW2008LO	1.1560 ± 0.0064
Pythia 8	AU2-CTEQ6L1	1.1537 ± 0.0064
Pythia 8	AU2-MSTW2008LO	1.1548 ± 0.0064
Pythia 8	Monash 2013	1.1552 ± 0.0064
Pythia 6	Default	1.1768 ± 0.0066

Table 4.5: Extrapolation factors obtained from some Pythia 8 tunes and the Pythia 6 default tune. To calculate the extrapolation factors private simulations were produced generating 200000 events per sample. The uncertainties shown are only statistical.

Filling equation 4.6 with the values calculated so far, I obtain the number of visible interactions per bunch crossing,

$$\mu = 0.36189 \pm 0.00012.$$

Table 4.6 shows a summary of the results obtained so far.

N_{vis}	156531800 ± 12511
N_{bkg}	599019 ± 599019
N_{Bx}	529837568
ε_{evt}	0.97558 ± 0.00025
μ	0.36189 ± 0.00012
$\mathcal{L}$	$(3.37 \pm 0.12)\,\mathrm{nb}^{-1}$

Table 4.6: Results summary.

Plugging these values into Equation 4.3 yield a cross-section in the detector acceptance of

$$\sigma^{acc} = 56.88 \pm 0.02(stat) \pm 2.12(syst)\,\mathrm{mb}.$$

Using the extrapolation factor calculated above and propagating the uncertainties, the inelastic cross-section in the full phase-space obtained is

$$\sigma = 65.72 \pm 0.02(stat) \pm 2.49(syst)\,\mathrm{mb}.$$

4.3 pp inelastic cross-section at 13 TeV

4.3.1 Data sets

From June to mid August 2015, during the early measurements period, LHCb collected pp collisions at a centre-of-mass energy of $\sqrt{s} = 13$ TeV and 50 ns of bunch spacing in both magnet configurations, up and down.

As for the 5 TeV data, the cross-section measurement is performed using the no bias stream. Table 4.7 shows the number of triggered events (N_{Bx}) and integrated luminosity luminosity collected per run. I am using all data collected by LHCb in both magnet configurations and registered in good working conditions of all detector sub-systems. Due to technical issues the available sample in MD configuration consists of 7 out of the 41 available runs. This is not a problem for the analysis, since the statistics is large enough and the final result will be dominated by the luminosity systematic uncertainty. The integrated luminosities are $(3175 \pm 130)\,\mu b^{-1}$ for MU configuration and $(959 \pm 37)\,\mu b^{-1}$ for MD.

Data were reconstructed using version Reco15em. The trigger line used in this sample is `Hlt1MBNoBiasLeadingCrossingDecision` that is slightly different from the one used in the 5 TeV sample (`Hlt1NoBiasLeadingCrossingDecision`). Nevertheless from the point of view of this analysis the two trigger lines perform identically.

Magnet	Run	N_{Bx}	$\mathcal{L}[\mu b^{-1}]$	$d\mathcal{L}$
MU	158517	11794975	206.0	3.9%
	159978	121398080	1658.8	4.0%
	159986	104643520	1310.2	3.9%
	Total	237836575	3175.0	4.0%
MD	157584	1398009	21.3	4.0%
	157596	14850881	232.0	3.9%
	157597	3372194	51.8	4.0%
	157704	14899561	285.1	3.9%
	157706	14912089	285.5	3.9%
	157803	2449149	25.0	3.9%
	157817	3726938	58.3	3.9%
	Total	55608821	959.0	3.9%

Table 4.7: pp collision runs collected by LHCb at 13 TeV in the no bias stream and used in this analysis.

As in the 5 TeV runs, the pile up variation is quite high, as shown in Figure 4.15. Furthermore, the number of primary vertices per interaction is about 3 times higher than in 5 TeV data.

A Monte Carlo sample, based on the LHCb tune of Pythia 8 was generated with an average number of $\nu = 1.6$ pp interactions per bunch crossing and 50 ns of bunch space. The TCK applied in this case was `0x40f9014e` and the reconstruction version Reco15em.

Figure 4.16 shows the distributions of data and MC of some key variables after applying the fiducial cuts.

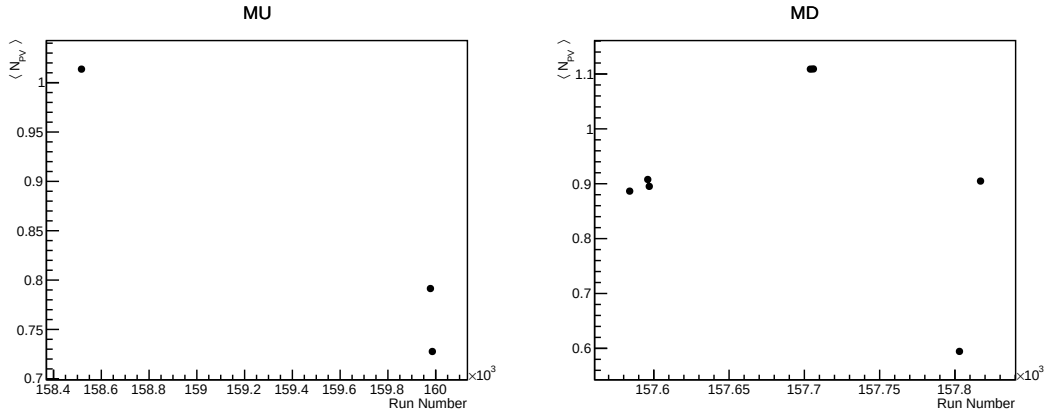

Figure 4.15: Average number of primary vertices per run for the random triggered events. Magnet up on the left plot and magnet down on the right one.

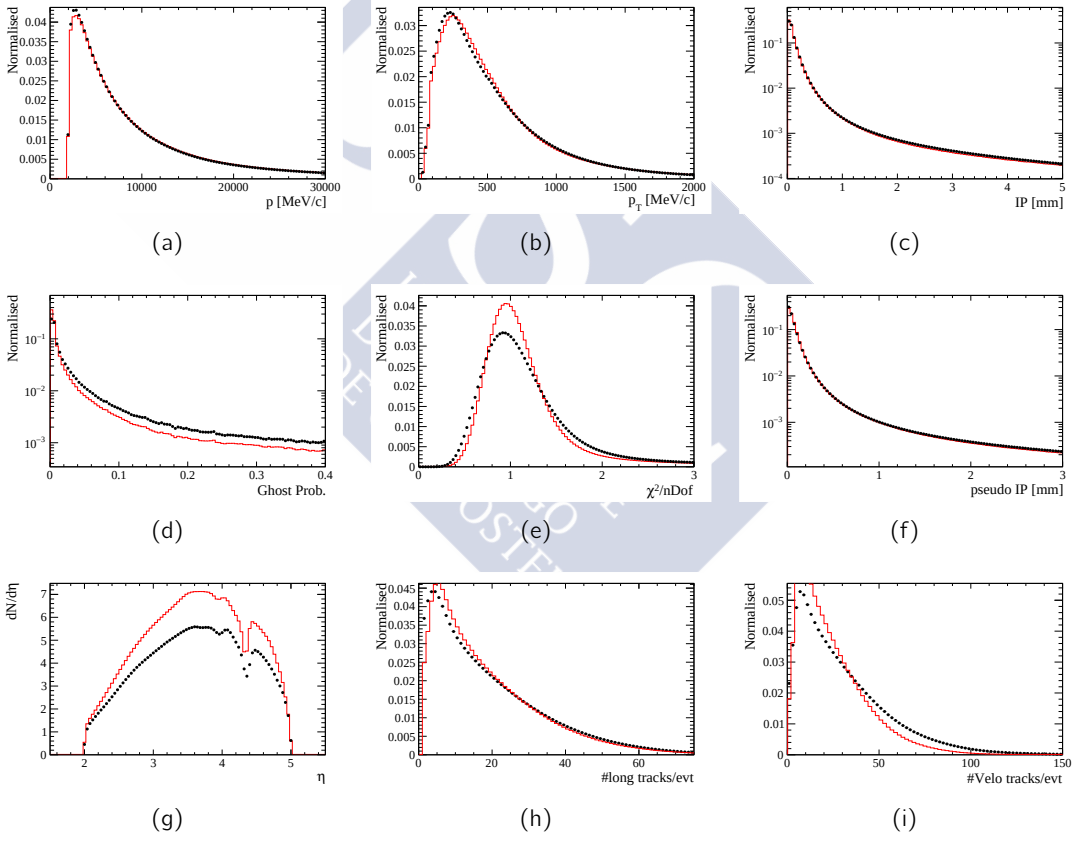

Figure 4.16: MC *vs.* data distributions of different variables after applying the fiducial cuts. In all cases MC distributions are represented with red lines and data using black dots. (a) Momentum, (b) transverse momentum, (c) impact parameter with respect to the reconstructed primary vertex, (d) ghost probability, (e) χ^2 over the number of degrees of freedom, (f) pseudo impact parameter, (g) differential multiplicity over η with respect to η, (h) long tracks multiplicity, (i) VELO tracks multiplicity

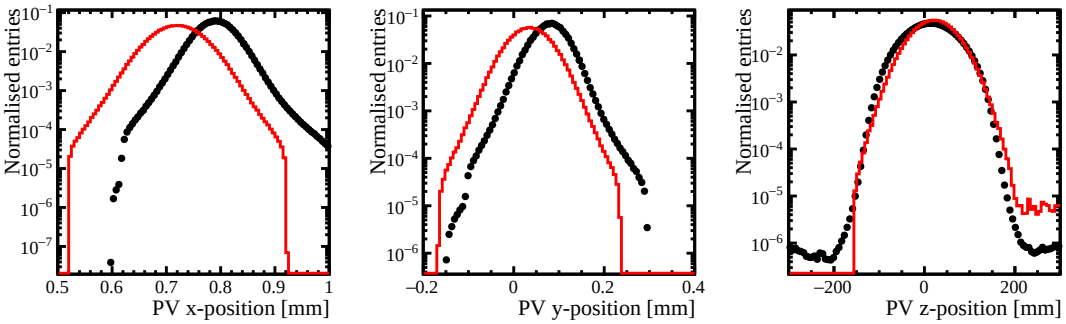

Figure 4.17: Projections of the luminous region in x, y and z axis for MC (red line) and data (black dots) in magnet up configuration.

4.3.2 Event and track selection

As mentioned above, the trigger line selecting no bias interactions from leading bunches is `Hlt1MBNoBiasLeadingCrossing`. So I require all events to pass this trigger line and to come from a beam-beam interaction.

Figure 4.17 shows the one dimensional position distributions of the reconstructed primary vertices for MC and data for magnet up configuration. Magnet down polarity plots present a similar behaviour. The luminous region of data and MC are slightly displaced in some coordinates. Since background in MC and data is negligible, I do not apply any cut in the luminous area. As for the 5 TeV sample, I find a right hand tail in the z-position of the MC primary vertices distribution. These vertices are actual MC truth vertices generated as a consequence of the interaction of a particle with the detector material.

Similarly to the 5 TeV analysis the fiducial region is defined as $2 < \eta < 5$ and $p > 2\,\text{GeV}/c$. Furthermore, the cuts on the track $\chi^2/\text{nDoF} < 3$ and GhostP < 0.3 are also applied as in the 5 TeV case to select the prompt charged particles consistently for the two beam energies.

The fraction of clone tracks in MC and data samples taken at 13 TeV and magnet up polarity can be seen in Figure 4.18. All clone tracks are removed from the analysis.

Figure 4.19 shows the distributions of the signal MC truth particles reconstructed (Signal), the distributions of the reconstructed particles that cannot be matched to a MC truth particle (fake) and those matched to a secondary MC truth particle (secondary). The distributions follow the same behaviour seen in 5 TeV simulation and, again, the ghost probability and pseudo impact parameter are used to discriminate between signal and background tracks. These figures represent magnet up polarity data. Magnet down configuration follows a very similar pattern. The background rejection of these two variables, defined as indicated in Equation 4.15, is shown in Figure 4.20. The maximum background rejection is obtained for GhostP < 0.19 and psIP < 0.78 mm for magnet up and GhostP < 0.19 and psIP < 0.86 mm for magnet down. For simplicity I am going to use the magnet up cut values for both magnet configurations.

A summary of the cuts applied to the 13 TeV data sample is shown in Table 4.8. In magnet up configuration, these cuts remove 43.1% of the background in the MC sample with a signal efficiency of 97.6%, obtaining a sample with a purity of 90.6% In magnet down, the background rejection is of 42.7% with a signal efficiency of 97.7%. The purity of the final sample is 90.8%.

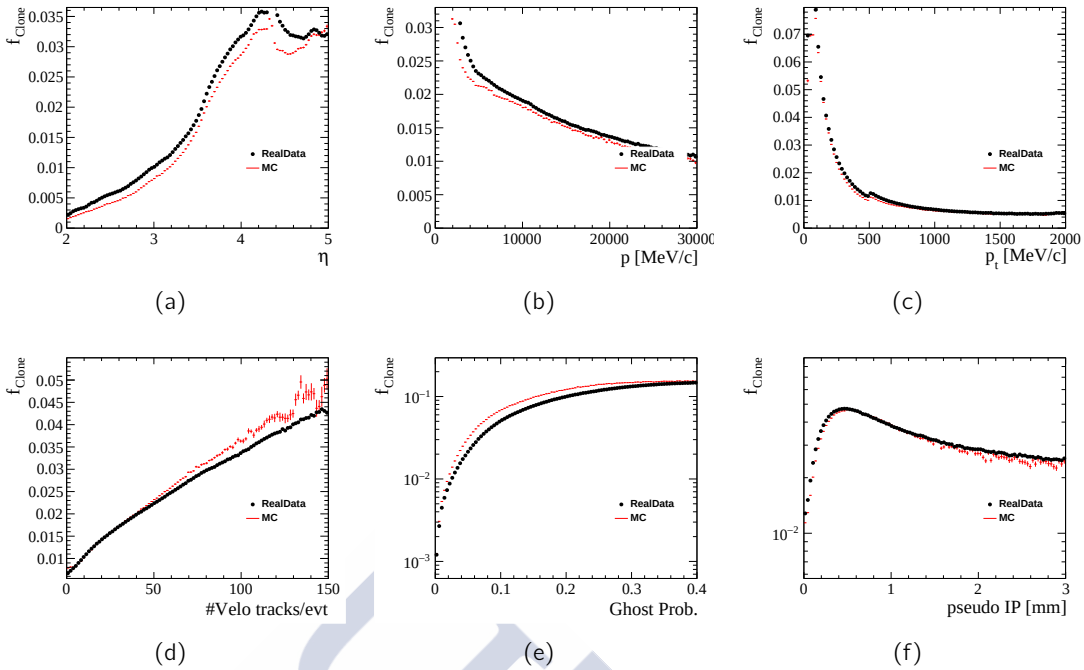

Figure 4.18: Fraction of clone tracks found in the 13 TeV data samples in magnet up configuration with respect to different variables. MC results are drawn using red lines and data using black dots. (a) Pseudorapidity, (b) momentum, (c) transverse momentum, (d) VELO tracks multiplicity, (e) ghost probability, (f) pseudo impact parameter.

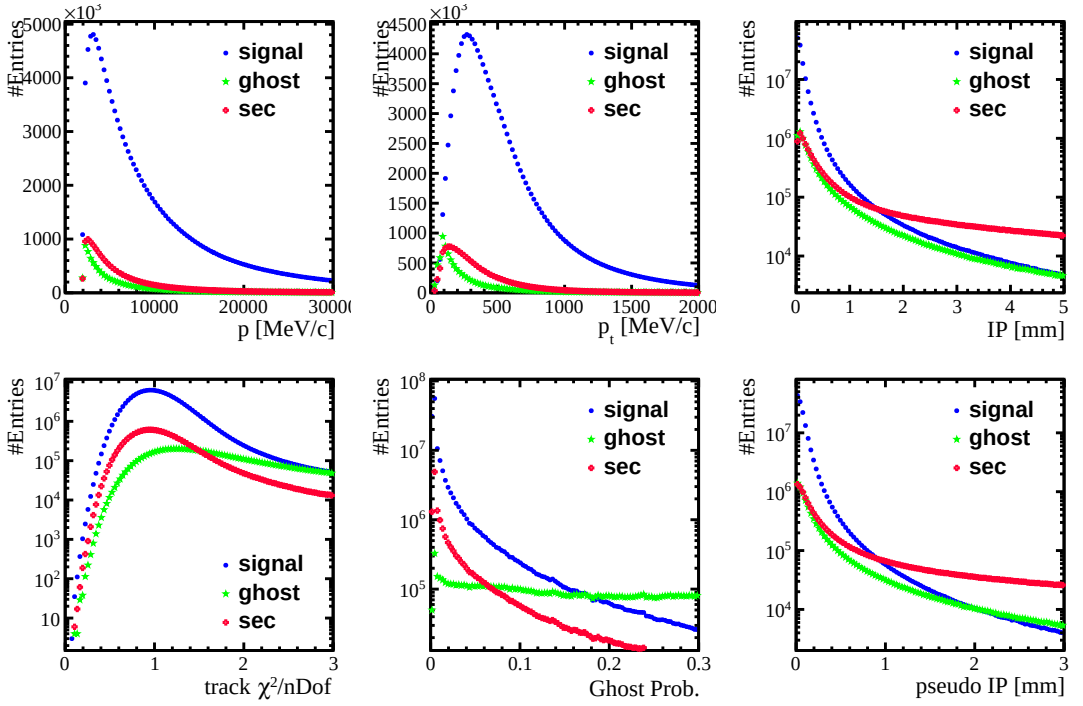

Figure 4.19: Distributions of the signal, fake and secondary tracks obtained from the MC sample with magnet up polarity.

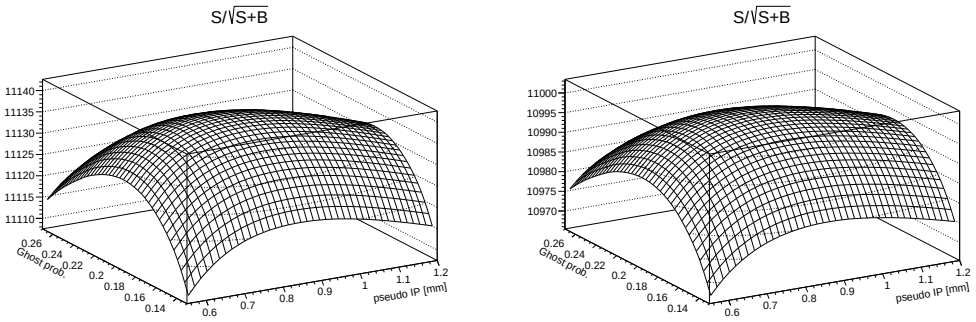

(a) (b)

Figure 4.20: Background rejection defined as $S/\sqrt{S + Bkg}$ with respect to ghost probability and pseudo impact parameter for data at 13 TeV with (a) magnet up and (b) magnet down polarity.

Event cuts	`Hlt1MBNoBiasLeadingCrossingDecision` == `True` Bunch crossing type == beam-beam
Fiducial cuts	$2 < \eta < 5$ $p > 2$ GeV/c
Tracks selection	Clone == `False` χ^2/nDoF < 3 Pseudo IP < 0.78 mm GhostP < 0.19

Table 4.8: Summary of cuts applied to the 13 TeV sample.

4.3.3 Measurement of the pp inelastic cross-section

4.3.3.1 Event efficiency

The four components in which the tracking efficiency can be factorised, as indicated in section 4.1.1.1, are summarized in Table 4.9. The tracking efficiency correction calculated by the LHCb tracking group is in this case $1.0096 \pm 0.0039(stat) \pm 0.0081(syst)$, and it is common for both magnet configurations.

	ε^{Acc}	ε^{Reco}	$\rho^{Tracking}$	ε^{Cuts}
MU	0.72388 ± 0.00009	0.85154 ± 0.00010	1.0096 ± 0.0039	0.97778 ± 0.00014
MD	0.72395 ± 0.00009	0.83676 ± 0.00012	1.0096 ± 0.0039	0.97784 ± 0.00014

Table 4.9: Factors of the tracking efficiency. The uncertainties are only statistical.

These values yield the following tracking efficiencies for data

$$\varepsilon^{MU} = 0.6085 \pm 0.0024(stat),$$
$$\varepsilon^{MD} = 0.5980 \pm 0.0023(stat).$$

Taking again equation 4.7 I obtain the following event efficiencies

$$\varepsilon_{evt}^{MU} = 0.9833 \pm 0.0018(stat),\ \varepsilon_{evt}^{MD} = 0.9850 \pm 0.0016(stat).$$

As a cross check, I compare these results with the event efficiencies calculated using MC true data

$$\varepsilon_{evt}^{MC_{True}\,MU} = 0.9884 \pm 0.0011(stat),$$
$$\varepsilon_{evt}^{MC_{True}\,MD} = 0.9879 \pm 0.0010(stat),$$

and also with the results calculated using the reconstructed simulation data

$$\varepsilon_{evt}^{MC\,MU} = 0.9907 \pm 0.0015(stat),$$
$$\varepsilon_{evt}^{MC\,MD} = 0.9902 \pm 0.0016(stat).$$

The efficiencies obtained from the MC reconstructed data are slightly higher than the MC true results. As it was mentioned in the 5 TeV analysis, this effect is, partially, due to the ghost and secondary tracks that bias the distribution at low multiplicities. Removing the ghost and secondary tracks from the reconstructed data I obtain

$$\varepsilon_{evt}^{MC\,MU} = 0.9895 \pm 0.0017(stat),$$
$$\varepsilon_{evt}^{MC\,MD} = 0.9891 \pm 0.0017(stat).$$

The difference between the nominal method applied to MC and the one obtained from the MC truth data is taken as a systematic.

4.3.3.2 Number of visible events

The total number of bunch crossings in the data sample is $N_{Bx}^{MU} = 237836575$ for MU polarity and $N_{Bx}^{MD} = 55608821$ for MD. After reconstruction and applying the selection cuts, the number of visible events is $N_{vis}^{MU} = 130484132 \pm 11423$ and $N_{vis}^{MD} = 35833430 \pm 5986$ events.

The `Hlt1NoBiasLeadingCrossingDecision` only triggered events from beam-beam interactions. In contrast to the 5 TeV data sample, during the 13 TeV data taking the `Hlt1LumiDecision` triggered events were reconstructed and saved into the nobias stream. The `Hlt1LumiDecision` trigger line also includes *be*, *eb* and *ee* events, so it is possible to estimate the number of background events from these type of interactions. The fraction of *be*, *eb* and *ee* reconstructed events is indicated in Table 4.10.

Using equation 4.16 and taking into account that

$$q_0^{bb} = 1 - \varepsilon_{evt},$$

I estimate the number of background events, obtaining $N_{bkg}^{MU} = 56.0 \pm 56.0(stat)$ for MU and $N_{bkg}^{MD} = 110 \pm 84.0(stat)$ for MD. This background contribution is negligible and it will not be taken into account.

The second source of background events is given by events with only secondary or ghost tracks detected. The estimation of the amount of this type of events is done via MC. The fractions of background events in simulation are $f_{bkg}^{MU} = (2.405 \pm 0.016) \times 10^{-3}$ and $f_{bkg}^{MD} = (2.421 \pm 0.017) \times 10^{-3}$. Assuming that the fraction of background events is the same in data and MC I obtain that $N_{bkg}^{MU} = 313802$ events in the MU sample and $N_{bkg}^{MD} = 86738$ events in MD are actually background events.

		N_{Bx}	N_{vis}	fr
MU	be	1073008	4	$(3.7 \pm 2.5) \cdot 10^{-6}$
	eb	1500773	460	$(3.07 \pm 0.14) \cdot 10^{-4}$
	ee	530318	0	$(0.0^{+2.4}_{-0.0}) \cdot 10^{-6}$
MD	be	16477692	46641	$(2.831 \pm 0.013) \cdot 10^{-3}$
	eb	24727435	26668	$(1.0808 \pm 0.0066) \cdot 10^{-3}$
	ee	8062412	11	$(1.36 \pm 0.47) \cdot 10^{-6}$

Table 4.10: N_{Bx} indicates the number of be, eb and ee triggered events, N_{vis} shows the number of reconstructed events, and fr the fraction of reconstructed events with respect to the total number of bunch crossings.

4.3.3.3 Extrapolation to the full phase-space

The extrapolation factors obtained from the official LHCb MC sample are

$$s_{ext}^{MU} = 1.14018 \pm 0.00089,$$
$$s_{ext}^{MD} = 1.13998 \pm 0.00090,$$

where the uncertainty shown is only statistical.

4.3.4 Systematic uncertainties

Since the analysis procedure followed is exactly the same as for the 5 TeV data sample, the list of systematics affecting this measurement is also the same. The integrated luminosity is again the dominant uncertainty contribution. Since I do not have a luminosity measurement yet, in order to provide the most detailed description of the analysis I took the next two luminosities as reference: $(3175 \pm 130)\ \mu b^{-1}$ for MU and $(959 \pm 37)\ \mu b^{-1}$ for MD. Propagating the uncertainties to the final cross-section result I obtain a systematic uncertainty of 2.49 mb and 2.36 mb for MU and MD configurations respectively.

As it was already mentioned in Section 4.2.4, the beam energy uncertainty is 0.65%. Following the same approach as in the 5 TeV sample, I obtain that the systematic uncertainty in the final cross section due to the beam energy uncertainty is 0.071 mb.

The tracking efficiency systematics yields an uncertainty of 0.00039 in MU configuration and 0.00035 in MD. The systematics related to the event efficiency calculation method are obtained from MC, and they are estimated as the difference between the event efficiency provided by this thesis method and the MC truth data. This yields a systematic uncertainty of 0.0023 for both magnet configurations. The tracking efficiency systematics are one order of magnitude lower than the ones obtained from the method, so they are going to be neglected. The method yields a systematic of 0.17 mb to the final cross-section for both magnet configurations.

The systematic due to the ghost probability distributions mismatch between data and MC is calculated varying the ghost probability cut to the position where the ratio of data at both sides of the cut in real data is the same as in MC using the original cut. The difference between the nominal cross-section and the calculated with this new cut is taken as the systematic uncertainty. The values of the ghost probabilities obtained are 0.238

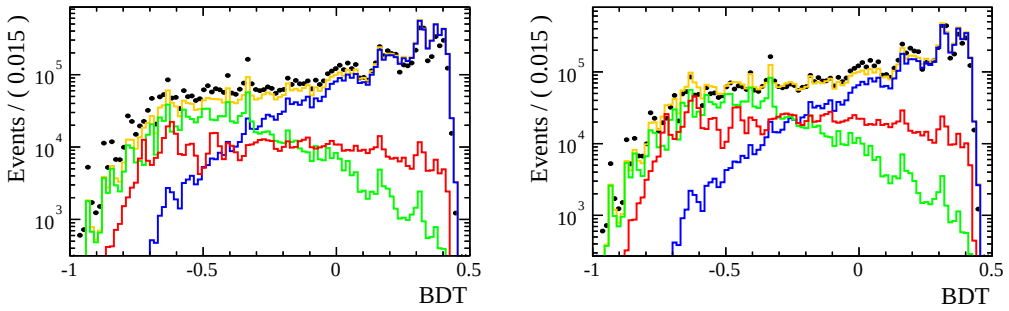

Figure 4.21: BDT distributions before (a) and after (b) the fit in logarithmic scale and for MD configuration. Black points represent real data and the lines represent results form MC. The Blue line represents the signal distribution, green line represent the ghost tracks and the red line the secondary tracks. The Yellow line represent the sum of the three MC components.

for MU and 0.248 for MD. The systematic associated to this source is 0.083 mb for MU and 0.095 mb for MD.

Following the same approach as for the 5 TeV data, a BDT created from $\log(p_T)$, χ^2/nDoF, $\log(P(\texttt{GhostP}))$ and $\log(\texttt{psIP})$ distributions is applied to data. Then, a PDF with three components (signal, secondary tracks and ghost tracks) is fitted to data. This analysis was made only for MD configuration assuming the same behaviour for MU configuration. Figure 4.21 shows the BDT MC distributions before and after the fit to data. The fraction of secondary and ghost tracks obtained from MC and the fit to real data are shown in Table 4.11. The differences between data and MC are larger than in the 5 TeV case. Looking to these results I can assume that applying a systematic uncertainty of 100% covers the difference between MC and data. These uncertainties propagated to the final cross-section contribute with of 0.23 mb and 0.26 mb to the cross-section systematic uncertainty in MU and MD respectively.

	13 TeV MC	13 TeV fit
f_{sec}	0.0883	0.1811 ± 0.0005
f_{ghost}	0.1244	0.1806 ± 0.0003

Table 4.11: Fraction of events in the Monte Carlo sample and obtained from a fit to the 13 TeV data sample.

Combining these uncertainties and assuming that all of them are not correlated, the systematic uncertainty of the inelastic cross-section in the detector acceptance is 2.51 mb for MU configuration and 2.38 mb for MD.

The extrapolation systematic uncertainty is calculated using the tunes indicated in Section 4.1.4. The extrapolation factors obtained from these tunes are shown in Table 4.12 The standard deviation of the extrapolation factors obtained from the private MC generations is 0.0094 in both magnet configurations. After combining the statistical uncertainty of the nominal factor obtained from official LHCb MC with the standard deviation calcu-

lated from the different private samples, the systematic uncertainty of the extrapolation factor is 0.0094 for both magnet configuration.

Generator	Tune	s_{ext}^{MU}	s_{ext}^{MD}
Pythia 8	LHCb	1.14018 ± 0.00089	1.13998 ± 0.00090
Pythia 8	4Cx	1.1391 ± 0.0066	1.1391 ± 0.0066
Pythia 8	A2-CTEQ6L1	1.1392 ± 0.0066	1.1390 ± 0.0066
Pythia 8	A2-MSTW2008LO	1.1408 ± 0.0066	1.1408 ± 0.0066
Pythia 8	AU2-CTEQ6L1	1.1392 ± 0.0066	1.1393 ± 0.0066
Pythia 8	AU2-MSTW2008LO	1.1406 ± 0.0066	1.1405 ± 0.0066
Pythia 8	Monash 2013	1.1415 ± 0.0066	1.1416 ± 0.0066
Pythia 6	Default	1.1663 ± 0.0068	1.1662 ± 0.0068

Table 4.12: Extrapolation factors obtained from some Pythia 8 tunes and the Pythia 6 default tune. To calculate the extrapolation factors private simulations were produced generating 200000 events per sample. The uncertainties shown are only statistical.

4.3.5 Results

Table 4.13 shows a summary of the results for the two magnet configurations.

	MU	MD
N_{vis}	130484132 ± 11423	35833430 ± 5986
N_{bkg}	313802 ± 313802	86738 ± 86738
N_{Bx}	237836575	55608821
ε_{evt}	0.9833 ± 0.0018	0.9850 ± 0.0016
μ	0.8133 ± 0.0023	1.0573 ± 0.0031
$\mathcal{L}$	$(3175 \pm 130)\ \mu b^{-1}$	$(959 \pm 37)\ \mu b^{-1}$

Table 4.13: Results summary.

The cross-sections result in the LHCb acceptance are

$$\sigma_{MU}^{acc} = 60.93 \pm 0.17(stat) \pm 2.51(syst)\,\text{mb},$$
$$\sigma_{MD}^{acc} = 61.31 \pm 0.18(stat) \pm 2.38(syst)\,\text{mb},$$

and he cross-section in the full phase-space are

$$\sigma_{MU} = 69.47 \pm 0.19(stat) \pm 2.92(syst)\,\text{mb},$$
$$\sigma_{MD} = 69.89 \pm 0.21(stat) \pm 2.77(syst)\,\text{mb}.$$

4.4 Conclusions

Measurements of the pp interaction inelastic cross-sections at a centre-of-mass energy of $\sqrt{s} = 5$ TeV and $\sqrt{s} = 13$ TeV have been performed with no bias triggered data collected by the LHCb detector in 2015.

The result obtained at $\sqrt{s} = 5\,\text{TeV}$ inside the LHCb acceptance is

$$\sigma^{acc} = 56.88 \pm 0.02(stat) \pm 2.12(syst)\,\text{mb}.$$

This result is not definitive and will be updated using a luminosity calculated exclusively with the events of the sample.

The cross-section at $\sqrt{s} = 13\,\text{TeV}$ was measured to be

$$\sigma^{acc}_{MU} = 60.93 \pm 0.17(stat) \pm 2.51(syst)\,\text{mb},$$
$$\sigma^{acc}_{MD} = 61.31 \pm 0.18(stat) \pm 2.38(syst)\,\text{mb}$$

for magnet up and magnet down configurations respectively.

The *pp* cross-section extrapolation to full phase-space was calculated using the official LHCb simulation based on the LHCb tune of Pythia 8. The cross-section at the full phase-space at 5 TeV is

$$\sigma = 65.72 \pm 0.02(stat) \pm 2.49(syst)\,\text{mb}.$$

At 13 TeV the cross-sections obtained for the two magnet configurations are

$$\sigma_{MU} = 69.47 \pm 0.19(stat) \pm 2.92(syst)\,\text{mb},$$
$$\sigma_{MD} = 69.89 \pm 0.21(stat) \pm 2.77(syst)\,\text{mb}.$$

Figure 4.22 shows the inelastic cross-section *vs.* energy made by the LHC experiments and the results presented in this thesis. The full triangles represent the measurements presented in this thesis.

The yellow band represents the 1σ uncertainty region of the phenomenological extrapolation calculated using the model proposed in [89]. As it can be seen, the measured value at 5 TeV is consistent with the extrapolation within 1σ. Note here that this is not a final result, since I used the luminosity value calculated by the LHCb luminosity group and it needs to be updated. The measurements at 13 TeV are significantly lower than the model prediction, nevertheless they are compatible within 1σ with the CMS preliminary result and 2σ with ATLAS. The measurements using the LHCb detector are consistent, since the cross-section increases with energy, although the three measurements are systematically below the prediction.

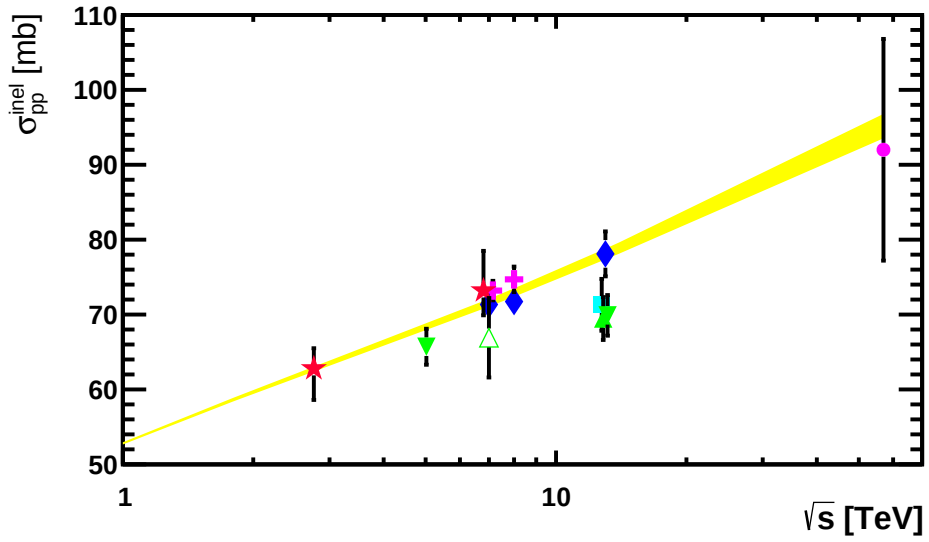

Figure 4.22: Inelastic cross-section *vs.* energy of measurements made by different experiments. Some data points have been slightly shifted in the horizontal position for display purposes. The green full triangles represent the measurements presented in this thesis. The up triangle represents measurement performed with magnet up configuration and the down triangles the performed using magnet down. The empty triangle represent the measurement made by LHCb at 7 TeV [83]. The cross marks represent the results from TOTEM [76,77]. The stars represent the results from ALICE [80,84]. Full diamonds represent the ATLAS [75,81,85] measurements. Full square shows the CMS [86] measurement and the circle represent the result obtained by the Pierre Auger Collaboration [87]. In all cases the vertical black bars represent the total uncertainty of each measurement. The yellow band represents the 1σ uncertainty region of the phenomenological extrapolation calculated using the model proposed in [89].

Appendices

4.A Dealing with background and efficiencies

This section deals with event counts for poisson distributed interactions per bunch crossing. As a starting point consider a single Poissonian with average μ and an efficiency ε to record a single interaction. Then let p_n be the probability to have n interactions in a single event and q_n the probability to record n interactions. It will be assumed that the different interactions in the same event are independent, i.e. the efficiency to record each interaction is not affected by the presence of the others. One then has

$$p_n = e^{-\mu}\,\frac{\mu^n}{n!} \tag{4.17}$$

and

$$\begin{aligned} q_n &= \sum_{k=n}^{\infty} p_k \binom{k}{n} \varepsilon^n (1-\varepsilon)^{k-n} = \sum_{k=n}^{\infty} e^{-\mu}\,\frac{\mu^k}{k!}\,\frac{k!}{n!(k-n)!}\,\varepsilon^n (1-\varepsilon)^{k-n} \\ &= e^{-\mu}\,\frac{(\varepsilon\mu)^n}{n!} \sum_{k=n}^{\infty} \frac{\mu^{k-n}}{(k-n)!}\,(1-\varepsilon)^{k-n} = e^{-\mu}\frac{(\varepsilon\mu)^n}{n!}e^{\mu(1-\varepsilon)} = e^{-\varepsilon\mu}\,\frac{(\varepsilon\mu)^n}{n!}\ . \end{aligned} \tag{4.18}$$

The distribution of the number of observed interactions is still a Poissonian with a modified mean value $\varepsilon\mu$. It follows, that the mean value μ can be inferred from the observed empty-event probability q_0 via

$$\mu = -\frac{1}{\varepsilon}\,\ln q_0\ . \tag{4.19}$$

The above requires knowledge of the efficiency ε to record a single interaction, which can be determined e.g. from simulation. Alternatively one can consider the event efficiency ε_{evt}, i.e. the efficiency to record an event, which includes the effect of pileup and, for the cross-section measurement, can be determined from the actual data. One has

$$\varepsilon_{\text{evt}} = \frac{1-q_0}{1-p_0}\ , \tag{4.20}$$

i.e. the event efficiency is the fraction of the number of recorded non-empty events over the number of events that actually are non-empty. It follows

$$p_0 = 1 - \frac{1-q_0}{\varepsilon_{\text{evt}}} \quad \text{and thus} \quad \mu = -\ln p_0 = -\ln\left(1 - \frac{1-q_0}{\varepsilon_{\text{evt}}}\right)\ . \tag{4.21}$$

Next consider the case that several independent interaction types can contribute to an event, with mean values $\mu_1, \mu_2, \ldots$ and interaction efficiencies $\varepsilon_1, \varepsilon_2, \ldots$. Since the Poissonians are independent, the respective probabilities to have an empty event are

$$p_0 = e^{-(\mu_1+\mu_2+\ldots)} \quad \text{and} \quad q_0 = e^{-(\varepsilon_1\mu_1+\varepsilon_2\mu_2+\ldots)} \tag{4.22}$$

and one finds

$$-\ln\left(1 - \frac{1-q_0}{\varepsilon_{\text{evt}}}\right) = -\ln p_0 = \mu_1 + \mu_2 + \ldots\ . \tag{4.23}$$

The above shall now be applied to the inelastic cross-section measurement. Here interaction counts are to be determined in beam-beam bunch-crossings. In these bunch-crossings there are three sources of background interactions, background from beam1,

background from beam2 and (noise) background when there are no beams. Denoting the average number of interactions from all sources as $\mu_{bb}, \mu_{be}, \mu_{eb}$ and μ_{ee} one has

$$\begin{aligned} -\ln p_0^{bb} &= \mu_{bb} + \mu_{be} + \mu_{eb} + \mu_{ee} \\ -\ln p_0^{be} &= \mu_{be} + \mu_{ee} \\ -\ln p_0^{eb} &= \mu_{eb} + \mu_{ee} \\ -\ln p_0^{ee} &= \mu_{ee} \end{aligned} \tag{4.24}$$

and thus

$$\mu_{bb} = -\ln p_0^{bb} + \ln p_0^{be} + \ln p_0^{eb} - \ln p_0^{ee} \ . \tag{4.25}$$

If the efficiencies are unity, which is the case if the observables are visible interactions, as for the luminosity measurement, the fraction of empty events for the different bunch-crossing types can be directly substituted into Equation 4.25. Otherwise the relevant values p_0 can be determined from the observed fractions of empty events q_0 and the respective event efficiencies.

As a final remark and a word of caution, assuming unit efficiencies for the sake of simplicity, consider the following to deal with background,

$$\mu_{bb} = -\ln\left(1 - \frac{N_{\text{vis}}^{bb} - N_{\text{bkg}}}{N_{bb}}\right) = -\ln(q_0^{bb} + f_{\text{bkg}}) \tag{4.26}$$

where the fraction of empty events is corrected for a background fraction. Formally such a decomposition is always possible, and as a way to measure the background fraction one might consider

$$f_{\text{bkg}} = \frac{N_{\text{vis}}^{be}}{N_{\text{BX}}^{be}} + \frac{N_{\text{vis}}^{eb}}{N_{\text{BX}}^{eb}} - \frac{N_{\text{vis}}^{ee}}{N_{\text{BX}}^{ee}} = f_{\text{bkg}}^{be} + f_{\text{bkg}}^{eb} - f_{\text{bkg}}^{ee} = (1 - q_0^{be}) + (1 - q_0^{eb}) - (1 - q_0^{ee}) \tag{4.27}$$

i.e. the background fractions in beam-empty plus empty-beam reduced by once the empty-empty contribution which is contained twice in the single-beam contributions. After the last equal sign, the same is expressed through the observed fractions of empty events.

Unfortunately Equation 4.27 is seriously flawed. It defines an absolute measurement of the background in bunch crossings that can only contribute background, which misses the fact that a background interaction only is background to the event count in beam-beam interactions when the beam-beam interaction itself is empty. The proper background fraction would be

$$f_{\text{bkg}} = p_0^{bb}(1 - p_0^{be} p_0^{eb} p_0^{ee}) \ . \tag{4.28}$$

Noting that the probability for a beam-beam crossing to be empty is $q_0^{bb} = p_0^{bb} p_0^{be} p_0^{eb} p_0^{ee}$, one sees that substituting Equation 4.28 into Equation 4.26, the correct μ is recovered. Here the true empty-event probabilities enter. To see the connection with Equation 4.27, these have to be expressed via the observables q_0, and using

$$\begin{aligned} q_0^{bb} &= p_0^{bb} p_0^{be} p_0^{eb} p_0^{ee} \\ q_0^{be} &= p_0^{be} p_0^{ee} \\ q_0^{eb} &= p_0^{eb} p_0^{ee} \\ q_0^{ee} &= p_0^{ee} \end{aligned} \tag{4.29}$$

one obtains

$$f_{\text{bkg}} = q_0^{bb}\left(\frac{q_0^{ee}}{q_0^{be}q_0^{eb}} - 1\right) = q_0^{bb}\left(\frac{1 - f_{\text{bkg}}^{ee}}{(1 - f_{\text{bkg}}^{be})(1 - f_{\text{bkg}}^{eb})} - 1\right) . \tag{4.30}$$

The relation to Equation 4.27 can be seen in the limit $f_{\text{bkg}} \to 0$. The leading order expansion then is

$$f_{\text{bkg}} = q_0^{bb}\,(f_{\text{bkg}}^{be} + f_{\text{bkg}}^{eb} - f_{\text{bkg}}^{ee}) \tag{4.31}$$

i.e. Equation 4.27 times the factor q_0^{bb}. Only in the limit of small pileup and small background Equation 4.27 is the correct expression for the background fraction.

In summary, the correct way to deal with background and efficiencies is to determine the poisson average μ_{bb} via

$$\mu_{bb} = -\ln p_0^{bb} + \ln p_0^{be} + \ln p_0^{eb} - \ln p_0^{ee} \quad \text{with} \quad p_0^{\{\cdots\}} = 1 - \frac{1 - q_0^{\{\cdots\}}}{\varepsilon_{\text{evt}}^{\{\cdots\}}} , \tag{4.32}$$

where $q_0^{\{\cdots\}}$ are the observed empty event fractions and $\varepsilon_{\text{evt}}^{\{\cdots\}}$ the event efficiencies for the different bunch crossing types.

4.B Impact parameter and point of closest approach

Parametrizing a particle trajectory by a straight line in space,

$$r(\lambda) = q + \lambda p \tag{4.33}$$

with the column vector q the spatial coordinates of the first track state, p its momentum vector and λ a parameter enumerating the points on the trajectory, the point of closest approach to a vertex with coordinates v is obtained by minimizing the squared distance

$$S^2 = (s + \lambda p)^T (s + \lambda p) = s^T s + 2\lambda s^T p + \lambda^2 p^T p \quad \text{with} \quad s = q - v \tag{4.34}$$

with respect to λ. One obtains

$$\lambda = -\frac{s^T p}{p^T p} \quad \text{and thus} \quad S^2 = s^T s - \frac{(s^T p)^2}{p^T p} , \tag{4.35}$$

where S is the impact parameter of the trajectory at the vertex.

In a similar way the point of closest approach to a line

$$v = w + \mu\, n \tag{4.36}$$

with offset vector w and direction n can be determined. One obtains

$$\begin{aligned} S^2 &= (s + \lambda\, p - \mu\, n)^T (s + \lambda\, p - \mu\, n) \\ &= s^T s + \lambda^2 p^T p + \mu^2 n^T n + 2\lambda s^T p - 2\mu s^T n - 2\lambda\mu p^T n \\ &\quad \text{with} \quad s = q - w \end{aligned} \tag{4.37}$$

Minimizing S^2 leads to a system of equations

$$\begin{pmatrix} p^T n & -p^T p \\ n^T n & -p^T n \end{pmatrix} \begin{pmatrix} \mu \\ \lambda \end{pmatrix} = \begin{pmatrix} s^T p \\ s^T n \end{pmatrix} \tag{4.38}$$

which leads to

$$\lambda = \frac{(p^T n)(s^T n) - (n^T n)(s^T p)}{(p^T p)(n^T n) - (p^T n)^2} \tag{4.39}$$

for the point of closest approach to v. For the special case of cartesian coordinates the parameter λ of the point of closest approach to the z-axis is obtained by $w = 0$, i.e. $s = q$, and $n^T = (0, 0, 1)$

$$\lambda = -\frac{p_x q_x + p_y q_y}{p_x^2 + p_y^2} \ . \tag{4.40}$$

4.C Pseudo impact parameter

In absence of actual PV coordinates the impact parameter of a track cannot be rigorously calculated. However, given the primary vertex density, the point of origin of a track can be estimated by the location on the trajectory which maximizes the vertex density $\rho(r)$. Parametrizing the trajectory by a straight line

$$r(\lambda) = g + \lambda p \tag{4.41}$$

with the column vector g the spatial coordinates of the first track state, p its momentum vector and λ a parameter enumerating the points on the trajectory, the point of largest density is obtained by minimizing S^2, as defined in Equation 4.10, with respect to λ. From

$$\frac{d}{d\lambda}\left(s^T C^{-1} s - 2\lambda\, p^T C^{-1} s + \lambda^2\, p^T C^{-1} p\right) = 0 \quad \text{with} \quad s = g - v \tag{4.42}$$

the parameter values λ and the value at the minimum are obtained as

$$\lambda = -\frac{p^T C^{-1} s}{p^T C^{-1} p} \ \text{ and } \ S^2_{\text{min}} = s^T C^{-1} s - \frac{(p^T C^{-1} s)^2}{p^T C^{-1} p} \ . \tag{4.43}$$

Since the transverse size of the luminous region is driven by the primary vertex resolution, which is significantly better than the impact parameter resolution of the individual tracks, even for prompt tracks S^2_{min} does not follow a χ^2-distribution with two degrees of freedom. This would only be the case if the full covariance matrix of the track parameters would be taken into account in the definition of S^2. For simplicity this is not done here, with the consequence that a cut on the luminous region has to be based on purely geometrical information. Since the transverse location of the primary vertices is very well defined, while the longitudinal positions are smeared out, an appropriate geometrical quantity, referred to a "pseudo impact parameter" in this note, is the transverse distance of the estimated point of origin to the average PV.

4.D The unfolding of the multiplicity distribution

Given a value for the single track efficiency ε, proper unfolding of the observed multiplicity distribution can be performed by means of the probability generating function.

$$\phi_p(z) = \sum_{n=0}^{\infty} z^n p_n \tag{4.44}$$

from which the actual probabilities can be inferred via

$$p_n = \frac{1}{n!} \left. \frac{d^n \phi_p(z)}{dz^n} \right|_{z=0} . \tag{4.45}$$

Using the relation between the true distribution p_n and the observed q_n

$$q_n = \sum_{k=n}^{\infty} p_k \binom{k}{n} \varepsilon^n (1-\varepsilon)^{k-n} , \tag{4.46}$$

one finds

$$\begin{aligned} \phi_q(z) &= \sum_{n=0}^{\infty} z^n \sum_{k=n}^{\infty} p_k \binom{k}{n} \varepsilon^n (1-\varepsilon)^{k-n} = \sum_{k=0}^{\infty} p_k \sum_{n=0}^{k} \binom{k}{n} (z\varepsilon)^n (1-\varepsilon)^{k-n} \\ &= \sum_{k=0}^{\infty} p_k (1 + z\varepsilon - \varepsilon)^n = \phi_p(1 + z\varepsilon - \varepsilon) \end{aligned} \tag{4.47}$$

or

$$\phi_p(z) = \phi_q \left(\frac{z + \varepsilon - 1}{\varepsilon} \right) . \tag{4.48}$$

Since ϕ_q is known from the measured distribution, one can directly calculate the unfolded distribution p_n. In a first step one finds

$$\left. \frac{d^n \phi_p(z)}{dz^n} \right|_{z=0} = \frac{1}{\varepsilon^n} \phi_q^{(n)} \left(\frac{\varepsilon - 1}{\varepsilon} \right) \quad \text{and} \quad \phi_q^{(n)}(z) = \sum_{k=n}^{\infty} \frac{k!}{(k-n)!} q_k z^{k-n} , \tag{4.49}$$

which leads to

$$p_n = \frac{1}{n!} \left. \frac{d^n \phi_p(z)}{dz^n} \right|_{z=0} = \frac{1}{n!\,\varepsilon^n} \sum_{k=n}^{\infty} \frac{k!}{(k-n)!} q_k \left(\frac{\varepsilon - 1}{\varepsilon} \right)^{k-n} = \sum_{k=n}^{\infty} q_k \binom{k}{n} \frac{1}{\varepsilon^n} \left(\frac{\varepsilon - 1}{\varepsilon} \right)^{k-n} . \tag{4.50}$$

One finds a nice formal symmetry between Equation 4.50 and Equation 4.46. However, while the step from $p_n \to q_n$ is stable, summing only positive numbers, the inverse $q_n \to p_n$ is a sum of alternating terms in powers of $(\varepsilon - 1)/\varepsilon$. For $\varepsilon > 0.5$ those terms are less than one and the sum is guaranteed to converge, for $\varepsilon < 0.5$ the sum becomes unstable. Only in cases where the q_n are known exactly, or where $q_k = 0$ beyond a small value of k the inversion works also numerically.

4.E Determination of the event efficiency

In the previous section the explicit expression was given, how to correct for the binomial model a measured multiplicity distribution q_n for efficiency losses. The result can be used to determine the event efficiency ε_{evt} directly from the observed multiplicity distribution.

For the interaction types under consideration for this analysis one has by definition $p_0 = 0$, i.e. the true multiplicity distribution must have at last one track. Furthermore, an event is seen unless the observed multiplicity is zero, i.e.

$$\varepsilon_{\text{evt}} = 1 - q_0 \tag{4.51}$$

where q_0 is the probability that no track is seen. Since empty events are not counted, the measured multiplicity distribution is not q_n, but the zero-suppressed distribution $\hat{q}_n$, with

$$\hat{q}_n = \frac{q_n}{1 - q_0} \quad \text{for} \quad n \geq 1 \; . \tag{4.52}$$

Using now $p_0 = 0$ in eq.(4.50), one finds

$$0 = \sum_{k=0}^{\infty} q_k \left(\frac{\varepsilon - 1}{\varepsilon} \right)^k = q_0 + \sum_{k=1}^{\infty} \hat{q}_k (1 - q_0) \left(\frac{\varepsilon - 1}{\varepsilon} \right)^k \tag{4.53}$$

which can be solved to give

$$\frac{1}{\varepsilon_{\text{evt}}} = \frac{1}{1 - q_0} = 1 - \sum_{k=1}^{\infty} \hat{q}_k \left(\frac{\varepsilon - 1}{\varepsilon} \right)^k \; . \tag{4.54}$$

In this expression only the normalized observed multiplicity distribution enters, and the single track efficiency ε.

In practical application this simple expression for the event efficiency works surprisingly well, even if the assumption of a track finding efficiency which is independent of the multiplicity can be disputed. The reason for this becomes evident when expanding $1/\varepsilon_{\text{evt}}$ around the point $\varepsilon = 1$. For the leading order terms one finds

$$\begin{aligned} \frac{1}{\varepsilon_{\text{evt}}} =& 1 + \hat{q}_1 x + (\hat{q}_1 - \hat{q}_2) x^2 + (\hat{q}_1 - 2\hat{q}_2 + \hat{q}_3) x^3 + (\hat{q}_1 - 3\hat{q}_2 + 3\hat{q}_3 - \hat{q}_4) x^4 + \ldots \\ & \text{with} \quad x = 1 - \varepsilon \; . \end{aligned} \tag{4.55}$$

The behaviour for large values ε is dominated by the normalized observed multiplicities $\hat{q}_1$ and $\hat{q}_2$, i.e. the event efficiency is determined by that fraction of events with very low multiplicities – and for those events the assumption of a single track efficiency is a good approximation. This is illustrated in Figure 4.23 which shows the dependence of the event efficiency as a function of the track efficiency ε, overlaid with the second order expectation according to Equation 4.55.

4.F Numerical studies

In the following a few model systems for the true and the observed multiplicity distribution will be discussed, which are related by a single track efficiency ε and which treat all tracks as independent. The translation from true to observed after efficiency losses is most conveniently handled by the probability generating

$$F(z) = \sum_{n=0}^{\infty} p_n z^n \quad \text{with} \quad F(0) = p_0 \quad \text{and} \quad F(1) = 1 \; . \tag{4.56}$$

The condition $F(0) = p_0$ is convenient when one wants to derive the generating function of the zero-suppressed probability distribution from the generating function of the full distribution, $F(1) = 1$ follows from the normalization of the p_n and can be used to determine

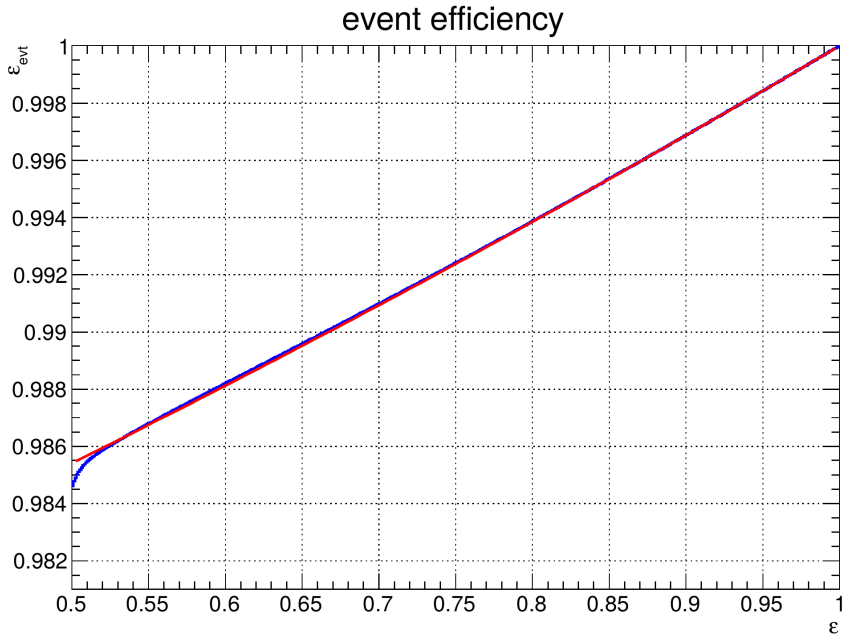

Figure 4.23: Event efficiency ε_{evt} as a function of the single track efficiency ε, determined according to Equation 4.54 (blue line) compared to the second order approximation according to Equation 4.55 (red line).

the normalization of $F(z)$. As shown before, given $F(z)$, the generating function of the observed distribution $F^{obs}(z)$ is then obtained by $F^{obs}(z) = F(1-\varepsilon+\varepsilon z)$.

Turning now to zero-suppressed distributions, the generating function for the zero suppressed initial distribution is given by

$$F_1(z) = \frac{F(z) - F(0)}{1 - F(0)} \,, \tag{4.57}$$

and the generating function of the observed distribution becomes

$$F_0^{obs}(z) = \frac{F(1-\varepsilon+\varepsilon z) - F(0)}{1 - F(0)} \,. \tag{4.58}$$

This distribution in general will have a finite probability for $n = 0$, and the event efficiency can be read off as

$$\varepsilon_{\text{evt}} = 1 - F_0^{obs}(0) = \frac{1 - F(1-\varepsilon)}{1 - F(0)} \,. \tag{4.59}$$

Finally, the generating function of the zero-suppressed observed distribution becomes

$$F_1^{obs}(z) = \frac{F_0^{obs}(z) - F_0^{obs}(0)}{1 - F_0^{obs}(0)} = \frac{F(1-\varepsilon+\varepsilon z) - F(1-\varepsilon)}{1 - F(1-\varepsilon)} \,, \tag{4.60}$$

i.e. it is the zero-suppressed distribution of the observed distribution derived from the full initial distribution, $F(1-\varepsilon+\varepsilon z)$.

In the following three distributions will be discussed: the binomial, the exponential and the poisson distribution. The mathematical details are given in the subsequent subsections. For the numerical example the mean value of the full distributions is $\langle n \rangle = 5$, in

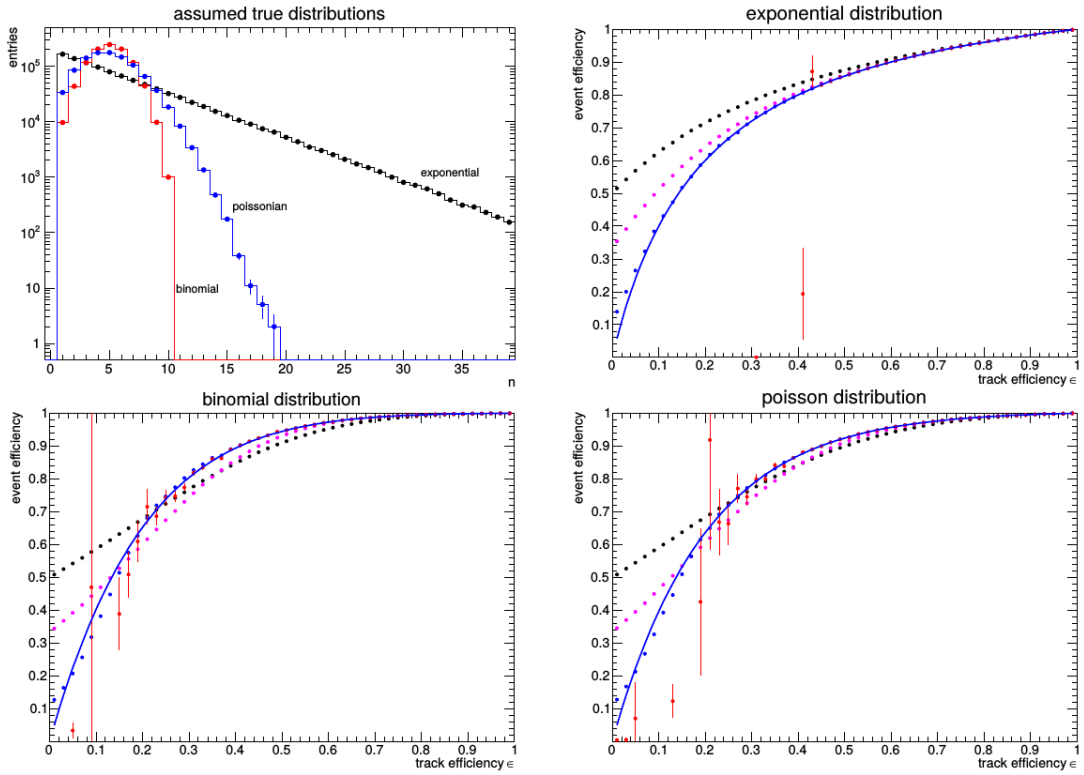

Figure 4.24: Study of event efficiencies for three types of discrete probability distributions. The top left frame shows the assumed shapes for the true distributions, the others show the event efficiencies for the three cases as a function of the single track efficiency. The plots compares the true event efficiencies as given by the solide lines (blue) to the exact calculation according to Equation 4.54 (red) and the leading order expansions in 1st order (black) 2^{nd} order (magenta) and 8^{th} order (blue). The error bars show the statistical uncertainties due to the limited sample size of the simulation.

case of the binomial the number of trials is set to $N = 10$. Results are shown in Fig. 4.24. In all cases 10^6 events were generated, and the leading order expansions for order 1, 2 and 8 compared to the all-orders expression Equation 4.54 and the true event efficiencies. The exact expression agrees within error bars with the true values, but becomes numerically unstable for small track efficiencies. The leading order expression are all stable and for large track efficiencies are very close to the exact values. At small efficiencies the low-order expansions start to deviate. The plots show that the corresponding systematic uncertainties can e.g. be estimated by the difference between subsequent orders.

4.F.1 Binomial distribution

Here one has for the case of N trials and a success probability p

$$p_n = \binom{N}{n} p^n (1-p)^{N-n} \tag{4.61}$$

which leads to

$$F(z) = \sum_{n=0}^{\infty} p_n z^n = \sum_{n=0}^{\infty} \binom{N}{n} (pz)^n (1-p)^{N-n} = (pz + 1 - p)^N \,. \tag{4.62}$$

With the replacement $z \to 1 - \varepsilon + \varepsilon z$ the generating function of the observed distribution is obtained as

$$F^{obs}(z) = (\varepsilon p z + 1 - \varepsilon p)^N \,, \tag{4.63}$$

i.e. a binomial distribution with reduced success probability εp, and for a zero-suppressed true distribution the zero-suppressed observed distribution is a zero-suppressed binomial distribution. For the event efficiency one finds

$$\varepsilon_{\text{evt}} = \frac{1 - (1 - \varepsilon p)^N}{1 - (1 - p)^N} \,. \tag{4.64}$$

4.F.2 Poisson distribution

Here the generating function is given by

$$F(z) = \sum_{n=0}^{\infty} p_n z^n = e^{-\mu} \sum_{n=0}^{\infty} \frac{(\mu z)^n}{n!} = e^{\mu(z-1)} \,, \tag{4.65}$$

and the replacement $z \to 1 - \varepsilon + \varepsilon z$ leads to

$$F^{obs}(z) = e^{\varepsilon\mu(z-1)} \,. \tag{4.66}$$

The observed distribution is still a Poissonian with reduced mean value $\varepsilon\mu$, and starting from a zero-suppressed true distribution the zero-suppressed observed distribution is a zero-suppressed Poissonian. The event efficiency is given by

$$\varepsilon_{\text{evt}} = \frac{1 - e^{-\varepsilon\mu}}{1 - e^{-\mu}} \,. \tag{4.67}$$

4.F.3 Exponential distribution

For the case of an exponential distribution with $p_n \propto \alpha^n$ one obtains

$$F(z) \propto \sum_{n=0}^{\infty} (\alpha z)^n = \frac{1}{1 - \alpha z} \quad \text{and thus} \quad F(z) = \frac{1 - \alpha}{1 - \alpha z} \tag{4.68}$$

The normalization is determined by the requirement $F(1) = 1$. Here the replacement $z \to 1 - \varepsilon + \varepsilon z$ leads to

$$F^{obs}(z) = \frac{1 - \alpha'}{1 - \alpha' z} \quad \text{with} \quad \alpha' = \frac{\alpha\varepsilon}{1 - \alpha(1 - \varepsilon)} \,. \tag{4.69}$$

One still deals with an exponential function, but with a redefined parameter α'. As before, starting from a zero suppressed exponential, the zero-suppressed observed distribution is exponential, with the parameter α' given in Equation 4.69. The event effciency becomes

$$\varepsilon_{\text{evt}} = \frac{\varepsilon}{1 - \alpha(1 - \varepsilon)} = \frac{\alpha'}{\alpha} \,. \tag{4.70}$$

As a final remark, note that for comparison with the other models, the relation between α and μ, the mean value of the not zero-suppressed probability distribution, is

$$\alpha = 1 - \frac{1}{1+\mu} \ . \tag{4.71}$$

For the zero-suppressed probability distribution, the relation is $\alpha = 1 - 1/\mu$.

5 The LHCb upgrade

LHCb collected $3\,\text{fb}^{-1}$ in 2011-2012 (Run 1) and $2\,\text{fb}^{-1}$ in 2015-2016 (Run 2) of p-p collisions. We expect to collect $\sim 1.5\,\text{fb}^{-1}$ per year more in 2017-2018, before the second long shut-down of the LHC (LS2), expected at the end of 2018. So far, the detector performance was excellent: all detectors have being working with more than 99% of their channels active, the overall detector efficiency is larger than 94% and about ∼98% of the acquired data is registered in good working conditions of all detector sub-systems.

Precision measurements and the study of rare decays have in common the need for high statistics. Nowadays, almost all LHCb results are dominated by statistical uncertainties, so we need to collect more data. In the current conditions, duplicating the statistics after the LS2 in 2019 would take 5 years more, which it is not very rewarding. Thus, the running conditions need to be modified to allow a higher data collection rate.

The only way to get more data is to increase the overlap between the two beams in order to get a higher number of proton-proton interactions in each bunch crossing. Apart from other issues, the main limitation of LHCb to run in such conditions is the 1 MHz readout rate of the front-end electronics. what means that the L0 trigger rate cannot be increased above this value. Increasing the instantaneous luminosity and keeping the L0 trigger rate below 1 MHz, means that the thresholds must be tighten. The decays with muons in the final states can be easily distinguished due to the readout of the muon detectors for the L0 decision, but the calorimeter information only allows for the selection of high energy objects, and it is unable to distinguish high energy hadrons produced in the primary vertex from those occurring in b-hadronic decays. This leads to a loss in efficiency for hadronic-only final states with increasing instantaneous luminosity. As can be seen in Figure 5.1, the luminosity can be increased up to $4 \times 10^{32}\,\text{cm}^{-2}\text{s}^{-1}$ but there the hadronic triggers saturate. Furthermore, the current detector is not designed to work at higher luminosity, what would lead to a faster ageing. This is the reason why the LHCb detector was running at $4 \times 10^{32}\,\text{cm}^{-2}\text{s}^{-1}$ and also why it needs to be improved in order to allow higher data acquisition rates.

The most remarkable change with respect to the trigger strategy is the elimination of the L0 hardware trigger to become a software-only trigger system. This is a very challenging upgrade due to the high collision rate in LHCb and it will require the replacement of almost all the front-end electronics. Even though the increase in luminosity is not the final goal of the upgrade, but the increase in the trigger efficiency, LHCb will be able to run at an instantaneous luminosity of $2 \times 10^{33}\,\text{cm}^{-2}\text{s}^{-1}$. The whole detector will be read out at 40 MHz and we expect an increment of a factor 10 and 20 in the muonic and hadronic channels yield respectively. We aim to record about $10\,\text{fb}^{-1}$ per year.

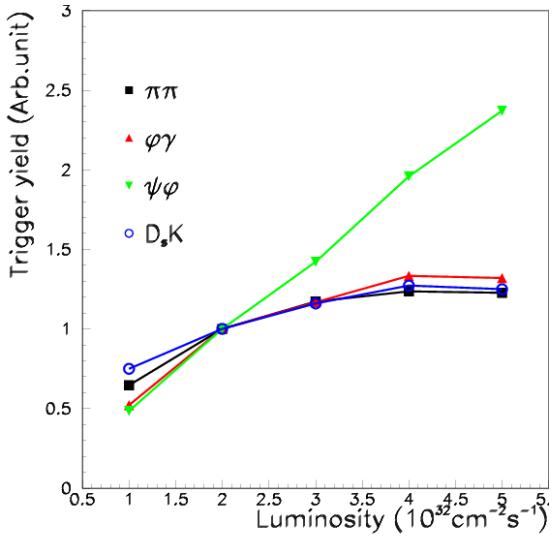

Figure 5.1: Trigger yield *vs.* instantaneous luminosity for 4 different channels using the current LHCb trigger. The $J/\psi\,\phi$ channel has two muons in the final state so its yield increases constantly with luminosity. The other channels saturate at $4 \times 10^{32}\,\mathrm{cm}^{-2}\mathrm{s}^{-1}$ and above this value there is no benefit in increasing the luminosity.

5.1 Changes to LHCb subdetectors

The VELO: As it was already mentioned, the VELO front-end readout ASIC (Beetle ASIC) has a maximum readout rate of 1.1 MHz, that is incompatible with the upgraded running conditions. Furthermore, the higher number of interactions per bunch crossing leads to occupancies that the current VELO cannot resolve, an amount of data that it cannot manage and a higher radiation damage. All of these implies that the full VELO modules must be replaced [96, 97]. Furthermore, due to different module geometries, a new RF-foil must also be produced. On the other hand, the vacuum tank, the cooling plant and the motion system will be refurbished.

The TT: As with the VELO, the TT needs to be completely replaced to meet the upgrade requirements. The new Upgrade Tracker (UT) [98] will follow the philosophy of the current TT and will be based in silicon micro-strip detectors. These sensors will be read out by a custom ASIC called Silicon ASIC for LHCb Tracker (SALT). The upgraded detector will use the small magnetic field that exists between the VELO and the UT to make a preliminary momentum measurement before the track extrapolation through the magnet. This would allow a reduction in the search area for the downstream tracking and a faster online reconstruction for the trigger. This idea was already intended to be used in the current detector.

The downstream tracking stations: As it was mentioned before, the IT uses the same technology as the TT, so it will suffer the same problems. On the other hand, the current OT is already experiencing high occupancy levels. Thus, the downstream stations need also to be changed by detectors with higher granularities. The new tracker was decided to be fully based in scintillating fibre technology (SciFi) [98].

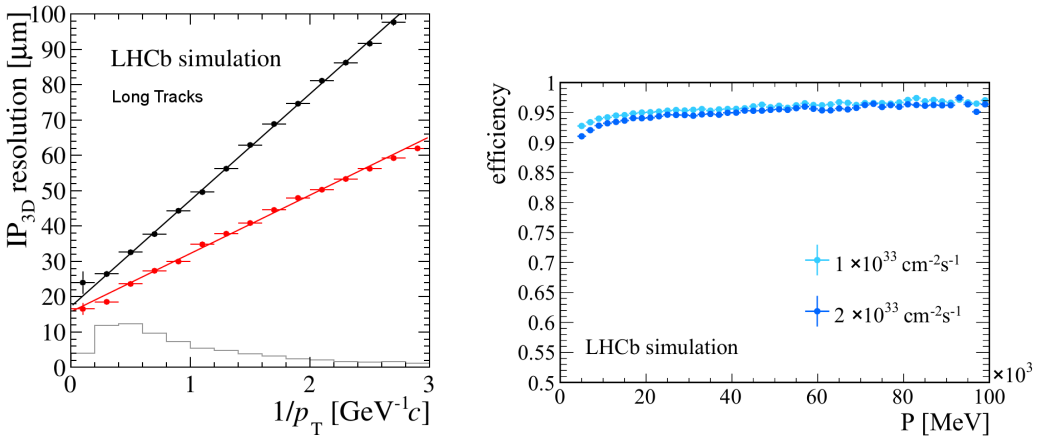

(a) (b)

Figure 5.2: (a) IP resolution *vs.* $1/p_T$ of the upgraded tracking system calculated in simulation using long tracks. Black dots represent the results of the current VELO and red dots the results of the upgraded one. The grey line represent the relative population of *b*-hadron daughter tracks. (b) Tracking efficiency *vs.* p of the upgraded tracking system calculated in simulation for two different instantaneous luminosities.

Following the existing detector design, there will be three downstream tracking stations. Each station will consist of four detecting layers, being rotated +5° and -5° with respect to the vertical axis the second and third planes respectively. The detection layers will be formed by five or six stacked layers of fibres read out by Silicon Photo-Multipliers (SiPMs). There will be needed more than 10000 km of fibres to build this subdetector.

Expected tracking performance: The expected tracking performance at the moment of the writing of the Technical Design Report is shown in Figure 5.2. A better IP resolution with respect to p_T is expected. The tracking efficiency of the current experiment will be kept. Since the writing of the TDR's some changes were made and others are expected, so the tracking performance can suffer variations.

The RICH detectors: The changes in the RICH detectors are presented in detail in [99]. The upgrade of the RICH detectors will consist in the replacement of the photon detectors, the front-end electronics, and the redesign of the RICH1 optics in order to reduce the occupancy on the focal plane. Multi-anode Photo Multiplier Tubes (MaPMTs) will be used as photon detectors, read out by a custom ASIC which will contain the signal shaping, discriminating and further amplification stages.

The Calorimeter and Muon system: As for the RICH detectors, the changes in the calorimeter and muon systems will be very small. For the calorimeter system, the front-end electronics will be replaced and the gain will be reduced in order to enhance the lifetime of the MaPMTs. The PS and SPD will be removed since they are not expected to play any role in the upgraded trigger system. The electronics of the muon chambers will be replaced, but the first muon detector plane M1, the one placed before the calorimeters will be removed. A new inner section for additional

shielding will be put in place behind the hadronic calorimeter in order to reduce the rate of the particles entering the muon detection sub-system.

PID performance: The RICH is expected to keep its current performance after the upgrade, despite the higher multiplicities. The expected PID efficiency is shown in Figure 5.3(a). On the other hand, the muon detectors performance is expected to degrade about ∼5%. This will be caused by the dead time in the electronics that will not be replaced. An upgrade to the muon system has been proposed to be installed in LS3, but the existing spare chambers and the off-detector electronics upgrade is considered sufficient to provide high efficiency (∼93%) in muon identification. The muon identification efficiencies for the current and the upgrade conditions is shown in Figure 5.3(b).

Trigger system: In principle, the upgraded LHCb data acquisition system was intended to be based on a trigger-less readout system and a full software trigger [100]. The full software trigger provides the maximum flexibility and is robust against fast obsolescence of technological products. It should be composed by two stages similarly to the current HLT1 and HLT2. The trigger strategy of the LHCb upgrade can be seen in Figure 5.4. In the first level the tracks will be reconstructed in subsequent steps, applying cuts at the end of each reconstruction stage. Thus, the processing time can be reduced enough to fit within the available computing resources. Using the resulting information, candidates for the various inclusive and exclusive trigger lines can be selected and written to disk. Furthermore, an online calibration and alignment will be performed. The output rate is under review and will vary between 20 and 100 kHz.

After analysing this alternative it was decided to include a Low Level Trigger (LLT) analogous to the current L0. The computing power needed after the upgrade is still not known, so moving the whole trigger system to the CPU farm has some risks. So, adding a new level before the software trigger will reduce the input data rate and also the computing needs. This is basically an upgrade of the L0 trigger, but with much looser requirements and a higher output bandwidth. Once the trigger farm will be able to take care of the full event load it will be removed. This LLT reduces the efficiency for hadronic channels which is the reason it was not chosen as part of the baseline design. The expected trigger yield for muonic and hadronic channels after the upgrade is a factor 10 and 20 higher than the current one respectively.

5.2 The VELO upgrade

The new VELO needs to meet several requirements. It has to be read out at 40 MHz. It needs a higher granularity to work at the new luminosity and provide a fast and robust track reconstruction, that is essential for the new software trigger. It has to be radiation hard. At the end of its lifetime the dose will be $8 \times 10^{15}\,1\,\mathrm{MeV\,n_{eq}/cm^2}$. Furthermore, it will have to cope with a highly non-uniform radiation environment. The hit multiplicity will vary with the following equation:

$$5.2 \times r^{-1.9}\,\mathrm{hits\,event^{-1}\,cm^{-2}}, \tag{5.1}$$

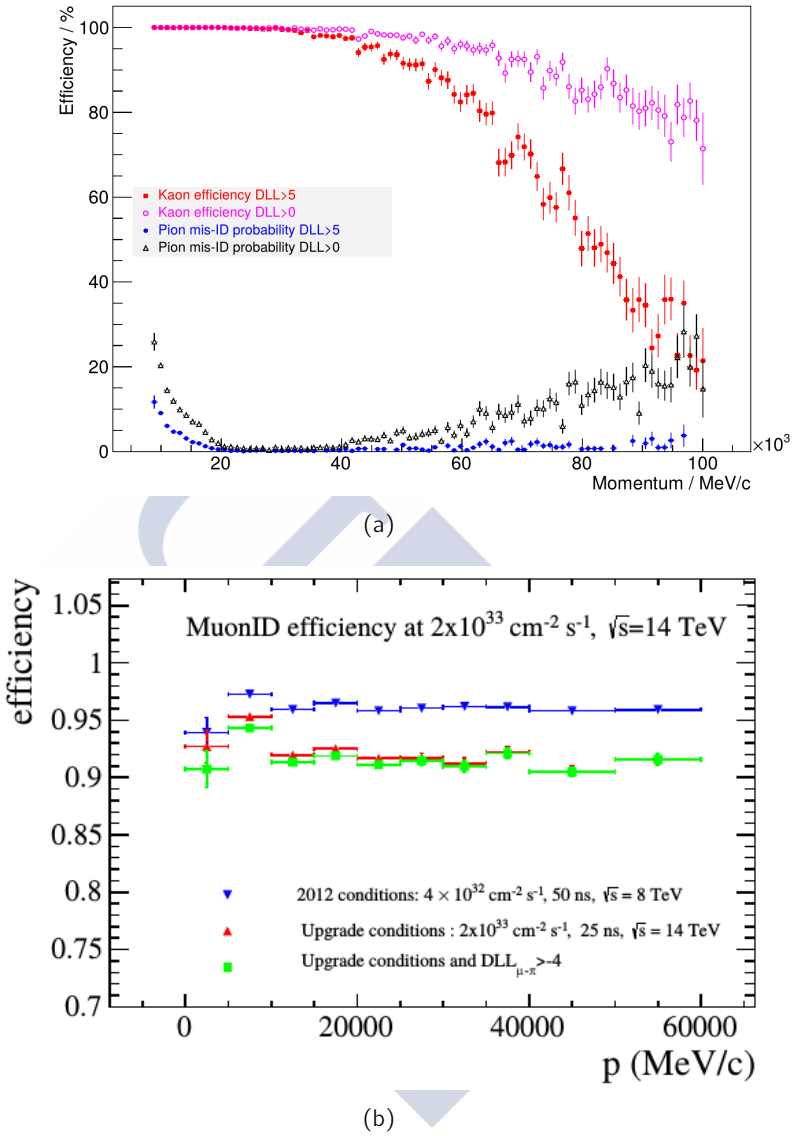

Figure 5.3: (a) Expected kaon identification efficiency (magenta and red) and pion misidentification probability (grey and blue) *vs.* the track momentum. (b) Muon identification efficiencies *vs.* momentum for the current (blue triangles) and the upgrade (red triangles and green squares). Blue and red points use only the information of the isMuon variable. The extrapolated muon identification efficiency at the upgrade luminosity of $2 \times 10^{33}\,\mathrm{cm}^{-2}\mathrm{s}^{-1}$ is found to be a 5% lower than the observed in the 2012 LHCb running conditions.

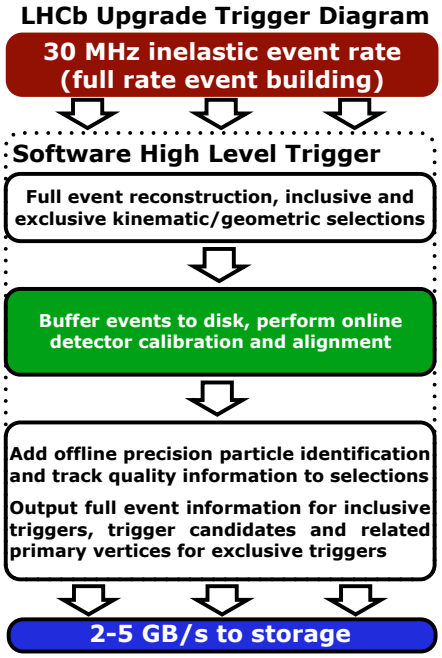

Figure 5.4: Trigger scheme for the upgraded LHCb detector.

being r the distance from the beam axis. So, the difference in fluence between the tip and far corner will be of a factor 40. Moreover, it has to minimise the material in the detector acceptance and to keep or improve the current detector performance.

To fulfill these criteria two technologies were proposed: silicon micro-strips and silicon pixels. The micro-strips option is the technology used in the current detector. Some micro-strip detectors were designed and produced, and many of them were characterized in our laboratories in Santiago. Furthermore, we developed an optimised technique to fabricate high density pitch adapters using laser ablation of metal-on-glass layers [101, 102]. The main drawback of this technology is that it needs more time than pixels to reconstruct the tracks and the resulting number of ghost tracks is also higher. Because of mainly these two reasons it was decided to discard this option and build the new VELO using pixels.

Regarding the pixel technology, the proposed detector is based on an evolution of the Timepix ASIC [103]. The new VELO will consist of 26 stations, where each of them is made up of 2 modules, one on either side of the beam and following the same philosophy of the current detector. The first sensitive pixel will be at 5.1 mm from the beam axis. Its geometrical efficiency will be greater than 99% for a radius smaller than 10 mm. This means that the 99% of the tracks will have 4 or more hits inside the VELO. It will be separated from the beam vacuum by a 250 μm RF foil.

5.2.1 Modules

The high speed pixel readout chips produce about $\sim$1.5 W/ cm^2. The sensors need to be cooled below -20°C in order to prevent thermal runaway after heavy irradiation, and to control the annealing of the sensors. The solution adopted for the cooling was the

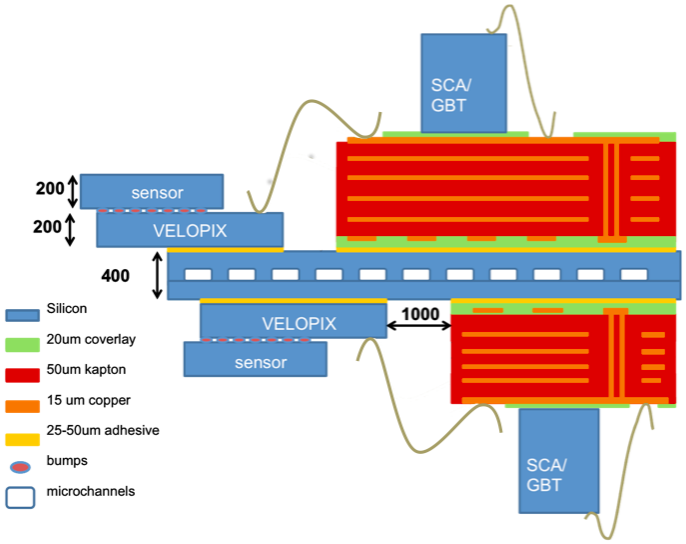

Figure 5.5: Cross section of a VELO module. The colour indicates the material type.

use of microchannel cooling. This method consist of channels directly etched in the mechanical substrate through which the cooling fluid is directed. The microchannels can be seen in the cross section of the module shown in Figure 5.5. The main advantage of this method is that the cooling fluid can be taken to the heat source using least material, since the cooling substrate acts at the same time as the mechanical support of the module. Furthermore, since the substrate material is silicon, as well as the ASICs and sensors, the thermal tensions are reduced to a minimum. The fluid used in the cooling will be evaporative CO_2. The dimensions of the channels will be of the order of $120 \times 200\,\mu m$, being the total thickness of the substrate $400\,\mu m$.

On top of the substrate will be mounted the VeloPix ASICs, and the kapton-mounted circuitry required to transmit the detector data to the edge of the vacuum tank. Each module will carry 4 sensors, 2 in each side of the substrate with a small overlap between them to eliminate inefficient regions, as it can be seen in Figure 5.6(a). Each sensor will be bump bonded to 3 VeloPix ASICs for readout, as shown in Figure 5.6(b). In order to reduce the amount of material close to the interaction point, the cooling substrate is retracted and does not cover the whole area of the innermost chip. The material in the active region will be around 0.9% of the radiation length.

5.2.2 VeloPix

The VeloPix [104] is a hybrid readout chip on which the upgraded VELO will be based. It is a successor of the Timepix3, and it consist of a square pixel matrix of 256×256 pixels of $55\,\mu m \times 55\,\mu m$. The readout is one of the most challenging aspects in the upgrade of the VELO. The readout will be binary, this means that no deposited charge data will be collected, and it will use a data driven readout method: each hit will be time-stamped, labelled and sent off the chip immediately in a superpixel structure. These superpixels consist of a group of 2×4 pixels sharing a central analogue circuitry, with the digital blocks placed on the outer regions. This allows the information to be sent off-chip to be

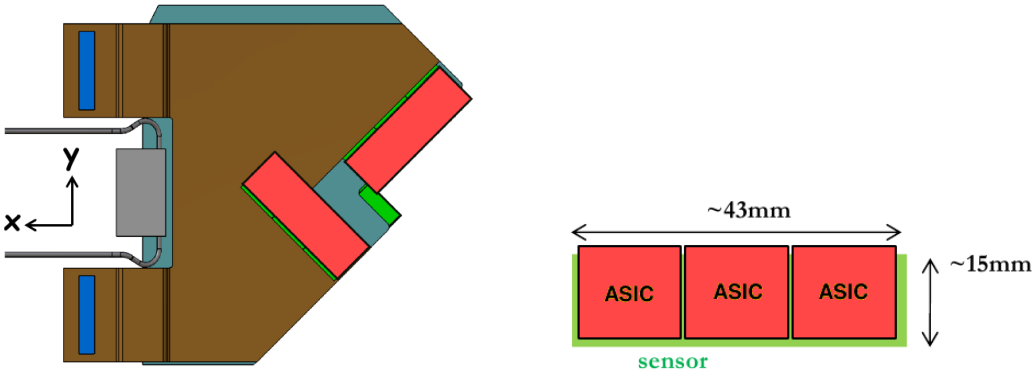

(a) (b)

Figure 5.6: (a) Module layout. On the left part of the module it can be appreciated the cooling tubes and the connector. The central part is composed by the hybrid and the microchannel silicon substrate underneath. On the right part of the module two sensors on top of three VeloPix ASICs can be seen. The other two sensors are not visible because are on the other side of the module. (b) Three VeloPix ASICs on top of a sensor. The colours of this figure match the colours of (a).

compressed. This superpixel structures permit a gain of roughly 30% in output data. In every bunch collision, a mean of 32.8 tracks will traverse each module, with an average cluster size of 2.2 pixels. With a collision frequency of ∼30 MHz, the average data rate will be 36.8 Gbits/s per module. Moreover, the variation between the inner and outer chips will be very large due to their distance to the beam, as it can be seen in Figure 5.7. The inner chips will be required to transmit data at a average rate of 10.2 Gbits/s with a peak rate of around 15.1 Gbits/s.

The VeloPix will be radiation hard and keep fully operational after a radiation dose of 400 mrad. Furthermore, it will be Single Event Upset (SEU) tolerant.

5.2.3 VELO sensors

In order to reduce the inactive area of the detector, it was decided to mount one sensor on every three VeloPix ASICs. The dimensions of the sensor will be 43 mm × 14 mm and a thickness of 200 µm. As the readout chip, the sensors pixel size will be 55 µm × 55 µm, with elongated pixels implants of 110 µm in the region between the ASICs. In Figure 5.9 can be seen a picture of a sensor bump bonded to three Timepix3 chips for testing, and Figure 5.8 shows a more closer view of the sensor where the elongated pixels can be seen in the centre of the picture.

The most important issue that the sensor design has to face is the non-uniformity in the radiation damage across the sensor. A difference of a factor ∼40 in fluence between tip and far corner is expected at the end of lifetime of the VELO upgrade. This implies that the bias voltage for the most damaged regions must be ∼1000 V, and the region less irradiated must be able to operate at these voltages without risk of electrical breakdown. Taking into account these restrictions, the sensor will be equipped with one guard ring of ∼450 µm.

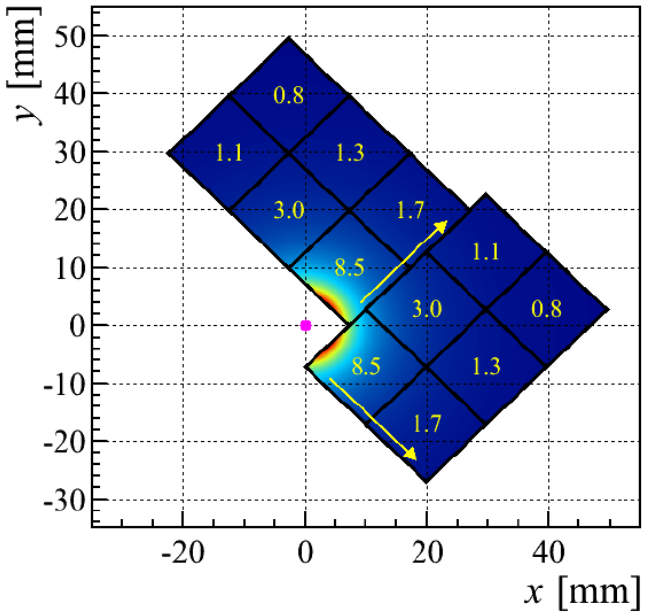

Figure 5.7: Mean number of particles crossing an ASIC per event.

Figure 5.8: Hammamatsu prototype sensor. The elongated pixels that will be located between the ASICs can be seen in the middle of the picture.

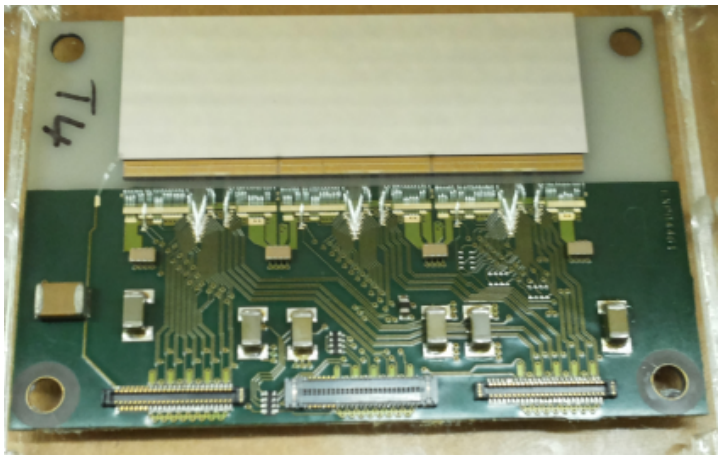

Figure 5.9: n^+-on-p, 200 µm thick, with a guard ring of 450 µm and an implant of 35 µm silicon sensor bump bonded to three Timepix3 and mounted on a hybrid test board.

5.2.4 The RF foil

The RF foil is an Aluminium alloy foil that separates the LHC vacuum from the secondary vacuum of the VELO and shields them from beam induced RF currents. Actually, the RF foil is *de facto* a beam pipe. Due to the new geometry of the VELO it must be redesigned.

Since it is the first element between the collision point and the detector, it is of crucial importance. The current RF foil is the largest single contributor to the total material thickness of the VELO detector. It must be vacuum tight, radiation hard, light, thermally stable and conductive and have a good electrical conductivity to mirror beam currents and shield against RF noise. The current RF foil was produced by metal pressing of a single massive sheet but this method leaves significant fluctuations in the thickness. To produce the more complicated shape required for the upgraded VELO the new RF foil will be milled from a solid Al alloy block. With this method a thickness of about 250 µm with the required shape will be achieved. A final thinning of the central region using chemical methods will reduce the thickness to 100-200 µm in the region around the interaction point.

6 Radiation tolerance of the Medipix3 chip

The upgraded VELO will be based on the VeloPix ASIC. The VeloPix is a descendant of the Medipix3 [105]. One of the most important requirements of the VeloPix is that it has to be radiation hard. It must keep working after receiving a fluence of $8 \times 10^{15}\,1\,\mathrm{MeV}\,\mathrm{n_{eq}}/\mathrm{cm}^2$, that is the fluence expected after 5 years of operation. Furthermore, it will have to cope with a highly non uniform radiation environment. At the end of its lifetime, the fluence in tip will be 40 times much higher than in far corner. Before starting the VeloPix design, it is necessary to study the radiation hardness of the registers to build it. The most similar device to the planned VeloPix three years ago was the Medipix3 ASIC, so it was studied extensively in order to improve the VeloPix design. On one hand, it was used to build silicon detectors that were characterized in charged particle beams [106], and on the other hand, it was studied stand alone as presented in this thesis.

As indicated in Ref. [107], radiation effects in electronic devices can be divided in two main categories: cumulative effects and Single Event Effects (SEE).

Cumulative effects are due to the creation or activation of microscopic defects in the device. Individually, each of these effects is not of significant importance to the device behaviour, but the accumulation of them can cause important effects and even the device destruction. These effects have two contributions:

- Total ionizing dose: The electron-hole pairs creation degrades the component behaviour.
- Displacement damage: An incident particle collides against the nucleus and move it from its lattice position because of non-ionizing energy loss. This degrades the component performance.

Single Event Effects are caused by the direct ionization of a single particle, able to deposit enough energy to disturb the operation of the device. The charged hadrons and the neutrons present in the LHC environment do not directly deposit enough energy to generate SEE. Nevertheless, they could induce a SEE through nuclear interaction in the semiconductor device or in its close proximity. The recoil from this interaction is often capable of deposit enough energy to create a SEE. The three main types of SEEs are:

- Static SEEs: These effects are not permanent or destructive and can be solved by just reloading the corrupted bits. The consequence may be a flip in an information bit stored by the logic circuit. This effect is defined as Single Event Upset (SEU). An special case of SEU is when the ionisation changes one bit of information controlling a special function of the circuit and it is necessary to reset it in order to bring it back to normal operation. In this case the effect is called Single Event Functional Interrupt (SEFI).
- Transient SEEs: The charge collected from an ionisation event creates a spurious signal that can propagate in the circuit. Typical examples are transient pulses in combinational logic, which can propagate and ultimately be latched in a register,
- Permanent SEEs: These effects may be destructive.

  Single Event Latchup (SEL) occurs in CMOS technologies, where a structure usually equivalent to a thyristor, a *pnpn* structure which acts as a *pnp* and an *npn* transistor stacked next to each other, is triggered by the ionizing energy deposition in a sensitive point of the circuit. This leads to an almost short-circuit current on the power lines, which can permanently damage the device.

  Single Event Burnout (SEB) occurs in power MOSFETs, BJT and diodes when these power devices are in the "off" state. The short-circuit current induced across the high voltage junction can permanently damage the device.

  Single Event Gate Rupture (SEGR) also affects power MOSFETs in the "off" state. The gate dielectric can be permanently damaged when, due to the energy deposited by an incoming particle, the electric field across the oxide is temporarily increased beyond the breakdown limit.

6.1 The Medipix3 chip

The Medipix3 chip is a pure counting device designed for applications with photons. The Medipix3 contains an array of 256 $\times$ 256 of 55 µm square pixels. The structure of the matrix is implemented as a mosaic repeating a 4 pixel structure. Each of these 4 pixels present a different layout. The position of the 4 pixels with respect to the matrix edges is shown in Figure 6.1. The Medipix3 was the first ASIC of the Medipix family to be built in 130 nm IBM CMOS technology and, at that moment, it was also the technology planned to use for the VeloPix design. These characteristics made the Medipix3 the perfect device to study the actual status of the VeloPix design.

An schematic view of the pixel logic can be seen in Figure 6.2. Every pixel contains an analog and a digital part. In the digital part of the circuit can be identified two 12-bit counters. These counters can be written and read out so they are the ones that are going to be used to study the SEU cross section.

6.2 Single Event Upsets

A SEU is caused by a very high energy deposition in a very small volume of the electronics. The charge released is collected by one node and the resulting current might generate a SEU. The SEUs occurrence depends on two variables: The sensitive volume in which the

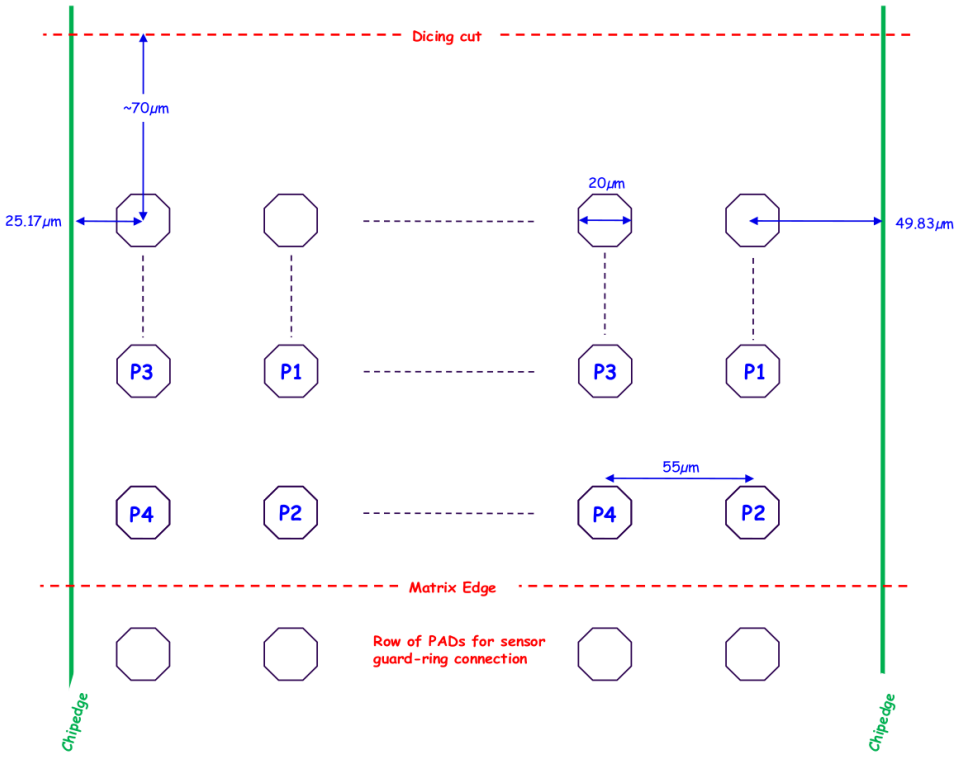

Figure 6.1: Distances between the centre of the passivation openings to the left and right of the chip edge. The position of the regular structure in the full matrix is shown. Figure taken from Medipix3 manual [105].

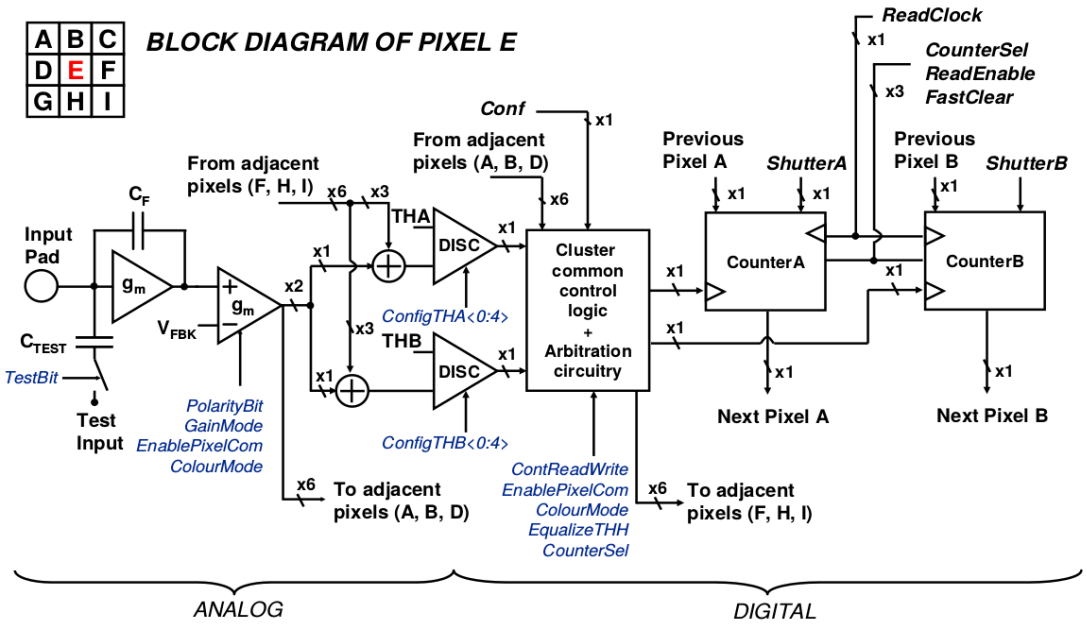

Figure 6.2: Block diagram of the pixel cell showing its analog and digital parts. The digital part contains some control logic, 13 configuration bits, arbitration circuits and two 12-bit counters. Figure taken from Medipix3 manual [105].

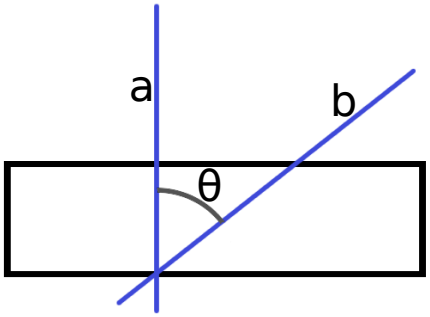

Figure 6.3

ionization has to take place for the charge to be collected in the node, and the threshold value to be exceeded by the deposited ionizing energy in the sensitive volume in order to flip a bit.

Since the sensitive volume is a design property of the chip, in order to study the SEUs sensitivity, the electronics must be irradiated with different linear energy transfer (LET) particles. Assuming that the shape of each bit register is a rectangular prism, the particle LET inside the sensitive volume can be modified by just changing the particle angle of incidence. As indicated in Figure 6.3, taking a particle traversing the sensitive volume perpendicularly to it as reference, the LET of the same particle going through the sensitive volume following a trajectory rotated an angle θ with respect to the first one is

$$\mathrm{LET}_b = \frac{\mathrm{LET}_a}{\cos\theta}. \tag{6.1}$$

So, many different LETs can be achieved using only one projectile.

SEU cross-section with respect to the LET of the incident particles follows a typical shape showed in Figure 6.4. It has a very sharp threshold at low LET, below which value the electronics is not affected by SEUs. Above this value, first the cross section increases very quickly and then saturates. The saturation is due to the fact that all sensitive parts of the device upset when a particle of those LETs hits them, so higher LETs do not increase the cross section.

A Weibull function can be fitted to data. This function is defined as

$$\sigma = \sigma_{\mathrm{sat}} \left\{ 1 - \exp\left[- \left(\frac{\mathrm{LET} - \mathrm{LET}_{\mathrm{th}}}{\mathrm{W}} \right)^{\mathrm{S}} \right] \right\}, \tag{6.2}$$

where σ_{sat} is the value of the cross-section at the plateau, $\mathrm{LET}_{\mathrm{th}}$ is the threshold value, and W and S are two shape parameters. So, there are four free parameters to be fitted.

6.3 Setup and measurements

Heavy-ion irradiations are the most convenient way of characterising the electronics in terms of the SEU sensitivity. To characterise the device we need to measure the SEU cross-section at different LETs. There are dedicated facilities around the world that allows to irradiate a device with different LETs. The facility chosen to perform the Medipix3

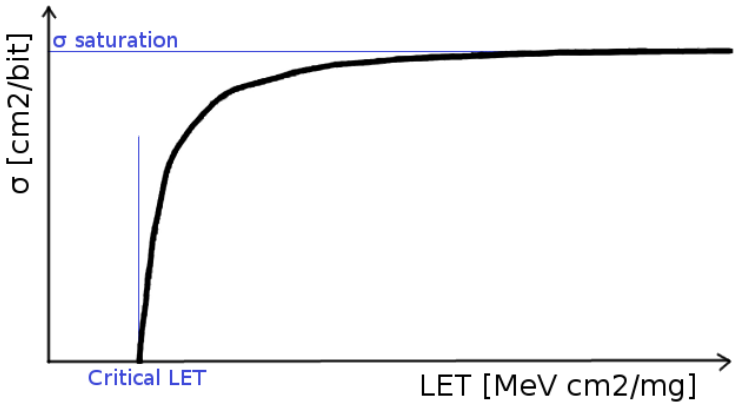

Figure 6.4: Black line shows the typical shape of the SEU cross-section *vs.* LET. In colour blue, the level of the critical LET and the value of the saturation cross-section are indicated.

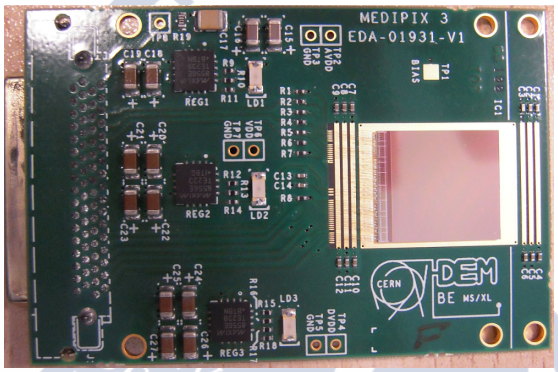

Figure 6.5: Medipix3 chip mounted on a CERN chipboard.

characterization was the Heavy Ion Irradiation Facility (HIF) [108] in the Cyclotron Resource Centre at Louvain-la-Neuve, Belgium. This facility allows to choose between two ion cocktails, each of them containing many ion types and one LET per ion. Furthermore, the device under test (DUT) can be rotated, so we can obtain more than one LET measurements per ion type, as it was explained before.

I took to the beam test two Medipix3 chips with references W100_F7 and W100_D7, mounted each on a CERN PCB chipboard. One of these assemblies can be seen in Figure 6.5.

6.3.1 Readout

Medipix3 chips can be read out using a FITPix [109] USB box. A generic testing software application from the Medipix group was modified to implement the necessary features to perform the tests. As it can be seen in Figure 6.6, the GUI window was divided in 3 main parts.

Pad 1: This pad is divided into in five subpads. In the textbox called "Directory" it is possible to configure the path where the logfile with data will be saved. The

logfile is saved only in case that the check box "Save log file" is ticked. "Chip reset" check box configures the reset of the chip every time a new measurement starts. "Measurement VDDA" and "Measurement T°C" activate the measurement of the running voltage of the chip and its temperature respectively. "Digital Test" activates a check just before the starting of the measurement to detect errors in the chip. "Random values" configures to write random data in the chip cells to be tested. If unchecked only zeros are written. "Fake SEU" writes some fake SEUs in the log file to permit the test of the analysis tools. If a frame contains more than "Threshold(%)" SEUs, the frame is counted as "bad" in for the statistics. If the check box "Enable timing" is ticked, the system will take a set of automatic measurements. Every write and read operation is named as frame. The number of frames to take is configured in the "Frames" box, and the time between each write and read operation in the "Time" box. If "Enable timing" is not ticked, the start and stop commands are given manually clicking on the start/stop button.

Pad 2: This section of the window is only for online information. When a measurement starts, the chip reference, its type and its running voltage and temperature, appear at the top of the pad. Besides the text "SEU(bits flip/%)" it will be indicated the number of SEUs detected. This data is presented in absolute value and as the percentage of the total number of bits checked. "Frame(bad/total)" indicates the number of frames with at least "Threshold(%)" of bit flips over the total number of frames measured.

Pad 3: The aim of this pad is to fill in information about the beam and take notes about the data taking. This information will be saved in the log file and it is needed, or at least can be useful, for the analysis.

Text boxes and buttons not shaded are a heritage from the former software utilities and they were not removed to permit in depth diagnostics if needed.

All configurations are written up in the log file as well as the test results to provide a complete source of information for every run taken. An example of log file can be seen in Figure 6.7. This log file was generated as part of a software test. This can be deduced by the fact that the fake check box was activated.

6.3.2 Mechanics

The device under test has to be placed in vacuum to permit the heavy ions to reach it. Figure 6.8 shows the barrel facility vacuum tank opened and ready to install the device to examine. The ions pass exactly through the middle of the square frame so our Medipix3 has to be attached and placed in that position. This square frame can be rotated, so using one ion specie more than one LET can be measured.

The mechanical elements needed to attach the Medipix3 to the frame can be seen in Figure 6.9. The barrel frame only provides four screw holes. Element labelled as "1" is an aluminium frame needed to increase the number of screw holes where to attach the elements. Due to the small size of the Medipix3 chipboard, I have to use two methacrylate pieces labelled as "2" and "3" to attach it to the aluminium frame.

Since the chip is going to work in vacuum, it will not be able to dissipate heat by convection and it can overheat. To keep the temperature at acceptable levels, I decided

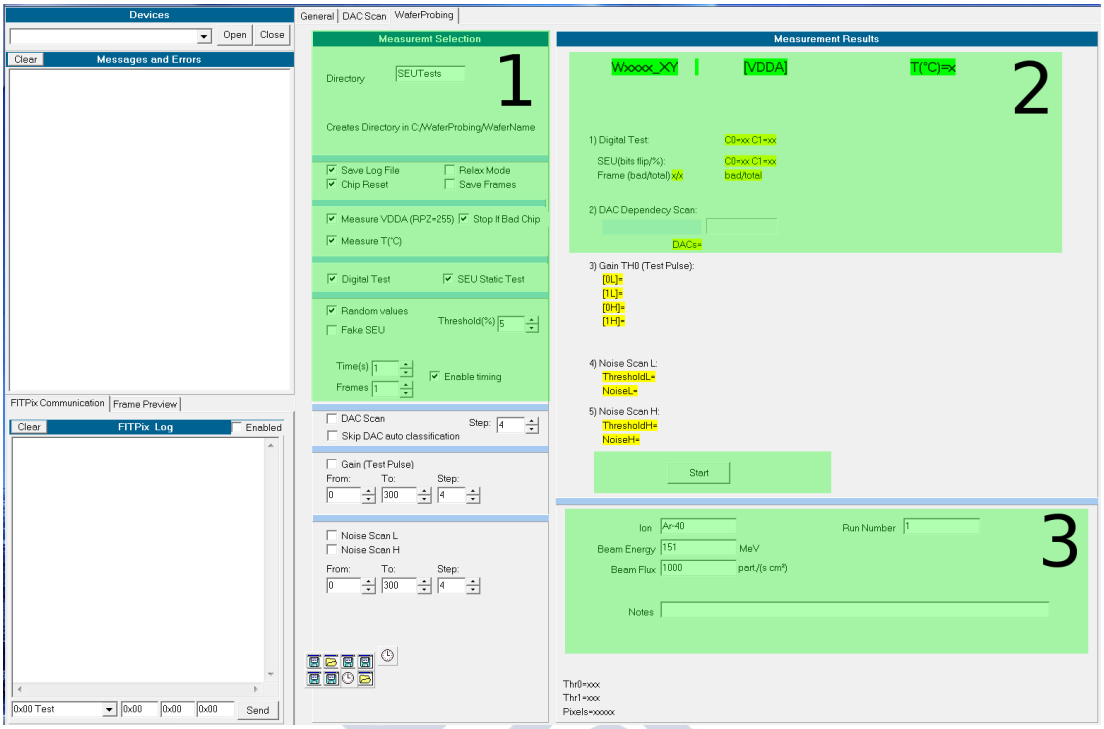

Figure 6.6: Readout software user interface main window.

```
**SEUs software test**
Program Start TS:       15/08/2013 11:26:47
Chip Reset TS:  15/08/2013 11:26:47
Chip:   W100_H7
ChipClass:      AA
VDDA Start:     1.470
T(°C) Start:    60.891

HF Digital Test:
 C0=0 bad columns
 C1=0 bad columns
 C0-C1: [0-0]
00000000000
```

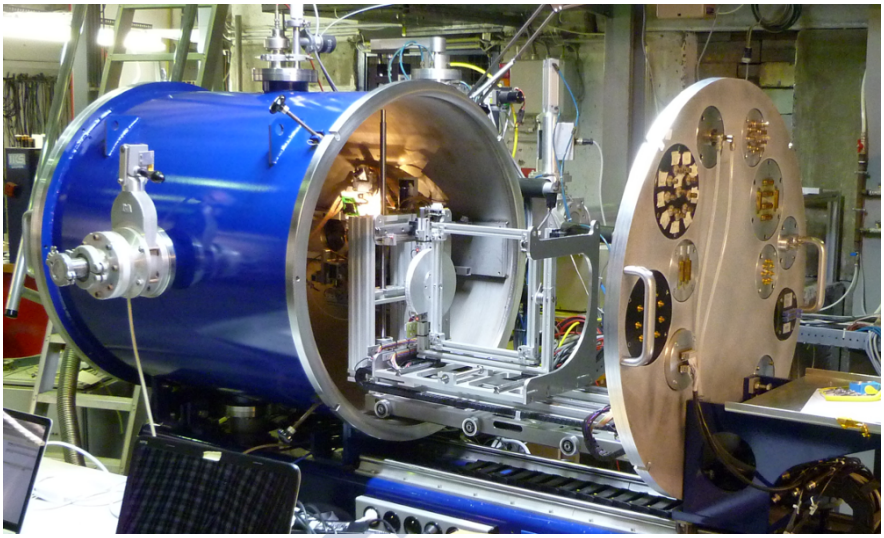

Figure 6.8: Vacuum barrel for testing. Inside the barrel can be seen the square frame where the device to test has to be attached.

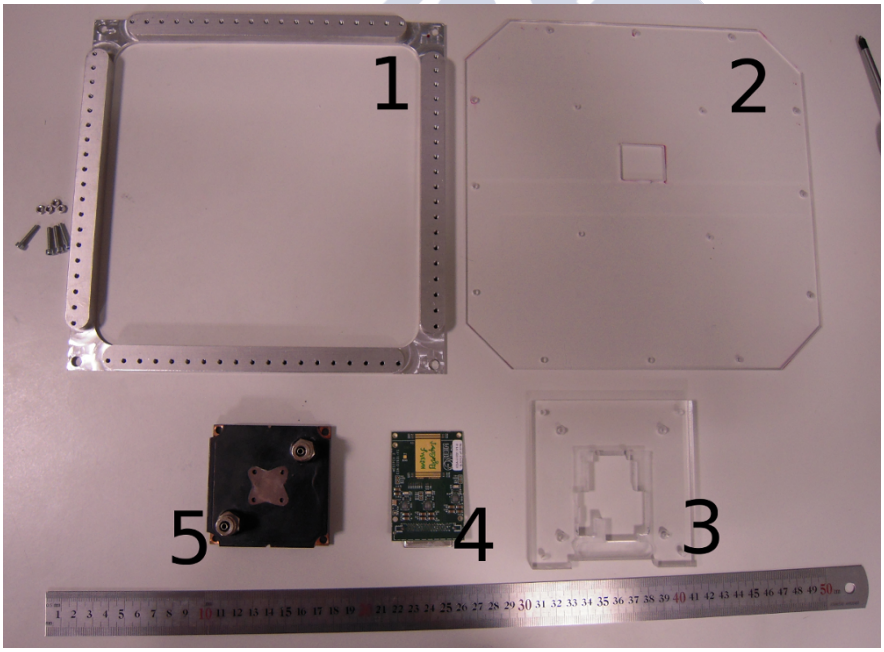

Figure 6.9: Elements needed to perform the tests. (1) Aluminium frame to attach our elements to the vacuum barrel. (2)(3) Metachrylate structures to fix the Medipix3 chipboard to the aluminium frame. (4) Spare Medipix3 chipboard without chip to test the structures. (5) Cooling block.

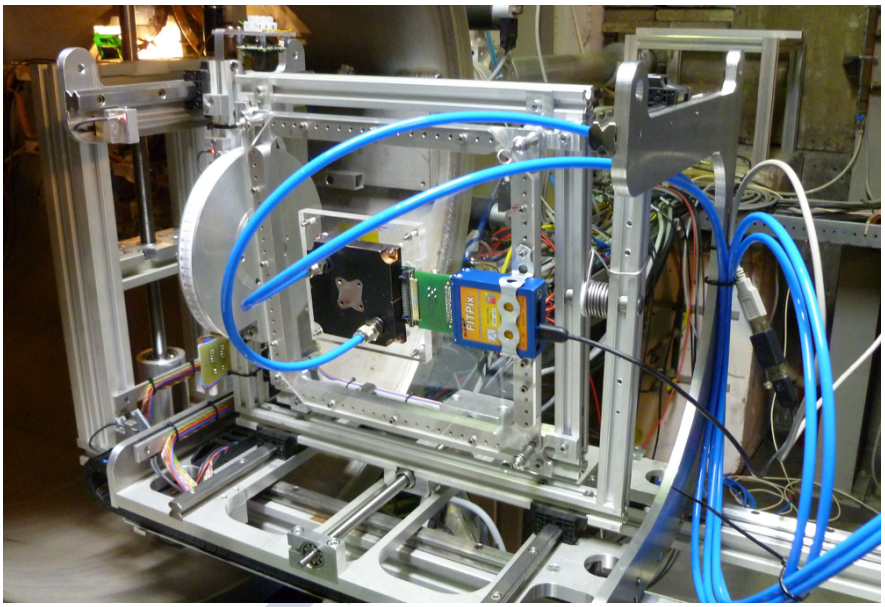

Figure 6.10: Mechanical setup ready to work. Medipix3 chip is not visible in the image since it is placed on the other side of the cooling block.

to use liquid refrigeration. The facility provides a source of water at 5°C that I connected to a cooling block. This cooling block is showed in Figure 6.9 and labelled as element '5'. It is attached to the back side of the chip board, opposite to the beam incidence. It had to be etched to increase the contact surface with the chip.

The final setup ready to be used can be seen in Figure 6.10.

6.3.3 Irradiations and data taking

CYCLONE110 is the accelerating machine of the facility. It can provide two cocktails of ions with different properties per ion, showed in tables 6.1 and 6.2. The ion species are sent individually to the device under test position. Change between ion types takes only a few minutes but change between cocktails requires much longer. Taking into account the time scale of this test beam only one set of ions could be used. I selected cocktail number two, in order to reach a lower LET and to have the possibility of collecting the maximum number of data points.

Ion	Ion Mean Energy [MeV]	Range [µm Si]	LET [MeV cm^2/mg]
$^{15}N^{+3}$	62	60.4	3.2
$^{20}Ne^{+4}$	80.5	46.3	6.1
$^{40}Ar^{+8}$	155	41.1	15.1
$^{84}Kr^{+17}$	324	41.1	40.0
$^{124}Xe^{+25}$	461	38.5	69.2

Table 6.1: Cocktail 1

Ion	Ion Mean Energy [MeV]	Range [μm Si]	LET [MeV cm^2/mg]
$^{13}C^{+4}$	131	269.3	1.3
$^{14}N^{+4}$	122	170.8	1.9
$^{22}Ne^{+7}$	238	202.0	3.3
$^{40}Ar^{+12}$	379	120.5	10.0
$^{58}Ni^{+18}$	582	100.5	20.4
$^{84}Kr^{+25}$	769	94.2	32.4
$^{124}Xe^{+35}$	995	73.1	62.5

Table 6.2: Cocktail 2

The beam flux can be adjusted from a few particles/(s cm^2) to ∼17000 particles/(s cm^2). The homogeneity is ±10% on 25 mm diameter, so this is the absolute uncertainty I am going to take for the flux.

As mentioned before, by rotating the chip, it is possible to measure different LET values. An initial setup test revealed that it was not possible to reach 60°. At this rotation angle, the metachrylate mechanics gets in the way of the beam and shadowed regions appear in the chip. Finally, I decided to take data at 0° and 45°. These angles in combination with the number of ion species provide us 10 LET points, that is enough to meet the goals of the analysis.

In order to commission the setup, with the beam turned off, I took a run of 20 frames with a delay of 2 seconds between each writing and reading operation. The performance was the expected and I proceeded to turn on the beam.

It is necessary to avoid the possibility of inducing double flips in the chip. I let a maximum SEU rate of 1% per frame, so the probability of having a double flip was 0.01%, that can be considered negligible. This means that the beam flux and data taking time must be modified to avoid having more than 15000 upsets per frame. To check how the chip performed, I configured the beam to provide $^{84}Kr^{+25}$ with a flux of 5000 particles/ s. I took 10 runs of 1 frame each with different data taking intervals. The longest frame interval was 30 s long, and I measured 4773 upsets in counter 1 and 4497 in counter 2. This is clearly below the maximum rate so these flux and time interval were taken as reference for the species with highest LET.

Tables 6.3 and 6.4 show the information of every run taken using chip W100_F7 in automatic and manual mode respectively. All these runs were taken writing random values in both counters. In Table 6.5 it can be seen the characteristics of the runs taken using chip W100_D7. No manual runs were taken using this chip. During data acquisition I was controlling the consistency of data between counters and between runs. Every frame with inconsistent data was taken again.

6.4 Data analysis

By plotting the raw data I already detected many frames with inconsistent data. In some runs, a lot of pixels located in some regions of the chip flipped with a higher rate than the rest of their neighbours. Examples of these data can be seen in Figure 6.11. In these

Ion	ϕ [part./ s]	θ [°]	#Runs	Frames/Run	Frame Δt [s]
$^{84}Kr^{+25}$	5000	0	1	10	30
$^{84}Kr^{+25}$	5000	45	1	10	30
$^{58}Ni^{+18}$	5000	0	2	10	30
$^{58}Ni^{+18}$	5000	35	1	10	30
$^{40}Ar^{+12}$	5000	0	2	10	30
$^{40}Ar^{+12}$	5000	45	1	10	30
$^{40}Ar^{+12}$	5000	45	1	4	30
$^{22}Ne^{+7}$	10000	0	2	10	30
$^{22}Ne^{+7}$	10000	45	1	10	30
$^{13}C^{+4}$	10000	0	1	10	30
$^{13}C^{+4}$	15000	0	1	10	30
$^{13}C^{+4}$	15000	45	2	10	30

Table 6.3: Characteristics of data taking runs in automatic mode using chip W100_F7. Random data were written at every frame.

plots, the vertical axis represents the pixel row and the horizontal axis represents the bits of the counters for every pixel. This means that every 24 columns represent a single pixel. The first 12 columns represent counter 1 and the next 12 columns belong to counter 2. Black points represent a SEU detected in one bit. As showed in Figure 6.11, these SEUs are organized in columns, in an specific place of the chip with sharp borders, covering the whole chip or a combination of them. This behaviour takes place independently in counter 1 and counter 2, and does not depend on the information written at the beginning of the process, as it can be seen in Figure 6.12. In some runs a huge amount of SEUs was measured at the time of stopping the data taking. Thus the most probable hypothesis is that this behaviour is due to some failure in the data acquisition system. This behaviour was impossible to be reproduced in absence of irradiation. The SEUs located in a small region of the chip and corresponding to a small fraction of the total number of SEUs were impossible to detect at the moment of their production. So it is not possible to ensure that they were produced by the same process. In any case, since SEUs are expected to happen homogeneously in the detector, all these frames were tagged as bad data and removed from the analysis.

As it can be seen in Figure 6.1, the Medipix3 pixel matrix is a repetition of a layout of 4 different pixel types. Plotting together each pixel type and each of their counters I obtain the histograms of Figure 6.13. In this figure, bins from 0 to 11 represent the bits from counter 1 and from 12 to 23 represent data from counter 2. Note that all pixels from counter 1 and every pixel type present a huge amount of SEUs, unlike counters type 2 that detected one order of magnitude less flips.

Dividing the counters data word in groups of 3 bits, I can analyse the cluster behaviour. In normal conditions, the most of SEUs would be created isolated, since the incident particles should not have enough LET to flip more than one bit. I expect clusters of 2 and 3 SEUs in rare occasions, and clusters of more than 4 bits are not expected. Figure 6.14 shows the cluster size of the SEUs detected for each counter divided in groups of 3 bits. Of course, clusters involving bits from two groups are also possible but, since I am only

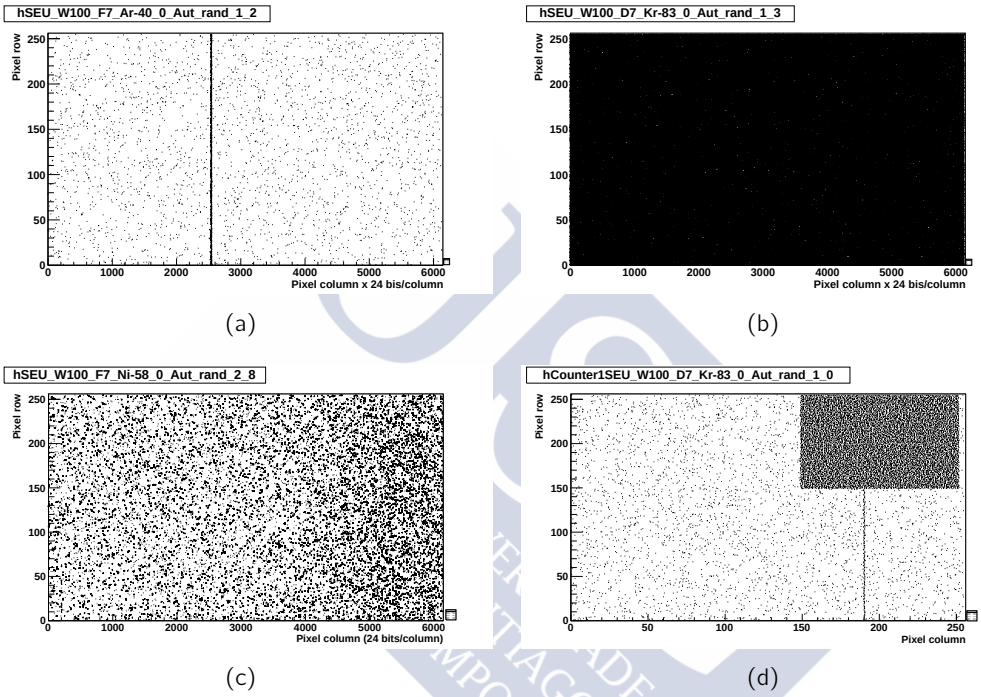

Figure 6.11: SEUs produced from a misbehaviour of the chip or data acquisition. The vertical axis represents the pixel rows. The horizontal axis represents the bits of the counters of every pixel. Every 24 columns represent a single pixel, being the first 12 columns from counter 1 and the next 12 columns from counter 2.

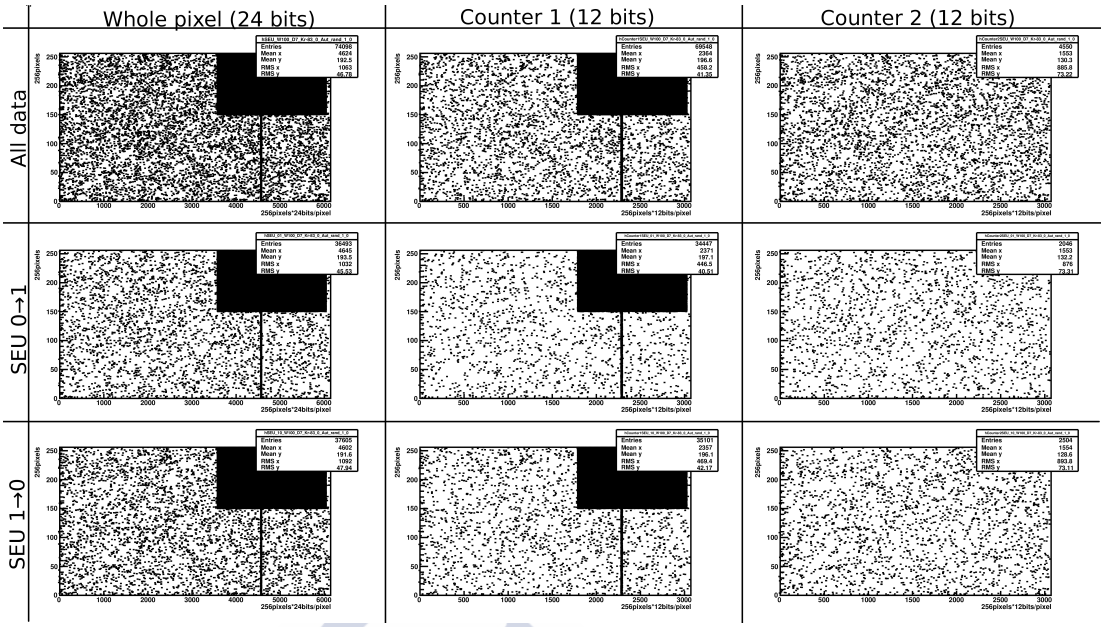

Figure 6.12: The top row plots represent the SEUs detected independently of the direction of the flip, from 0 to 1 or vice versa. Middle row plots show the SEUs changing the bit value from 0 to 1, and bottom plots represent the flips from 1 to 0. The left column represents the two counters per pixel. Mid and right rows represent the SEUs detected in counters 1 and 2 respectively.

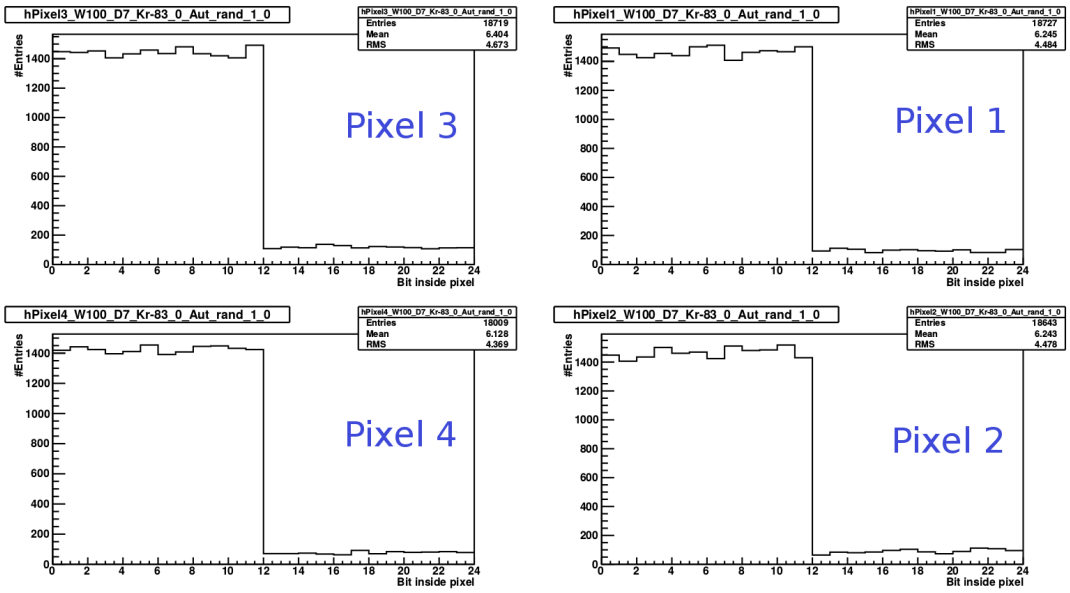

Figure 6.13: Number of SEU detected per bit of each counter and per pixel type. Bins from 0 to 11 represent the bits from counter 1 and from 12 to 23 represent data from counter 2. Plots are arranged as the pixel positions in the chip.

Ion	ϕ [part./ s]	Fluence [part./ cm^2]	θ [°]
$^{84}Kr^{+25}$	5000	150188	0
$^{84}Kr^{+25}$	5000	150308	0
$^{84}Kr^{+25}$	5000	156305	0
$^{84}Kr^{+25}$	5000	28456	0
$^{84}Kr^{+25}$	5000	28579	0
$^{84}Kr^{+25}$	5000	107228	45
$^{84}Kr^{+25}$	5000	104097	45
$^{40}Ar^{+12}$	5000	156117	0
$^{40}Ar^{+12}$	5000	161786	0
$^{40}Ar^{+12}$	5000	149883	0
$^{22}Ne^{+7}$	10000	313171	0
$^{22}Ne^{+7}$	10000	322141	0

Table 6.4: Characteristics of data taking runs in manual mode using chip W100_F7. Two runs of $^{84}Kr^{+25}$ were taken at the end of the accelerator fill, so the flux received was much less than expected. Random data were written at every frame.

Ion	ϕ [part./ s]	θ [°]	#Runs	Frames/Run	Frame Δt [s]	Data
$^{84}Kr^{+25}$	5000	0	1	10	30	Random
$^{84}Kr^{+25}$	5000	0	1	20	30	Random
$^{84}Kr^{+25}$	5000	0	1	10	30	All zeros
$^{40}Ar^{+12}$	15000	0	1	10	30	Random
$^{40}Ar^{+12}$	15000	0	1	8	30	All zeros
$^{40}Ar^{+12}$	15000	0	1	10	30	All zeros
$^{13}C^{+4}$	15000	0	2	10	30	Random

Table 6.5: Characteristics of data taking runs in automatic mode using chip W100_D7.

looking for a qualitative result, these groups of 3 bits will give us enough information. In Figure 6.14, counter 1 present a large fraction of clusters of 2 and 3 SEUs compared to counter 2. Furthermore, the amount of 3 SEUs clusters is similar to the 2 SEUs clusters, which indicates again a problem in the measurement.

Since a similar number of SEUs counts is expected in the two counters and in every single measurement, the asymmetry defined as

$$\text{Asymmetry} = \frac{\#C2 - \#C1}{\#C2 + \#C1}, \tag{6.3}$$

is a good discriminant between good and bad data. Data with an asymmetry larger than 13% between counters of all pixels averaged, or larger than 13% between counters in one single pixel type are tagged as bad. Figure 6.15 shows the asymmetry between the two counters for every frame. The region inside the two red thick lines indicates the good data area. Bad data region is marked with oblique fine red lines. Reproducing this analysis for

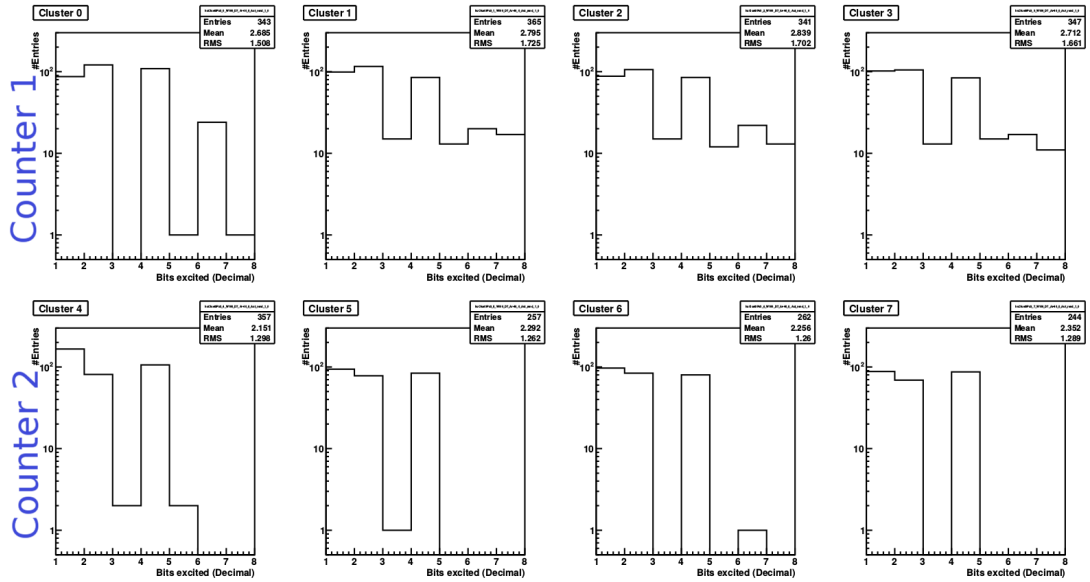

Figure 6.14: The two rows of histograms represent the two counters of the pixels. Each of the four plots represent a group of 3 bits from the data word of the counter and written in decimal format. The clusters of 1 flip will be represented as 1, 2 or 4 ('001', '010' or '100' in binary). The clusters of 2 flips will appear as 3, 5 or 6 ('011', '101' or '110'), and the 3 flips clusters will appear as 7 ('111') in the histogram. Clusters of more than 3 bits are not expected to happen in normal conditions.

each pixel type I obtain the results of Figure 6.16. The layout of the plots is again the same as the pixels inside the chip.

Applying this criterion I discard 93 out of 254 frames, and I lose all data with LET = 46.1 MeV cm^2/mg. This LET corresponds to data taken with ^{83}Kr at 45°.

- 38/93 bad frames present vertical lines. 37 affecting counter 1 and one more in both counters.
- 6/93 bad frames present a big black area, affecting only counter 1, and only 1 affecting counter 2.
- 2/93 bad frames present vertical lines and a big black area.
- 2/93 bad frames present no data in counter 1 and SEUs flipping from 0 to 1.
- 45/93 bad frames do not have a specific pattern.

The fraction of bad frames with respect to the LET of the incident particles is showed in Figure 6.17. From this graphic I can conclude that fraction of bad data increases with LET. It is not possible to go further and study the asymmetry dependence on LET due to the lack of statistics.

After data selection and using only good data I can get the SEU cross-section for every run. The cross-section and its uncertainty are defined as

$$\sigma = \frac{\text{Flips}}{\text{Fluence} \times \text{N}} \tag{6.4}$$

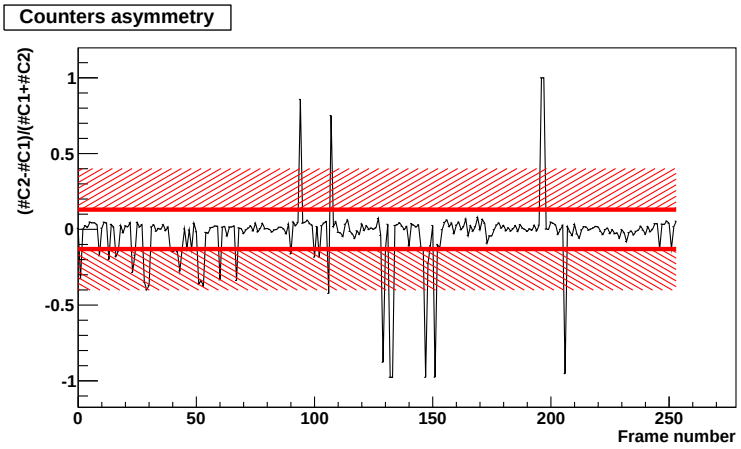

Figure 6.15: Counters asymmetry, defined as indicated in Equation 6.3, averaged over all pixels *vs.* frame number. Region between the two thick red lines define the region with less than 13% asymmetry.

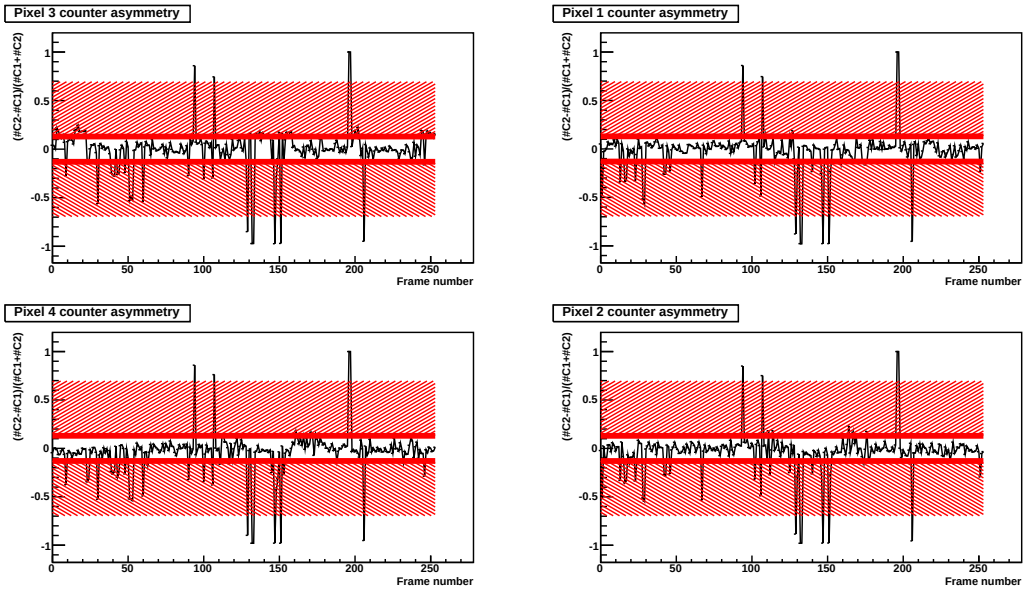

Figure 6.16: Counters asymmetry defined as 6.3 for each pixel type *vs.* frame number. Region between the two thick red lines define the region with less than 13% asymmetry.

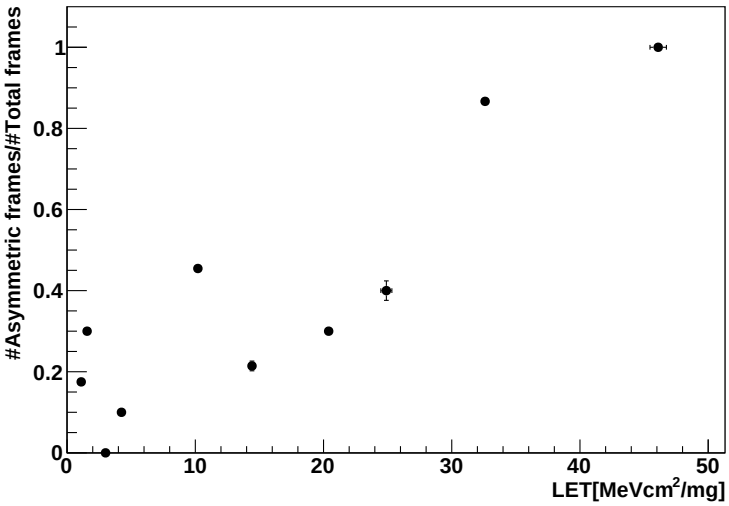

Figure 6.17: Fraction of frames with an asymmetry larger than 13% over the total number of frames *vs.* LET.

and

$$S(\sigma) = \sqrt{\left(\frac{\mathrm{S(Flips)}}{\mathrm{Fluence} \times \mathrm{N}}\right)^2 + \left(\frac{\mathrm{Flips} \times \mathrm{S(Fluence)}}{\mathrm{Fluence}^2 \times \mathrm{N}}\right)^2}. \tag{6.5}$$

"Flips" is the number of upsets detected in the measurement. Its uncertainty is calculated as

- S(Flips) = Poisson table; if Flips ≤ 20, and
- S(Flips) = $\sqrt{\mathrm{Flips}}$: if Flips > 20.

"Fluence" is the amount of ions traversing the chip during one measurement. It is calculated as

$$\mathrm{Fluence} = \Phi \times \cos(\theta) \times \Delta t, \tag{6.6}$$

being θ the angle with respect to the perpendicular of the chip surface, Φ the particle flux and Δt the the data taking interval. Propagating uncertainties, the fluence uncertainty can be calculated as

$$S(\mathrm{Fluence}) = \sqrt{(S(\Phi)\cos(\theta)\Delta t)^2 + (\Phi \sin(S(\theta))\Delta t)^2 + (\Phi \cos(\theta) S(\Delta t))^2}. \tag{6.7}$$

The uncertainties given by the facility operators are $S(\Phi) = 5\%\Phi$ and $S(\theta) = 1^\circ$. The interval is measured by the computer in charge of the data taking, and it is assumed to be $S(\Delta t) = 1\,\mathrm{ms}$. In manual mode, I asked the operators to send a fix fluence to the chip, so the uncertainty is given directly by the machine precision measuring it. In this case, the uncertainty of the fluence is S(Fluence) = 5%Fluence. Finally, "N" is the number of cells available in the chip. The uncertainty in the LET of an ion crossing the the chip at 0° is taken as 1%.

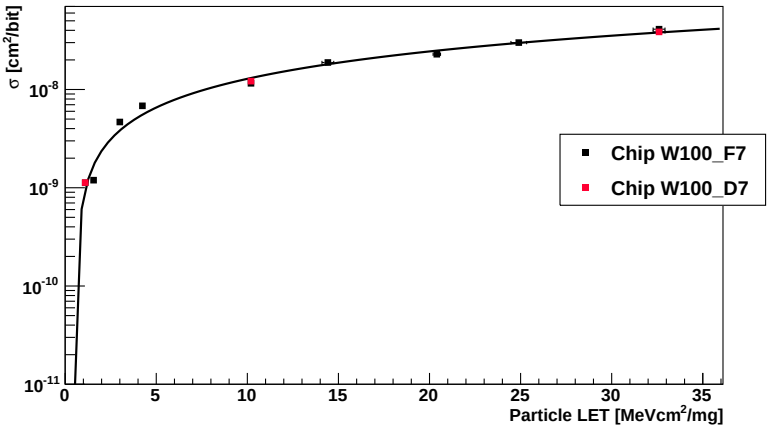

Figure 6.18: SEU cross-section results *vs.* LET. Black squares represent data measured using chip W100_F7 and red squares represent chip W100_D7. The black line represents the result of fitting a Weibull function to data obtained with chip W100_F7.

6.5 Results

Figure 6.18 shows the resulting cross-section points measured using the two chips available W100_F7 and W100_D7. First two points were measured using $^{13}C^{4+}$. Next two points measured with $^{22}Ne^{7+}$. The fourth and fifth points from the left were measured using $^{40}Ar^{12+}$. For the measurement of the sixth and seventh points from the left I used $^{58}Ni^{18+}$ and for the last point $^{83}Kr^{25+}$ was used. As indicated above, data from runs taken with $^{83}Kr^{25+}$ and with the chip rotated were removed from the analysis due to readout errors. Furthermore, the black line represents the Weibull function fitted to data measured using chip W100_F7. As can be seen, the fit is quite good, presenting a $\chi^2/nDoF = 60/5$. Moreover, the results from two chips are consistent.

I also studied the chip behaviour with respect to flips from 0 to 1 and 1 to 0. Figure 6.19 shows the results obtained after dividing the SEUs from its flipping direction and after writing only zeros or random values. As can be seen, the minimum LET needed to create a SEU is lower if the bits flips from 1 to 0 than vice versa. Medipix3 designers told us that this is an expected behaviour due to the pixels architecture. The fitted parameters can be seen in Table 6.6. Note here that fits to cross-sections of partial data do not converge. This is the reason why some values present higher uncertainties than the fitted value. Also in this figure, the pink circles indicate the cross-sections measured when data written to the chip are only zeros. Cross-sections at LET = 10.2 MeV cm^2/mg are consistent with results from random values within uncertainties, but result at LET = 32.6 MeV cm^2/mg is clearly below of the random value. This cannot be explained as a statistical fluctuation and it points to that the cross-section of one particular bit depends also on the information stored in its neighbour bits.

Bonacini *et al.* [110] studied the SEU cross-section in chips formed by 130 nm standard library cells and SEU-robust cells registers. The results of this analysis can be seen in Figure 6.20. The irradiations were performed in the Heavy-ion Irradiation Facility (HIF) as in our measurement. They used only three ion species tilted at three and four different angles to obtain 10 LET points. The lowest LET measured by them was 3 MeV cm^2/mg.

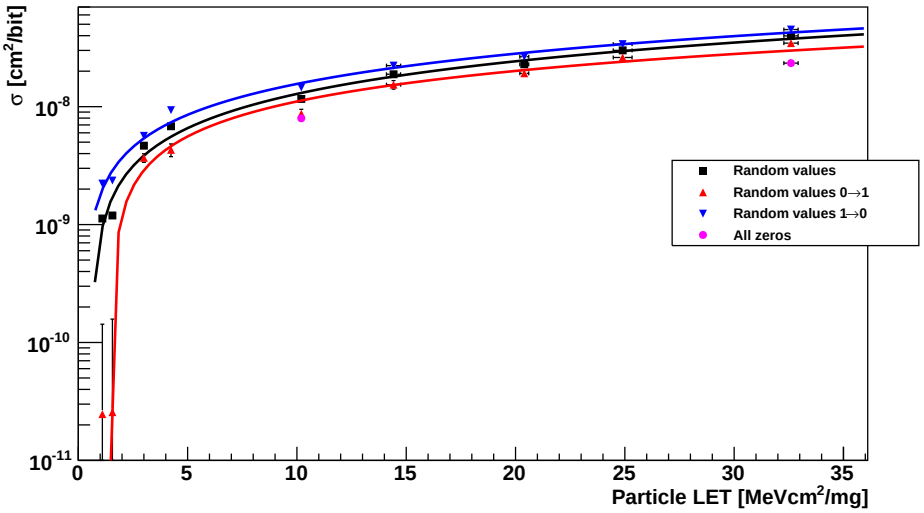

Figure 6.19: Pink circles represent the results obtained from runs where the pixels counters were written with only zeros. The other symbols represent runs where the written information was random. Blue triangles represent the SEUs flipping from 1 to 0. Red points are the result from bits changing from 0 to 1, and black points represent results from all SEUs. Blue, red and black lines represent the fits to the same colour data.

	SEUs 1→0	SEUs all	SEUs 1→0
χ^2/nDoF	38/5	60/5	24/5
σ_{sat} [cm^2]	$(0.39 \pm 1.1) \times 10^{-5}$	$(2.00 \pm 0.47) \times 10^{-6}$	$(2.4 \pm 6.1) \times 10^{-5}$
LET$_{\text{th}}$ [MeV cm^2/mg]	0.25 ± 0.15	0.586 ± 0.085	1.547 ± 0.038
W [MeV cm^2/mg]	$(0.68 \pm 2.3) \times 10^4$	$(26.9 \pm 8.2) \times 10^2$	$(2.0 \pm 6.0) \times 10^5$
S	0.843 ± 0.044	0.894 ± 0.031	0.763 ± 0.044

Table 6.6: SEUs fit results

This LET was higher than the LET$_{\text{th}}$ of the chip, so it could not be calculated. Hence, I cannot compare their result with the Medipix3 one. The value of σ_{sat} does can be compared, and it is lower in the Medipix3. I can conclude that the Medipix3 is a little bit more tolerant to single event upsets than the standard library register. This is the expected behaviour, since Medipix3 chip uses a smaller cell technology and it do not use any radiation tolerance design strategy.

6.6 Conclusions

Medipix3 Single Event Upset cross-sections were measured for different linear energy transfers. The tests were performed at the Heavy Ion Irradiation Facility (HIF) in the Cyclotron Resource Centre at Louvain-la-Neuve, Belgium. At the moment of planning these tests, they were of crucial importance for the VELO upgrade program since Medipix3 was the first chip built in 130 nm IBM technology. This technology was the one planned

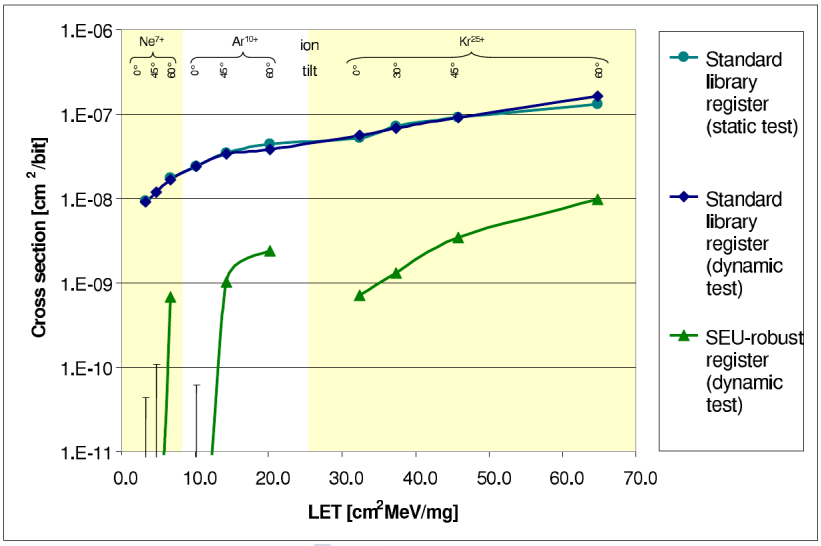

Figure 6.20: SEU cross-section *vs.* LET for two devices taken from [110].

to use in the VeloPix. At some point, the Medipix collaboration had to change the manufacturer company, so the SEU tolerance tests had to be repeated for the new technology.

The tests demonstrated that the Medipix3 architecture is more sensitive to SEUs flipping from 1 to 0 than from 0 to 1. Comparing the results with the ones obtained by Bonacini *et al.* [110] I can conclude that the Medipix3 chip is more tolerant to single event upsets than the standard library register. This is what was expected due to the smaller cell technology. Since it was not designed using any radiation tolerance technique, it is a good starting point for the VeloPix design.

7 Timepix3 telescope

The new VELO will be based in hybrid pixel detectors. They are a very interesting choice for the inner tracking regions of current and future particle detectors, as they provide high granularity, radiation hardness, ease of pattern recognition and high signal to noise ratio. The LHCb VELO group already employed hybrid pixel detectors for reconstruction of trajectories of high energy charged particles [111, 112]. The ASIC used was the Timepix. This chip could be configured in "Counter", "Time-of-Arrival" (ToA) or "Time-over-Threshold" (ToT) mode. The counter mode just count the number of hits per pixel. The ToA mode time stamps the moment of the particle hitting the pixel, and the ToT mode registers the interval while the charge deposited in the pixel is higher than a predefined level. This interval is proportional to the total deposited charge of the particle. The Timepix telescope was formed by eight planes in ToT mode that registered the position of the track traversing the telescope. The planes were rotated 9° in x and y axes to increase the cluster size. This permits to calculate the centre-of-gravity of the cluster and enhance the spatial accuracy of the telescope. The telescope also had one ninth plane at the end of the telescope configured in ToA mode. The aim of this last plane is to register the position of a track and its time stamp with an accuracy of 25 ns. The Timepix telescope also has two scintillators located at the front and the rear. These scintillators create the trigger signals when a coincidence between them is detected. A NIM crate was used to measure the trigger time stamp with an accuracy of $\sim$1 ns. Once the triggers are matched to the ToA of the tracks the final accuracy of the tracks is $\sim$1 ns. The telescope provides two places where to install the devices to test, one in the middle of the two planes and the other at the end of the telescope. At both locations the devices under test can be moved, rotated and cooled by a portable CO_2 cooling plant. At the central stage, the spacial accuracy achieved was 1.6 µm. Furthermore, bulky devices under test can be located behind the telescope at a cost of a lower spacial resolution. At 500 mm from the centre of the telescope a resolution of 8 µm is predicted.

The new Timepix3 telescope is based on the Timepix3 [113] ASIC. As its predecessor, the Timepix chip, it was built in 130 nm CMOS technology and it also contains 256×256 pixels of $55 \times 55\,\mu m^2$. In contrast to the Timepix, Timepix3 can operate in ToT and ToA modes simultaneously in each pixel. It provides a resolution of 1.5625 ns without the need of an external device. Its maximum particle rate is 40 MHits/(cm^2 s), and it can operate in data-driven mode, *i.e.* the chip sends data off the chip as fast as possible without external command. The charge collected on a pixel is integrated by a Charge Sensitive Amplifier (CSA) based on the Krummenacher architecture [114]. This preamplifier output return to zero is controlled with a bias current I_{Krum} which is sent globally to the pixels. The

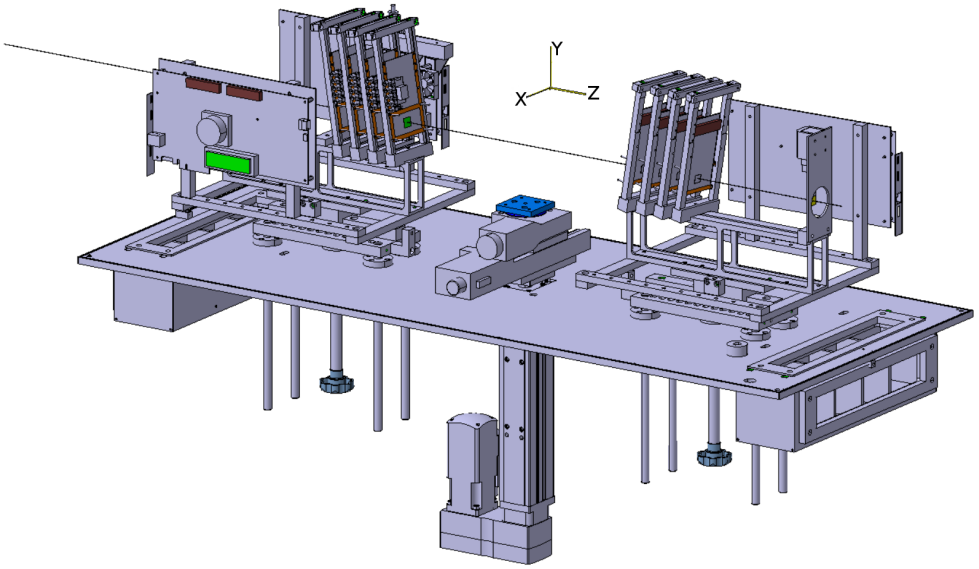

Figure 7.1: Schematic view of the Timepix3 telescope. It can be seen how the eight planes are located at both sides of the central stage. The plates located perpendicularly to the planes represent the SPIDR boards.

value of this current affects the count rate capabilities, and as a second order effect the gain of the chip.

The Timepix3 telescope consists in eight layers of 300 µm thick silicon pixel sensors bump bonded to Timepix3 chips.

7.1 Timepix3 telescope hardware description

The layout of the Timepix3 telescope is very similar to the Timepix one as it can be seen in Figure 7.1. It consists in two arms containing four planes each. Each plane is formed by a 300 µm thick *p*-on-*n* silicon sensor bump bonded to a Timepix3 chip. The width of the Timepix3 is ∼700 µm. The printed board circuit part behind the chip is removed to reduce the material budget. As in the Timepix telescope, the planes were rotated 9° in *x* and *y* axes to increase the cluster size and improve the spatial resolution. The cooling of the planes is achieved with pre-cooled air circulating inside of the telescope enclosure. A device under test (DUT) can be installed between the two arms or at the end of the telescope. The central position permits to move the device in the three axes and rotate it around the *y* axis. Furthermore, this location with a symmetric placement of the planes provides the best pointing resolution of ∼2 µm. The position at the rear of the telescope is thought for bulky devices that do not fit in the central position or that are less demanding in terms of pointing resolution. The telescope also provides two scintillators, one at the front and the other at the rear of the telescope. These scintillators create a trigger signal when a coincidence between them is detected. The scintillators are included to permit the integration of devices that need to be triggered. Timepix3 devices do not need them since they can work in data-driven mode.

7.2 Data acquisition

Data is read out from ASICs using the Speedy PIxel Detector Readout (SPIDR) system [115]. This system is based on a field-programmable gate array (FPGA) running a soft-core processor. A soft-core processor is a microprocessor core that can be wholly implemented using logic synthesis. The Timepix3 telescope utilises a SPIDR prototype which uses a Xilinx VC707 evaluation board. The chip can send out up to 80 MHits/s. The SPIDR is designed to read out Timepix3 and Medipix3 chips at their maximum rate. The load of a SPIDR system reading out a single Timepix3 at maximum rate is about 55%. In the typical telescope configuration using 8 planes, each SPIDR board reads two planes. When a high particle rate is expected each plane is connected to one SPIDR board.

SPIDR handles data using three different channels: the slow control to and from the board via TCP/IP, the full data stream from SPIDR to computer via UDP, and the monitoring data stream from SPIDR to computer via UDP. The monitoring stream is just a copy of a fraction of the full data stream that can be used for online monitoring of the system. The copied fraction is a slice of the data that is synchronised across the different SPIDR boards.

The synchronisation of the telescope SPIDR boards is performed by the Telescope Logic Unit (TLU). The firmware of this trigger unit was developed by the author of this thesis. This unit provides a common reference clock of 40 MHz to the boards. Furthermore, it also distributes a T0-Signal that synchronise all time counters and the shutter signal. The TLU can use its internal clock as reference or it can use one provided externally. Moreover, the T0-Signal can also be supplied by an external source. The aim of a common shutter signal generated by the TLU is to synchronise the start and stop of the data flow. This shutter must be always active when taking data. Each SPIDR board can send a *busy* signal to the TLU. If any of the boards issue a *busy* signal, the TLU closes the shutter and the data taking is paused. When all *busy* signals recover the low level, the data taking is resumed automatically. The commands from the computer to the TLU are sent via UDP using the IPbus protocol [116].

The TLU is composed by three elements: a Xilinx Spartan 601 evaluation board, a mother board and up to 5 daughter boards. The evaluation board consists of a Spartan 601 FPGA connected to many peripheral devices. It is the computational core of the unit. The board can receive commands from a desktop pc via UDP using the IPbus protocol. Using these commands the length of the T0-Synch signal can be modified and individual inputs and outputs can be disabled. Furthermore, the T0-Synch signal can be issued. Combining the information received from the mother board and from the PC the FPGA generates the telescope control signals. The mother board contains three two-pole LEMO connectors from where it can receive an external clock or an external T0-Synch signal. It also has five 64 DIN connectors to plug up to 5 daughter boards. Each of the daughter boards consists of 6 HDMI connectors where the cables from the telescope are plugged in. The boards carry the LVDS signals from the HDMI connectors to the 64 DIN connector of the mother board. A picture of the TLU is shown in Figure 7.2. The telescope components can be distinguished in Figure 7.3.

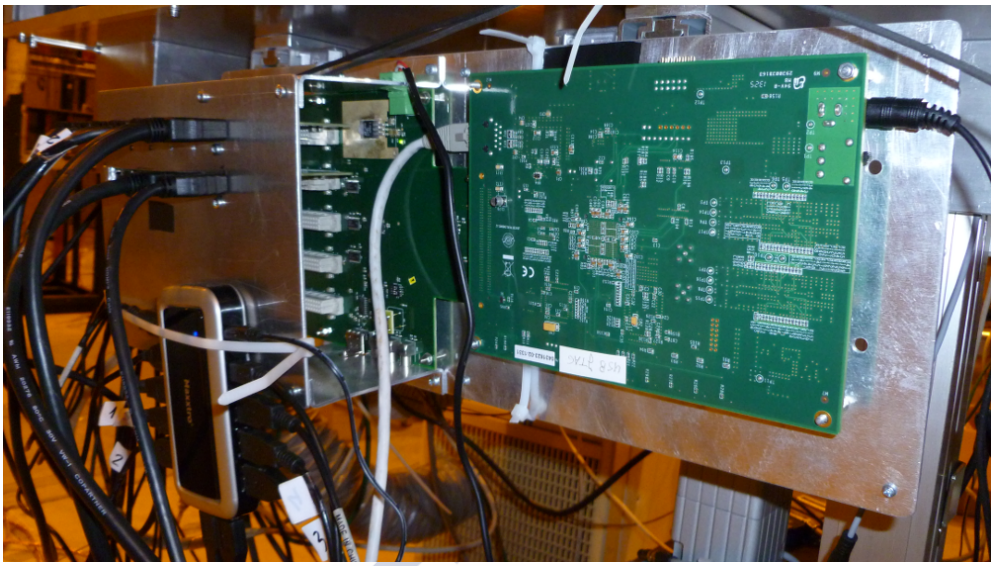

Figure 7.2: Picture of the Timepix3 telescope TLU installed in the telescope.

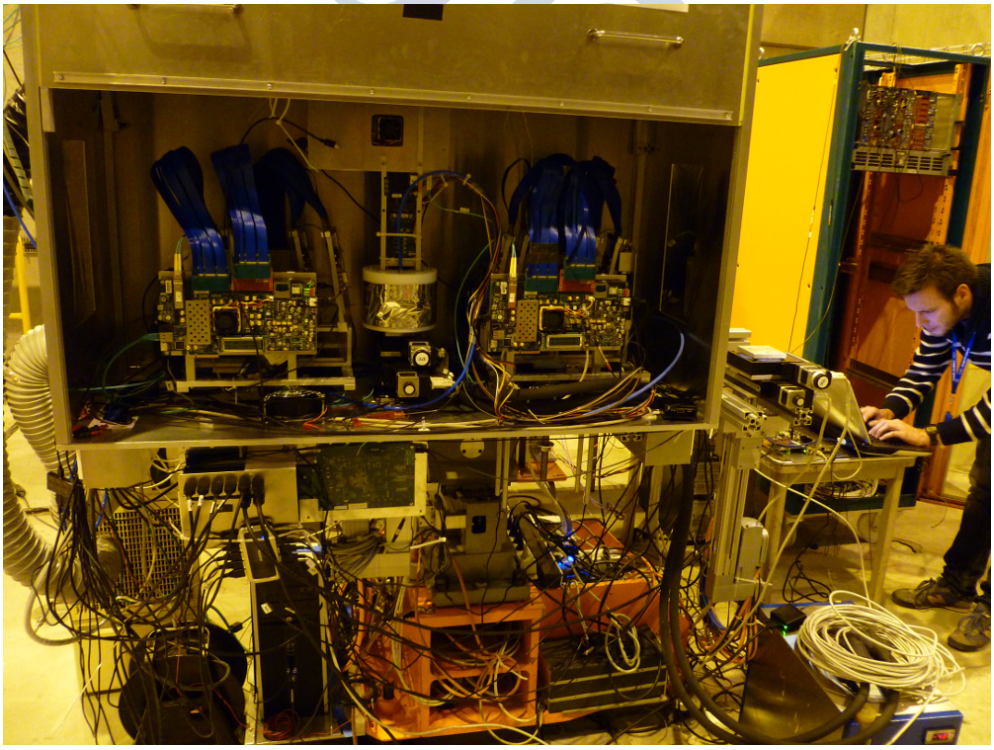

Figure 7.3: Picture of the Timepix3 telescope. Inside the telescope box can be seen the DUT in the middle of the telescope. Two SPIDR boards and the four planes per arm are behind the two visible SPIDR boards. The telescope TLU is located below the enclosure. The $C0_2$ portable plant can be seen in the bottom right corner of the figure.

7.3 Offline reconstruction software

The software used for the offline analysis is called "Kepler", after the German Astronomer Johannes Kepler. It is based on the Gaudi [58] framework. This software permits the alignment, calibration, track fit and also the data analysis.

The Gaudi based projects are designed to work with data from colliders, where the bunch crossing defines the event length. In the beam test area, the SPS provides beam spills of about 9 s length. Furthermore, the Timepix3 telescope runs in data-driven mode, so it can uninterruptedly acquire data from a spill. In this situation, the amount of data is too high that it is not practical to treat it as one unique event. Kepler slices these data in parts with configurable length and each slice is processed individually. The typical event length is 400 µm.

Kepler works as a sequence of different algorithms. The first one decodes the raw data files from each plane. Pixel hits are not organised chronologically, so the software needs to read the whole data to create an event. Then it creates pixel hit objects where the time stamp, the column and row and the ToT are saved. Moreover, if the calibration constants are available, it also calculates and stores the hit charge.

The next algorithm in the queue groups the neighbouring hits within a time window of 100 ns into clusters. The cluster position is calculated as the charge-weighted centre-of-gravity of the group of pixels. The time stamp of the earliest pixel is taken as the cluster time stamp.

The track reconstruction is performed by a seed method. Track seeds are created by pairs of clusters not tagged as part of a track, located in adjacent planes and separated in time less than 10 ns. The seed track is extrapolated to the next downstream plane and the closest hit in time and inside the configured spatial window is included as part of the track. This process is repeated until all planes are included in the search. If the candidate track has the same or more than the configured minimum number of clusters, the track is accepted and a straight line fit is performed. The track time stamp is calculated as the average time stamp of the clusters belonging to the track.

Finally the software produces a Root [59] file with histograms and, if requested, ntuples for further analysis.

7.3.1 Alignment

The alignment of the telescope planes is performed using the Millipede algorithm [117]. The main advantage of this method is the simultaneous fit of both the track states and the geometry. The algorithm is run iteratively with progressively more restrictive selections on the tracks used. The telescope planes are aligned by minimising the average distance between clusters and the expected position of the corresponding track.

There is a small misalignment between the planes because of the different cable lengths. This is calibrated by minimising the variance in the track time with a set of constant offsets. This is equivalent to subtracting the mean of the biased track time residuals. The offsets are measured for all runs and were found to be consistent with each other within a spread of $\sim$15 ps.

After the alignment, a pixel check can be made in order to look for noisy pixels. These pixels are masked to avoid them to be used by the reconstruction algorithm. Furthermore, the clusters containing masked pixels are not going to be used in the tracking process.

Figure 7.4: Photo of the VELO LHCb experimental box in the CERN north area experimental hall.

7.4 Experimental area

Many facilities exist around the world that provide particle beams with different characteristics and allow to study in-beam detector performance. At CERN there are two experimental areas of this type: East area and North area [40]. East area receives the beam from PS (*Proton Synchrotron*). The maximum energy of the beam is 15 GeV and it has four different outputs. On the other hand, the North area receives the beam from the SPS (*Super Proton Synchrotron*). The SPS can provide beams composed of p, π or Pb nucleus. The particle momentum can be configured between 10 and 400 GeV/c, depending on the particle type and the intensity.

The VELO LHCb group performs its tests in a box fed by the H8 line of the SPS. This area is shown in Figure 7.4. The particle beam is composed by charged hadrons (primarily pions) with a momentum of 180 GeV/c. The particles arrive to the experimental area in spills of $\sim$9 s, with a frequency of about 47 s. This frequency depends on the the number of lines that the accelerator must feed.

7.5 Dataset

Data were taken in the north experimental area at CERN. Opening and closing some collimators the particle beam received in the experimental hall can be customised. Table 7.1 shows the runs taken during the high rate special runs and their characteristics. The column "Rate" indicates the incident particle rate measured by the multiwire detectors at the entrance of the test area. The beam particle rate is controlled by a set of collimators located upstream the experimental area. Opening the collimators window increases the particle rate and vice versa. As indicated in the table, the first run was configured in a typical low particle rate beam configuration. In each of the following runs we only modi-

fied one collimator with respect to the previous run. The "Data status" column indicates the problems that appeared during the data taking. Runs 2176 and 2181 were tagged as bad and they are not used in the analysis. Last three runs were taken using the same collimators configuration. The difference between them is that the DAQ buffer size was increased in run 2185 and 2186. Furthermore, in run 2186 the so-called *Krummenacher* current (I_{Krum}) of the Timepix3 chips was increased to a configuration value of 20.

Run	Rate [part/spill]	Comments	Data status
2172	7.0e5	Collimator 0 = +/-10	ok
2173	1.1e6	Collimator 064 = +/-22	ok
2174	1.1e6	Collimator 128 = +/-25	ok
2175	1.5e6	Collimator 185 = +/-25	ok
2176	2.0e6	Collimator 202 = +/-25	Track eff extremely low
2177	2.3e6	Collimator 203 = +/-25	ok
2178	7.8e6	Collimator 407 = +/-8	ok
2179	2.2e7	Collimator 407 = +/-9	ok
2180	2.6e7	Collimator 407 = +/-10	ok
2181	2.5e7	Collimator 407 = +/-11	Bad run
2182	2.5e7	Collimator 407 = +/-11	ok
2183	2.3e7	Collimator 407 = +/-12	ok
2184	2.3e7	Collimator 407 = +/-20	ok
2185	2.3e7	Large DAQ buffer	ok
2186	2.5e7	Large DAQ buffer. I_{Krum}=20	ok

Table 7.1: Properties of runs acquired during the high rate data taking. Data status column indicates the problems that appeared while data taking.

Figure 7.5 shows the average particle rate per run measured using two different methods. Using the multiwire detectors at the entrance of the experimental area we obtained the rates drawn in blue squares. The uncertainty associated to these values is 10%. Red circles represent the average particle rate measured using the number of clusters detected in the first telescope plane. The error bars are smaller than the mark size. None of these values is valid as a estimation of the particle rate received by the telescope. The multiwire measurement indicates the number of beam particles but since the beam is not necessary aligned to the telescope, a fraction of the particles will not be detected. On the other hand, not all particles detected by one telescope plane are in the telescope fiducial area, so many of them cannot be reconstructed. In fact, as it can be seen in Figures 7.6 and 7.7, at low particle rates the beam spot fits inside the first plane, but at high rates it goes outside of the telescope active area. Moreover, some particles will decay inside the telescope material and generate new clusters and δ particles will create huge clusters that usually the reconstruction software breaks and process as many independent clusters. Thus, this plot is only valid as a estimation of the available particle rate.

Figure 7.5 shows that the maximum particle rate is achieved in run 2180. In this run the collimators allowed passage of the full-size beam, so we achieved the highest intensity that the SPS can provide. The rate fluctuations in the next runs are due to the beam instability. It is also interesting to note that it was not possible to maintain this beam intensity too long, since the facility radiation alarms get triggered and dumped the beam.

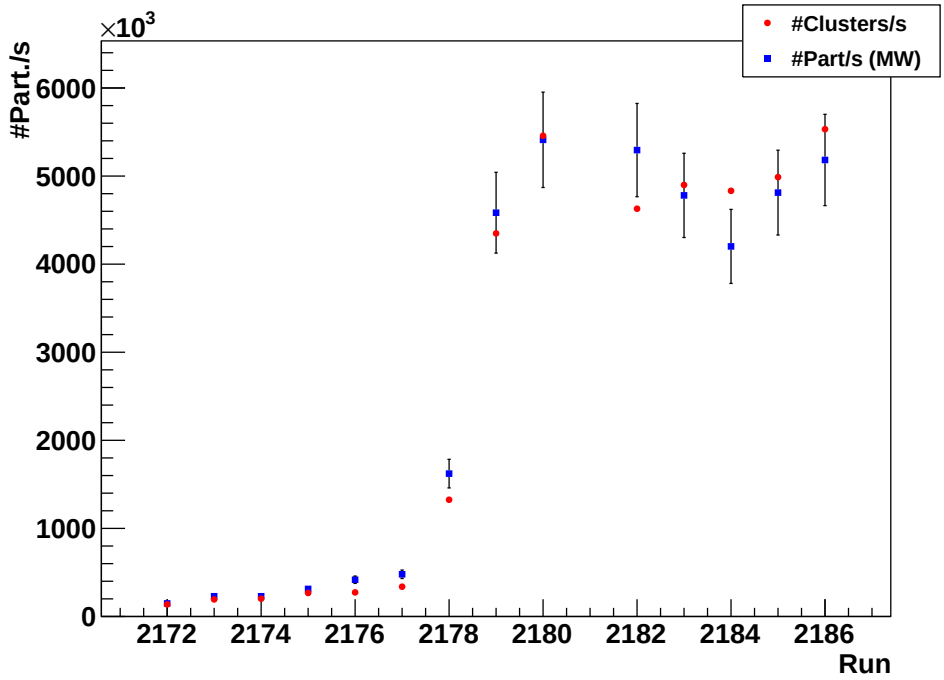

Figure 7.5: Average particle rate per run. Blue squares represent the rate measured by the beam multiwire detectors and red dots represent the rates measured from the clusters found in the first telescope plane.

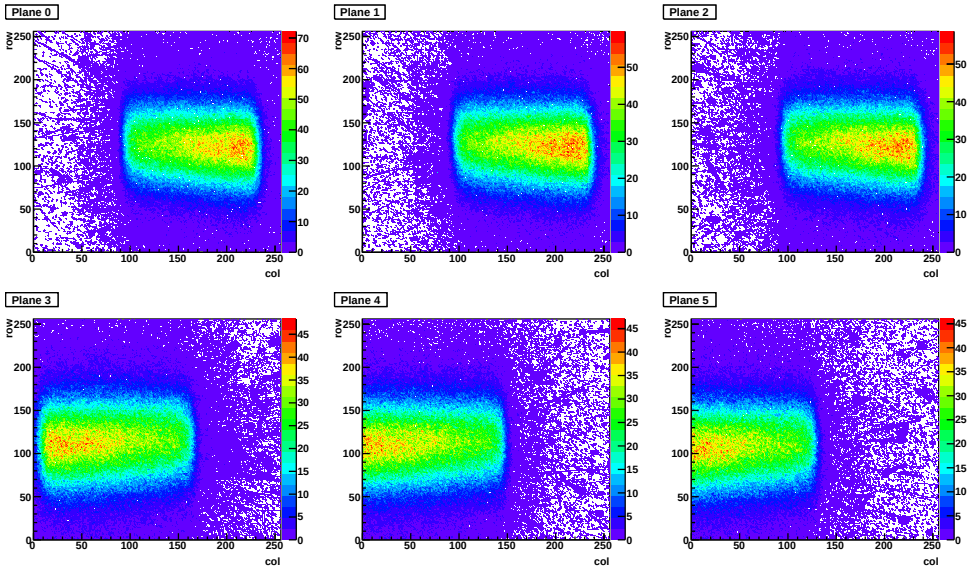

Figure 7.6: Beam spot position in the six telescope planes for run 2172. The beam goes outside of the sensitive are in planes 4 and 5.

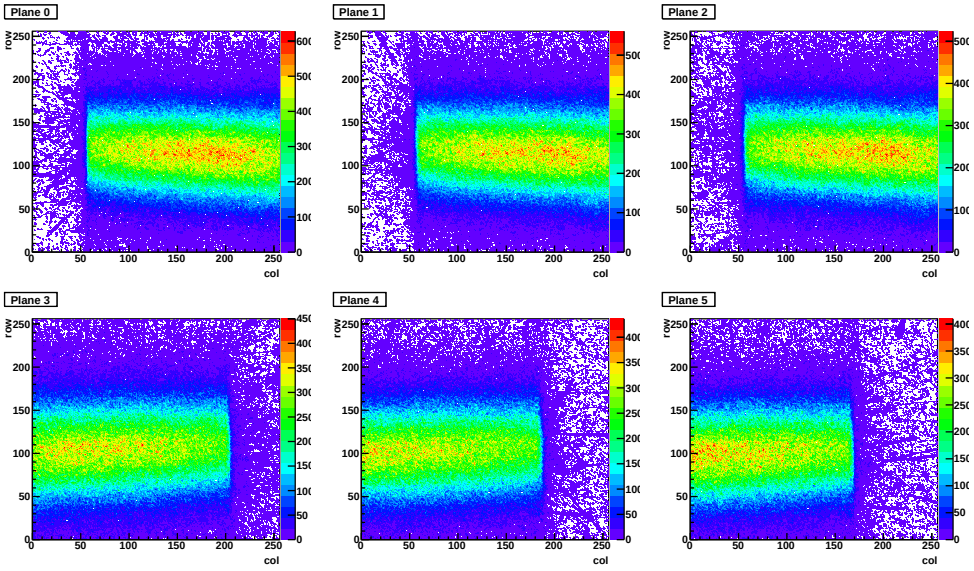

Figure 7.7: Beam spot position in the six telescope planes for run 2183. The beam does not fit inside the acceptance of any plane due to its wide shape.

These alarms are triggered after detecting a fluence higher than a certain value in the last minutes. This means that we can configure the beam to work at the highest intensity and take data for one or two minutes, but then we need to wait at least for other two minutes to start over.

7.6 Data analysis

In order to study the Timepix3 telescope performance with respect to the particle rate I are going to analyse three different parameters. The cluster charge collected by each plane of the telescope is the first variable to study. The average sustainable hit rate in ToA/ToT mode per pixel is $\sim$1.2 kHz. The maximum pixel rate achieved in the tests was about 0.1 kHz, so I do not expect to see any effect in the telescope clustering. If the rate would be comparable to the limit we could find clusters with a larger ToT due to the overlap of two or more clusters. The second study is the quality of the reconstructed tracks. If the particle rate is too high the reconstruction software can create fake tracks. These tracks should have a worse χ^2/nDoF than the actual reconstructed tracks. Finally, I can estimate the telescope tracking efficiency with respect to the particle rate. As it was mentioned before, it is impossible to know the number of particles that traverse the telescope and that are likely to be reconstructed. The most accurate method to estimate the efficiency is to measure the fraction of associated and non associated clusters to the tracks. In the case that all particles hitting one telescope plane traverse the whole telescope through its acceptance and no secondary tracks would be created, the fraction of associated clusters in one plane with respect to the total number of tracks would coincide with the telescope efficiency. I am going to call this fraction as "cluster finding efficiency", since it represents the probability of a track to find a cluster in a plane. Since not all particles are reconstructed in the telescope I calculate the fraction of non associated clusters with respect to the total number of clusters in each plane. Furthermore, the fraction of non

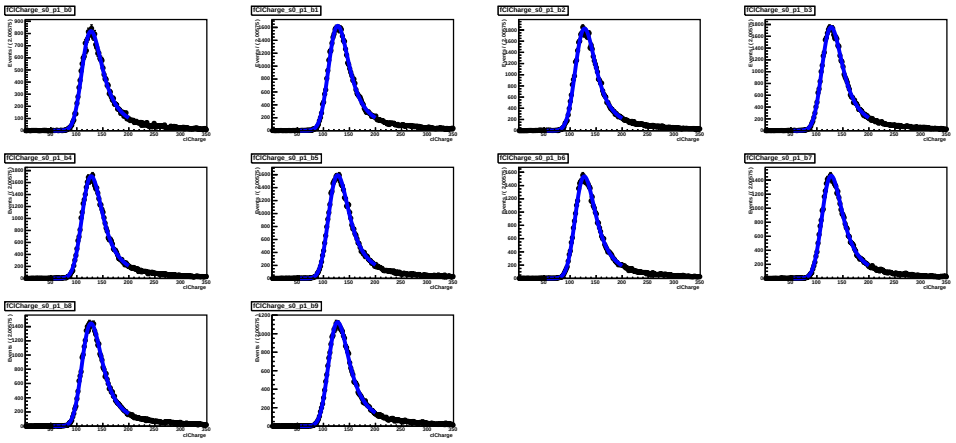

Figure 7.8: Example of ToT distributions of plane 1 in run 2172. Each plot represents an interval of 0.5 s of one spill. Black points represent the ToT measured and blue lines represent the Landau convoluted with a Gaussian fit to data.

associated clusters is less sensitive to the masked pixels than the cluster finding efficiency, as will be explained later. This measurement will provide us an idea of the number of non reconstructed tracks.

The ToT value given by the Timepix3 is proportional to the collected charge. To study the ToT behaviour during the spill, I divide the spill in intervals of 0.5 s and fit a Landau [118] convoluted with a Gaussian to the ToT distribution. An example of the distribution and fits can be seen in Figure 7.8.

The the most probable value (MPV) and the full with at half maximum (FWHM) of the Landau distributions are compared to analyse the behaviour of the planes in the different runs. Figure 7.9 shows the MPVs per plane and for the different runs but run 2186. This run was eliminated from the plot to permit a better view of the rest of the runs since it has a different I_{Krum} configuration and its MPV is systematically lower than the other runs. The first three planes present a higher MPV of the ToT in the low rate runs than in the high rate ones. On the other hand, the last three planes measured a higher MPV ToT in the high rate than in the low rate runs. These differences are small and can be caused by small differences in the DACs configuration. In Figure 7.10 is presented the MPV of the Landau fit for each plane in run 2180. The difference between planes is quite high, and it is due to different equalisations. After a calibration we should see the same charge MPV for every telescope plane. It is important to note that the calibration is not important since I want to study the variations of a chip performance with the track rate. The conclusion is that no ToT variations can be appreciated in each telescope plane with respect to the particle rate.

The FWHM of the Landau distributions is plotted in Figure 7.11. No differences can be appreciated between low and high rate runs. Figure 7.12 shows the FWHM of the Landau fits for the telescope planes. As in the MPV, it can be seen that the Landau FWHM is constant along the spill.

At high rates the quality of the tracks can be compromised. As a quality estimator of the tracks I am going to use the χ^2/nDoF of the tracks. In this case the tracks are required to have one associated cluster in each telescope plane. Clusters containing

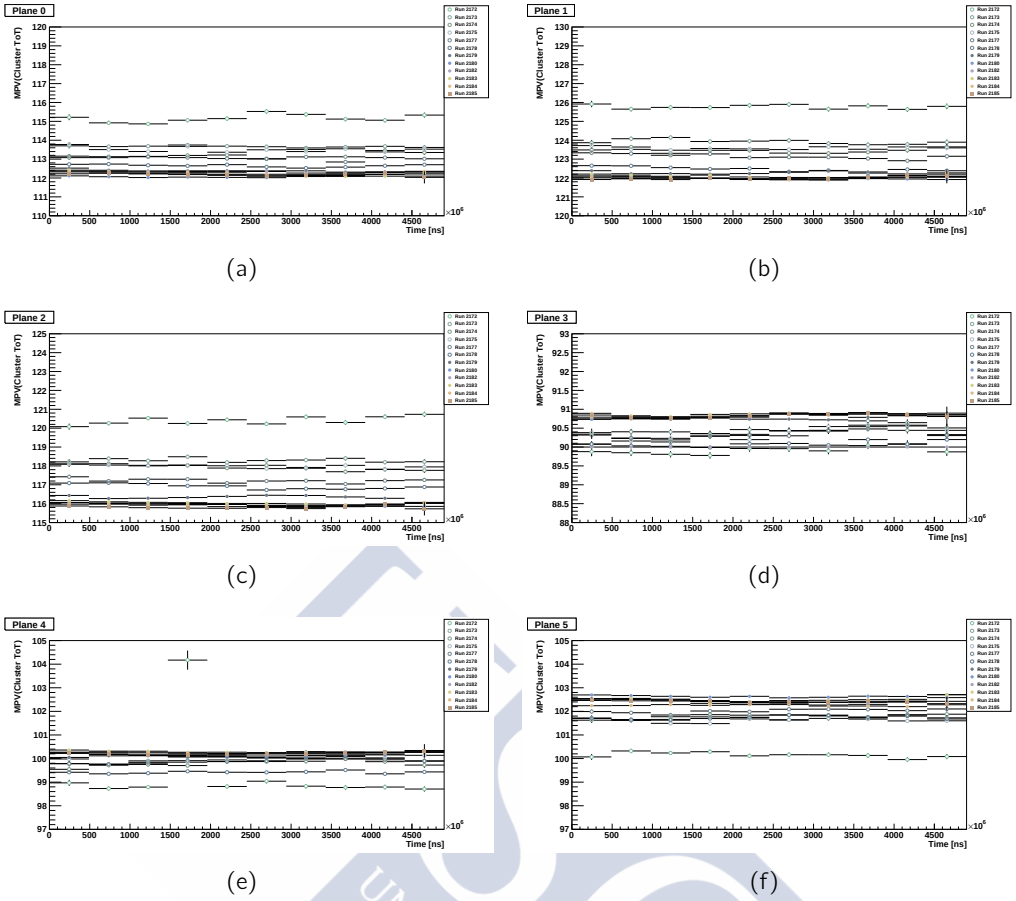

Figure 7.9: Plots of the Landau MPV fitted to the ToT distributions of each telescope plane. Each bin represents intervals of 0.5 sec in one spill. Empty circles represent low rate runs, from 2172 to 2178. Full circles represent high rate runs, from 2179 to 2184. Full squares represent data from run 2185, that was a special run with a larger DAQ buffer. Plots from (a) to (f) represent telescope planes from 0 to 5 respectively.

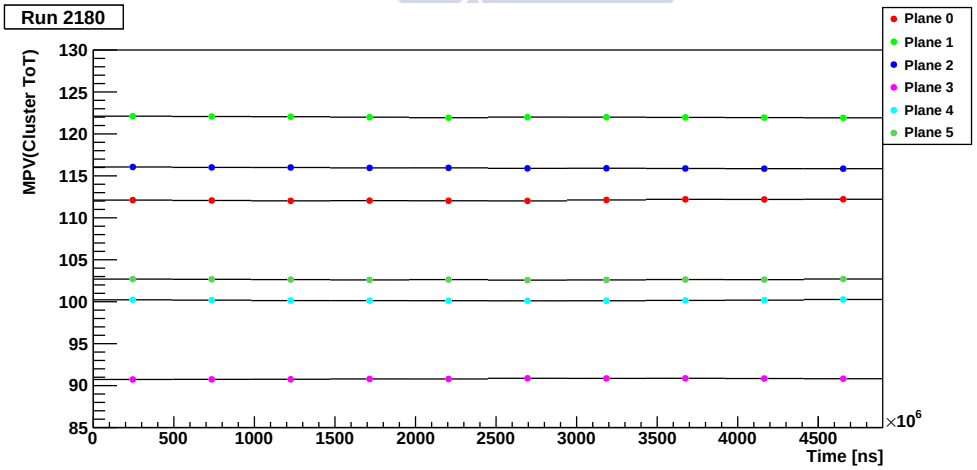

Figure 7.10: MPV of the Landau fit for every telescope plane in run 2180.

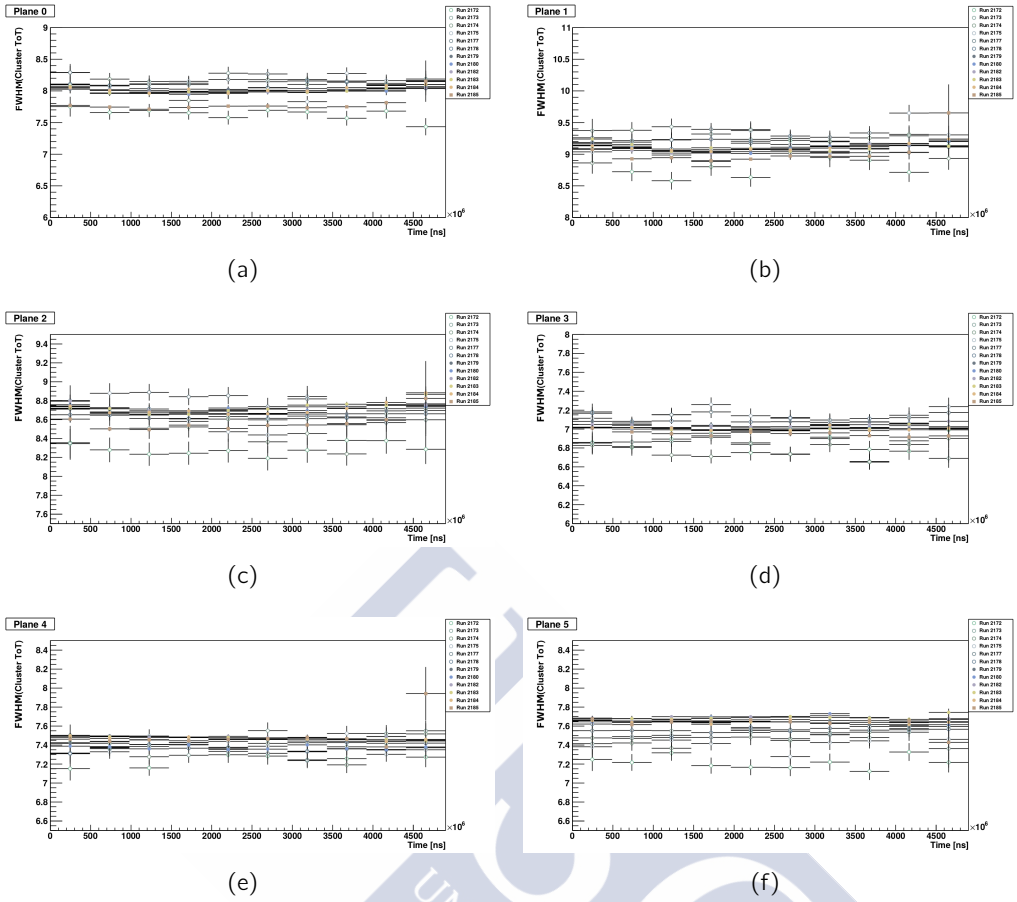

Figure 7.11: Plots of the Landau FWHM fitted to the ToT distributions of each telescope plane. Each bin represents intervals of 0.5 sec in one spill. Empty circles represent low rate runs, from 2172 to 2178. Full circles represent high rate runs, from 2179 to 2184. Full square represent data from run 2185, that was a special run with a larger DAQ buffer. Plots from (a) to (f) represent telescope planes from 0 to 5 respectively.

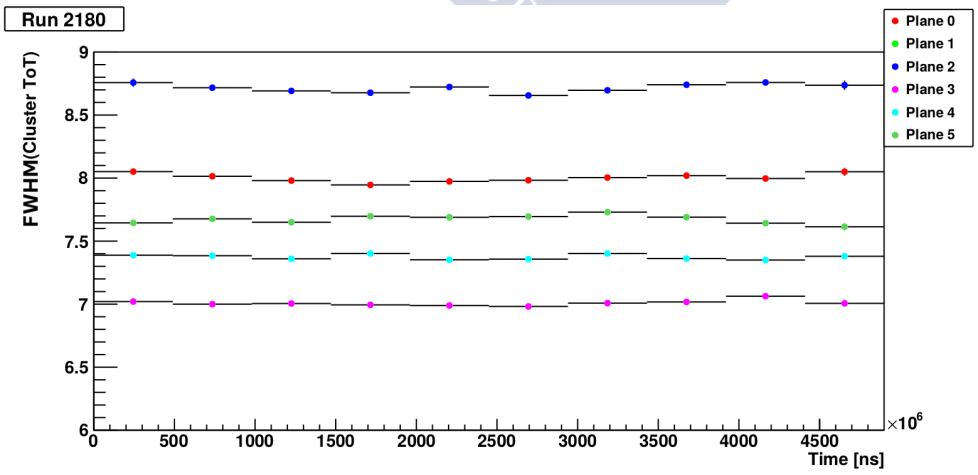

Figure 7.12: FWHM of the Landau fit for every telescope plane in run 2180.

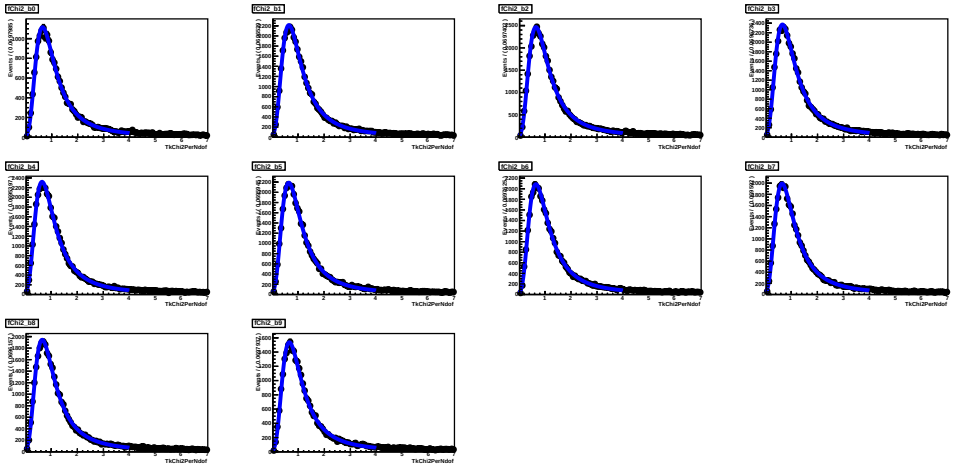

Figure 7.13: Example of χ^2/nDoF distributions of tracks in run 2172. Each plot represents an interval of 0.5 s of one spill. Black points represent the χ^2/nDoF measured and the blue lines represent the Landau fit to data.

masked pixels are vetoed, and tracks intercepting a cluster that contains a masked pixel are removed from the analysis. I fit a Landau to the χ^2/nDoF distribution and then compare the resulting MPVs. Figure 7.13 shows the χ^2/nDoF distributions of tracks reconstructed in intervals of 0.5 s in a spill of run 2172 and the Landau fits to them.

Figures 7.14 and 7.15 show the MPV and FWHM of the Landau fitted to the χ^2/nDoF distributions of the tracks of all runs. The MPVs differences between runs are small and negligible compared to FWHM. Furthermore the MPVs are independent of the incident particle rate and no trends are visible inside each run. This means that the telescope is capable of reconstructing tracks at its best quality independently of the particle rate and at least during the 9 s of the SPS particle spill.

The study of the telescope efficiency will be performed through the study of the cluster finding efficiency and the fraction of non associated tracks. The beam spot does not fit completely inside the telescope acceptance so a fiducial region will be defined. This fiducial window is defined as the region between $3\,\text{mm} < x < 11\,\text{mm}$ and $0.5\,\text{mm} < y < 12.3\,\text{mm}$ in the global telescope coordinates. Outside of this region tracks cannot be reconstructed or the efficiencies are very low. As in the χ^2/nDoF analysis, the clusters containing a masked pixel are vetoed and the tracks intercepting a cluster that includes a masked pixel are removed from the analysis. To calculate the cluster finding efficiency I am going to use 5 out of the 6 telescope planes as a partial telescope and the plane left as a device under test. The tracks are reconstructed using the 5 telescope planes and then I look for a cluster inside a time (ΔT) and a spacial (Δr) window around the interception between the track and the plane left. If a cluster is found the cluster is tagged as "associated" and cannot be used in another track. The cluster finding efficiency is defined as

$$\text{Cluster finding eff.} = \frac{\text{Number of associated clusters}}{\text{Number of tracks}}. \tag{7.1}$$

Note that this efficiency is very dependent on the number of masked pixels in each plane, so I cannot expect a common value for every plane. This is not an issue here, since the aim of this analysis is to study the dependence of the efficiency with respect to the track

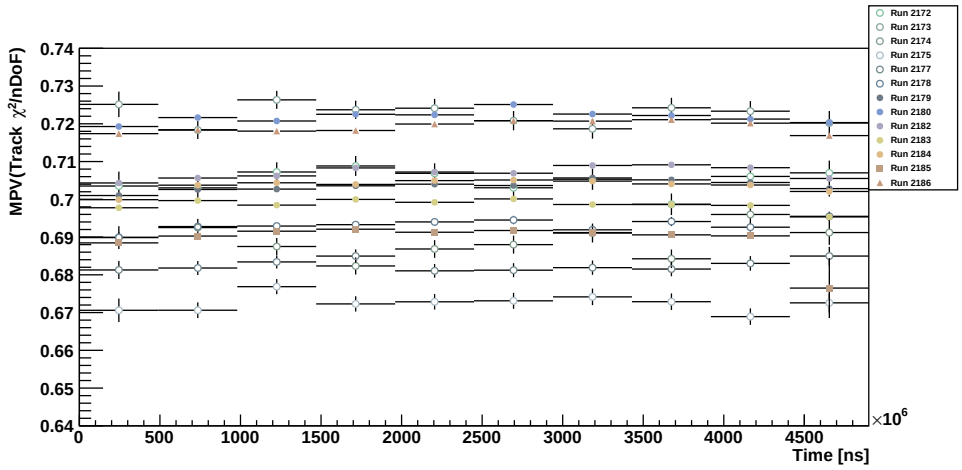

Figure 7.14: MPV of the χ^2/nDoF distributions of the tracks reconstructed in the different runs.

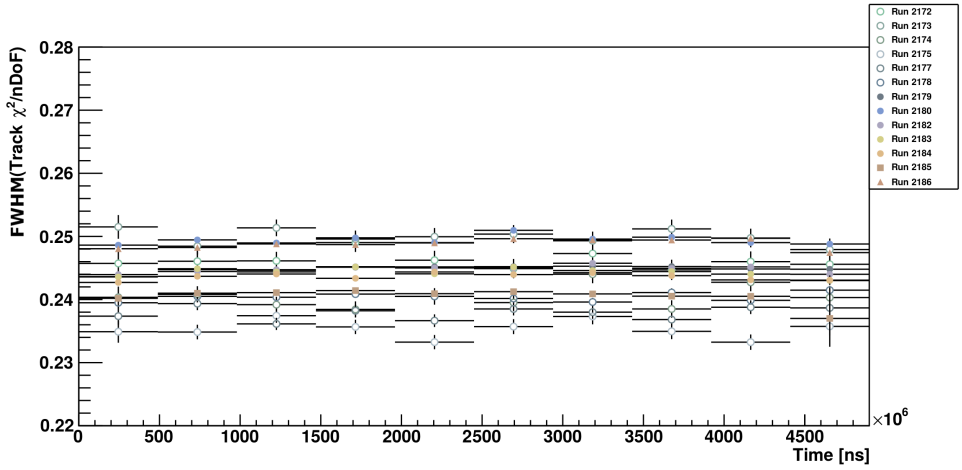

Figure 7.15: FWHM of the χ^2/nDoF distributions of tracks reconstructed in the different runs.

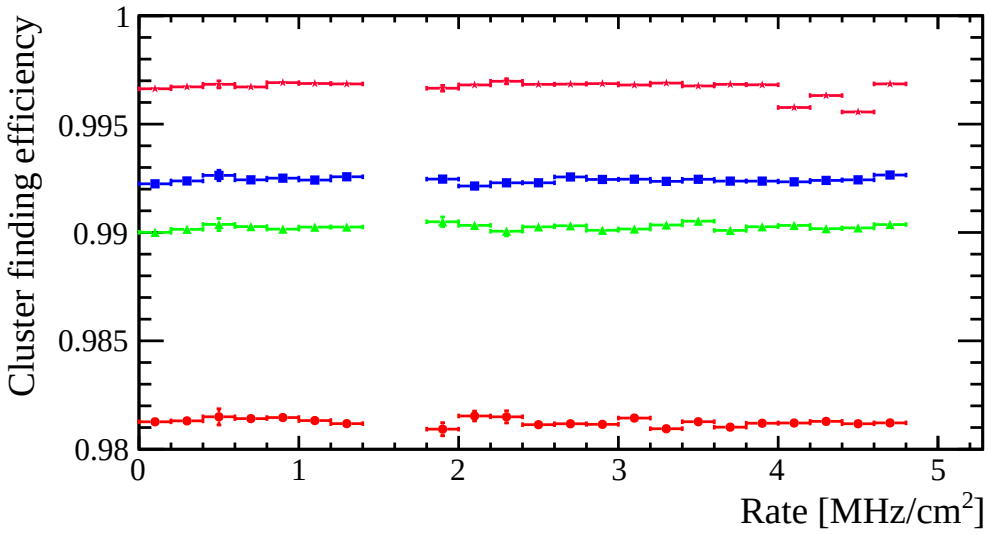

Figure 7.16: Cluster finding efficiency *vs.* track rate of the four internal planes of the telescope. Red, blue, green and pink points represent the efficiencies of the second, third, fourth and fifth planes respectively.

rate. I am looking for trends in the cluster finding efficiency *vs.* track rate plots, and this is independent of the masked pixels. Figure 7.16 shows the results of the cluster finding efficiency measured. No decreasing trends are appreciated in any plane up to the highest particle rate.

The fraction of non associated clusters is a good estimator of the telescope inefficiency. Non associated clusters are due to primary non reconstructed particles, secondary particles created after a particle interaction with a telescope plane or broken clusters. Secondary tracks are removed applying a cut on the maximum cluster occupancy per plane in a time interval. If more than a selected number of clusters are detected in one plane in coincidence all these clusters and the tracks are removed from the analysis. The fraction of non associated clusters is calculated as

$$\mathrm{Fr}_{\text{Non associated clusters}} = \frac{\text{Number of non associated clusters}}{\text{Number of clusters}}. \tag{7.2}$$

Finally, the track rate is calculated as

$$\text{Track Rate/area} = \frac{\text{Number of reconstructed tracks}}{\text{Time interval} \times \text{Fiducial area}}. \tag{7.3}$$

The time interval used in all cases is 0.2 s. Figure 7.17 shows the fraction of non associated clusters in the four inner planes *vs.* track rate and for three different data sets. Green triangles represent the results using the high rate dedicated runs indicated in Table 7.1. In these runs the telescope was configured using 6 planes read out each of them by one SPIDR board. The fraction of non associated clusters measured is constant up to the maximum rate, so the tracking system performance does not lose efficiency at least up to 5 MHz/ cm^2. In run 2115 the beam was accidentally configured as high rate. The telescope configuration in this run consisted in 8 planes read out by 4 SPIDR boards. Each SPIDR reads out 2 telescope planes. These data is plotted in red full circles in the

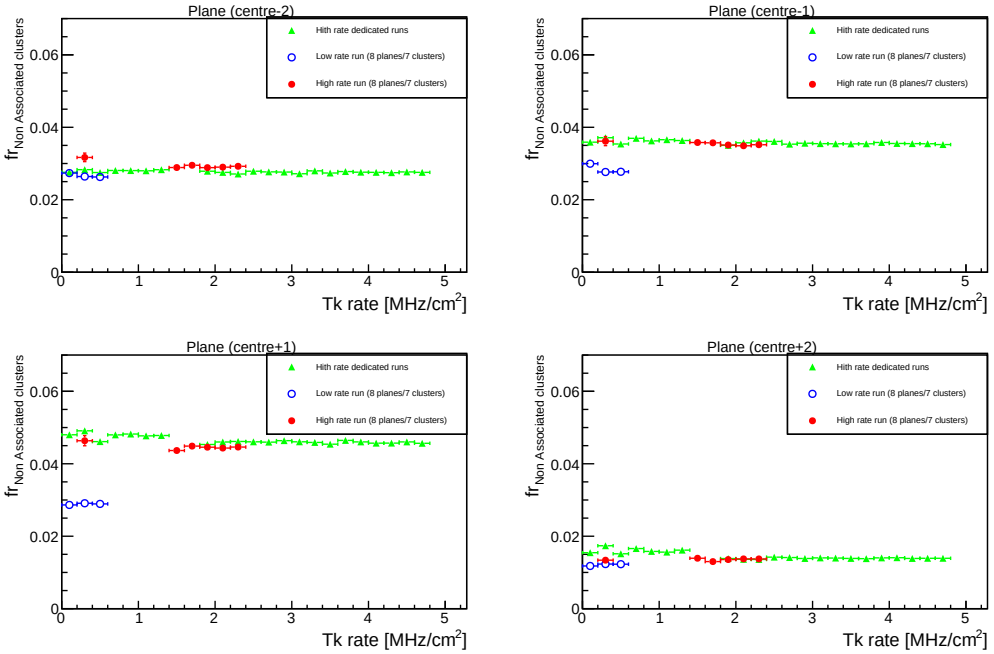

Figure 7.17: Fraction of non associated clusters in the four inner planes of the telescope *vs.* reconstructed track rate. Green triangles represent data taken during the high rate dedicated runs indicated in Table 7.1. Red circles are the results from run 2115. This is a regular run when by mistake the beam was configured in high rate mode. Blue empty circles show the results from run 9110, that is a typical low rate run. In these last two samples, the telescope was composed by 8 planes, and every two planes were readout by one SPIDR board.

figure. As in the high rate dedicated runs I only plot the inner planes, that in this case are the third, fourth, fifth and sixth planes. As in the previous case, I do not observe any decreasing trend. This means that at least up to 2.5 MHz/ cm^2 the telescope can be operated using 8 planes without efficiency lost. Blue empty circles represent data from run 9110. This is a regular low rate run and was included in the plot as a reference. The telescope configuration was 8 planes read out by 4 SPIDR boards. Furthermore, there was a DUT installed that was masked for this analysis.

This measurement is dependent on the fiducial area selected. On one hand, the expected number of non associated clusters decreases when reducing the fiducial area. Multiple clusters created by δ particles or by secondary tracks, that of course are not associated to tracks, are less likely to be included in the analysis if the window is narrower. Reducing the fiducial window only a small fraction of them are selected, and the fraction of non associated clusters decreases. These effect can be seen in Figure 7.18. On the other hand, since the particle beam is not uniform, selecting the maximum rate region I obtain a higher average rate. As in the cluster finding efficiency results, I do not see any trend in the fraction of non associated clusters with respect to the particle rate. So, I can conclude that the telescope is capable of reconstructing tracks without loosing efficiency at particle rates up to 5 MHz/ cm^2. This also means that the Timepix3 telescope can efficiently reconstruct all particles provided by the SPS accelerator at CERN when working at the highest intensity.

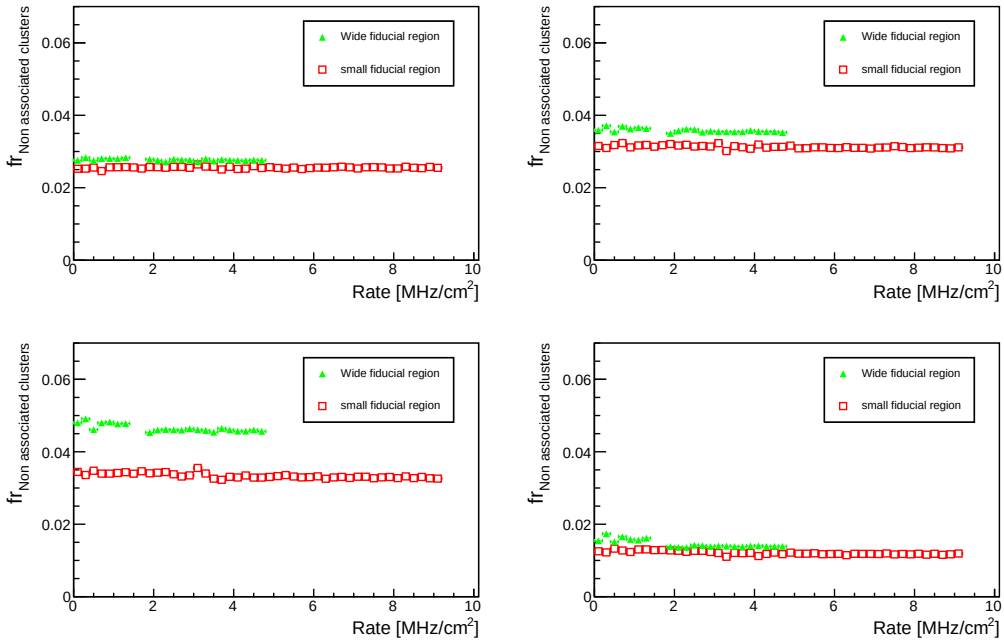

Figure 7.18: Fraction of non associated clusters in the four inner planes of the telescope *vs.* reconstructed track rate. Green triangles represent the results using the fiducial window indicated above: $3 < x < 11$ and $0.5 < y < 12.3$. Red squares represent results using a smaller window $3 < x < 9$ and $4 < y < 10$.

7.7 Conclusions

A new tracking telescope based on Timepix3 chips was built to characterize new sensors and chips for the LHCb upgrade. This Timepix3 telescope was performing with efficiencies higher than 99% at rates comparable to the ones used with its predecessor the Timepix telescope. In order to study the full capacity of the telescope we arranged a test using the highest particle intensity provided by the SPS accelerator at CERN. We changed the telescope configuration from its typical 8 planes read out by 4 SPIDR boards to 6 planes read out each of them by one dedicated SPIDR board. The results show that the telescope performance keeps constant up to the highest particle rates sent by the SPS. Furthermore, one run was measured using the 8 planes configuration and at high particle rate. Also in this case, no efficiency loss is observed.

USC
UNIVERSIDADE
DE SANTIAGO
DE COMPOSTELA

8 Conclusions

In this thesis three main goals were achieved. First, using the LHCb detector the proton-proton cross-sections at a centre-of-mass energies of $\sqrt{s} = 5\,\text{TeV}$ and $\sqrt{s} = 13\,\text{TeV}$ were measured. The result obtained at $\sqrt{s} = 5\,\text{TeV}$ inside the LHCb acceptance is

$$\sigma^{acc} = 56.88 \pm 0.02(stat) \pm 2.12(syst)\,\text{mb}.$$

Regarding the $\sqrt{s} = 13\,\text{TeV}$ sample, the cross-sections obtained are

$$\sigma^{acc}_{MU} = 60.93 \pm 0.17(stat) \pm 2.51(syst)\,\text{mb},$$
$$\sigma^{acc}_{MD} = 61.31 \pm 0.18(stat) \pm 2.38(syst)\,\text{mb}$$

for magnet up and magnet down configurations respectively. The luminosity of the 13 TeV data sample was calculated using only leading bunch crossing collisions. The luminosity used in the 5 TeV sample was provided by the luminosity group.

The *pp* cross-section extrapolation to full phase-space was calculated using the official LHCb simulation based on the LHCb tune of Pythia 8. The cross-section at the full phase-space at 5 TeV is

$$\sigma = 65.72 \pm 0.02(stat) \pm 2.49(syst)\,\text{mb}.$$

At 13 TeV the cross-sections obtained for the two magnet configurations are

$$\sigma_{MU} = 69.47 \pm 0.19(stat) \pm 2.92(syst)\,\text{mb},$$
$$\sigma_{MD} = 69.89 \pm 0.21(stat) \pm 2.77(syst)\,\text{mb}.$$

Since the extrapolation was obtained by means of a simulation, it is necessarily model dependent. This dependence is taking into account in the systematic uncertainties of the results, nevertheless to avoid ambiguities, any comparison between theory and the measurement presented should be done for the kinematic range $2 < \eta < 5$ and $p > 2\,\text{GeV}/c$.

The results are showed in Figure 8.1 with other LHC measurements and the extrapolation model proposed by Block *et al.* The cross-section obtained at 5 TeV is compatible within 1σ with the cross-section extrapolation model. The measurements at 13 TeV are significantly below the expected value provided by the phenomenological model and the ATLAS measurement. However the results are compatible within 1σ with the CMS preliminary result.

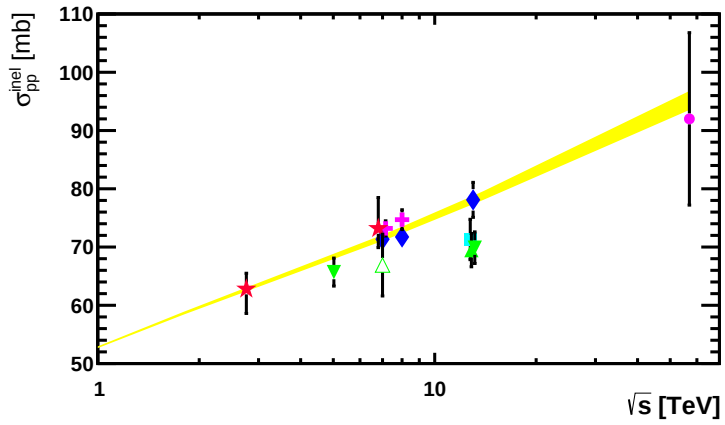

Figure 8.1: Inelastic cross-section *vs.* energy of measurements made by different experiments. Some data points have been slightly shifted in the horizontal position for display purposes. The grey full triangles represent the measurements presented in this thesis. The up triangle represents measurement performed with magnet up configuration and the down triangles the performed using magnet down. The empty triangle represent the measurement made by LHCb at 7 TeV. The cross marks represent the results from TOTEM. The stars represent the results from ALICE. Full diamonds represent the ATLAS measurements. Full square shows the CMS measurement and the circle represent the result obtained by the Pierre Auger Collaboration. In all cases the vertical black bars represent the total uncertainty of each measurement. The yellow band represents the 1σ uncertainty region of the phenomenological extrapolation calculated using the model proposed by Block *et al.*

The other goals of this thesis are related to the VELO upgrade project. Since the new VELO will have to cope with a very high radiation environment, in order to optimise the performance of the new front-end readout electronics, a deep understanding of the behaviour of the basic building cells is needed. This was studied in this thesis by evaluating the Single Event Upsets tolerance of the Medipix3 ASIC under heavy ions irradiation. The Medipix3 is an ancestor of the readout ASIC that will be used in the upgraded VELO, the VeloPix. These tests confirmed that the 130 nm Medipix3 registers perform better than other standard library registers and they do not have other unexpected weaknesses. This result established the starting point of the VeloPix ASIC design in terms of radiation hardness.

The performance of the VELO sensor and electronics prototypes is assessed using particle beams. To reconstruct the tracks that go through the device under test an instrument called telescope is used. The VELO upgrade group designed and built a telescope based on the Timepix3 readout chip. In this thesis the performance of this telescope under a high incidence particle rate was studied. The analysis of the beam test data revealed that the telescope keeps performing fully efficiently even at the maximum particle rate that can be achieved in the CERN north experimental area.

9 Summary

The Standard Model (SM) of Particle Physics is the most reliable description of the fundamental particles and their interactions. It is a very successful theory, since it predicted a whole set of new particles discovered in the last decades. Nevertheless, we know that is an incomplete theory, since it cannot explain certain phenomena such as neutrino's oscillation, Dark Matter or gravity. Several New Physics (NP) models have been proposed to solve these issues. Accelerators such as the Large Hadron Collider (LHC), at CERN, have been built to test the SM and the NP models.

9.1 The *pp* collisions

A proton is a complex structure formed by three valence quarks in a sea of quarks and gluons. When two protons collide in the LHC many of the constituents, called partons, of the proton interact. Thus, the resulting particle composition of a *pp* collision is very complicated.

The interactions that take place in a *pp* collision can be classified depending on the momentum transfer. If the momentum transfer is small, the interaction is classified as *soft* and the collision can be described by the scattering of two compound objects. When the momentum transfer is large the process is called *hard*. In this case the proton breaks up and the quarks and gluons join the collision. The large amount of energy involved in a hard process allows the creation of heavy particles. Hard processes can be calculated theoretically using perturbation theory. On the other hand, the theoretical calculation of a soft process is too complicated and it can only be described using phenomenological models. These models incorporate experimental results and extrapolate them in order to do predictions in the unexplored regions.

The cross-section is a fundamental observable in high energy hadronic interactions. Currently it is not possible to calculate it using quantum chromodynamics (QCD) first principles. Experimental measurements such as the elastic and inelastic cross-sections are crucial inputs to the phenomenological models.

Phenomenological models as well as perturbation theory techniques are incorporated in the Monte Carlo (MC) software packages that simulate the particle physics events with the same probability as they occur in nature. MC generators are widely used for signal and background estimates. There are many different generators that use different approaches to simulate the particle interactions. Some examples of MC event generators are Pythia, EPOS or Herwig.

9.2 The LHCb experiment at the LHC

LHCb is one of the four big detectors placed along the LHC accelerator at CERN. It was designed to study flavour physics exploiting the enormous production cross sections of B and C hadrons at the LHC. The identification of the primary vertex (PV), where the proton-proton collision took place, and the secondary vertex (SV), where the b-hadron decays, is essential for the physics of the experiment. This task becomes more difficult as the instantaneous luminosity increases, due to the large number of pp interactions per bunch crossing. For this reason the LHCb design instantaneous luminosity is $2 \times 10^{32}\,\mathrm{cm}^{-2}\mathrm{s}^{-1}$, that is two orders of magnitude smaller than the LHC nominal luminosity.

As can be appreciated in Figure 9.1, LHCb is a forward spectrometer. Its angular coverage goes from 10 to 300 (250) mrad in the bending (non-bending) plane with respect to the incoming proton beams. With this geometry, the detector covers about 2% of the solid angle and around 27% of the b quarks produced. The figure represents a cross-section of the detector, all its subdetectors can be identified. The main elements of LHCb are:

Magnet: Warm dipole that provides an integrated field of 4 Tm.

Vertex Locator (VELO): Silicon strip detector that provides precise information of the production and decay vertices of b-hadrons (PV and SV).

Tracking System: Composed of the *Tracker Turiciensis* (TT) before the magnet and the *Inner Tracker* (IT) and *Outer Tracker* (OT) after the magnet. This system allows the reconstruction of the trajectory of charged particles. The TT and IT use silicon strip sensors and the OT uses drift tubes.

Two Ring Imaging Cherenkov Detectors (RICH): These two detectors (RICH-1 before the magnet and RICH-2 after the magnet) identify charged particles in the momentum range from 2 to 100 GeV/c.

Calorimeter System: Composed by the *Scintillator Pad Detector* (SPD), the *PreShower* (PS), the *Electromagnetic CALorimeter* (ECAL) and the *Hadronic CALorimeter* (HCAL). The aim of this subsystem is to provide identification of electrons and hadrons with measurements of position and energy.

Muon System: It is composed by a combination of MWPC (*Multi Wire Proportional Chambers* and GEM (*Gas Electron Multiplier*) with iron absorbers. It identify muons that have passed through the calorimeters.

The amount of data produced by the LHC collisions is too large to be directly stored. The LHCb trigger system uses information from the subdetectors to select interesting events and to reduce the rate of visible interactions to a data volume allowed by the long term data storage resources. The trigger system must achieve this goal with a minimum loss of interesting events, that are mainly B mesons. During 2015 the trigger system reduced the data rate from 40 MHz to 12.5 kHz.

The LHCb online system is the responsible for transferring the data from the front-end electronics to the storage, for monitoring and controlling the detector and for distributing the beam synchronous clock and fast commands.

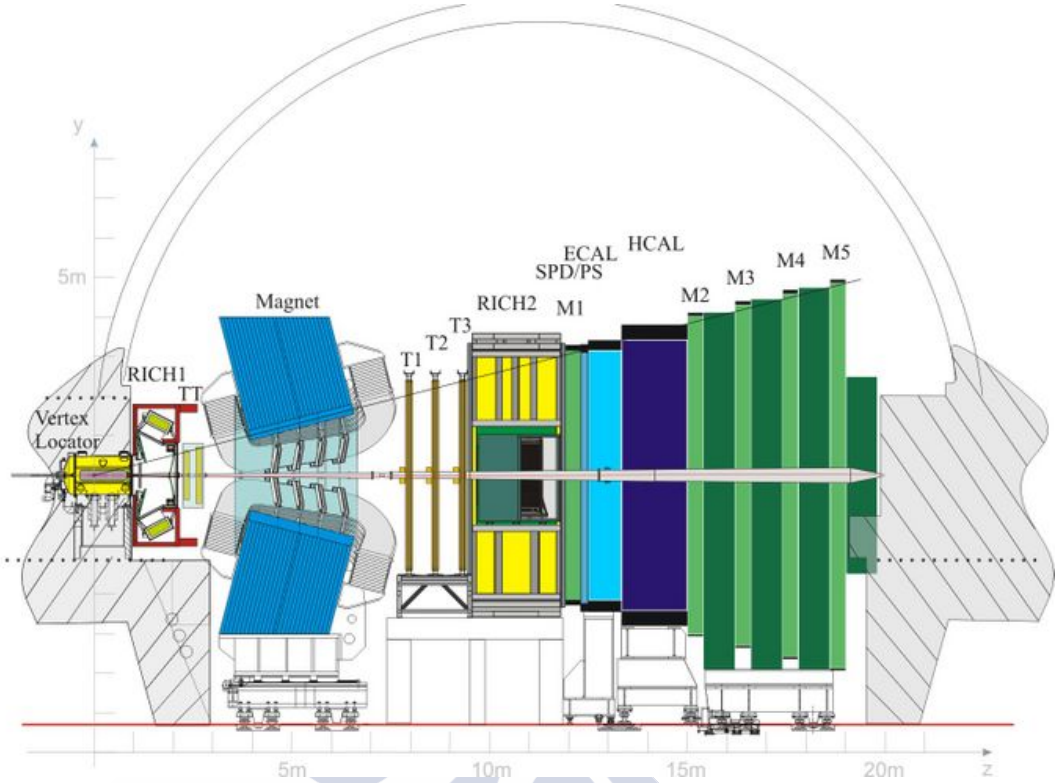

Figure 9.1: Side view of the LHCb detector.

Finally, the data analysis is performed using several software packages that are based in the Gaudi and Root frameworks. Gauss and Boole simulate and digitise physics events respectively. Afterwards, the software packages Moore, Brunel and DaVinci are used to apply the trigger decisions, reconstruct the full event or analyse it by combining the particles in decay chains. These three last steps can be used in simulation and real data.

9.3 Inelastic *pp* cross-section measurements

In particle physics the cross-section is defined as the probability that two particles collide and react in a certain way. In this thesis, the measurements of the proton-proton inelastic cross-section at centre-of-mass energies of $\sqrt{s} = 5\,\text{TeV}$ and $\sqrt{s} = 13\,\text{TeV}$ with at least one charged prompt long-live particle in the pseudorapidity region between $2 < \eta < 5$ and $p > 2\,\text{GeV}/c$ are presented. Long-lived particles are those quasi stable particles that live enough to traverse the tracking stations so they can be reconstructed as "long tracks". These particles are mainly e^-, μ^-, K^-, π^-, p and their respective antiparticles. Prompt particles are those that have originated directly from the *pp* interaction vertex or when the sum of the lifetime of their ancestors is less than 10 ps. These measurements are afterwards extrapolated to the full phase-space using the official LHCb simulation generated using the LHCb tune of Pythia 8. The data used in this analysis were collected using the LHCb detector during 2015.

The inelastic cross-section can be calculated as the ratio between the number of

interactions (N_{int}) and integrated luminosity ($\mathcal{L}$) of the sample,

$$\sigma = \frac{N_{int}}{\mathcal{L}}. \tag{9.1}$$

The elastic interactions are not included in the calculation since they are not expected to be detected by LHCb due to the very low angle of the resulting particles.

The total number of interactions cannot be measured due to the inefficiency of the detector. Nevertheless it can be calculated from the total number of bunch crossings of the sample N_{Bx} and the average number of visible interactions per bunch crossing (μ)

$$\sigma = \frac{N_{Bx}\mu}{\mathcal{L}}. \tag{9.2}$$

The number of interactions per bunch crossing is a random variable that follows a binomial distribution. Using the binomial distribution to calculate the probability of finding a bunch crossing with no tracks it is easy to extract an equation for the computation of μ. Moreover, taking into account the number of background events and the detector efficiency we obtain the following equation,

$$\mu = -\ln\left(1 - \frac{N_{vis} - N_{bkg}}{\varepsilon_{evt}\ N_{Bx}}\right). \tag{9.3}$$

In the following I will explain the calculation of the different parameters to finally obtain the inelastic cross-section.

9.3.1 Luminosity

The luminosity of a data sample is calculated by the LHCb luminosity group. To perform this calculation they calibrate the counters using some special runs and then extrapolate the results to the full data sample. The calibration assumes that all bunches in a fill are equivalent, nevertheless this assumption is not completely true. If we select some special bunch of the fill we cannot use the measurement provided by the luminosity group and we must perform a dedicated measurement. The no bias 5 TeV data sample is fully composed by leading bunches collisions, so a new measurement needs to be done. Regarding the 13 TeV data, the no bias data sample is small and for consistency I am going to follow the same method as for the 5 TeV data.

9.3.2 Event efficiency

The efficiency of LHCb detecting a single event can be calculated using the following equation,

$$\frac{1}{\varepsilon_{evt}} = 1 - \sum_{k=1}^{\infty} \hat{q}_k \left(\frac{\varepsilon - 1}{\varepsilon}\right)^k, \tag{9.4}$$

where $\hat{q}_k$ is the zero-suppressed measured multiplicity distribution, k the number of tracks ($k = 1, .., \infty$) and ε is the single tracking efficiency of the detector.

The single tracking efficiency can be calculated from MC with some corrections obtained from real data. This efficiency can be calculated as

$$\varepsilon = \varepsilon^{Acc} \times \varepsilon^{Reco} \times \rho^{Tracking} \times \varepsilon^{Cuts}, \tag{9.5}$$

where ε^{Acc} is the acceptance efficiency, ε^{Reco} is the reconstruction efficiency, ε^{Cuts} is the offline cuts efficiency and $\rho^{Tracking}$ is a data/MC correction factor.

9.3.3 Event and track selection

The leading bunches collisions of the samples are selected using dedicated no bias trigger lines. Since these trigger lines provide a completely random sample, the efficiency of the trigger is 100%. Furthermore, it is also required every collision to come from a beam-beam interaction and no cuts are applied on the luminous region.

The reconstruction of a primary vertex needs at least 3 VELO tracks pointing to one point. Hence, the use of any PV related variable to select tracks would bias the sample towards higher multiplicities. To avoid this issue, instead of using the impact parameter of a track with respect to the PV I used the transverse distance of the estimated point of origin of a track to the average PV locations. This distance is called pseudo impact parameter (psIP).

The track selection is based in the detector acceptance and in the background rejection obtained using MC data. The background rejection is defined as

$$\text{Bkg rejection} = \frac{\text{Signal}}{\sqrt{\text{Signal+Bkg}}}. \tag{9.6}$$

Background events can be divided in two different types: events not coming from pp interaction and those with at least one reconstructed track in the detector acceptance but with none of their tracks created by an actual charged, prompt and long-lived particle.

Background events from non pp interactions can be estimated using a sample of beam-empty (be), empty-beam (eb) and empty-empty (ee) events. Using equation

$$f_{bkg} = q_0^{bb}(f_{bkg}^{be} + f_{bkg}^{eb} - f_{bkg}^{ee}), \tag{9.7}$$

I extrapolate the fraction of these kind of events to the beam-beam data sample.

To calculate the fraction of visible events with no charged, prompt and long-lived particles we can only use data from simulation. The evaluation of this kind of events is done in MC and extrapolated to real data assuming the same behaviour in the two samples. The systematic uncertainties related to this assumption are detailed in the systematics section.

9.3.4 Extrapolation to full phase-space

The inelastic cross-section in the full-phase space is computed using the LHCb MC sample, multiplying the measured cross-section in the LHCb fiducial phase-space by a factor computed as the ratio of the number of events with one primary vertex and more than two protons in the final state and the number of events with one primary vertex and at least one prompt charged particle with $2 < \eta < 5$ and $p > 2\,\text{GeV}/c$.

9.3.5 Systematic uncertainties

The systematic uncertainties of the measurement are attributed to five different sources: integrated luminosity, beam energy, event efficiency, differences between data and MC and background events.

The integrated luminosity is by far the dominant systematic contribution, with the other systematics and the statistical uncertainties being negligible.

The beam energy uncertainty is 0.65%. Since this parameter is not included in the analysis, the systematic associated is calculated as the difference of the expected cross-sections at $\pm 1\sigma$ of the nominal energy.

The systematics affecting the event efficiency come from the tracking efficiency correction and from the calculation method itself, that includes the biases of the long tracks multiplicity. The uncertainty due to the calculation method is determined from MC as the difference in the event efficiency calculated using this method and using the MC truth information.

The estimation of the background events with none of its tracks being a charged long-lived prompt track is done using simulation. In order to estimate how well the MC reproduces this background we use a BDT. This BDT is optimized using charged long-lived prompt tracks from simulation as signal, and secondary and ghost tracks as background. Afterwards, this BDT is applied to data and then a PDF with three components (signal, secondary and ghosts) is fitted to data. The comparison between the results from data and MC will give and idea of how well the number of background events is simulated.

The extrapolation is performed using MC, and it is necessarily model dependent. I generated different MC samples using the default tune of Pythia 6 and some tunes of Pythia 8. The systematic uncertainty of the extrapolation is calculated as the square root of the quadratic sum of the statistical uncertainty of the extrapolation factor obtained using the official LHCb simulation and the standard deviation of the factors obtained from the different tunes of Pythia 8 and Pythia 6.

9.4 5 TeV cross-section

The data sample of this analysis consist of $(3.37 \pm 0.12)\,\text{nb}^{-1}$ of pp collisions at 5 TeV with a bunch space of 25 ns collected by LHCb on November 2015 and data were reconstructed under version Reco15a.

A Monte Carlo sample of 1 million events based on the LHCb tune of Pythia 8 was generated with an average number of $\nu = 1.5$ pp interactions per bunch crossing and 25 ns of bunch space and reconstructed using version Reco15.

Table 9.1 summarises the cuts applied to the events and tracks of the sample, and Table 9.2 shows the values of the parameters needed to calculate the cross-section. Note that the uncertainties are only statistical. The integrated luminosity uncertainty is 2.06 mb being the dominant systematic. The rest of the systematics are negligible.

Finally, the cross-section in the acceptance of the detector is

$$\sigma^{acc} = 56.88 \pm 0.02(stat) \pm 2.12(syst)\,\text{mb}.$$

The extrapolation factor obtained using the LHCb MC sample is $s_{ext} = 1.1555 \pm 0.0026(stat) \pm 0.0078(syst)$, yielding the following cross-section in the full phase-space

$$\sigma = 65.72 \pm 0.02(stat) \pm 2.49(syst)\,\text{mb}.$$

Event cuts	`Hlt1NoBiasLeadingCrossingDecision` == `True` Bunch crossing type == beam-beam
Fiducial cuts	$2 < \eta < 5$ $p > 2$ GeV/c
Tracks selection	Clone == `False` χ^2/nDoF < 3 Pseudo IP < 0.93 mm Ghost Prob. < 0.13

Table 9.1: Summary of cuts applied to the 5 TeV sample.

N_{vis}	156531800 ± 12511
N_{bkg}	599019 ± 599019
N_{Bx}	529837568
ε_{evt}	0.97558 ± 0.00025
μ	0.36189 ± 0.00012
$\mathcal{L}$	(3.37 ± 0.12) nb^{-1}

Table 9.2: Results summary.

9.5 13 TeV cross-section

The 13 TeV data sample used in this analysis was collected from June to August 2015 using the LHCb detector. In this case the bunch space was 50 ns and two magnet configurations were used up (MU) and down (MD). The integrated luminosities were calculated for these data samples and resulted to be $(3175 \pm 130)\,\mu$b^{-1} for MU configuration and $(959 \pm 37)\,\mu$b^{-1} for MD. Data were reconstructed using version Reco15em.

The trigger line selecting leading bunches is `Hlt1MBNoBiasLeadingCrossingDecision`. This trigger line is essentially equal to the one used in the 5 TeV data sample.

In Table 9.3 a summary of the event and track cuts applied can be seen. Table 9.4 shows the values of the parameters needed to calculate the cross-sections in the fiducial area of LHCb. Note that all uncertainties shown in the table are only statistical.

Event cuts	`Hlt1MBNoBiasLeadingCrossingDecision` == `True` Bunch crossing type == beam-beam
Fiducial cuts	$2 < \eta < 5$ $p > 2$ GeV/c
Tracks selection	Clone == `False` χ^2/nDoF < 3 Pseudo IP < 0.78 mm Ghost Prob. < 0.19

Table 9.3: Summary of cuts applied to the 13 TeV sample.

As in the 5 TeV analysis, the integrated luminosity is the dominant systematic uncer-

	MU	MD
N_{vis}	130484132 ± 11423	35833430 ± 5986
N_{bkg}	313802 ± 313802	86738 ± 86738
N_{Bx}	237836575	55608821
ε_{evt}	0.9833 ± 0.0018	0.9850 ± 0.0016
μ	0.8133 ± 0.0023	1.0573 ± 0.0031
$\mathcal{L}$	$(3175 \pm 130)\,\mu b^{-1}$	$(959 \pm 37)\,\mu b^{-1}$

Table 9.4: Results summary.

tainty, being 2.51 mb and 2.38 mb for MU and MD configurations respectively. The other contributions are negligible.

The cross-section results in the LHCb acceptance are

$$\sigma^{acc}_{MU} = 60.93 \pm 0.17(stat) \pm 2.51(syst)\,\text{mb},$$
$$\sigma^{acc}_{MD} = 61.31 \pm 0.18(stat) \pm 2.38(syst)\,\text{mb},$$

The extrapolation factors are

$$s^{MU}_{ext} = 1.14018 \pm 0.00089(stat) \pm 0.0094(syst),$$
$$s^{MD}_{ext} = 1.13998 \pm 0.00090(stat) \pm 0.0094(syst),$$

that yield the following cross-sections in the full phase-space

$$\sigma_{MU} = 69.47 \pm 0.19(stat) \pm 2.92(syst)\,\text{mb},$$
$$\sigma_{MD} = 69.89 \pm 0.21(stat) \pm 2.77(syst)\,\text{mb}.$$

9.5.1 Conclusions

Figure 9.2 represents the inelastic cross-section *vs.* energy made by the LHC experiments. The full triangles represent the measurements presented in this thesis. The yellow band represents the 1σ uncertainty region of the phenomenological extrapolation calculated using the model proposed by Block *et al.* in Ref. [89]. As it can be seen, the measured value at 5 TeV is consistent with the extrapolation within 1σ. Note here that this is not a final result, since I used the luminosity value calculated by the LHCb luminosity group and it needs to be updated. On the other hand, the measurements at 13 TeV are 3σ away from the prediction. Nevertheless they are compatible within 1σ with the CMS measurement. The measurements made by LHCb at 7 TeV, 5 TeV and 13 TeV, the later two presented in this thesis, are systematically below predictions.

9.6 The LHCb upgrade

Nowadays almost all LHCb physics analyses are dominated by their statistical uncertainties. In spite of its very good performance, LHCb can only collect up to $\sim 1.5\,\text{fb}^{-1}$ per year. Hence it needs an upgrade to increase the data acquisition rate and therefore reduce the statistical uncertainties in a more rewarding time scale.

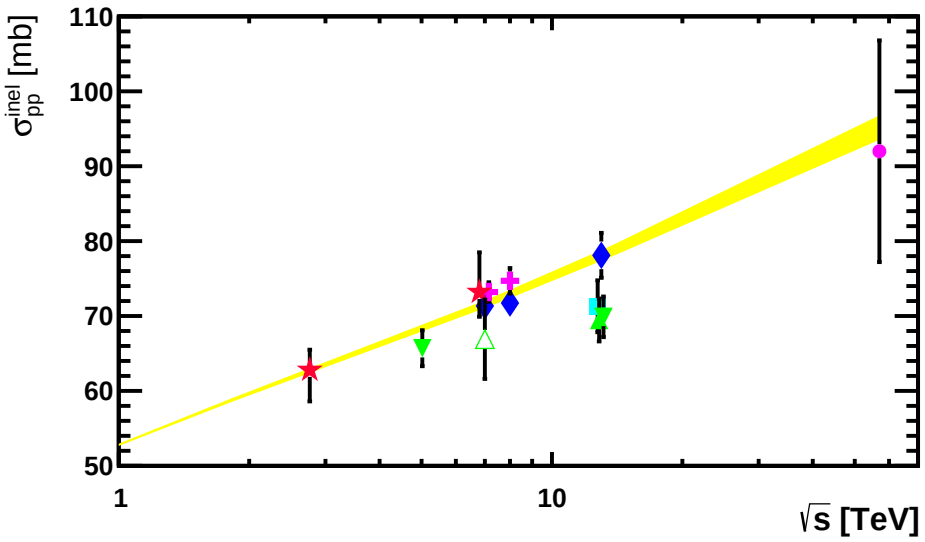

Figure 9.2: Inelastic cross-section *vs.* energy of measurements made by different experiments TOTEM (cross marks), ALICE (stars), ATLAS (diamonds), CMS (square), Pierre Auger (circle) and LHCb at 7 TeV (empty triangle). The green full triangles represent the measurements presented in this thesis. Some data points have been slightly shifted in the horizontal position for display purposes. The yellow band represents the 1σ uncertainty region of the phenomenological extrapolation calculated using the model proposed by Block *et al.*.

An upgrade of the whole detector was designed with the aim of increasing the trigger yield. All subdetectors will be modified and the whole detector will be read out at 40 MHz. Furthermore, the instantaneous nominal luminosity will be increased to $2 \times 10^{33}\,\mathrm{cm}^{-2}\mathrm{s}^{-1}$. The trigger output rate is under review and will vary between 20 and 100 kHz.

9.6.1 The VELO upgrade

The requirements for the new VELO are very demanding. It has to be read out at 40 MHz. It needs a higher granularity to work at the new luminosity and provide a fast and robust track reconstruction. It has to be radiation hard and withstand the highly non uniform radiation environment of the interaction proximities. Moreover, it has to minimise the material in the detector acceptance and to keep or improve the current detector performance.

To fulfil these criteria, the new detector will be based in silicon pixel technology and it will use a readout chip called VeloPix that is a descendant of the Timepix3 ASIC. The new VELO will consist in 26 stations, where each of them will be composed of 2 modules, one on either side of the beam and following the same philosophy of the current detector. Each module will carry 4 sensors, 2 in each side of the substrate. Each sensor will be bump-bonded to 3 VeloPix ASICs for readout arranged in a tile of 3×1. The ASIC will consist of a matrix of 256×256 pixels of $55\,\mu\mathrm{m} \times 55\,\mu\mathrm{m}$. The inner chips of the module will have to transmit data up to 15.1 Gbits/s. Assuming a collision frequency of ~ 30 MHz, the mean data rate will be 36.8 Gbits/s per module.

The dimensions of the sensor will be $43\,\mathrm{mm} \times 14\,\mathrm{mm}$ and a thickness of $200\,\mu\mathrm{m}$.

As the readout chip, the sensors pixel size will be 55 μm × 55 μm, with elongated pixels implants of 110 μm in the region between the ASICs. The sensors will be cooled using a microchannel cooling system. This is a novel method where the channels are directly etched in the mechanical substrate through which the cooling fluid is directed.

The first sensitive pixel will be at 5.1 mm from the beam axis. Its geometrical efficiency will be greater than 99% for a radius smaller than 10 mm. This means that the 99% of the tracks will have 4 or more hits inside the VELO. It will be separated from the beam vacuum by a 250 μm RF foil.

9.7 Radiation tolerance of the Medipix3 chip

Three years ago, the most similar device to the planned VeloPix was the Medipix3 ASIC, so it was studied extensively in order to improve the VeloPix design. The Medipix3 chip is a pure counting device designed for applications with photons. Medipix3 contains an array of 256 × 256 of 55 μm side square pixels. Medipix3 was the first ASIC of the Medipix family to be built in 130 nm IBM CMOS technology and, at that moment, it was also the technology planned to be used for the VeloPix design. These characteristics made the Medipix3 the perfect device to study the actual status of the VeloPix design.

A Single Event Upset (SEU) is caused by a very high energy deposition in a very small volume of the electronics. The charge released is collected by one node and the resulting current might generate a SEU. The SEUs occurrence depends on two variables: The sensitive volume in which the ionization has to take place for the charge to be collected in the node, and the critical energy that has to be exceeded by the deposited ionizing energy within the sensitive volume to flip a bit. Since the sensitive volume is a design property of the chip, in order to study the SEUs sensitivity, the electronics must be irradiated with different linear energy transfer (LET) particles.

I evaluated the SEU tolerance of the Medipix3 by irradiating it with different heavy ion species at the Heavy Ion Irradiation Facility (HIF) in the Cyclotron Resource Centre at Louvain-la-Neuve, Belgium. This facility allows to choose between two ion cocktails, each of them containing many ion types and one LET per ion. Furthermore, the device under test can be rotated, so we can obtain more than one LET measurements per ion type. The heavy ion species used in the test were $^{13}C^{+4}$, $^{22}Ne^{+7}$, $^{40}Ar^{+12}$, $^{58}Ni^{+18}$ and $^{84}Kr^{+25}$, that combined with two rotation angles of the chip yielded 10 measurement points.

Two equal Medipix3 chips with references W100_F7 and W100_D7 were tested. Figure 9.3 shows the results obtained in the tests using the chip W100_F7. The four colour points represent the results selecting all bit flips (black), only flips from 1 to 0 (blue) or flips from 0 to 1 (red). The pink points represent the results obtained when writing only zeros in the chip. A Weibull function defined as

$$\sigma = \sigma_{sat}\left\{1 - \exp\left[-\left(\frac{LET - LET_{th}}{W}\right)^{S}\right]\right\}, \tag{9.8}$$

is fitted to data with the same colours as the corresponding points. The results are shown in Table 9.5.

The main parameter is the LET_{th} that indicates the minimum particle LET to induce a SEU. From the results saw above, I can conclude that the Medipix3 ASIC is more sensitive

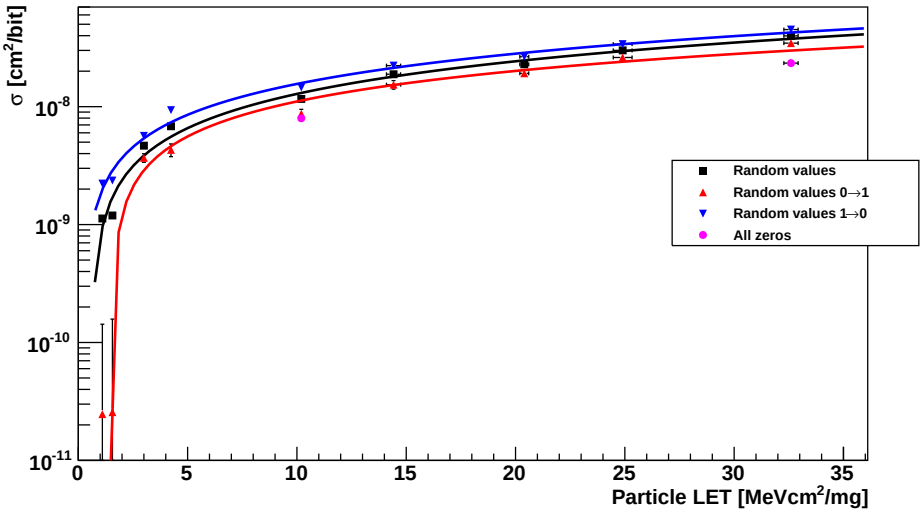

Figure 9.3: Pink circles represent the results obtained from runs where the pixels counters were written with only zeros. The other symbols represent runs where the written information was random. Blue triangles represent the SEUs flipping from 1 to 0. Red points are the result from bits changing from 0 to 1, and black points represent results from all SEUs. Blue, red and black lines represent the fits to the same colour data.

	SEUs 1→0	SEUs all	SEUs 1→0
χ^2/nDoF	38/5	60/5	24/5
σ_{sat} [cm^2]	$(0.39 \pm 1.1) \times 10^{-5}$	$(2.00 \pm 0.47) \times 10^{-6}$	$(2.4 \pm 6.1) \times 10^{-5}$
LET$_{\text{th}}$ [MeV cm^2/mg]	0.25 ± 0.15	0.586 ± 0.085	1.547 ± 0.038
W [MeV cm^2/mg]	$(0.68 \pm 2.3) \times 10^4$	$(26.9 \pm 8.2) \times 10^2$	$(2.0 \pm 6.0) \times 10^5$
S	0.843 ± 0.044	0.894 ± 0.031	0.763 ± 0.044

Table 9.5: SEUs fit results

to SEUs flipping from 1 to 0 than from 0 to 1. Furthermore, comparing the results with some standard cells I can conclude that the Medipix3 ASIC is a little bit more tolerant to SEUs than them. This an expected result due to the smaller cell technology. Since it was not designed using any radiation tolerance technique, it is a good starting point for the VeloPix design.

9.8 Timepix3 telescope

To study the sensor prototypes different tools are needed. One of these tools is a telescope. The telescope is the equipment used to reconstruct the particle tracks that go through the device under test. The VELO upgrade group designed a telescope consisting of 8 planes of silicon pixel sensors read out by Timepix3 ASICs. Each plane is formed by a 300 µm thick p^+-on-n silicon sensor bump bonded to a Timepix3 chip. The device under tests (DUT) can be located at the centre of the telescope or at the rear. The former

position provides the best pointing resolution ($\sim 2\,\mu$m), and the later one is thought for bulky devices.

Data is read out from ASICs using the Speedy PIxel Detector Readout (SPIDR) system. The chip can send out up to 80 MHits/s. The SPIDR is designed to read out Timepix3 and Medipix3 at their maximum rate. The load of a SPIDR system reading out a single Timepix3 at maximum rate is about 55%. In the typical telescope configuration using 8 planes, each SPIDR board reads two planes. When a high particle rate is expected each plane is connected to one SPIDR board.

The synchronisation of the telescope SPIDR boards is performed by the Telescope Logic Unit (TLU). The firmware of this trigger unit was developed by the author of this thesis. This unit provides a common reference clock of 40 MHz to the boards. Furthermore, it also distributes a T0-Signal that synchronise all time counters and the shutter signal. The TLU can use its internal clock as reference or one provided externally. Moreover, the T0-Signal can also be supplied by an external source.

The LHCb VELO upgrade group usually tests its prototypes in the CERN north experimental area. This area is fed by the SPS accelerator and provides a beam composed of charged hadrons with a momentum of 180 GeV/c. The particles reach the experimental area in spills of $\sim$9 s, with a frequency of about 47 s.

To study the performance of the Timepix3 telescope under a high incidence particle rate it was installed in the LHCb VELO box at the CERN north experimental area. The telescope was configured with 3 planes per arm and one dedicated SPIDR board per plane. First, the beam collimators were configured to provide a beam intensity of $\sim 7 \times 10^5$ part/spill. We took 13 runs increasing the intensity the particle intensity in steps from $\sim 7 \times 10^5$ part/spill to $\sim 2.3 \times 10^7$ part/spill. This is the maximum particle intensity that can be achieved in the north experimental area since this beam intensity triggers the radiation alarms. Finally we took two more runs at the highest intensity increasing the DAQ buffer and changing the I_{Krum} from 10 to 20.

The inefficiency of the telescope at high particle rate can be detected by studying three different variables: The cluster charge collected by each plane of the telescope, the quality of the reconstructed tracks and the telescope tracking efficiency with respect to the particle rate.

The Time over Threshold (ToT) value given by the Timepix3 is proportional to the collected charge. I divided the spill in intervals of 0.5 s and fit a Landau convoluted with a Gaussian to the ToT distribution. If the particle rate would be comparable to the maximum acceptable rate of the ASIC we could find clusters with a larger ToT due to the overlap of two or more clusters. Comparing the Most Probable Value (MPV) of the fits no effect is appreciated.

At high rates the quality of the tracks can be compromised. The reconstructed tracks are required to have one associated cluster in each telescope plane. I fitted a Landau to the χ^2/nDoF of the tacks and measured the MPV. No differences on the MPVs are appreciated at the different particle rates.

In order to study the cluster finding efficiency I reconstructed the tracks of the telescope requiring hits only in 5 planes and looked for a cluster in the 6^{th} plane. Furthermore since the telescope was not perfectly aligned with the beam, I only analysed the fiducial area where a particle is likely to go through the sensitive area of the six planes. The efficiency of finding a cluster in the plane not included in the reconstruction is another

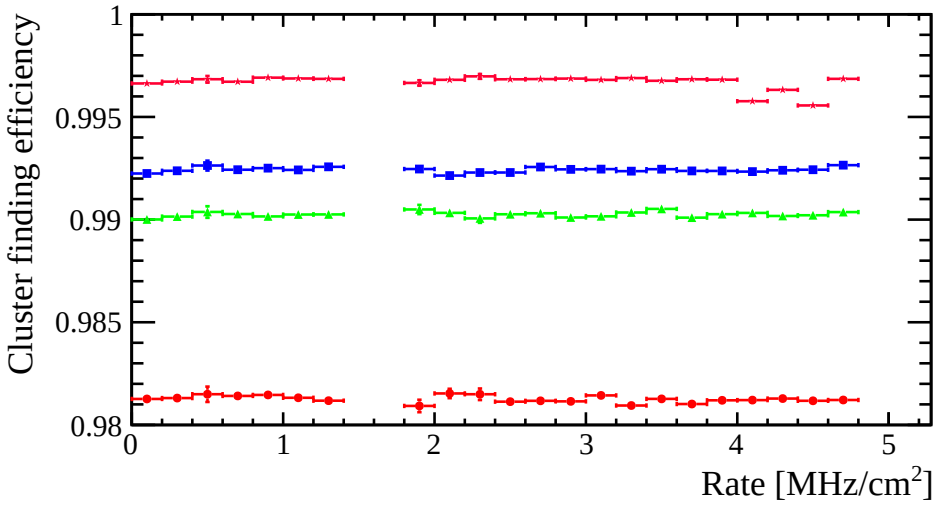

Figure 9.4: Cluster finding efficiency *vs.* track rate of the four internal planes of the telescope. Red, blue, green and pink points represent the efficiencies of the second, third, fourth and fifth planes respectively.

indicator of the inefficiency of the telescope at high particle incidence rate. Figure 9.4 shows the results of the cluster finding efficiency. In the figure can be clearly seen how the particle incidence rate has no effect on the cluster finding efficiency.

After analysing the data I can conclude that the telescope maintains its efficiency up to 5 MHz/ cm^2.

USC
UNIVERSIDADE
DE SANTIAGO
DE COMPOSTELA

10 Resumo

O Modelo Estándar da física de partículas é a descrición mais fiable das partículas fundamentais e as súas interaccións. É unha teoría moi exitosa, xa que predixo unha gran cantidade de partículas descubertas nas décadas pasadas. Sen embargo, sabemos que é unha teoría incompleta, xa que non pode explicar certos fenómenos como a oscilación dos neutrinos, a materia escura ou a gravidade. Moitos modelos de nova física foron propostos para solucionar estes problemas. Aceleradores coma o Gran Colisor de Hadróns (LHC), no CERN, foron construídos par aprobar o modelo estándar e os modelos de nova física.

10.1 As colisións *pp*

Un protón é unha estrutura complexa formada por tres quarks de valencia nun mar de quarks e gluóns. Cando dous protóns chocan no LHC moitos dos seus constituíntes, chamados partóns, interaccionan. Polo tanto, a composición de partículas final dunha colisión *pp* é moi complicada.

As interaccións que teñen lugar nunha colisión *pp* poden ser clasificadas dependendo da transferencia de momento que se produza. Se a transferencia de momento é pequena, a interacción clasifícase coma *suave* e a colisión pode ser descrita como a dispersión de dous obxectos compostos. Cando a transferencia de momento é grande o proceso é chamado *duro*. Neste caso o protón rompe e os quarks e gluóns entran en xogo na colisión. Un proceso duro involucra necesariamente un ou dous partóns con unha gran fracción de momento. A gran cantidade de enerxía involucrada nun proceso duro permite a creación de novas partículas.

Os procesos duros poden ser calculados teoricamente usando teoría de perturbacións. Por outro lado, o cálculo teórico dun proceso suave é demasiado complicado e só pode ser descrito usando modelos fenomenolóxicos. Estes modelos incorporan resultados experimentais e extrapólanos para facer predicións nas rexións inexploradas. A sección eficaz é un observable fundamental en interaccións hadrónicas de alta enerxía. Actualmente non é posible calcularla usando principios fundamentais de cromodinámica cuántica (QCD). Resultados experimentais coma as seccións eficaces elástica e inelástica son datos cruciais para os modelos fenomenolóxicos.

Tanto os modelos fenomenolóxicos coma técnicas de teoría de perturbacións están incorporados nos paquetes software tipo Monte Carlo (MC) que simulan os eventos de física de partículas coa mesma probabilidade de que ocorran na natureza. Os xeradores tipo MC son amplamente usados para facer estimacións da sinal e do fondo. Hai moitos

xeradores distintos que usan diferentes enfoques para simular as interaccións entre as partículas. algúns exemplos de xeradores tipo MC son Pythia, EPOS ou Herwig.

10.2 O experimento LHCb no LHC

LHCb é un dos catro grandes detectores situados no acelerador LHC do CERN. Foi deseñado para estudar a física do sabor explotando a enorme produción de hadróns tipo B e C no LHC. A identificación do vértice primario (PV), onde ten lugar a colisión protón-protón, e o vértice secundario (SV), onde o quark tipo b decae, son esenciais para a física do experimento. Esta tarefa vólvese mais difícil segundo a luminosidade instantánea aumenta, xa que tamén aumenta o número de colisións pp en cada cruce de partículas. Por esta razón LHCb foi deseñado para traballar a unha luminosidade instantánea de $2 \times 10^{32}\,\mathrm{cm}^{-2}\mathrm{s}^{-1}$, que é dúas ordes de magnitude menor ca nominal do LHC.

Como se pode apreciar na Figura 10.1, LHCb é un detector cara adiante. A súa cobertura angular vai dende 10 a 300 (250) mrad no plano horizontal (vertical) con respecto á dirección de chegada dos protóns. Con esta xeometría, o detector cubre arredor do 2% do ángulo sólido e preto do 27% dos quarks tipo b producidos. A figura representa unha sección do detector, onde todos os seus subdetectores poden ser identificados. Os elementos principais de LHCb son:

Imán: Dipolo a temperatura ambiente que proporciona un campo integrado de 4 Tm.

Localizador de vértice (VELO): Detector de pistas de silicio que proporciona información precisa da produción e os vértices onde decaen os hadróns con quarks b (PV e SV).

Sistema de trazado: Está composto por *Tracker Turiciensis* (TT) antes do imán e o *Inner Tracker* (IT) e *Outer Tracker* (OT) despois do imán. Este sistema permite a reconstrución da traxectoria das partículas cargadas. O TT e IT usan sensores de pistas de silicio e o OT usa tubos de deriva.

Dous detectores de anel Cherenkov (RICH): Estes dous detectores (RICH1 antes do imán e RICH2 despois do imán) identifican partículas cargadas no rango de momento entre 2 e 100 GeV/c.

Sistema de calorimetría: Composto por *Scintillator Pad Detector* (SPD), a *PreShower* (PS), o *Calorímetro electromagnético* (ECAL) e o *calorímetro hadrónico* (HCAL). O obxectivo deste subsistema é identificar electróns e hadróns con medidas de posición e enerxía.

Sistema de muóns: Está composto por unha combinación de MWPC (*Cámara proporcional multifios*) e GEM (*Multiplicador de electróns con gas*) con absorbentes de ferro. Identifica aqueles muóns que atravesaran os calorímetros.

A cantidade de datos producida nas colisións do LHC é demasiado grande para ser manexada. O sistema de disparo (*trigger*) de LHCb usa información dos subdetectores para seleccionar eventos interesantes e reducir o ratio de interaccións visibles a un volume de datos admisible polos recursos dispoñibles de almacenamento de datos. O sistema de trigger debe acadar este obxectivo cunha pérda mínima de eventos interesantes, que son

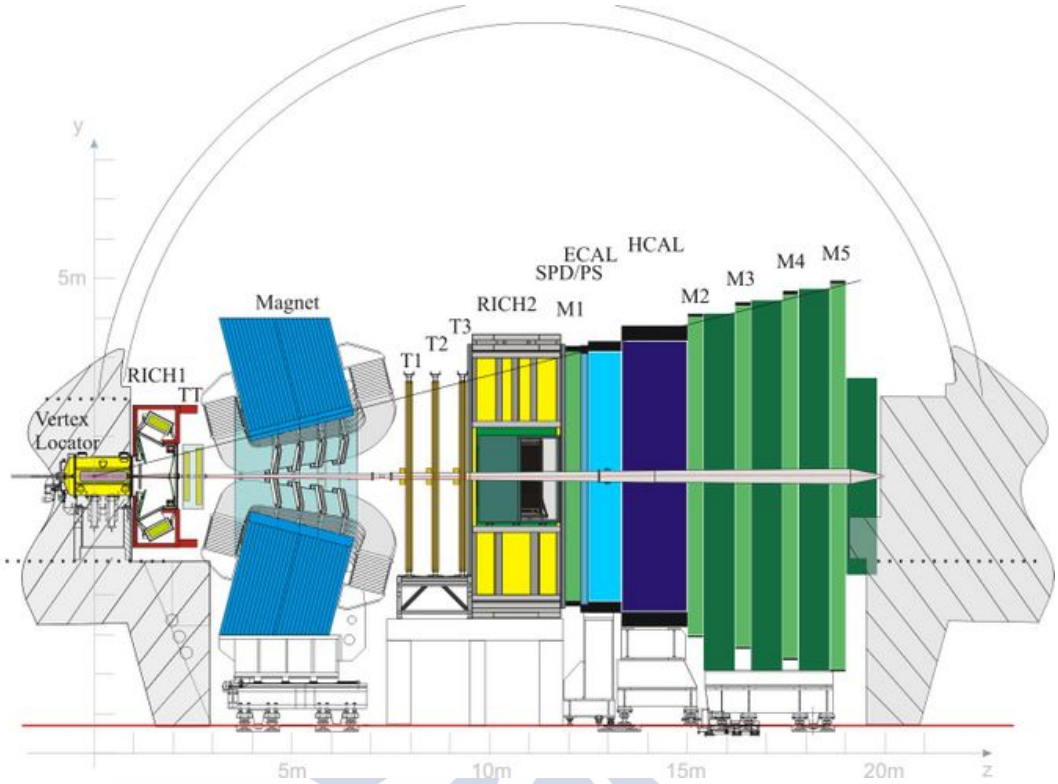

Figure 10.1: Vista lateral da sección do detector LHCb.

principalmente mesóns B. Durante 2015 o sistema de trigger reduciu o ratio de datos dende 40 MHz a 12.4 kHz.

O sistema en liña (*online*) é responsable de transferir os datos dende a electrónica de lectura ata o almacenamento, de monitorizar e controlar o detector e de distribuír o reloxo síncrono co feixe de partículas e os comandos rápidos.

Finalmente, para a análise de datos úsanse moitos paquetes de software que se basean en nos entornos de traballo Gaudi e Root. Gauss e Boole simulan e dixitalizan os eventos respectivamente. Despois, os paquetes Moore, Brunel e DaVinci aplican as decisións de trigger, reconstrúen o evento completo e analízano combinando as partículas en cadeas de desintegración. Estes tres últimos pasos poden ser usados tanto en simulación coma con datos reais.

10.3 Medida da sección eficaz inelástica *pp*

En física de partículas a sección eficaz defínese coma a probabilidade de que dúas partículas coliden e reaccionen dunha certa maneira. Nesta tese, preséntase a medida da sección eficaz inelástica protón-protón a enerxías no centro de masas de $\sqrt{s} = 5\,\text{TeV}$ e $\sqrt{s} = 13\,\text{TeV}$ con polo menos unha partícula cargada, de vida longa e xerada na interacción primaria na rexión de pseudorapidez $2 < \eta < 5$ e $p > 2\,\text{GeV}/c$. As partículas de vida longa son aquelas partículas que viven o suficiente como para atravesar o sistema de trazado do detector e poden ser reconstruídas como trazas tipo largas. Estas partículas son principalmente e^-, μ^-, K^-, π^-, p e as súas respectivas antipartículas. As partículas

xeradas na interacción primaria son aquelas que se crearon directamente na interacción pp ou aquelas que a suma do tempo de vida das súas antecesoras é menor ca 10 ps. A medida da sección eficaz é logo extrapolada a todo o espazo-fase usando o MC oficial de LHCb xerado con Pythia 8 configurado para LHCb. Os datos usados nesta análise foron recollidos usando o detector LHCb durante o 2015.

A sección eficaz inelástica pode ser calculada como o ratio entre o número de interaccións (N_{int}) e a luminosidade integrada ($\mathcal{L}$) da mostra.

$$\sigma = \frac{N_{int}}{\mathcal{L}}. \tag{10.1}$$

As interaccións elásticas non están incluídas no cálculo xa que non se espera que sexan detectadas por LHCb debido ao pequeno ángulo de saída das partículas resultantes.

O número total de interaccións non pode ser medido debido á ineficiencia do detector. Sen embargo pode ser calculado a partires do número total de cruces de paquetes de protóns da mostra N_{Bx} e o número de interaccións visibles por cruce (μ)

$$\sigma = \frac{N_{Bx}\mu}{\mathcal{L}}. \tag{10.2}$$

O número de interaccións por cruce é unha variable aleatoria que segue unha distribución binomial. Usando a distribución binomial para calcular a probabilidade de atopar un cruce de protóns sen trazas é sinxelo extraer unha ecuación para o cálculo de μ. Ademais, tendo en conta o número de eventos de fondo e a eficiencia do detector obtemos a seguinte ecuación,

$$\mu = -\ln\left(1 - \frac{N_{vis} - N_{bkg}}{\varepsilon_{evt}\ N_{Bx}}\right). \tag{10.3}$$

A continuación explicarei o cálculo dos diferentes parámetros necesarios para obter finalmente a sección eficaz inelástica.

10.3.1 Luminosidade

A luminosidade dunha mostra de datos é calculada polo grupo de luminosidade de LHCb. Para levar a cabo este cálculo calibran uns contadores usando configuracións especiais do acelerador e logo extrapolan os resultados a toda a mostra de datos. A calibración asume que todos os paquetes de protóns do acelerador son equivalentes, sen embargo eso non é totalmente certo. Se seleccionamos algún paquete especial non podemos usar o a medida da luminosidade proporcionada polo grupo de luminosidade e precisamos facer unha medida exclusiva para esa mostra. A mostra de datos sen nesgo a 5 TeV está composta unicamente por colisións daqueles paquetes que encabezan un tren de paquetes, polo tanto é preciso facer unha nova medida da luminosidade. No caso dos datos a 13 TeV, a maioría dos datos tamén proveñen de colisións de paquetes encabezando trens de paquetes, polo tanto usarase o mesmo método ca para a mostra a 5 TeV.

10.3.2 Eficiencia de detección de eventos

A eficiencia de LHCb en detectar un evento pódese calcular usando a seguinte ecuación,

$$\frac{1}{\varepsilon_{evt}} = 1 - \sum_{k=1}^{\infty} \hat{q}_k \left(\frac{\varepsilon - 1}{\varepsilon}\right)^k, \tag{10.4}$$

onde $\hat{q}_k$ é a distribución de multiplicidade medida eliminando o bin cero, k o número de trazas ($k = 1, .., \infty$) e ε é a eficiencia do detector en reconstruír unha traza.

A eficiencia en reconstruír unha traza pódese calcular a partir do MC e aplicando correccións obtidas dos datos reais. Esta eficiencia pode ser calculada como

$$\varepsilon = \varepsilon^{Acc} \times \varepsilon^{Reco} \times \rho^{Tracking} \times \varepsilon^{Cuts}, \tag{10.5}$$

onde ε^{Acc} é a eficiencia da aceptancia, ε^{Reco} é a eficiencia de reconstrución, ε^{Cuts} é a eficiencia dos cortes feitos na análise e $\rho^{Tracking}$ é un factor de corrección datos/MC.

10.3.3 Selección de eventos e trazas

As colisións de paquetes encabezando un tren de paquetes seleccionanse usando liñas de trigger dedicadas. Dado que estas liñas proporcionan unha mostra de datos totalmente aleatoria, a eficiencia do trigger é do 100%. Ademais, tamén se require que todas as colisións procedan de unha interacción feixe-feixe e non se aplicaron cortes no volume de interacción.

A reconstrución de un vértice primario necesita de polo menos 3 trazas tipo VELO apuntando cara un mesmo punto. Polo tanto, o uso de calquera variable relacionada co PV para seleccionar trazas nesgaría a mostra de datos cara multiplicidades mais altas. Para evitar este problema, en vez de usar o parámetro de impacto de unha traza con respecto ao PV eu usei a distancia transversa dende o punto estimado de orixe dunha traza á media das posicións dos vértices primarios. Esta distancia chámase pseudo parámetro de impacto (psIP).

A selección de trazas basease na aceptancia do detector e no rexeitamento do fondo obtido usando datos de MC. O rexeitamento do fondo defínese como

$$\text{Rexeitamento of fondo} = \frac{\text{Sinal}}{\sqrt{\text{Sinal+Fondo}}}. \tag{10.6}$$

Os eventos de fondo pódense dividir en dous tipos: eventos que non proveñen de unha interacción *pp* e aqueles con polo menos unha traza reconstruída na aceptancia do detector pero sen ningunha creada por unha partícula cargada, xerada na interacción primaria e de vida longa.

Os eventos de fondo non provintes de interaccións *pp* pódense estimar usando unha mostra de eventos feixe-vacío (be), vacío-feixe (eb) e vacío-vacío (ee). Usando a ecuación

$$f_{bkg} = q_0^{bb}(f_{bkg}^{be} + f_{bkg}^{eb} - f_{bkg}^{ee}), \tag{10.7}$$

extrapolo a fracción de esta clase de eventos á mostra de datos feixe-feixe.

Para calcular a fracción de eventos visibles con partículas non cargadas, xeradas na interacción primaria ou de longa vida só é posible usar datos simulados. A avaliación desta clase de eventos faise en MC e extrapólase aos datos reais asumindo o mesmo comportamento nas dúas mostras. As incertezas sistemáticas derivadas de esta asunción detállanse na sección de sistemáticos.

10.3.4 Extrapolación a todo o espazo-fase

A extrapolación da sección eficaz inelástica medida na aceptancia de LHCb calcúlase usando a mostra de MC oficial de LHCb. Compútase como o número de eventos xerados con un vértice primario e máis de dous protóns no estado final con respecto ao número de eventos con un vértice primario e polo menos unha traza cargada xerada na interacción primaria e na rexión $2 < \eta < 5$ e $p > 2\,\text{GeV}/c$.

10.3.5 Incertezas sistemáticas

As incertezas sistemáticas da medida atribúense a cinco fontes diferentes: a luminosidade integrada, a enerxía do feixe, a eficiencia de detectar un evento, diferencias entre os datos e o MC e eventos de fondo.

A luminosidade integrada e de lonxe a contribución dominante, sendo os outros sistemáticos e as incertezas estatísticas desprezables.

A incerteza na enerxía do feixe é do 0.65%. Dado que este parámetro non está incluído na análise, o sistemático asociado calcúlase como a diferencia da sección eficaz esperada a $\pm 1\sigma$ da enerxía nominal.

Os sistemáticos que afectan á eficiencia de detectar un evento proveñen da corrección da eficiencia de trazado e do método de cálculo mesmo, que inclúe os nesgos da multiplicidade de trazas longas. A incerteza debida ao cálculo determínase dende o MC como a diferencia das eficiencias de detectar un evento calculadas usando este método e usando a información de MC do xerador.

A estimación dos eventos de fondo nos cales ningunha das súas trazas sexa cargada, provinte da interacción primaria e de vida longa faise usando simulación. Para estimar como de ben o MC reproduce este fondo usamos unha BDT. Esta BDT está optimizada usando trazas cargadas, de vida longa e provintes da interacción inicial como sinal, e secundarias e trazas pantasma como fondo. Despois, esta BDT aplícase aos datos e logo axustase unha PDF con tres compoñentes (sinal, secundarias e pantasmas) aos datos. A comparación entre os resultados usando os datos e o MC daranos unha idea de como de ben o MC simula os eventos de fondo.

A extrapolación faise usando MC, polo tanto depende necesariamente dun modelo teórico. Eu xerei distintas mostras de datos de MC usando a configuración por defecto de Pythia 6 e distintas configuracións de Pythia 8. A incerteza sistemática da extrapolación calcúlase como a raíz cadrada da suma cadrática da incerteza estatística do factor de extrapolación obtido usando a simulación oficial de LHCb e a desviación estándar dos factores obtidos usando as diferentes configuracións de Pythia 8 e Pythia 6.

10.4 Sección eficaz a 5 TeV

A mostra de datos desta análise consiste en $(3.37 \pm 0.12)\,\text{nb}^{-1}$ de colisións pp a 5 TeV con unha distancia entre paquetes de 25 ns recollidos por LHCb en novembro de 2015. Os datos foron reconstruídos usando a versión Reco15a.

A simulación Monte Carlo usada contén 1 millón de eventos e está baseada na configuración de Pythia 8 para LHCb. Foi xerada cun número medio de $\nu = 1.5$ interaccións pp por cada cruce de paquetes e 25 ns de distancia entre paquetes. A versión de reconstrución usada foi Reco15.

A Táboa 10.1 resume os cortes aplicados aos eventos e trazas da mostra, e a Táboa 10.2 móstra os valores dos parámetros usados para calcular a sección eficaz inelástica. Nesta táboa todas as incertezas son só estatísticas. A incerteza da luminosidade integrada é de 2.06 mb sendo ademais a incerteza sistemática dominante. O resto dos sistemáticos son desprezables.

Cortes nos eventos	`Hlt1NoBiasLeadingCrossingDecision` == `True` Tipo de cruce == Feixe-Feixe
Cortes na aceptancia	$2 < \eta < 5$ $p > 2$ GeV/c
Selección de trazas	Clones == `False` χ^2/nDoF < 3 Pseudo IP < 0.93 mm Prob. pantasma. < 0.13

Table 10.1: Resumo de cortes aplicados á mostra de 5 TeV.

N_{vis}	156531800 ± 12511
N_{bkg}	599019 ± 599019
N_{Bx}	529837568
ε_{evt}	0.97558 ± 0.00025
μ	0.36189 ± 0.00012
$\mathcal{L}$	(3.37 ± 0.12) nb^{-1}

Table 10.2: Resumo dos resultados.

Finalmente, a sección eficaz na aceptacia do detector é

$$\sigma^{acc} = 56.88 \pm 0.02(stat) \pm 2.12(syst) \text{ mb}.$$

O factor de extrapolación obtido usando a mostra de MC é $s_{ext} = 1.1555 \pm 0.0026(stat) \pm 0.0078(syst)$, resultando a seguinte sección eficaz en todo o espazo-fase

$$\sigma = 65.72 \pm 0.02(stat) \pm 2.49(syst) \text{ mb}.$$

10.5 Sección eficaz a 13 TeV

A mostra de datos a 13 TeV usada nesta análise foi tomada dende xuño a agosto do 2015 usando o detector LHCb. Neste caso a distancia entre paquetes de protóns foi de 50 ns e usáronse dúas configuracións do imán cara arriba (MU) e cara abaixo (MD). A luminosidade integrada foi calculada para esta mostra de datos e resultou ser (3175 ± 130) μb^{-1} para a configuración MU e (959 ± 37) μb^{-1} para MD. Os datos foron reconstruídos usando a versión Reco15em.

A liña de trigger usada para seleccionar os paquetes de protóns situados á cabeza dun tren é `Hlt1MBNoBiasLeadingCrossingDecision`. Esta liña de trigger é en esencia igual á usada nos datos a 5 TeV.

Na Táboa 10.3 móstrase un resumo dos cortes aplicados aos eventos e as trazas. A Táboa 10.4 indícanse os valores obtidos dos parámetros necesarios para calcular a sección eficaz na aceptacia de LHCb. As incertezas mostradas na táboa son só estatísticas.

Cortes nos eventos	`Hlt1MBNoBiasLeadingCrossingDecision` == `True` Tipo de cruce == Feixe-Feixe
Cortes na aceptancia	$2 < \eta < 5$ $p > 2\,\text{GeV/c}$
Selección de trazas	Clone == `False` $\chi^2/\text{nDoF} < 3$ Pseudo IP $< 0.78\,\text{mm}$ Prob. pantasma < 0.19

Table 10.3: Resumo dos cortes aplicados á mostra de 13 TeV

	MU	MD
N_{vis}	130484132 ± 11423	35833430 ± 5986
N_{bkg}	313802 ± 313802	86738 ± 86738
N_{Bx}	237836575	55608821
ε_{evt}	0.9833 ± 0.0018	0.9850 ± 0.0016
μ	0.8133 ± 0.0023	1.0573 ± 0.0031
$\mathcal{L}$	$(3175 \pm 130)\,\mu\text{b}^{-1}$	$(959 \pm 37)\,\mu\text{b}^{-1}$

Table 10.4: Resumo dos resultados.

Igual ca na análise a 5 TeV, a luminosidade integrada é a incerteza sistemática dominante, sendo 2.51 mb e 2.38 mb para as configuracións MU e MD respectivamente. As outras contribucións son desprezables.

Os resultados da sección eficaz son

$$\sigma^{acc}_{MU} = 60.93 \pm 0.17(stat) \pm 2.51(syst)\,\text{mb},$$
$$\sigma^{acc}_{MD} = 61.31 \pm 0.18(stat) \pm 2.38(syst)\,\text{mb},$$

Os factores de extrapolación son

$$s^{MU}_{ext} = 1.14018 \pm 0.00089(stat) \pm 0.0094(syst),$$
$$s^{MD}_{ext} = 1.13998 \pm 0.00090(stat) \pm 0.0094(syst),$$

os cales levan á seguinte sección eficaz en todo o espazo-fase

$$\sigma_{MU} = 69.47 \pm 0.19(stat) \pm 2.92(syst)\,\text{mb},$$
$$\sigma_{MD} = 69.89 \pm 0.21(stat) \pm 2.77(syst)\,\text{mb}.$$

10.5.1 Conclusións

A Figura 10.2 representa a sección eficaz inelástica con respecto á enerxía medidas polos experimentos do LHC. Os triángulos recheos representan as medidas presentadas nesta

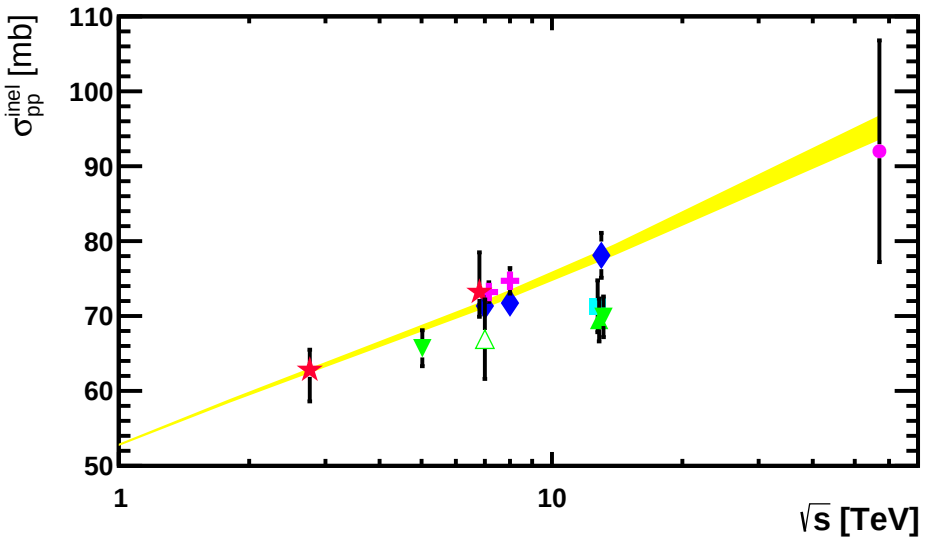

Figure 10.2: Sección eficaz inelástica con respecto á enerxía medidas por TOTEM (cruces), ALICE (estrelas), ATLAS (diamantes), CMS (cadrado), Pierre Auger (círculo) e LHCb a 7 TeV (triángulo oco). Os triángulos verdes recheos representan as medidas presentadas nesta tese. Algúns dos puntos foron desprazados lixeiramente no eixo horizontal para mellorar a visibilidade. A banda amarela representa a rexión de incerteza de 1σ do modelo de extrapolación fenomenolóxico proposto por Block *et al.*

tese. A banda amarela representa a rexión de incerteza de 1σ de grosor do modelo fenomenolóxico proposto por Block *et al.* en Ref. [89]. Como se pode observar, a medida a 5 TeV é consistente ca extrapolación no rango de 1σ. Por outro lado, as medidas a 13 TeV están a 3σ de distancia da predición. Sen embargo son compatibles a 1σ ca medida de CMS. Todas as medidas feitas por LHCb a 7 TeV, 5 TeV e 13 TeV, estas dúas últimas presentadas nesta tese, están sistematicamente por baixo das predicións.

10.6 A mellora de LHCb

Hoxe en día case todas as análises de física de LHCb están dominadas polas súas incertezas estatísticas. A pesares do seu excelente rendemento, LHCb só pode tomar ata $\sim 1.5\,\text{fb}^{-1}$ cada ano. Polo tanto precisa unha mellora para aumentar a taxa de adquisición de datos e polo tanto reducir as incertezas estatísticas nunha escala de tempo razoable.

Deseñouse unha mellora de todo o detector co obxectivo de incrementar a taxa de saída de datos do trigger. Todos os subdetectores serán modificados e lerase todo o detector a 40 MHz. Ademais, a luminosidade instantánea nominal incrementarase ata $2 \times 10^{33}\,\text{cm}^{-2}\text{s}^{-1}$. A taxa final de saída de datos do trigger está en revisión en variará entre 20 e 100 kHz.

10.6.1 A mellora do VELO

Os requirimentos para o novo VELO son moi esixentes. Debe ser lido a 40 MHz. Precisa dunha alta granularidade para traballar á nova luminosidade e permitir unha reconstrución

de trazas rápida e robusta. Ten que ser resistente á radiación e soportar o ambiente con alta radiación e moi variable das proximidades do punto de interacción. Ademais, ten que minimizar o material na aceptancia do detector e manter ou mellorar o rendemento do detector actual.

Para cumprir con estes requirimentoos, o novo detector basearase en tecnoloxía de píxeles de silicio e será lido usando un chip chamado VeloPix que é un descendente do ASIC Timepix3. O novo VELO consistirá en 26 estacións, onde cada unha delas estará composta por 2 módulos, un a cada lado do feixe e seguindo a mesma filosofía ca o detector actual. Cada módulo terá 4 sensores, 2 a cada lado do substrato. Cada sensor estará soldado a 3 VeloPix para a súa lectura formando un conxunto de 3×1. O ASIC consistirá nunha matriz de 256×256 píxeles de $55\,\mu m \times 55\,\mu m$. Os chips mais internos do módulo terán que transmitir datos ata 15.1 Gbits/s. Asumindo unha frecuencia de colisións de ~ 30 MHz, a media de saída de datos será 36.8 Gbits/s por módulo.

As dimensións do sensor serán de $43\,mm \times 14\,mm$ e $200\,\mu m$ de grosor. Igualmente ca o chip de lectura, os píxeles dos sensores serán de $55\,\mu m \times 55\,\mu m$, con píxeles alargados de $110\,\mu m$ na rexión entre os ASICs. Os sensores serán arrefriados usando un sistema de microcanais. Este é un método novo onde os canais se escavan directamente no substrato mecánico e a través deles se fai circular o fluído refrixerante.

O primeiro píxel sensible estará situado a só 5.1 mm do eixo do feixe. A súa eficiencia xeométrica será maior do 99% para radios menores de 10 mm. Esto significa que o 99% das trazas terá 4 ou mais interaccións dentro do VELO. Estará separado do vacío do acelerador por unha lámina de aluminio $250\,\mu m$.

10.7 Tolerancia á radiación do chip Medipix3

Fai tres anos, o dispositivo mais parecido ao futuro VeloPix era o ASIC Medipix3, polo tanto foi estudado de forma intensiva para na medida do posible mellorar o deseño do VeloPix. O chip Medipix3 é un chip de contaxe puro deseñado para aplicacións con fotóns. O Medipix3 contén unha matriz de 256×256 píxeles cadrados $55\,\mu m$ de lado. Foi ademais o primeiro ASIC da familia Medipix en ser construído en tecnoloxía de CMOS de 130 nm de IBM e, naquel momento, esa era a tecnoloxía planeada para usar no deseño do VeloPix. Estas características facían do Medipix3 o dispositivo perfecto para avaliar o estado do deseño do VeloPix.

As alteracións de un evento simple (SEU polas siglas en inglés) son provocadas por unha alta deposición de enerxía nun volume pequeno da electrónica. A carga liberada é recollida por un nodo e a corrente resultante pode xerar un SEU. A ocorrencia dun SEU depende de dúas variables: Do volume sensible no cal ten que ocorrer a ionización para que a carga resultante sexa recollida no nodo, e a enerxía crítica que ten que ser superada pola enerxía depositada pola ionización dentro do volume sensible para cambiar un bit de estado. Xa que o volume sensible é unha propiedade de deseño do chip, para estudar a sensibilidade aos SEUs, a electrónica debe ser irradiada con partículas con diferentes transferencias de enerxía lineal (LET).

Avaliei a tolerancia aos SEUs do Medipix3 irradiandoo con diferentes ións pesados na Heavy Ion Irradiation Facility (HIF) que se atopa no Cyclotron Resource Centre en Louvain-la-Neuve, Bélxica. Esta instalación permite escoller entre dous cócteis de ións, cada un dos cales contén varios tipos de ións e cada un deles con un LET distinto.

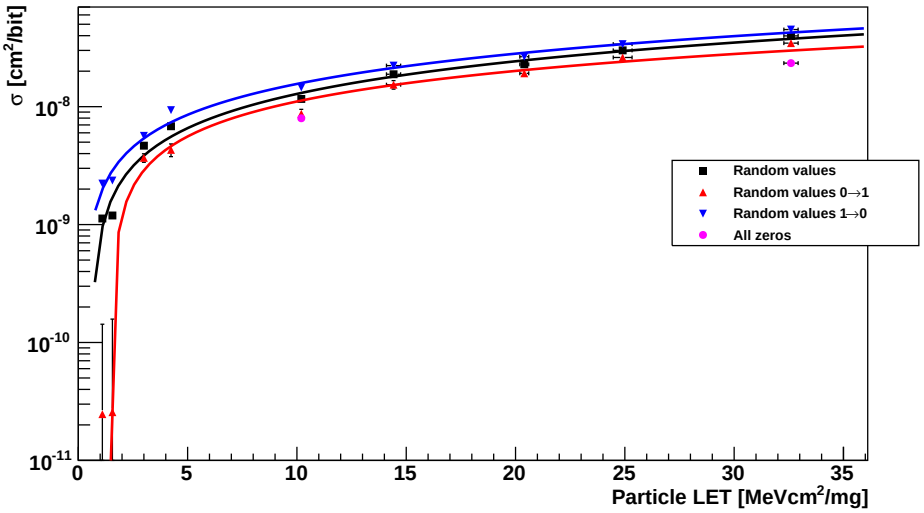

Figure 10.3: Os círculos rosas representan os resultados obtidos en medidas onde os contadores dos píxeles se encheron só con ceros. Os outros símbolos representan medidas onde a información escrita foi aleatoria. Os triángluos azuis representan SEUs cambiando de 1 a 0. Os puntos vermellos son o resultado de bits cambiando de 0 a 1, e os puntos negros representan resultados de todos os SEUs. As liñas azul, vermella e negra representan os axustes aos datos da mesma cor.

Ademais, o dispositivo a probar pode ser rotado, co cal podemos obter mais de unha medida de LET por tipo de ión. As especies de ións pesados usados nas probas foron $^{13}C^{+4}$, $^{22}Ne^{+7}$, $^{40}Ar^{+12}$, $^{58}Ni^{+18}$ e $^{84}Kr^{+25}$, que combinados con dous ángulos de rotación do chip permiten 10 puntos de medida.

Estudáronse dous chips Medipix3 iguais, con referencias W100_F7 e W100_D7. A Figura 10.3 mostra os resultados obtidos no tests usando o chip W100_F7. As catro cores dos puntos representan os resultados seleccionando todos as transicións dos bits (negro), transicións de 1 a 0 (azul) ou transicións de 0 a 1 (vermello). Os puntos rosas representan os resultados obtidos despois de escribir só ceros no chip. Unha función Weibull definida como

$$\sigma = \sigma_{sat}\left\{1 - \exp\left[-\left(\frac{LET - LET_{th}}{W}\right)^{S}\right]\right\}, \tag{10.8}$$

axustouse aos datos e o resultado representouse na mesma cor dos puntos correspondentes. Os resultados dos axustes móstranse na Táboa 10.5.

O parámetro principal é o LET_{th} que indica o mínimo LET co cal se pode inducir un SEU. A partires dos resultados anteriores, podo concluír que o ASIC Medipix3 é mais sensible aos SEUs cambiando de 1 a 0 ca de 0 a 1. Ademais, comparando os resultados con algunhas celas estándar podo concluír que o Medipix3 é lixeiramente mais tolerante aos SEUs que elas. Este é un resultado esperado debido a que o Medipix3 usa unha tecnoloxía con celas mais pequenas. Dado que non foi deseñado usando ningún tipo de técnica para aumentar a súa tolerancia á radiación, é un bo punto de partida para o deseño do VeloPix.

	SEUs 1→0	Todos os SEUs	SEUs 1→0
χ^2/nDoF	38/5	60/5	24/5
σ_{sat} [cm^2]	$(0.39 \pm 1.1) \times 10^{-5}$	$(2.00 \pm 0.47) \times 10^{-6}$	$(2.4 \pm 6.1) \times 10^{-5}$
$\mathrm{LET_{th}}$ [MeV cm^2/mg]	0.25 ± 0.15	0.586 ± 0.085	1.547 ± 0.038
W [MeV cm^2/mg]	$(0.68 \pm 2.3) \times 10^4$	$(26.9 \pm 8.2) \times 10^2$	$(2.0 \pm 6.0) \times 10^5$
S	0.843 ± 0.044	0.894 ± 0.031	0.763 ± 0.044

Table 10.5: Resultados dos axustes

10.8 O telescopio Timepix3

Para estudar os prototipos de sensores precísanse diferentes instrumentos. Un deles é un telescopio. O telescopio é o equipamento usado para reconstruír as trazas de partículas que pasan a través do dispositivo a testar. O grupo de mellora do VELO deseñou un telescopio que consiste en 9 planos de sensores de píxeles de silicio lidos por ASICs Timepix3. Cada un dos planos está formado por sensores de silicio tipo *p*-en-*n* de 300 µm de grosor soldados a chips Timepix3. O dispositivo a testar (DUT) pódese colocar no centro do telescopio ou ao final. O centro do telescopio proporciona a mellor resolución espacial ($\sim 2\,\mu$m), e o final do telescopio está pensado para dispositivos grandes.

Os datos son lidos dos chips por medio do sistema Speedy PIxel Detector Readout (SPIDR). O chip pode transmitir ata 80 MHits/s. O SPIDR está deñado para ler Timepix3 e Medipix3 á súa máxima velocidade. A carga dun sistema SPIDR lendo un único chip Timepix3 á máxima velocidade ronda o 55%. Na configuración típica do telescopio úsanse 8 planos e cada SPIDR lee dous planos. Cando se espera unha alta intensidade de partículas cada plano conéctase a unha única tarxeta SPIDR.

A sincronización das tarxetas SPIDR do telescopio faina a Unidade Lóxica do Telescopio (TLU). O firmware desta unidade de triger foi desenvolvido polo autor desta tese. Esta unidade proporciona un reloxo de referencia común de 40 MHz a todas as tarxetas. Ademais, tamén distribúe o sinal T0, que sincroniza todos os contadores de tempo e o sinal de obturador. A TLU pode usar o seu reloxo interno como referencia ou un proporcionado externamente. Ademais, o sinal T0 tamén pode ser proporcionado externamente.

O grupo de mellora do VELO proba frecuentemente os seus prototipos na área experimental norte do CERN. Esta área está alimentada polo acelerador SPS e proporciona un feixe de partículas formado por hadróns cargados con un momento de 180 GeV/c. As partículas chegan á área experimental en chorros de ∼9 s con unha frecuencia de arredor de 47 s.

Para estudar o comportamento do telescopio Timepix3 baixo unha alta incidencia de partículas, este foi instalado no cubículo do grupo de mellora do VELO na área experimental norte do CERN. O telescopio configurouse con 3 planos por cada brazo e unha tarxeta SPIDR para cada plano. Primeiro, os colimadores configuráronse par proporcionar unha intensidade de $\sim 7 \times 10^5$ part/chorro. Tomamos 13 medidas incrementando a intensidade das partículas en diferentes pasos dende $\sim 7 \times 10^5$ part/chorro a $\sim 2.3 \times 10^7$ part/chorro. Esta é a máxima intensidade de partículas que pode ser acadada na área experimental norte debido ás medidas de seguridade contra a radiación. Finalmente tomamos dúas medidas mais á intensidade mais alta incrementando o buffer de

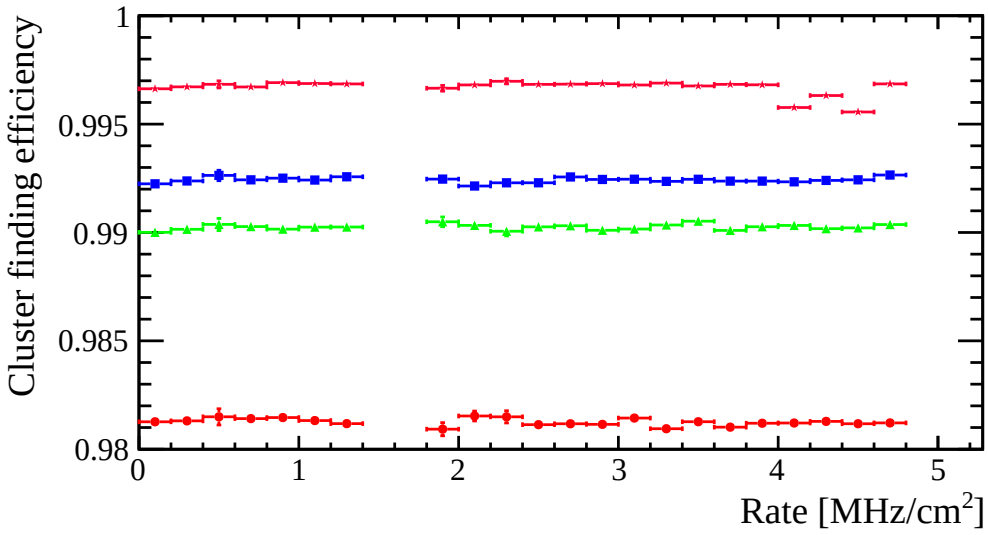

Figure 10.4: Eficiencia de atopar un clúster *vs.* ratio de trazas dos catro planos internos do telescopio. Os puntos vermello, azul, verde e rosa representan as eficiencias do segundo, terceiro, cuarto e quinto plano respectivamente.

adquisición de datos e cambiando a I_{Krum} de 10 a 20.

A ineficiencia do telescopio a alto ratio pode ser detectada estudando tres variables diferentes: A carga de cada clúster recollida por cada plano do telescopio, a calidade das trazas reconstruídas e a eficiencia de trazado do telescopio con respecto ao ratio de partículas.

O valor do tempo por encima do limite (ToT) dado polo Timepix3 é proporcional á carga recollida. Dividín o chorro en intervalos de 9.5 s e axustei unha Landau convolucionada cunha Gausiana á distribución de ToT. Se o ratio de partículas fose comparable co máximo ratio aceptable polo ASIC poderíamos atoparnos con clústers con un ToT mais grande debido á superposición de dous ou mais clústers. Comparando o valor mais probable (MPV) dos axustes non se aprecia ningún efecto.

A altos ratios a calidade das trazas pódese ver comprometida. Ás trazas reconstruídas requiríuselles que tiveran un clúster asociado en cada plano do telescopio. Axustei unha Landau ao χ^2/nDoF das trazas e medín o MPV. Non se aprecian diferencias entre os MPVs ás diferentes intensidades de partículas.

Para estudar a eficiencia de atopar un clúster reconstruín as trazas do telescopio requerindo sinal só en 5 dos planos e despois busquei por sinal no sexto plano. Ademais dado que o telescopio non está perfectamente aliñado co feixe, só analicei a rexión da superficie do sensor onde é probable que unha partícula atopada aí pase pola rexión sensible dos seis planos. A eficiencia de atopar un clúster no plano non incluído na reconstrución é outro indicador da ineficiencia do telescopio a altas intensidades de partículas. A Figura 10.4 mostra os resultados da eficiencia de atopar un clúster. Na figura pódese ver claramente como o ratio de incidencia de partículas non ten efecto algún na eficiencia de atopar un clúster.

Despois de analizar os datos podo concluír que o telescopio segue mantendo a súa eficiencia ata unha intensidade de 5 MHz/ cm^2.

USC
UNIVERSIDADE
DE SANTIAGO
DE COMPOSTELA

Bibliography

[1] K. Olive and P. D. Group, *Review of particle physics*, Chinese Physics C **38** (2014), no. 9 090001. [Cited in pages 5 and 39].

[2] D. Griffiths, *Introduction to Elementary Particles*. Physics textbook. Wiley, 2008. [Cited in page 5].

[3] S. L. Glashow, *Partial-symmetries of weak interactions*, Nuclear Physics **22** (1961), no. 4 579 . [Cited in page 5].

[4] A. Salam and J. Ward, *Electromagnetic and weak interactions*, Physics Letters **13** (1964), no. 2 168 . [Cited in page 5].

[5] S. Weinberg, *A Model of Leptons*, Phys. Rev. Lett. **19** (1967) 1264. [Cited in page 5].

[6] Wikipedia, *Figure of the Standard Model particles*, 2017. [Online; accessed 23-Jan-2017]. [Cited in page 6].

[7] LHCb Collaboration, R. Aaij, B. Adeva, M. Adinolfi, A. Affolder, and etal, *Observation of the resonant character of the $z(4430)^-$ state*, Phys. Rev. Lett. **112** (2014) 222002. [Cited in page 6].

[8] Particle Data Group, C. Patrignani *et al.*, *Review of Particle Physics*, Chin. Phys. **C40** (2016), no. 10 100001. [Cited in page 7].

[9] P. W. Higgs, *Broken Symmetries and the Masses of Gauge Bosons*, Phys. Rev. Lett. **13** (1964) 508. [Cited in page 7].

[10] F. Englert and R. Brout, *Broken Symmetry and the Mass of Gauge Vector Mesons*, Phys. Rev. Lett. **13** (1964) 321. [Cited in page 7].

[11] CMS collaboration, *Observation of a new boson at a mass of 125 GeV with the CMS experiment at the LHC*, Phys. Lett. B **716** (2012) 30 . [Cited in page 7].

[12] ATLAS collaboration, *Observation of a new particle in the search for the Standard Model Higgs boson with the ATLAS detector at the LHC* , Phys. Lett. B **716** (2012) 1 . [Cited in page 7].

[13] R. P. Feynman, *The theory of positrons*, Phys. Rev. **76** (1949) 749. [Cited in page 8].

[14] A. Efremov and A. Radyushkin, *Factorization and asymptotic behaviour of pion form factor in QCD*, Physics Letters B **94** (1980), no. 2 245 . [Cited in page 9].

[15] S. Dulat *et al.*, *New parton distribution functions from a global analysis of quantum chromodynamics*, Phys. Rev. **D93** (2016), no. 3 033006, `arXiv:1506.0744`. [Cited in page 9].

[16] L. A. Harland-Lang, V. A. Khoze, M. G. Ryskin, and W. J. Stirling, *Standard candle central exclusive processes at the Tevatron and LHC*, The European Physical Journal C **69** (2010), no. 1 179. [Cited in page 10].

[17] A. Donnachie and P. Landshoff, *Total cross sections*, Physics Letters B **296** (1992), no. 1 227 . [Cited in page 12].

[18] A. Donnachie and P. Landshoff, *Does the hard pomeron obey Regge factorisation?*, Physics Letters B **595** (2004), no. 1–4 393 . [Cited in page 12].

[19] M. Bahr, J. M. Butterworth, S. Gieseke, and M. H. Seymour, *Soft interactions in Herwig++*, in *Proceedings, 1st International Workshop on Multiple Partonic Interactions at the LHC (MPI08): Perugia, Italy, October 27-31, 2008*, pp. 239–248, 2009. arXiv:0905.4671. [Cited in pages 12 and 35].

[20] S. Dittmaier and M. Schumacher, *The Higgs boson in the standard model—From LEP to LHC: Expectations, searches, and discovery of a candidate*, Progress in Particle and Nuclear Physics **70** (2013) 1 . [Cited in page 13].

[21] C. Blanks, *Strangeness at LHCb*, imperialhep.blogspot.com.es/2011/08/strangeness-at-lhcb.h [Cited in page 14].

[22] Sjöstrand, Torbjörn and Mrenna, Stephen and Skands, Peter, *PYTHIA 6.4 Physics and manual*, JHEP **05** (2006) 026, arXiv:hep-ph/0603175. [Cited in page 14].

[23] T. Sjöstrand, S. Mrenna, and P. Skands, *A brief introduction to PYTHIA 8.1*, Computer Physics Communications **178** (2008), no. 11 852 . [Cited in page 14].

[24] I. Belyaev and etal, *Handling of the generation of primary events in Gauss, the LHCb simulation framework*, Nuclear Science Symposium Conference Record (NSS/MIC) **IEEE** (2010) 1155. [Cited in pages 15 and 41].

[25] H. Drescher, M. Hladik, S. Ostapchenko, T. Pierog, and K. Werner, *Parton-based gribov–regge theory*, Physics Reports **350** (2001), no. 2–4 93 . [Cited in page 15].

[26] www.cern.ch. [Cited in page 17].

[27] G. Arnison, A. Astbury, B. Aubert, and *et al.*, *Experimental observation of isolated large transverse energy electrons with associated missing energy at* $\sqrt{s} = 540\,GeV$, Physics Letters B **122** (1983), no. 1 103 . [Cited in page 17].

[28] ATLAS Collaboration, G. Aad, T. Abajyan, B. Abbott, and etal, *Observation of a new particle in the search for the standard model higgs boson with the ATLAS detector at the LHC*, Physics Letters B **716** (2012), no. 1 1 . [Cited in page 17].

[29] www.nobelprize.org. [Cited in page 17].

[30] www.nobelprize.org. [Cited in page 17].

[31] L. Evans and P. Bryant, *Lhc machine*, Journal of Instrumentation **3** (2008), no. 08 S08001. [Cited in page 17].

[32] ATLAS collaboration, *ATLAS: technical proposal for a general-purpose pp experiment at the Large Hadron Collider at CERN*. CERN-LHCC/94-43. (1994). [Cited in page 17].

[33] CMS collaboration, *Technical Proposal*. CERN-LHCC/94-38. (1994). [Cited in page 17].

[34] LHCb collaboration, *The LHCb detector at the LHC*, JINST **3** (2008) S08005. [Cited in page 17].

[35] LHCb collaboration, *LHCb detector performance*, International Journal of Modern Physics A **30** (2015), no. 07 1530022. [Cited in page 17].

[36] ALICE collaboration, *ALICE: Technical proposal for a Large Ion collider Experiment at the CERN LHC*. CERN-LHCC/95-71. (1995). [Cited in page 17].

[37] TOTEM Collaboration, *Total cross-section, elastic scattering and diffraction dissociation at the Large Hadron Collider at CERN: TOTEM Technical Design Report*, Tech. Rep. CERN-LHCC-2004-002 ; TOTEM-TDR-001, Geneva, 2004. [Cited in page 18].

[38] LHCf Collaboration, *LHCf experiment: Technical Design Report*, Tech. Rep. LHCF-TDR-001 ; CERN-LHCC-2006-004, Geneva, 2006. [Cited in page 18].

[39] MoEDAL Collaboration, *Technical Design Report of the MoEDAL Experiment*, Tech. Rep. CERN-LHCC-2009-006. MoEDAL-TDR-001, CERN, Geneva. [Cited in page 18].

[40] *Secondary beams and areas at CERN*, `http://sba.web.cern.ch`. [Cited in pages 18 and 116].

[41] LHCb Collaboration, R. Aaij, C. A. Beteta, B. Adeva, and etal, *Measurement of $\sigma(pp \to b\bar{b}X)$ at $\sqrt{s} = 7\,TeV$ in the forward region*, Physics Letters B **694** (2010), no. 3 209 . [Cited in page 19].

[42] R. Aaij, A. Affolder, K. Akiba, M. Alexander, and etal, *Performance of the LHCb Vertex Locator*, Journal of Instrumentation **9** (2014), no. 09 P09007. [Cited in page 21].

[43] LHCb Collaboration, R. Antunes-Nobrega, A. França-Barbosa, I. Bediaga, Cernicchiaro, and etal, *LHCb reoptimized detector design and performance: Technical Design Report*. Technical Design Report LHCb. CERN, Geneva, 2003. [Cited in page 21].

[44] LHCb collaboration, *LHCb inner tracker: Technical Design Report*, CERN-LHCC-2002-029. (2002). [Cited in page 21].

[45] LHCb collaboration, *LHCb outer tracker: Technical Design Report*, CERN-LHCC-2001-024. (2001). [Cited in page 21].

[46] LHCb collaboration, *LHCb magnet technical design report*, CERN-LHCC-2000-007. [Cited in page 22].

[47] E. Bos, *Reconstruction of charged particles in the LHCb experiment*. PhD thesis, Amsterdam University, Amsterdam, 2010. [Cited in page 25].

[48] R. Frühwirth, *Application of kalman filtering to track and vertex fitting*, Nuclear Instruments and Methods in Physics Research Section A **262** (1987) 444 . [Cited in page 27].

[49] The LHCb Collaboration, *Measurement of the track reconstruction efficiency at LHCb*, Journal of Instrumentation **10** (2015), no. 02 P02007. [Cited in page 27].

[50] M. Kucharczyk, P. Morawski, and M. Witek, *Primary Vertex Reconstruction at LHCb*, Tech. Rep. LHCb-PUB-2014-044. CERN-LHCb-PUB-2014-044, CERN, Geneva, Sep, 2014. [Cited in page 27].

[51] LHCb collaboration, *Precision measurement of the $B_s^0 - \bar{B}_s^0$ oscillation frequency with the decay $B_s^0 \to D_s^- \pi^+$*, New J. Phys. **15** (2013) 053021, `arXiv:hep-ex/1304.4741`. [Cited in page 29].

[52] LHCb, *LHCb: RICH technical design report*, . [Cited in page 29].

[53] LHCb Collaboration, P. R. Barbosa-Marinho *et al.*, *LHCb muon system: Technical Design Report*. Technical Design Report LHCb. CERN, Geneva, 2001. [Cited in page 29].

[54] LHCb, *LHCb calorimeters: Technical design report*, . [Cited in page 29].

[55] LHCb collaboration, *LHCb computing: Technical Design Report*, CERN-LHCC-2005-019. (2005). [Cited in page 33].

[56] LHCb Collaboration, *LHCb trigger system: Technical Design Report*, LHCb-TDR-10. [Cited in page 33].

[57] LHCb Collaboration, P. R. Barbosa-Marinho *et al.*, *LHCb online system, data acquisition and experiment control: Technical Design Report*. Technical Design Report LHCb. CERN, Geneva, 2001. [Cited in page 34].

[58] M. Clemencic *et al.*, *Recent developments in the LHCb software framework Gaudi*, J. Phys. Conf. Ser. **219** (2010) 042006. [Cited in pages 34 and 115].

[59] R. Brun and F. Rademakers, *ROOT - An Object Oriented Data Analysis Framework*, Nucl. Inst. & Meth. in Phys. Res. A **389** (1997) 81, Proceedings AIHENP'96 Workshop, Lausanne. [Cited in pages 34 and 115].

[60] M. Clemencic *et al.*, *The LHCb Simulation Application, Gauss: Design, Evolution and Experience*, J. of Phys: Conf. Ser. **331** (2011) 032023. [Cited in page 34].

[61] K. Werner, F.-M. Liu, and T. Pierog, *Parton ladder splitting and the rapidity dependence of transverse momentum spectra in deuteron-gold collisions at the BNL Relativistic Heavy Ion Collider*, Phys. Rev. C **74** (2006) 044902. [Cited in page 35].

[62] D. J. Lange, *The EvtGen particle decay simulation package*, Nucl. Instrum. Meth. A **462** (2001) 152. [Cited in page 35].

[63] P. Golonka and Z. Was, *Photos monte carlo: a precision tool for qed correctionsin z and w decays*, The European Physical Journal C - Particles and Fields **45** (2006), no. 1 97. [Cited in page 35].

[64] GEANT4 collaboration, S. Agostinelli *et al.*, *GEANT4: A simulation toolkit*, Nucl. Instrum. Meth. A **506** (2003) 250. [Cited in page 35].

[65] http://lhcb-release-area.web.cern.ch/LHCb-release-area/DOC/boole. [Cited in page 35].

[66] http://lhcb-release-area.web.cern.ch/LHCb-release-area/DOC/moore. [Cited in page 35].

[67] http://lhcb-release-area.web.cern.ch/LHCb-release-area/DOC/brunel. [Cited in page 35].

[68] http://lhcb-release-area.web.cern.ch/LHCb-release-area/DOC/davinci. [Cited in page 35].

[69] LHCb Collaboration, R. Aaij, B. Adeva, M. Adinolfi, A. Affolder, and etal, *Measurement of the ratio of branching fractions* $\mathcal{B}(\overline{b}^0 \to D^{*+}\tau^-\overline{\nu}_\tau)/\mathcal{B}(\overline{b}^0 \to D^{*+}\mu^-\overline{\nu}_\mu)$, Phys. Rev. Lett. **115** (2015) 111803. [Cited in page 36].

[70] *Measurements of long-range near-side angular correlations in proton-lead collisions in the forward region*, Physics Letters B **762** (2016) 473 . [Cited in page 36].

[71] M. Froissart, *Asymptotic behavior and subtractions in the mandelstam representation*, Phys. Rev. **123** (1961) 1053. [Cited in page 39].

[72] A. Martin, *Extension of the axiomatic analyticity domain of scattering amplitudes by unitarity-i*, Il Nuovo Cimento A (1965-1970) **42** (1966), no. 4 930. [Cited in page 39].

[73] A. Martin, *Froissart bound for inelastic cross sections*, Phys. Rev. D **80** (2009) 065013. [Cited in page 39].

[74] ATLAS Collaboration, G. Aad *et al.*, *Measurement of the total cross section from elastic scattering in pp collisions at* $\sqrt{s} = 7$TeV *with the ATLAS detector*, Nuclear Physics B **889** (2014) 486 . [Cited in page 39].

[75] ATLAS Collaboration, M. Aaboud *et al.*, *Measurement of the total cross section from elastic scattering in pp collisions at with the ATLAS detector*, Physics Letters B **761** (2016) 158 . [Cited in pages 39 and 70].

[76] TOTEM Collaboration, G. Antchev *et al.*, *First measurement of the total proton-proton cross-section at the lhc energy of* $\sqrt{s} = 7$ TeV, EPL (Europhysics Letters) **96** (2011), no. 2 21002. [Cited in pages 39 and 70].

[77] TOTEM Collaboration, G. Antchev *et al.*, *Luminosity-independent measurement of the proton-proton total cross section at* $\sqrt{s} = 8$ TeV, Phys. Rev. Lett. **111** (2013) 012001. [Cited in pages 39 and 70].

[78] TOTEM Collaboration, G. Antchev *et al.*, *Measurement of proton-proton elastic scattering and total cross-section at* $\sqrt{s} = 7\,\text{TeV}$, EPL (Europhysics Letters) **101** (2013), no. 2 21002. [Cited in page 39].

[79] TOTEM Collaboration, G. Antchev *et al.*, *Luminosity-independent measurements of total, elastic and inelastic cross-sections at* $\sqrt{s} = 7\,\text{TeV}$, EPL (Europhysics Letters) **101** (2013), no. 2 21004. [Cited in page 39].

[80] ALICE Collaboration, B. Abelev *et al.*, *Measurement of inelastic, single- and double-diffraction cross sections in proton–proton collisions at the LHC with ALICE*, The European Physical Journal C **73** (2013), no. 6 2456. [Cited in pages 39 and 70].

[81] ATLAS Collaboration, G. Aad *et al.*, *Measurement of the inelastic proton-proton cross-section at* $\sqrt{s} = 7\text{TeV}$ *with the ATLAS detector*, Nature Communications **2** (2011) . [Cited in pages 39 and 70].

[82] CMS Collaboration, S. Chatrchyan *et al.*, *Measurement of the inelastic proton - proton cross section at* $\sqrt{s} = 7\text{TeV}$, Physics Letters B **722** (2013), no. 1 - 3 5 . [Cited in page 39].

[83] LHCb Collaboration, R. Aaij *et al.*, *Measurement of the inelastic pp cross-section at a centre-of-mass energy of* $\sqrt{s} = 7\text{TeV}$, Journal of High Energy Physics **2015** (2015), no. 2 129. [Cited in pages 39 and 70].

[84] ALICE Collaboration, B. Abelev *et al.*, *Measurement of inelastic, single- and double-diffraction cross sections in proton–proton collisions at the LHC with ALICE*, The European Physical Journal C **73** (2013), no. 6 2456. [Cited in pages 39 and 70].

[85] ATLAS Collaboration, M. Aaboud *et al.*, *Measurement of the inelastic proton-proton cross section at* $\sqrt{s} = 13\text{TeV}$ *with the ATLAS detector at the LHC*, Phys. Rev. Lett. **117** (2016) 182002. [Cited in pages 39 and 70].

[86] CMS, H. Van Haevermaet, *Measurement of the inelastic proton-proton cross section at* $\sqrt{s} = 13$ *TeV*, PoS **DIS2016** (2016) 198, `arXiv:1607.0203`. [Cited in pages 39 and 70].

[87] The Pierre Auger Collaboration, P. Abreu and etal, *Measurement of the proton-air cross section at* $\sqrt{s}$=57 TeV *with the pierre auger observatory*, Phys. Rev. Lett. **109** (2012) 062002. [Cited in pages 40 and 70].

[88] J. Wenninger, *Energy Calibration of the LHC Beams at 4 TeV*, Tech. Rep. CERN-ATS-2013-040, CERN, Geneva, May, 2013. [Cited in page 47].

[89] M. M. Block, L. Durand, P. Ha, and F. Halzen, *Comprehensive fits to high energy data for* σ, ρ, *and B and the asymptotic black-disk limit*, Phys. Rev. **D92** (2015), no. 11 114021, `arXiv:1511.0240`. [Cited in pages 47, 56, 69, 70, 138, and 153].

[90] A. Hoecker *et al.*, *TMVA: Toolkit for Multivariate Data Analysis*, PoS **ACAT** (2007) 040, `arXiv:physics/0703039`. [Cited in page 47].

[91] R. Corke and T. Sjöstrand, *Multiparton interactions with an x-dependent proton size*, Journal of High Energy Physics **2011** (2011), no. 5 9. [Cited in page 48].

[92] *Summary of ATLAS Pythia 8 tunes*, Tech. Rep. ATL-PHYS-PUB-2012-003, CERN, Geneva, Aug, 2012. [Cited in page 48].

[93] P. Skands, S. Carrazza, and J. Rojo, *Tuning pythia 8.1: the monash 2013 tune*, The European Physical Journal C **74** (2014), no. 8 3024. [Cited in page 48].

[94] C. Barschel and M. Ferro-Luzzi, *Precision luminosity measurement at LHCb with beam-gas imaging*. PhD thesis, RWTH Aachen U., 2014, Presented 05 Mar 2014. [Cited in page 56].

[95] T. L. collaboration, *Precision luminosity measurements at lhcb*, Journal of Instrumentation **9** (2014), no. 12 P12005. [Cited in page 56].

[96] L. Collaboration, *LHCb VELO Upgrade Technical Design Report*, Tech. Rep. CERN-LHCC-2013-021. LHCB-TDR-013, Nov, 2013. [Cited in page 82].

[97] Álvaro Dosil Suárez, *The LHCb VELO upgrade*, Nuclear Instruments and Methods in Physics Research Section A: Accelerators, Spectrometers, Detectors and Associated Equipment **824** (2016) 396 , Frontier Detectors for Frontier Physics: Proceedings of the 13th Pisa Meeting on Advanced Detectors. [Cited in page 82].

[98] L. Collaboration, *LHCb Tracker Upgrade Technical Design Report*, Tech. Rep. CERN-LHCC-2014-001. LHCB-TDR-015, Feb, 2014. [Cited in page 82].

[99] L. Collaboration, *LHCb PID Upgrade Technical Design Report*, Tech. Rep. CERN-LHCC-2013-022. LHCB-TDR-014, Nov, 2013. [Cited in page 83].

[100] *LHCb Trigger and Online Upgrade Technical Design Report*, Tech. Rep. CERN-LHCC-2014-016. LHCB-TDR-016, May, 2014. [Cited in page 84].

[101] F. Rey-García *et al.*, *Fabrication of metal-on-glass high-pitch adapters between vlsi electronics and semiconductor sensors by laser ablation*, Journal of Lightwave Technology **31** (2013) 2327. [Cited in page 86].

[102] E. Pérez *et al.*, *Laser micromachining and characterization of metal-on-glass high density pitch adapters*, Journal of Microelectromechanical Systems **24** (2015) 1479. [Cited in page 86].

[103] X. Llopart, R. Ballabriga, M. Campbell, L. Tlustos, and W. Wong, *Timepix, a 65k programmable pixel readout chip for arrival time, energy and/or photon counting measurements*, Nuclear Instruments and Methods in Physics Research Section A: Accelerators, Spectrometers, Detectors and Associated Equipment **581** (2007), no. 1–2 485 , VCI 2007 Proceedings of the 11th International Vienna Conference on Instrumentation. [Cited in page 86].

[104] T. Poikela *et al.*, *Architectural modeling of pixel readout chips velopix and timepix3*, Journal of Instrumentation **7** (2012), no. 01 C01093. [Cited in page 87].

[105] R. Ballabriga, W. Wong, and X. Llopart, *Medipix3 manual*. 2009. [Cited in pages 91 and 93].

[106] K. Akiba *et al.*, *Characterisation of medipix3 silicon detectors in a charged-particle beam*, Journal of Instrumentation **11** (2016), no. 01 P01011. [Cited in page 91].

[107] F. Faccio, *COTS for the LHC radiation environment: The rules of the game*, in *Proceedidngs, 6th Workshop on Electronics for LHC experiments, Cracow, Poland, 11-15 Sep 2000*, pp. 50–65, 2000. [Cited in page 91].

[108] `Cyclotron Resource Centre at Louvain-la-Neuve`. [Cited in page 95].

[109] V. Kraus *et al.*, *Fitpix — fast interface for timepix pixel detectors*, Journal of Instrumentation **6** (2011), no. 01 C01079. [Cited in page 95].

[110] S. Bonacini, K. Kloukinas, and A. Marchioro, *Development of seu-robust, radiation-tolerant and industry-compatible programmable logic components*, Journal of Instrumentation **2** (2007), no. 09 P09009. [Cited in pages 108 and 110].

[111] K. Akiba *et al.*, *The timepix telescope for high performance particle tracking*, Nuclear Instruments and Methods in Physics Research Section A: Accelerators, Spectrometers, Detectors and Associated Equipment **723** (2013) 47 . [Cited in page 111].

[112] K. Akiba *et al.*, *Charged Particle Tracking with the Timepix ASIC*, `arXiv:1103.2739`. [Cited in page 111].

[113] T. Poikela *et al.*, *Timepix3: a 65k channel hybrid pixel readout chip with simultaneous toa/tot and sparse readout*, Journal of Instrumentation **9** (2014), no. 05 C05013. [Cited in page 111].

[114] F. Krummenacher, *Pixel detectors with local intelligence: an ic designer point of view*, Nuclear Instruments and Methods in Physics Research Section A: Accelerators, Spectrometers, Detectors and Associated Equipment **305** (1991), no. 3 527 . [Cited in page 111].

[115] J. Visser *et al.*, *SPIDR: a read-out system for Medipix3 & Timepix3*, Journal of Instrumentation **10** (2015), no. 12 C12028. [Cited in page 113].

[116] C. G. Larrea *et al.*, *IPbus: a flexible Ethernet-based control system for xTCA hardware*, Journal of Instrumentation **10** (2015), no. 02 C02019. [Cited in page 113].

[117] V. Blobel, *Software alignment for tracking detectors*, Nucl. Instr. Meth. **A566** (2006), no. 1 5 . [Cited in page 115].

[118] L. Landau, *On the energy loss of fast particles by ionization*, J. Phys. (USSR) **8** (1944) 201. [Cited in page 120].